

THÈSE DE DOCTORAT

Présentée à

L'Université de Lille

Pour l'obtention du

GRADE DE DOCTEUR

Ecole Doctorale : Sciences de la Matière, du Rayonnement et de l'Environnement

Discipline : Energétique, thermique, combustion

Par

Lucia GIARRACCA

Impact of lignocellulosic biofuels on NO_x formation in premixed laminar flames

Soutenue le 17 Décembre 2018 devant la commission d'examen :

V. DIAS	Chercheure, IMMC, Université Catholique de Louvain, Belgique	Rapportrice
P. A. GLAUDE	Directeur de Recherche CNRS, LRGP, Université de Lorraine	Rapporteur
Z. SERINYEL	Maître de Conférences, ICARE, Université d'Orléans	Examinatrice
C. LACOUR	Maître de Conférences, CORIA, INSA de Rouen	Examinatrice
P. DESGROUX	Directrice de Recherche CNRS, PC2A, Université de Lille	Directrice de thèse
L. GASNOT	Professeur, PC2A, Université de Lille	Co-directeur de thèse

«Siamo chimici, cioè cacciatori: nostre sono “le due esperienze della vita adulta” di cui parlava Pavese, il successo e l’insuccesso, uccidere la balena bianca o sfasciare la nave; non ci si deve arrendere alla materia incomprensibile, non ci si deve sedere. Siamo qui per questo, per sbagliare e correggerci, per incassare colpi e renderli. Non ci si deve mai sentire disarmati: la natura è immensa e complessa, ma non è impermeabile all’intelligenza; devi girarle intorno, pungere, sondare, cercare il varco o fartelo.».

(Primo Levi, “Il sistema periodico”)

*À mon père et à ma mère,
pour avoir toujours encouragé ma passion pour la science.*

Remerciements

Cette thèse s'est déroulée au laboratoire de Physico-Chimie des Processus de Combustion et de l'Atmosphère (PC2A-UMR 8522) à l'Université de Lille. Elle a été financée par la Région des Hauts de France et l'Université de Lille à qui j'adresse mes sincères remerciements.

Je tiens à remercier tout d'abord ma directrice de thèse Mme Pascale Desgroux, Directrice de Recherche CNRS, pour sa disponibilité, ses conseils et pour avoir su partager son savoir et sa rigueur scientifique. Je remercie aussi mon co-directeur de thèse M. Laurent Gasnot, Professeur à l'Université de Lille et Directeur du laboratoire PC2A pour son soutien tout au long de ce travail, ses compétences, son enthousiasme et sa disponibilité. Merci pour l'autonomie qu'ils ont su m'accorder.

Je souhaiterais de même remercier les membres du jury. Merci à M. Pierre Alexandre Glaude, Directeur de Recherche CNRS au laboratoire LRGP-Université de Lorraine, d'avoir endossé le double rôle de président du jury et de rapporteur, ainsi qu'à Mme Véronique Dias, Chercheur au IMMC-Université Catholique de Louvain d'avoir accepté d'être rapportrice. Merci également à Mme Corine Lacour, Maître de Conférences au CORIA-INSA-Université de Rouen, et Mme Zeynep Serinyel, Maître de Conférences à ICARE-Université d'Orléans, pour avoir accepté de faire partie de ce jury de thèse. Je suis très reconnaissant pour votre lecture attentive du manuscrit de thèse, ainsi que pour vos questions et remarques très pertinentes pendant la soutenance qui ont permis d'alimenter ma réflexion.

Je remercie vivement M. Guillaume Vanhove, Maître de Conférences au PC2A-Université de Lille, pour ses conseils lors des mesures par Chromatographie en Phase Gazeuse. Je remercie également Mme Nathalie Lamoureux, Ingénieure de Recherche au PC2A pour les importantes contributions apportées à ce travail de thèse.

Mes remerciements vont évidemment aux Enseignants et Chercheurs du PC2A et en particulier : Benjamin Hanoune, Xavier Mercier, Abderrahman El Bakali et Luc Sy Tran pour leur précieux conseils. Une pensée spéciale s'adresse à Laure Pillier et mon compatriote italien Alessandro Faccinnetto. Votre disponibilité, votre compétence, votre bonne humeur ainsi que votre soutien tant sur le plan scientifique que moral m'ont été d'une aide inestimable tout au long de ces années et pour mon avenir. Mention spéciale à Nicolas Visez, que je remercie pour avoir su capturer la beauté de mes flammes dans des photos magnifiques, mais également pour sa sympathie et son enthousiasme.

Je tiens à remercier l'ensemble du personnel du laboratoire PC2A et plus particulièrement Sylvie Gosselin, Valerie Vilain, Sadio Soumare, Pascal Demaux, Sébastien Germain, Sébastien Batut, Olivier Hombert et Hicham Kechmir, sans oublier Béatrice Lecrenier. Merci à toutes et tous pour votre gentillesse, votre disponibilité et votre bonne humeur. Je tiens à préciser que sans votre présence ce travail n'aurait pu aboutir. Un remerciement plus particulier s'adresse à Sylvie

Gosselin pour son aide et ses conseils lors des mesures par Chromatographie en Phase Gazeuse et par Spectrométrie de Masse.

Mes remerciements vont évidemment à l'ensemble des Doctorants, Post Doctorants, stagiaires du PC2A, les anciens comme les nouveaux, pour leur présence et tous les bons moments lors de ces années passées au laboratoire : Yann, Olivier, Damien, Hwasup, Junteng, Carolina, Quan, Nabil, Lambrini, Camille, Arnould, Sonia, Mona, Eliane, Mohamad, Linh-Dan, Florent et Manu. Je remercie particulièrement Ankita, Jinane, et Dorra pour votre présence dans les bons et les mauvais moments et pour votre précieuse amitié. Un remerciement spécial va à Lise, qui est arrivée au laboratoire à la fin de ma thèse, mais qu'est entrée tout de suite dans mon cœur.

Quel que soit le chemin que l'on emprunte, il est important de se souvenir d'où l'on vient. Je souhaiterais remercier à ce titre mes amis de longue date, et avec qui j'ai pu garder contact malgré la distance : Caterina, Imma, Marianna et Gabriella. Merci pour votre soutien quotidien à distance, pour les soirées au téléphone, pour les voyages, pour les rencontres à Paris et à Lille. Nous avons fait beaucoup de chemin, ce qui nous a amenées à être un peu loin les unes des autres, mais notre amitié solide nous fait surpasser la distance.

Je souhaiterais remercier M. Andrea D'Anna, Professeur à l'Université de Naples qui a su me transmettre sa passion pour la recherche sur la combustion pendant mes études d'ingénieur, pour l'estime qu'il m'a témoignée, pour son amitié et ses encouragements à suivre mes aspirations pour l'avenir.

Je tiens à exprimer ma plus profonde gratitude à ma famille et à ma belle-famille pour leur soutien, leur confiance ainsi que leurs encouragements. Un remerciement spécial va à mon frère Giorgio et ma tante Sara pour votre présence malgré la distance, votre bonheur et pour toutes les escapades à Lille dans les moments plus compliqués. Je remercie de tout cœur ma mère pour m'avoir appris à affronter les difficultés la tête haute sans perdre l'espoir et le sourire; et mon père pour avoir suscité mon enthousiasme pour la chimie dès mon plus jeune âge et pour avoir toujours cru en moi. Merci à vous deux pour tous les sacrifices que vous avez consentis pour que Giorgio et moi puissions avoir les moyens de réussir.

Enfin je remercie de tout cœur Cédric pour avoir toujours été à mes côtés dans les bons et les mauvais moments, pour m'avoir encouragée, soutenue et conseillée. Grâce à cette thèse nous nous sommes rencontrés, mais sans toi je ne serais pas arrivé jusqu'au bout.

Contents

General introduction.....	15
Chapter I Context of the study	19
1. Combustion and environment	19
1.1. World energy scenario	19
1.2. Impact of combustion on the atmosphere	21
1.3. Combating GHG and pollutant emissions	23
2. Biofuels	27
2.1. First generation of biofuels	29
2.2. Second generation of biofuels	31
2.3. Third generation of biofuels	32
2.4. Fourth generation of biofuels.....	33
3. Lignocellulosic biofuels	35
3.1. Lignocellulosic biomass: characteristics, processes... ..	35
3.2. ...and economical point of view.....	38
3.3. Advanced lignocellulosic biofuels.....	39
3.3.1. Introduction	39
3.3.2. Properties of some cyclic ethers	42
3.3.3. Review of oxidation studies of furan and THF in the intermediate and high temperature range	43
3.3.3.1. Furans	43
3.3.3.2. Tetrahydrofurans	50
4. Conclusion	58
Chapter II: Nitrogen oxides chemistry	59
1. Mechanisms of formation of NO in combustion processes	59
1.1. Thermal-NO mechanism	59
1.2. Prompt-NO mechanism	60
1.2.1. The “CH + N ₂ ⇌ products” reaction	61
1.2.2. Thermochemistry properties of NCN.....	64
1.2.3. NO modelling	65
1.3. Fuel-NO mechanism.....	67
1.4. NO formation mechanism via N ₂ O.....	69
1.5. NO formation mechanism via NNH	70

2.	Links between NO _x and oxygenated fuels	71
2.1.	Biodiesel	71
2.2.	Alcohols and ethers.....	75
3.	Conclusion	81
Chapter III Operating set-up.....		82
1.	Introduction.....	82
2.	The flames under investigation	83
3.	Experimental set-up	86
3.1.	Fuel feeding section.....	87
3.2.	The burner and combustion chamber	88
4.	Gas chromatography analysis set up.....	90
4.1.	The sampling system and the injection procedure.....	90
4.2.	The MS–Gas-Chromatograph (GC/MS).....	95
4.3.	The FID/TCD -Gas-Chromatograph (GC/FID/TCD).....	97
5.	The laser diagnostics set-up	103
5.1.	The laser source: Nd-YAG/Dye laser	104
5.2.	The collection signal system.....	105
6.	Chemical kinetics modelling.....	107
6.1.	The numerical approach to characterize premixed laminar flames	107
6.2.	Calculation tools: Cantera.....	108
6.2.1.	Introduction	108
6.2.2.	Description of the Cantera software.....	109
6.2.3.	Kinetic mechanism in the Cantera format.....	110
6.2.4.	Premixed laminar burner-stabilized flame code.....	116
7.	Conclusion	118
Chapter IV Study of fuel oxidation		119
1.	Experimental	119
1.1.	Identification of the chemical species.....	119
1.2.	Determination of species mole fractions	121
1.2.1.	Calibration methods	121
1.2.2.	Formaldehyde calibration.....	122
1.2.2.1.	Preparation of the solution.....	123
1.2.2.2.	Addition of internal standard.....	124
1.3.	H ₂ O calculation.....	126
1.4.	Main GC results.....	127

1.5. Error estimation	128
2. Modelling	129
2.1. The Tran mechanism	130
2.2. The Fenard mechanism.....	134
2.3. Experimental - modelling comparison.....	136
2.3.1. Study of the methane flames	139
2.3.1.1. Fuel and major species	139
2.3.1.2. Intermediate species C ₂ -C ₃	142
2.3.1.3. Oxygenated intermediates	144
2.3.2. Study of the furan flames	146
2.3.2.1. Fuel and major species	146
2.3.2.2. C ₂ intermediates.....	149
2.3.3. Study of the THF flames	150
2.3.3.1. Fuel and major species	151
2.3.3.2. C ₂ Intermediates.....	153
2.3.4. Comparison F -THF: C ₃ -C ₄ and oxygenated intermediates	154
2.3.4.1. C ₃ -C ₄ hydrocarbon intermediates	155
2.3.4.2. Oxygenated species	158
2.4. Summary of the comparison experiments/modelling results.....	160
3. Conclusion	161
Chapter V: Determination of NO and CH profiles by laser diagnostics	162
1. General theory of linear LIF	162
2. Fluorescence signal	168
3. NO concentration determination in flame.....	169
3.1. NO measurements in flames by LIF: bibliography study.....	169
3.2. Excitation and collection bands selection.....	172
3.3. Determination of the quenching rate	175
3.4. Determination of the profile of NO relative population	177
3.4.1. Raw LIF profile determination.....	177
3.4.2. Corrections of fluorescence signal	178
3.4.3. Furan absorption: specific correction of LIF signal for FM1.0 and FM1.2 flames	181
3.5. Linking procedure between the flames.....	185
3.6. NO doping method calibration	187
3.7. NO mole fraction profiles.....	189

4.	CH concentration determination in flame	191
4.1.	CH Spectroscopy	191
4.2.	Selection of the excitation/detection scheme for CH measurements.....	194
4.3.	Determination of the CH relative profiles	200
4.3.1.	Relative CH profile in each flame	200
4.3.2.	Linking procedure between the flames	201
4.3.3.	LIF signal calibration: Cavity ring down spectroscopy	202
4.4.	CH mole fraction profiles	205
5.	Results and discussion	207
5.1.	Equivalence ratio effect	207
5.2.	Fuel effect.	210
5.2.1.	Methane flames	211
5.2.2.	Furan flames	212
5.2.3.	THF flames.....	215
5.3.	Comparison between experimental and numerical results for CH	216
6.	Conclusions.....	219
	General conclusions and perspectives	221
	References	224
	Annex A.....	241
	Mass flow controller calibration.....	241
	Furan volumetric flow controller calibration.....	241
	Balloons method	241
	Mass Consumption Calibration (CMC)	244
	Annex B.....	247
	Temperature measurements by multi-line NO-LIF thermometry	247
	Annex C.....	250
	Mole profiles of chemical species in each flame	250
	Flame M1.0.....	250
	Hydrocarbons	251
	Oxygenated species.....	252
	Flame M1.2.....	253
	Stable species	253
	Hydrocarbons	254
	Oxygenated species.....	255
	Flame FM1.0.....	256

Stable species	256
Hydrocarbons	257
Oxygenated species	259
Flame FM1.2.....	260
Stable species	260
Hydrocarbons	261
Oxygenated species	263
Flame THFM1.0	264
Stable species	264
Hydrocarbons	265
Oxygenated species	267
Flame THFM1.2	269
Stable species	269
Hydrocarbons	270
Oxygenated species	272
Experimental peak mole fractions in each flame	274
Résumé	276
Abstract.....	278

General introduction

Energy production from combustion of fossil fuels has led to a significant increase of greenhouse gas (GHG) and air pollutants emissions, and thus has contributed to the greenhouse effect and induced global warming. Emissions of pollutants related to combustion processes also cause a lot of disturbances on the environment (photochemical pollution, acid rain, production of tropospheric ozone, ...) and on humans (respiratory disorders, carcinogens, ...). However, despite its known harmful effects, global energy production from fossil fuels combustion still accounts for over 80% of total primary energy production worldwide [1].

In order to limit the levels of environmentally harmful emissions from fossil fuels combustion, strict restrictions imposed by legislation have been implemented. This gives incentive to optimize the efficiency of energy production, to decrease pollutants emissions and more specifically to find cleaner energy sources. Particularly in 2015 during the COP21 organized in Paris, an agreement was signed, which provides the limitation of global temperature increase to 2°C by reducing GHG emissions caused by fossil fuels such as oil, gas and coal combustion. This agreement was adopted by 197 countries and was officially implemented on April 22, 2016, Earth Day. The European Community has also regulated the emissions of carbon monoxide (CO), nitrogen oxides (NO_x), unburned hydrocarbons (HC) and particulates since 1992 by introducing Euro standards. In addition to these standards, CO₂ emissions are also regulated for transportation. The European Parliament has set a target of 95 grams of CO₂ per kilometer by 2020 for passenger cars, by a regulation published on April 23, 2009. This new limitation should be the keystone of the new EURO 6d standard expected by 2021 at the latest.

Biofuels are commonly presented as an alternative to traditional automotive fuels, although their use is not new. The EU has defined a set of sustainability criteria to ensure that the use of biofuels (used in transport) and bioliquids (used for electricity and heating) is done in a way that guarantees real carbon savings and protects biodiversity. To be considered sustainable, biofuels must achieve greenhouse gas savings of at least 35% in comparison to fossil fuels [2]. This savings requirement rises to 60% in 2018 for new production plants. All life cycle emissions have to be taken into account when calculating greenhouse gas savings (emissions from crops,

processing, and transport. Depending on the sources and production processes, it is possible to distinguish four “generation” of biofuels:

- First-generation: biofuels mainly made from vegetable oils, sugars and edible starch;
- Second-generation: biofuels made from vegetable matter as agricultural or forestry residues;
- Third-generation: biofuels made from algae;
- Fourth generation: biofuels made from bio-engineered biomass and bacteria with high carbon capture efficiency.

There is a worldwide interest for second-generation biofuels. To increase the quantity of biofuels potentially available, new resources from non-food plants are used: agricultural residues and forest waste. In this way, the production of these biofuels can be made from a wide variety of non-food crops.

Biomass feedstock is mainly constituted by lignocellulose which yields to oxygenated molecules. These compounds are called "biochemical platforms" because they can serve as a basis for the synthesis of a wide variety of compounds of interest. Among the various compounds which can be obtained from bio-chemical platforms, the cyclic ethers as the furan and tetrahydrofuran family arouse particular interest due to their physical properties similar to transportation fossil fuels.

In order to understand their combustion, these cyclic ethers have been the subject of several fundamental studies about their kinetic behavior during oxidative and pyrolytic processes in laboratory reactors. Detailed chemical mechanisms representative of their oxidation and pyrolysis have been developed. However, it is worth noting that only few studies have been performed in flame conditions and they all concern the combustion of pure furanic compounds, while it is expected that as engine fuels, they will be blended with some other hydrocarbon fuels. The previous studies have highlighted the formation of different pollutant emissions, in particular toxic oxygenated compounds such as aldehydes (formaldehyde, acetaldehyde, acrolein, 2-butenal); but none has concerned the NO_x emissions, which nevertheless constitute a large family of pollutants in combustion processes and play a crucial role in atmospheric chemistry.

In this context, the aim of this thesis is twofold (1) to study the chemical structure of flames of methane/furan and methane/tetrahydrofuran blends in stoichiometric and slightly rich conditions, and (2) to evaluate the impact of the combustion of these oxygenated compounds on the non-thermal NO formation, mainly the prompt-NO formation. Furan (F) and tetrahydrofuran (THF) have been chosen because they are the core of the oxidation of the more complex furanic compounds, and the results made for these cyclic ethers can be applied also to the other derivatives. In particular, we are interested to how the different degree of unsaturation of these model-biofuels can affect the prompt-NO formation. Several studies mainly performed for linear oxygenated compounds in engines have shown a strong relationship between NO_x emissions and chemical characteristics of biofuels, especially their degree of unsaturation and ramification, and the oxygen content [3–5]. But to date there is no clear understanding of the involved process.

This thesis is essentially focused on obtaining a detailed database of quantitative species profiles in several low-pressure premixed flames aiming to serve as references for validating detailed chemical mechanisms. The intermediate and stable species have been measured by using Gas Chromatography (GC) apparatus coupled with FID/TCD or MS detectors, which has allowed to quantify 65 chemical species ranging from C₀ to C₆. For the NO formation analysis, the Laser Induced Fluorescence (LIF) technique has been applied in order to measure the NO mole fraction profiles together with the CH radical mole fraction profiles. Indeed, in non-thermal NO condition, the prompt-NO mechanism being predominant, it is essential to measure the CH radical involved in the initiation reaction of the prompt-NO sequence. Two literature chemical mechanisms have then been evaluated in our flame conditions: the mechanism of Tran et al. [6] and the mechanism of Fenard et al. [7]. Particularly their ability to predict the CH radical mole fraction has been tested. Results show that improvements of the mechanisms are necessary before the prompt-NO sub-mechanism [8] can be implemented.

Following this introduction, this thesis includes 5 main chapters and a general conclusion with perspectives:

- The first chapter presents the context of the study regarding the lignocellulosic biofuels and reviews the several studies in the literature on the oxidation of furanic compounds, particularly F and THF;
- In the second chapter the different mechanisms of NO formation are presented with a reference to the effect of biofuels on NO_x emissions in particular in engine conditions;
- The experimental set-up and the analytical techniques used to study low pressure CH₄/F/THF/O₂/N₂ flames are presented in the third chapter;
- In the fourth chapter, the GC study of the oxidation of F and THF in our flames by comparing experimental and simulated results is discussed;
- The fifth chapter is devoted to the NO and CH formation in our flames. The method to quantify the mole fraction profiles of NO and CH radical by using LIF are presented and the experimental and simulated results are discussed.

This thesis was funded by the Région Hauts-de-France and University of Lille.

Chapter I Context of the study

1. Combustion and environment

The world energy profile is currently dominated by the hegemony of fossil fuel resources and the combustion-based plants are the main sources of energy transformation for this century.

The energy transition is still out of reach and the technological progress achieved in the field of alternative and renewable energy is not yet sufficient to meet the world's energy needs. These needs are also growing strongly due to the increase in the world population and to the rising standard of living in emerging countries.

Energy, combustion and air pollution are three closely interrelated topics. The impact of combustion processes on the environment is the cause of a significant increase in air pollution, mainly due to emissions from plants for the production of electricity, diesel and gasoline engines, fires and coal combustion in industrial and domestic applications.

The strict restrictions imposed by legislation illustrate the willingness to reduce the levels of environmentally harmful emissions from fossil fuels combustion. This gives incentive to optimize the efficiency of energy production, to decrease pollutant emissions and more specifically to find cleaner energy sources.

1.1. World energy scenario

Energy and combustion have always been central in the history of humanity and have changed the lifestyle of people in society over the millennia.

Since the advent of the industrial era in the mid-nineteenth century, humanity has been increasing its energy consumption in multiple forms to meet the demands of modern society (industry, transport, heating, electricity, etc. ...). Nowadays, the increase of the population of the planet and the increase of the standard of living cause a big increase in the energy demand.

To illustrate this existing situation, the Fig.I.1 shows the evolution of world energy consumption in millions of tons of oil equivalent (Mtoe) from 1971 to 2016 in different economic areas. The energy demand of emerging countries, such as India and China, has grown exponentially in the last twenty years, with respect to the countries of the Organization for Economic Cooperation and Development (OECD), which regroups the more industrialized countries such as USA, European Community, Australia, Canada, and Japan. Globally the world energy demand has grown steadily, from nearly 5,523 Mtoe in 1971 to 13,761 Mtoe in 2016 [1]. This trend, if it were to continue for the next 40 years, would lead to more than doubling global energy demand by 2050 compared to the demand in 2016.

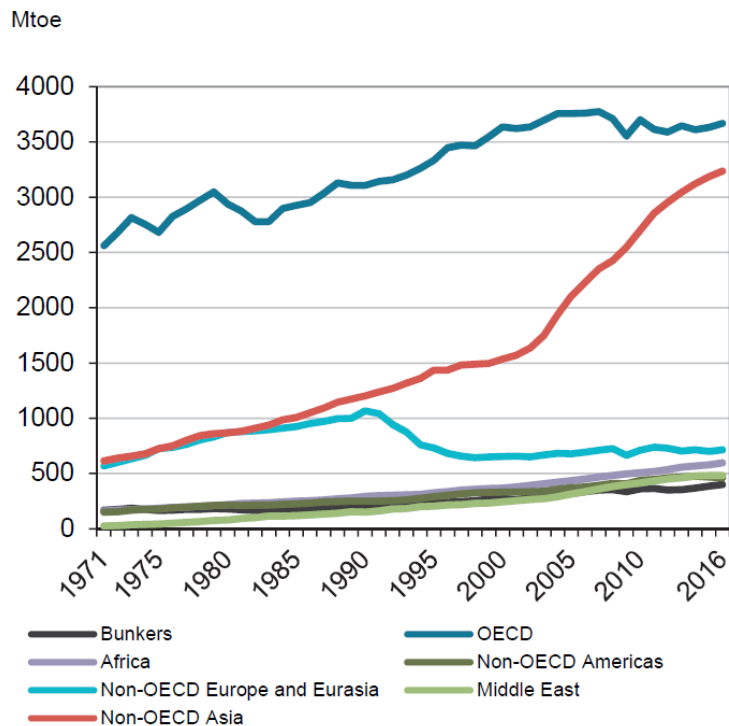
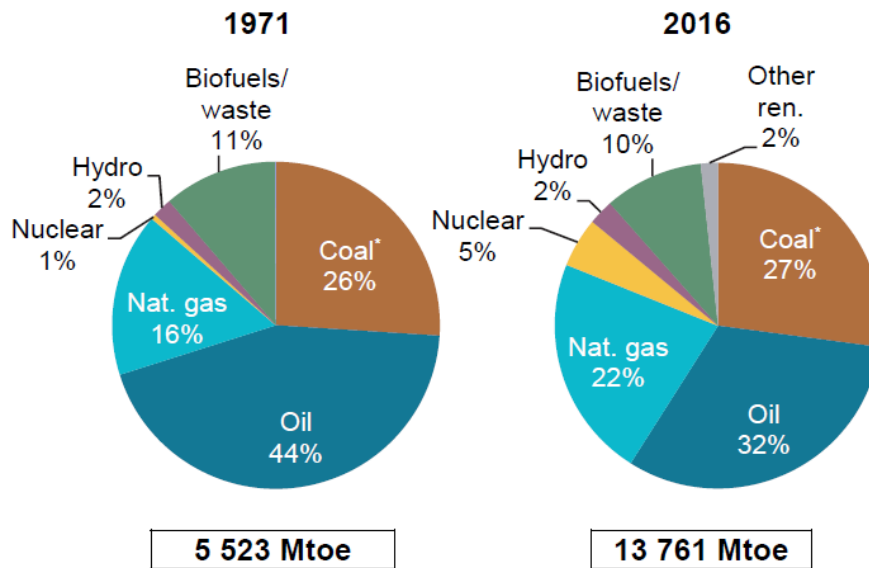


Fig I.1: World energy consumption by region [1].

Global energy production from combustion of fossil fuels accounts for over 80% of total primary energy production worldwide [1]. In 2016, oil is the primary source of energy, accounting for 32% of global requirements, followed by coal (27%) and natural gas (22%). Renewable energies reach 14% and nuclear energy accounts for 5% of global energy supply [1]. Fig.I.2 compares the global energy share in 1971 and 2016.



* In this graph peat and oil shale are aggregated with coal.

Fig I.2: Total primary energy supply by fuel. [1].

However, the excessive use of fossil fuels in the modern economic system is responsible for many water and air pollution phenomena, affecting the health of the people as well as ecosystems. This is notably the case for Greenhouse Gas (GHG) emissions of anthropogenic origin which lead to significant climatic changes.

1.2. Impact of combustion on the atmosphere

Pollutants emitted by combustion processes can have different effects on human health and the atmosphere. These pollutants can be classified into primary or secondary pollutants categories, according to the degree of their reactivity in the atmosphere. Primary pollutants are directly emitted into the atmosphere, while the secondary pollutants are all the pollutants which are formed in the atmosphere through chemical reactions between the various substances present.

The main primary emissions released to the atmosphere are carbon dioxide (CO₂), carbon monoxide (CO), nitrogen oxides (NO_x), sulfur dioxide (SO₂), volatile organic compounds (VOCs), polycyclic aromatic hydrocarbons (PAHs) and soot. Except CO₂, the others are pollutants that are hazardous to health.

CO₂ is the main greenhouse gas (GHG) from anthropogenic origin and is largely responsible for global warming.

CO is emitted during incomplete combustion processes. It can cause poisoning, cardiovascular disorders, and vertigo in humans that can lead to death.

NO_x includes nitrogen monoxide (NO), nitrogen dioxide (NO₂) and nitrous oxide (N₂O). NO is the main nitrogen compound mainly produced from combustion processes. The sources of NO_x emissions are varying and are related to both human activity and natural processes. However, the major one is anthropogenic and related to industrial processes and transportation. In 2015, in France the road traffic sector accounts for more than 50% of NO_x emissions, whereas heating accounts for almost 30% [9]. For its part, NO₂ which is mainly produced from NO oxidation is one of the precursors involved in the phenomena of acid rain. Hence, regarding human health, nitrogen oxides can cause discomfort in breathing by penetrating the finest pulmonary branches and reducing the oxygenating power of the blood.

SO₂ emission mainly depends on the sulfur content of fuels (oil, coal, etc.). This pollutant is transformed in contact with the moisture of the air into sulfuric acid (H₂SO₄) and thus participates to the phenomenon of acid rain. More than 50% of SO₂ is released into the atmosphere by industrial activities, including those related to energy production such as thermal power plants.

VOCs are emitted by car traffic, industrial processes, the residential sector, and the use of solvents. VOCs include in particular benzene, toluene, xylenes, vinyl chloride, dioxins, furans and formaldehyde. These compounds are involved in the formation of tropospheric ozone and cause irritation and respiratory disorders. Some of them are considered Carcinogenic, Mutagenic and Reprotoxic (CMR).

PAHs are a class of organic compounds mainly produced via incomplete combustion processes. Their formation is closely linked to both the fuel used and the conditions of combustion. Air quality regulations [10] request the identification and control of seven specific polycyclic aromatic hydrocarbons, including carcinogens compounds: benzo (a) pyrene, dibenzo (a, h) anthracene, benzo (a) anthracene, benzo (b) fluoranthene, benzo (j) fluoranthene, benzo (k) fluoranthene and dibenzo (a) pyrene. Emissions from combustion processes are characterized by a large number of aromatic species, which

cannot be easily identified. Their toxicity remains unclear, but their role as soot precursors is recognized.

Soot is a solid compound, generally black-colored, consisting essentially of carbon atoms with a certain hydrogen content which varies between one and twelve percent in mass [11]. Soot particles can be classified as function of the aerodynamic diameter PM₁₀ particles ($d < 10 \mu\text{m}$), PM_{2.5}, PM₁ and PM_{0.1} ($d < 0.1 \mu\text{m}$) and. In the last ten years the attention on soot particles is move towards nanometric scale which are the most abundant in number and can penetrate deeper human body tissues. Soot particles are also found in the atmosphere as aerosols (air pollutants) and can transport other pollutants such as PAHs (adsorption process). Such particles also affect human's health by irritating the respiratory tract and are carcinogenic.

On a global level, the pollutants emitted from combustion processes are linked to global warming through the “greenhouse” effect. This effect plays an important role in regulating the temperature of our planet.

The main GHGs are carbon dioxide (CO₂), methane (CH₄) and nitrous oxide (N₂O) [12]. CO₂ accounts for almost 76% of global GHG emissions of anthropogenic origin. It is mainly emitted from the combustion of fossil fuels, but also from direct human-induced impacts on forestry and other land use, for example through deforestation, land clearing for agriculture, and degradation of soils. CH₄ represents 16% of anthropogenic GHG emissions and is mainly emitted by agriculture and livestock. Part of these emissions also comes from the production and distribution of gas and oil, and coal mining. N₂O accounts for 6% and comes from the use of nitrogen fertilizer in agriculture and some chemical processes.

1.3. Combating GHG and pollutant emissions

The international awareness of the problems linked to climate change has led to a series of international agreements aimed at limiting the emissions of greenhouse gases. The first international measures were taken under the United Nations Framework Convention on Climate Change (UNFCCC) at the Earth Summit in Rio de Janeiro (Brazil, 1992). The objective of this convention was to stabilize atmospheric GHG concentrations at a level that limits any anthropogenic contribution to climate

disturbances. Next, Annual Conferences of Parties (COP) were organized to review the implementation of the Convention.

In 1997, the Kyoto Protocol (COP3) established for the first time the quantified commitments to reduce GHG emissions in developed countries. This protocol was intended to reduce GHG emissions by at least 5% between 2008 and 2012 compared to the 1990 level. According to the work of the Intergovernmental Panel on Climate Change (IPCC), the warming above 2°C (compared to the pre-industrial era) would have serious consequences, such as the increase in extreme weather events. In 2015 during the COP21 organized in Paris, an agreement was signed, which provides the limitation of global temperature increase to 2°C by reducing GHG emissions caused by fossil fuels such as oil, gas and coal combustion. This agreement was adopted by 197 countries and was officially implemented on April 22, 2016, Earth Day.

Concurrently, and due to the serious effects on health and the atmosphere, restrictions have been adopted to regulate pollutants emissions in various sectors, including transport. In particular, from 1992 the European community has regulated the emissions of carbon monoxide (CO), nitrogen oxides (NO_x), unburned hydrocarbons (HC) and particulates. The Euro I standard was implemented in 1993 and has been updated regularly since, as shown in Table 1.1 (gasoline engines) and Table 1.2 (diesel engines).

Gasoline	date	CO (mg/km)	HC (mg/km)	NMHC (mg/km)	NO _x (mg/km)	HC+NO _x (mg/km)	PM mass (mg/km)	PM number (#/km)
<i>Euro 1</i>	01/1993	2720	-	-	-	970	-	-
<i>Euro 2</i>	01/1996	2200	-	-	-	500	-	-
<i>Euro 3</i>	01/200	2300	200	-	150	-	-	-
<i>Euro 4</i>	01/2005	1000	100	-	80	-	-	-
<i>Euro 5a</i>	09/2009	1000	100	68	60	-	5	-
<i>Euro 5b</i>	09/2011	1000	100	68	60	-	4.5	-
<i>Euro 6b</i>	09/2014	1000	100	68	60	-	4.5	6x10 ¹²
<i>Euro 6c</i>	09/2017	1000	100	68	60	-	4.5	6x10 ¹¹

Table 1.1: Evolution of the EURO standard for gasoline engines [2], [13], [14].

Diesel	date	CO (mg/km)	NOx (mg/km)	HC+NOx (mg/km)	PM mass (mg/km)	PM number (#/km)
<i>Euro 1</i>	01/1993	2720	-	970	140	-
<i>Euro 2</i>	01/1996	1000	-	500	100	-
<i>Euro 3</i>	01/200	640	500	560	50	-
<i>Euro 4</i>	01/2005	500	250	300	25	-
<i>Euro 5a</i>	09/2009	500	180	230	5	-
<i>Euro 5b</i>	09/2011	500	180	230	4.5	6x10 ¹¹
<i>Euro 6b and 6c</i>	09/2014	500	80	170	4.5	6x10 ¹¹

Table 1.2: Evolution of the EURO standard for diesel engines [2], [13], [14].

The evolutions are important, and the limits imposed by the Euro 6 standard are much more restrictive than those of the initial standard. The tolerance for carbon monoxide was divided by six in the case of the diesel engine and by three in the case of the gasoline engine. The amount of nitrogen oxides and unburned hydrocarbons allowed has been divided by five. The most interesting evolution is for particles emissions. Considered only in mass in old EURO standard version, in the most recent version also considers the number of particles.

In addition to these standards, CO₂ emissions are also regulated for transportation. The European Parliament has set a target of 95 grams of CO₂ per kilometer by 2020 for passenger cars, by a regulation published on April 23, 2009. This new limitation should be the keystone of the new EURO 6d standard expected by 2021 at the latest.

In last decades, research and development (R&D) sector has faced technological challenges concerning the reduction of polluting emissions and the optimization of combustion systems.

Fig.I.3 shows the evolution of energy Research, Development and Demonstration (RD&D) budget from International Energy Agency (IEA).

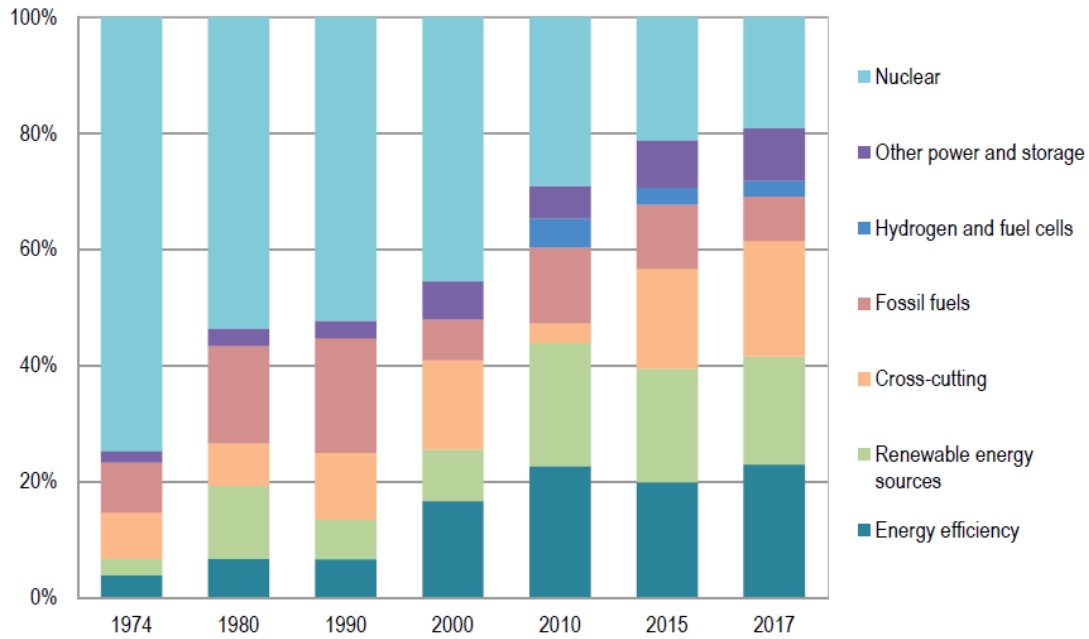


Fig I.3: Evolution of total public energy of the IEA countries by technology [15].

It is very interesting to notice how interests have become progressively more different in the last 40 years. In the seventies, with the oil crack, the interest in nuclear energy was dominant until the 2000's. Indeed, nuclear, dominant in 1974 with 74% of total public energy (RD&D) budget, witnessed year-on-year reductions to fall to 19% in 2017. With the awareness of global warming and the targets for greenhouse gas reductions, the interest of research has shifted towards finding new alternative and renewable sources with respect to fossil fuels and towards the optimization of energy efficiency. In 2017 the estimated total public energy RD&D budget for IEA member governments reached close to 18 USD billion. The budgets on fossil fuels, which were at their highest in the 1980s and 1990s, have been declining to 8% in 2017. More than 60% of the RD&D budget is represented by green and sustainable energy research such as energy efficiency (23%), renewables (18%) and cross-cutting RD&D (20%).

Within the RD&D budget for renewable energy, the studies on the development of new types of fuels (synthetic fuels and fuels derived from biomass) are essential to fight against GHG emissions and certain pollutants from transportation sector. Unlike the combustion of fossil fuels, the carbon emitted during the combustion of biofuels has been previously fixed by plants (rapeseed, wheat, maize ...) during photosynthesis, so we can consider that their CO₂ balance is theoretically equal to zero.

2. Biofuels

Biofuels are commonly presented as an alternative to traditional automotive fuels, but their use is not new. By the end of the 19th century, the use of denatured alcohol was already being considered in Europe. Indeed, Nikolaus Otto, inventor of the internal combustion engine (1876), designed it to work also with ethanol. The Ford T (produced from 1908 to 1927) also worked with this alcohol; and Rudolf Diesel, inventor of the engine bearing his name (1897), used peanut oil to run his machines [16].

Before the First World War (1914), Parisian buses were fueled with a mixture containing denatured alcohol. From 1920 until the 1950s, the use of ethanol as fuel was significant. In the middle of the twentieth century, oil became abundant and cheap, causing a lack of interest among industrialists and consumers for first biofuels.

From the 1970s, the oil cracks (1973 and 1979) as well as the fight against greenhouse gases (notably CO₂) led to the regain in interest for biofuels. Two countries, Brazil and the United States, have very quickly relaunched programs for the production and use of ethanol. In the early 1970s, gasoline/ethanol blends were marketed in Brazil and supported by tax incentives. From the late 1970s to the 1990s, in France and in Europe, research and development programs on biofuels were also launched with a reduction of the tax on the use of biofuels [17].

Since the beginning of the 1990s, the Institut Français du Pétrole (IFP) has been involved in the development of a process for the production of Ethyl Tertbutyl Ether (ETBE - used in blends with gasolines). Fatty Acid Methyl Esters (FAME- used in mixture with diesel fuels) obtained by reactions of rapeseed or sunflower oils with methanol were also developed in France in the same period [17].

According to the European Directive 2003/30/EC of 8 May 2003 [2], the E. D. 2009/28/EC defines biofuels as the following: “Liquid or gaseous fuels used for the transport and produced from biomass”, thus obtained from the non-fossil plant and animal organic matter. The EU has defined a set of sustainability criteria to ensure that the use of biofuels (used in transport) and bioliquids (used for electricity and heating) is done in a way that guarantees real carbon savings and protects biodiversity. To be considered sustainable, biofuels must achieve greenhouse gas savings of at least 35% in comparison to fossil fuels. This savings requirement rises to 60% in 2018 for new

production plants. All life cycle emissions have to be taken into account when calculating greenhouse gas savings (emissions from cultivation, processing, and transport).

The Directive 2009/28/EC [2] also lists 9 products considered as biofuels: bioethanol, biodiesel (oil esters plant or animal), biogas, bio dimethyl ether (bio-DME), bio-ETBE, bio-MethylTBE, synthetic biofuels, biohydrogen, and pure vegetable oils [18].

Depending on the sources and production processes, it is possible to distinguish four “generation” of biofuels, as shown in Fig I.4:

- First-generation: biofuels mainly made from vegetable oils, sugars and edible starch;
- Second-generation: biofuels made from vegetable matter as agricultural or forestry residues;
- Third-generation: biofuels made from algae;
- Fourth generation: biofuels made from bio-engineered biomass and bacteria with high carbon capture efficiency.



FigI.4: The generations of biofuels.

2.1. First generation of biofuels

In the 1970s with the rising price of oil and the awareness environmental issues, the development of 1st generation biofuels has been initiated. This generation of biofuels is mainly produced from starch sugar crops such as grain (rice, wheat), sugar cane, and oil seed plant such as palm and rape. The main liquid and gaseous biofuels of these categories are:

- Bioethanol: produced from sugar-containing plants or cereal; used as a gasoline substitute such as the E85 fuel, a commercial blend with 65-85% in volume of ethanol with unleaded gasoline, although research uses also ethanol in compression ignition engines;
- Biodiesel: produced from vegetable oils or animal fats, usually after conversion into a range of fatty acid methyl (or ethyl) esters; used pure or in blends with mineral diesel fuels in compression ignition engines;
- Biomethane: as landfill gas or biogas, produced by the anaerobic fermentation of organic wastes including animal manures. However, gaseous biofuels are far less popular than other liquid biofuels.

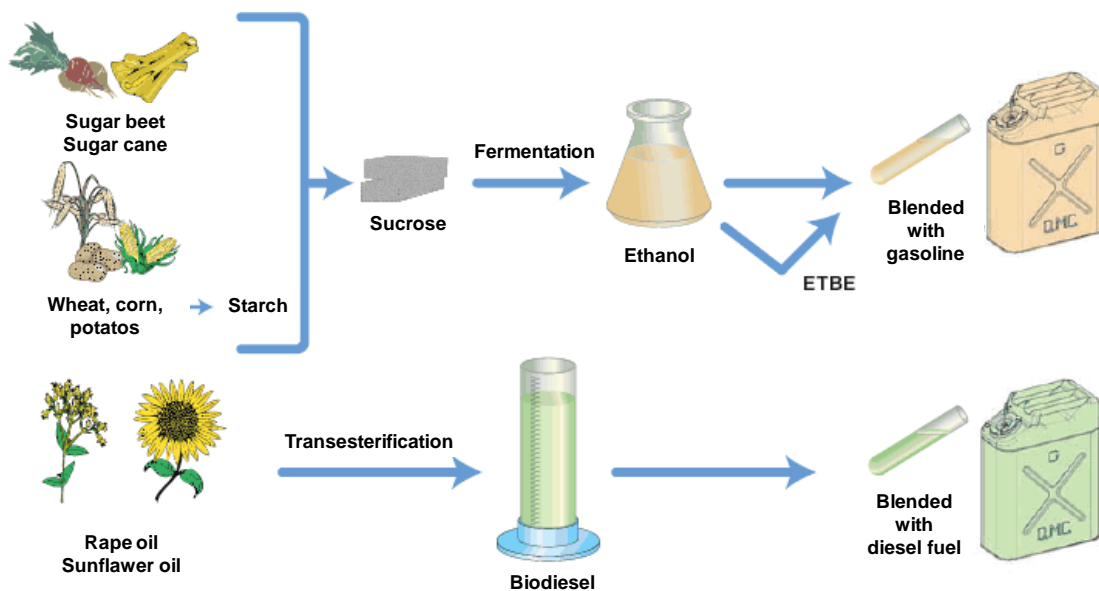


Fig.I.5: Typical processes for the production of the first generation of biofuels [19].

As shown in Fig.I.5, ethanol and ETBE are produced from fermentation processes. The main raw materials needing to be extracted are sucrose or starch. For sucrose from

sugar cane or sugar beet crops, the juices are first mechanically pressed from the cooked biomass followed by fractionation. The sucrose is metabolized by yeast cells and the ethanol is then recovered by distillation. Starch crops must first be hydrolyzed into glucose before the yeast cells can convert the carbohydrates into ethanol. Although highly efficient, the starch grain-based route consumes more energy (and thus potentially emits more CO₂ into the atmosphere) than the sucrose-based route.

Concerning biodiesel (Fig.I.5), it is produced by trans-esterification processes. The vegetable oil or animal fats, opportunely treated, are mixed with methanol in a catalytic reactor to obtain the FAMES. The crude biodiesel is then distilled.

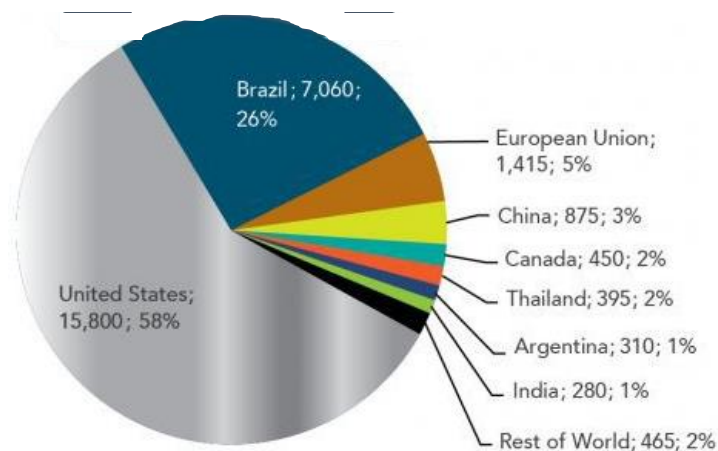


Fig.I.6: Global fuel ethanol production by country in 2017 (Country, million gallon, share of global production)[20].

In 2017, the world's two largest producers of ethanol are the United States (58% of the world supply, mostly from corn) and Brazil (26%, mainly from sugar cane), as shown in Fig I.6.

In response to the strong demand for this type of biofuels, there are several negative aspects to consider. The competition with food culture is one of the main criticisms of 1st generation biofuels. According to the World Bank, biofuels are responsible for 75% of the rise in food prices, which is one of the causes of the recent food crisis of 2007-2008. In addition, the biomass feedstock may not be produced sustainably and by using pesticides, which depletes plant biodiversity and facilitates soil erosion. It should also be noted that some plants grown to produce biofuels are very water-intensive [21].

From an environmental point of view, the GHG emissions linked to the production of this generation of biofuels are not always very favorable, particularly because of the energy required for their extraction (for example: heating for the distillation of bioethanol). Only ethanol from sugarcane can produce significant net savings in GHGs, particularly when the bagasse co-product is used to provide heat and power at the processing plant [21]. In addition, to increase the production of biodiesel from palm and soybeans, the deforestation of some regions, especially in Brazil, Malaysia and Thailand, increases significant GHG emissions. Indeed, tropical rainforests are the most efficient carbon sinks on earth. By contributing to their destruction, the carbon balance of biofuels is negative. Consequently, these considerations limit the viability of first-generation biofuels.

For the same reason, the European Environment Commission has voted in 2015 an agreement to limit the share of first generation biofuels at 7% to attend the propose to have at least 10% of the energy consumption of transport covered by renewable energy by 2020 [22].

The first generation of biofuels has reached a technological maturity in recent years such as to be the only type of biofuels to be produced on industrial scales. However, their production remains linked to a series of environmental and ethical issues that counterbalance any positive effects of reducing greenhouse gas emissions.

2.2. Second generation of biofuels

To increase the quantity of biofuels potentially available, new resources from non-food plants are used: agricultural residues, forest waste, and non-edible plants. In this way, the production of the second generation of biofuels can be made from a wide variety of non-food crops. These include biomass waste, stalks of wheat, corn, wood, fibrous biomass crops (i.e. miscanthus) or macroalgae, and lignocellulosic materials.

This 2nd generation, which is in continuous development, concerns mainly but not only two sectors - ethanol and biodiesel - with different technologies, more elaborated than those used in the 1st generation of biofuels: thermochemical production and biochemical production.

Lignocellulosic material will be detailed in section 3.

2.3. Third generation of biofuels

The high technological costs due to the production of second-generation biofuels led to the development of the third-generation biofuels, such as microalgae-based biofuels. The microalgae have a great potential for large scale-production. Microscopic algae, living in the aquatic environment, naturally produce lipids (oils) and carbohydrates. They can be grown under autotrophic conditions, i.e. for their growth they use only water, mineral salts, CO₂ and sunlight. Like terrestrial plants, they fix CO₂ through the mechanism of photosynthesis. Some species of microalgae can be grown in heterotrophic mode away from light and with a diet of sugars [23]. Cultivated under certain conditions (lack of certain nutrients for example) they can begin to produce and accumulate lipids, mainly triglycerides, whose content can reach up to 80% of the dry matter. About 300 algae species have already been identified for their richness in oil. Out of these various microalgae species, *Chlorella protothecoides* is a good candidate as the potential feedstocks to produce biodiesel due to having high oil content (58 %), faster growth rate and high biomass productivities ([24], [25]).

Algae are grown on surfaces that do not seem to compete with agricultural surfaces. They have yields of biomass per hectare, as well as higher oil content than oil plants such as rapeseed or even oil palm: the results obtained at the laboratory stage give hope for oil productivities per hectare 6 to 20 times more important [23]. Another advantage, the growth of lipid algae requiring large amounts of CO₂ (a ton of algae captures about 2 tons of CO₂ for growth).

Fig. I.7 presents the classical production process of biofuels from the microalgae cultures. The microalgae, previously selected for their richness in oil can be grown massively, either in large outdoor pools, or in photobioreactors. The oil is extracted according to different methods: centrifugation, solvent treatment, thermolysis. Depending on the algae families, several types of conversion of the oil or biomass into biofuels can be implemented:

- Fermentation, which transforms the algae biomass rich in carbohydrates and polysaccharides into ethanol;

- transesterification, which makes that the algal oil reacts with methanol or ethanol, produces an ester of algal oil or biodiesel, quite comparable to that obtained from other types of vegetable oils;
- catalytic hydrogenation, which reacts the oil in the presence of hydrogen, followed by hydrocracking, produces hydrocarbons which can be incorporated in large quantities with diesel fuels or with kerosene.

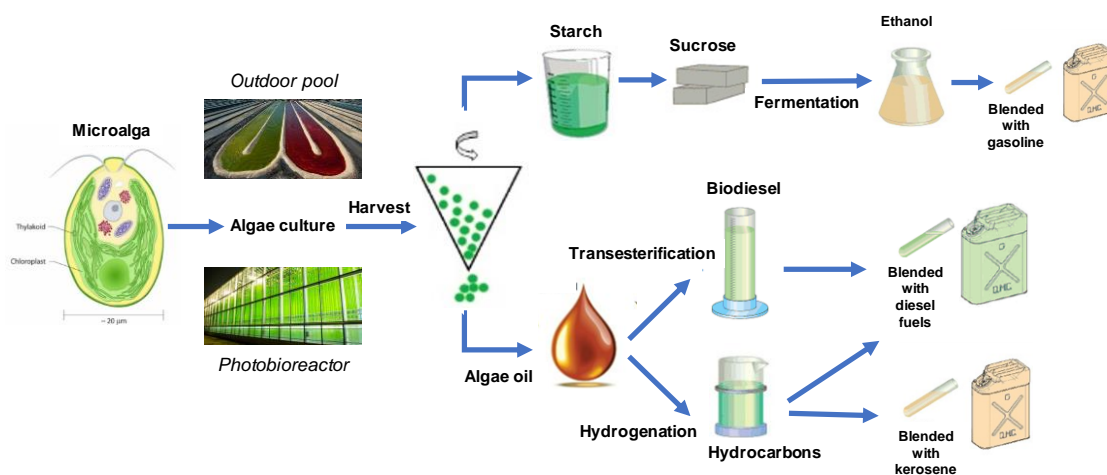


Fig.I.7: Typical processes for the production of third generation biofuels.

Environmental and energy balances represent the major issues. Indeed, to ensure the economic viability of the biofuel production chain from microalgae, it is necessary to significantly reduce energy consumption throughout the chain. The research aims first to select in the laboratory robust strains and high lipid content. It is also necessary to develop optimized cultivation processes, ensuring high productivity over long periods and for large volumes. Efforts should also focus on water / biomass separation and oil extraction processes that are particularly energy intensive.

2.4. Fourth generation of biofuels

In the last decades, biogenetic engineering has made great strides. Aware of the strengths and weaknesses of previous generations of biofuels, scientific research has focused on the creation of “ad hoc” biomass sources to meet current and future needs.

A first approach is based on the combination of biofuel production from biotech-plants and CO₂ capture and storage techniques.

In that way, new resources have been investigated: high biomass crops, trees with increased carbon storage capacity, drought tolerant crops, ... [26].

In fourth generation production systems, biomass crops are seen as efficient “carbon capturing” machines. The carbon-rich biomass is then converted into fuel and gases by means of second-generation techniques. Crucially, before, during or after the bioconversion process, the carbon dioxide is captured by utilizing so-called pre-combustion, oxyfuel or post-combustion processes. The greenhouse gas is then geo-sequestered, stored in depleted oil and gas fields, in old coal seams or in saline aquifers [27]. The resulting fuels and gases are not only renewable, they are also effectively carbon-negative. Fig.I.8 shows a conceptual architecture of this approach.

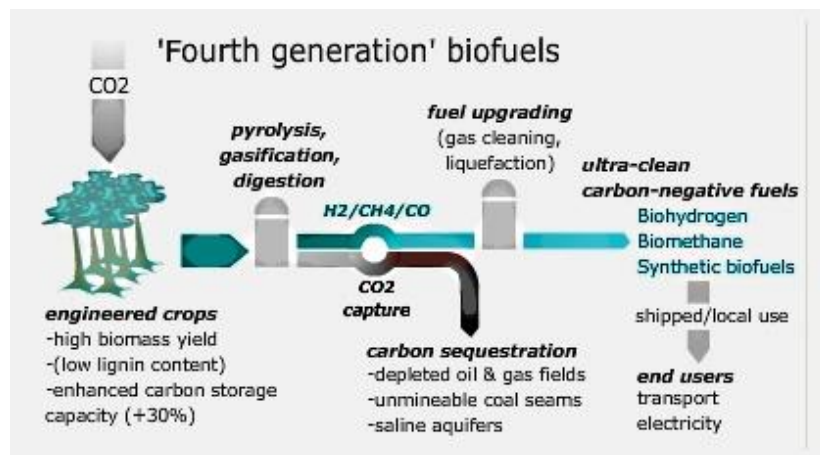


Fig.I.8:4th generation biofuels conceptual architecture [28].

A second approach of fourth generation biofuels takes advantage of synthetic biology of algae. Synthetic biology comprises the design and construction of new biological devices, and the re-design of existing, natural biological systems for useful purposes [29]. Cyanobacteria, for example, have been genetically engineered [30] to produce various fuels and chemicals such as H₂, ethanol, isobutanol, isoprene, and lactic acid.

Although the first results have shown their potential in fuel production, this field is still at the level of basic research. During the coming 10–20 years, it is expected that various biological fuels are gradually entering into the market [29].

3. Lignocellulosic biofuels

Non-edible feedstocks such as wood, agricultural residues, forestry waste and municipal and industrial wastes, commonly named lignocellulosic biomass, are the raw materials for second generation biofuels.

Compared to agricultural products, lignocellulosic biomass is more abundant and less expensive. This represents an advantage for the biofuels production. Other positive aspects of the production of biofuels from biomass is a limited competition between food and non-food uses of agricultural products, and a potential increased income from agriculture through a full recovery of the plant, both on the grain for food and the residue for fuel. This corresponds to an increase of the potential productivity per hectare and the improvement of the economic balance sheet and the environmental balance related to the agronomic aspects [31].

3.1. Lignocellulosic biomass: characteristics, processes...

The lignocellulosic biomass is structured in micro-fibrils in plant cell walls and consists of cellulose surrounded by the less crystalline polymers hemicellulose and lignin with small amounts of other components, like acetyl groups, minerals and phenolic substituents [32], as shown in Fig.I.9. Generally, lignocellulosic biomass consists of 35–50% cellulose, 20–35% hemicellulose, and 10–25% lignin.

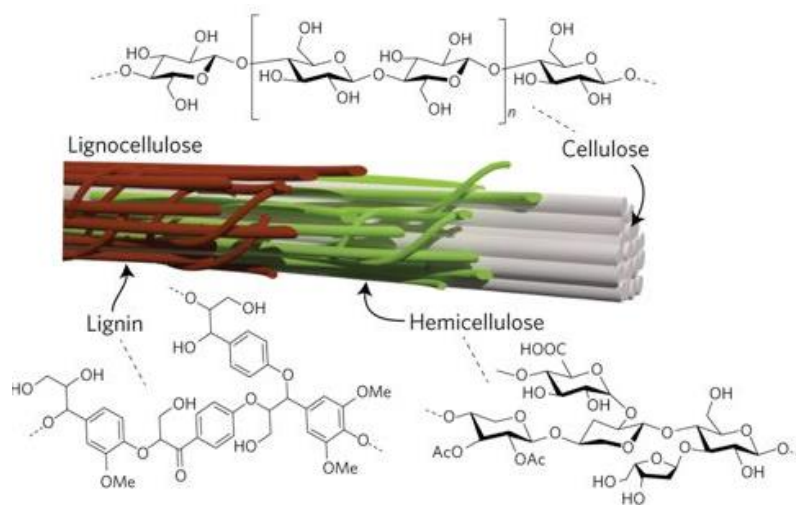


Fig.I.9: The main components and structure of lignocellulose. Modified from [33].

The major component of biomass is cellulose, a polysaccharide composed by a linear chain of glucose units. Hemicellulose is the second most abundant polymer. Unlike cellulose, hemicellulose has a random and amorphous structure, which is composed of heteropolymers with 5- and 6-carbon monosaccharide units such as pentoses (xylose, arabinose) and hexoses (mannose, glucose, galactose). Hemicelluloses are imbedded in the plant cell walls to form a complex network of bonds, which provides structural strength by linking cellulose fibers into microfibrils and cross-linking with lignin. The third main compound of lignocellulosic biomass is lignin. It is a three-dimensional polymer of phenylpropanoid units, whose functions is to provide the compressive strength to the plant tissue and the individual fibers, the stiffness to the cell wall and the resistance against insects and pathogens. Proteins, oils, and ash make up the remaining fraction [32].

The conversion of lignocellulosic biomass can be carried out according to two major technological pathways, which are likely to value their polymers (Fig.I.10): the **biochemical pathway** (hydrolysis and fermentation), which allows the production of ethanol; and the **thermochemical pathway** (pyrolysis and synthesis), which allows the production of methanol, biodiesel and a whole range of synthetic products.

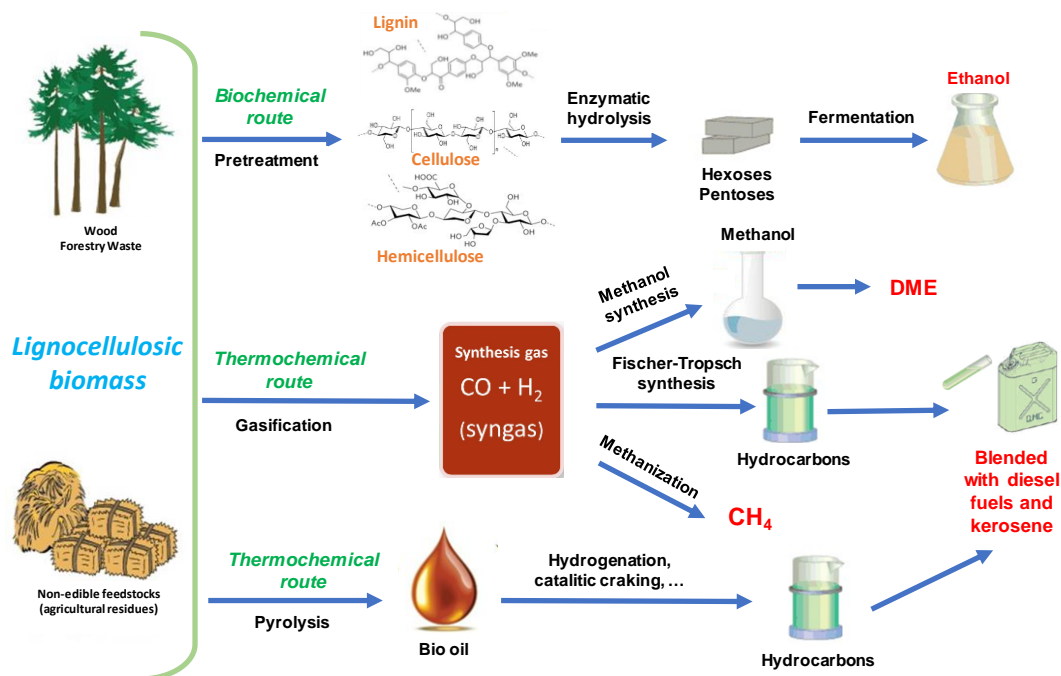


Fig.I.10: The main routes of lignocellulosic biofuels production.

The **biochemical way** is focused on the production of the lignocellulosic ethanol starting from physico-chemical conversion of cellulose and hemicellulose in sugars,

respectively hexoses (glucose) and pentoses. The three constituent polymers of the lignocellulosic material form a rigid matrix that has to be pre-treated to render cellulose and hemicellulose accessible to hydrolysis. The generic scheme of the cellulosic ethanol production process is articulated around four main stages:

- Pretreatment of the raw material, which can be performed via various thermal, mechanical, chemical or even enzymatic processes [34];
- Enzymatic hydrolysis of the cellulose and hemicellulose molecules into sugars [31]. Lignin can be converted catalytically into a wide variety of cyclic species;
- Bacterial fermentation of sugars in ethanol;
- Separation of ethanol from the fermentation must, distillation and drying in order to obtain anhydrous ethanol, suitable for use as a biofuel.

The *thermochemical route* or BTL (Biomass To Liquid) refers to the transformation chain of lignocellulosic biomass by gasification and then synthesis. The final product may be biodiesel, dimethyl ether (DME), methanol or also ethanol. It owes its name to the gasification reaction which combines thermal and chemical processes at high temperatures (> 800 °C). It produces hydrogen (H_2) and carbon monoxide (CO), which in a later stage of the process are upgraded to liquid hydrocarbons.

The conversion of biomass into biofuels through the thermochemical process is done through the following stages:

- Pretreatment of the biomass;
- Gasification by steam or oxygen reforming to obtain syngas (CO and H_2);
- Gas purification to eliminate undesirable products such as particles, tars, and inorganics, and to reach the specifications of synthesis reactors;
- Steam reforming of methane and other residual hydrocarbons converts these compounds in CO and H_2 ;
- Gas synthesis to produce fuels such as methanol, dimethyl ether (DME), synthesis natural gas (GNS), ethanol and mixture of long-chain paraffins by Fischer-Tropsch method.

In thermochemical processes is also considered the pyrolysis of biomass to produce bio-oil, which is upgraded in hydrocarbons for transportation by conventional oil processes such as hydrogenations (Mild hydrogenation, Hydro-deoxygenation, Hydrogen-donor solvents), catalytic cracking, and esterification.

3.2. ...and economical point of view.

In Europe, according to the census made by the German Nova-Institute consulting firm in 2017 [35], there are about 224 bio-refineries: 63 of these start from sugars and starch to produce bioethanol and chemical derivatives; over a hundred instead use oils and fats to obtain biodiesel, or other chemical products. There are also 33 bio-refineries which use lignocellulosic biomass: 25 of them use wood, 5 treat lignocellulose not from woody origin, and 13 bio-refineries are fed by organic waste.

In terms of R&D world prospects, Fig. I.11 shows the annual financial investments in biofuels technology between the 2010 and 2017. Ethanol is the biofuel which receives the more copious investments thanks to the incentive of Brazil and USA, the biggest producers of first-generation ethanol. Also, the investment for the ethanol from other sources without competition with food (Other Ethanol) results to be relevant on biofuels market with fluctuant contribution between 2010 and 2017. The Hydroprocessed Vegetable Oil (HVO), an upgraded biodiesel from vegetable fats and oils, will still represent significant investments with several units being opened in Europe and the United States, especially thanks to the interest shown by aeronautic sector for these types of biofuels. About advanced lignocellulosic biofuels, their market opportunities, especially in Europe, are still waiting for public policies incentives post 2020. Several technologies are able to archive a significant production of biodiesel and biokerosene from advanced resources (waste, straws, wood and other residues without competition with food) by 2030. France also has a potential for deployment across all sectors ethanol, biogas and biokerosene via a positioning existing R&D actors and tools (in particular projects Futurol and BioTfuel, promoted by IFPEN and partners) [36].

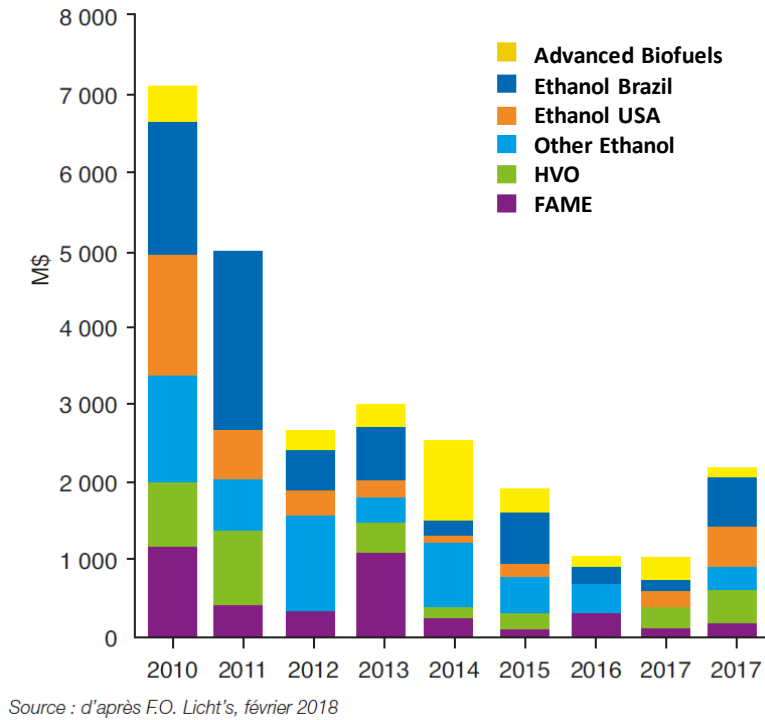


Fig.I.11: Annual global investments in the biofuels sector by product, in millions of dollars (M\$) [36].

3.3. Advanced lignocellulosic biofuels

3.3.1. Introduction

In addition to the “traditional” biofuels, which presents an interest on an industrial scale, there are some derivatives of lignocellulosic biomass that attract the attention of researchers for their possible use as innovative and advanced biofuels.

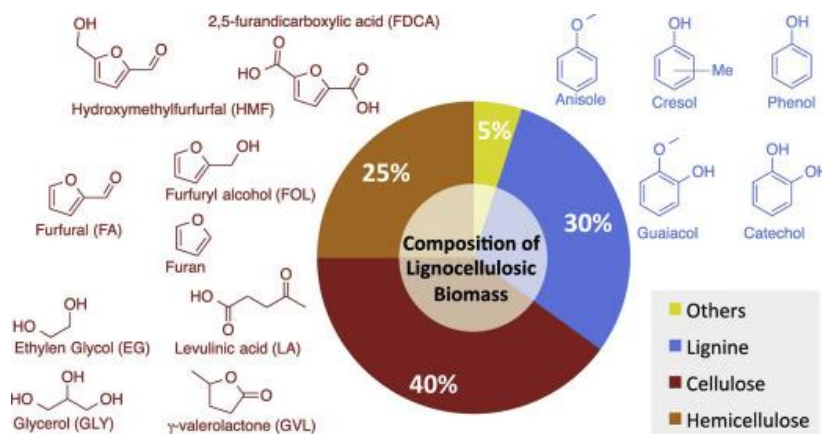


Fig.I.12: Composition of lignocellulosic biomass and main chemical derivatives [37].

Fig.I.12 shows the main chemical products from the different components of lignocellulosic biomass. A smaller but not least interesting part is lignin, from which, during the last two years, research has been devoted to lignin-derived chemicals, such as anisole, guaiacol, catechol, vanillin etc... Different studies have been carried out on experimental and kinetic characterization of the pyrolysis and combustion of some of these compounds [38], [39].

As shown in Fig. I.12, biomass feedstock is mainly made by cellulose and hemicellulose which yield to oxygenated molecules such as furfural, hydroxymethylfurfural (HMF) and levulinic acid. These compounds are called "biochemical platforms" because they can serve as a basis for the synthesis of a wide variety of compounds of interest in the fields of pharmacology, fine chemicals, agri-food, but also in the fuels field.

In recent years, several studies have focused on the direct transformation of sugars contained in cellulose and in hemicellulose in furfural, HMF and levulinic acid through catalytic processes [40-42]. Indeed, as shown in Fig. I.13, starting from glucose and fructose we can obtain HMF through a de-hydration process, from which the levulinic acid can be obtained. The processes for synthesizing this compound have recently made important advances, which suggest possibilities from a point of view of profitability [43]. Furfural, on the other hand, can be obtained by acid dehydration of pentoses such as arabinose or xylose.

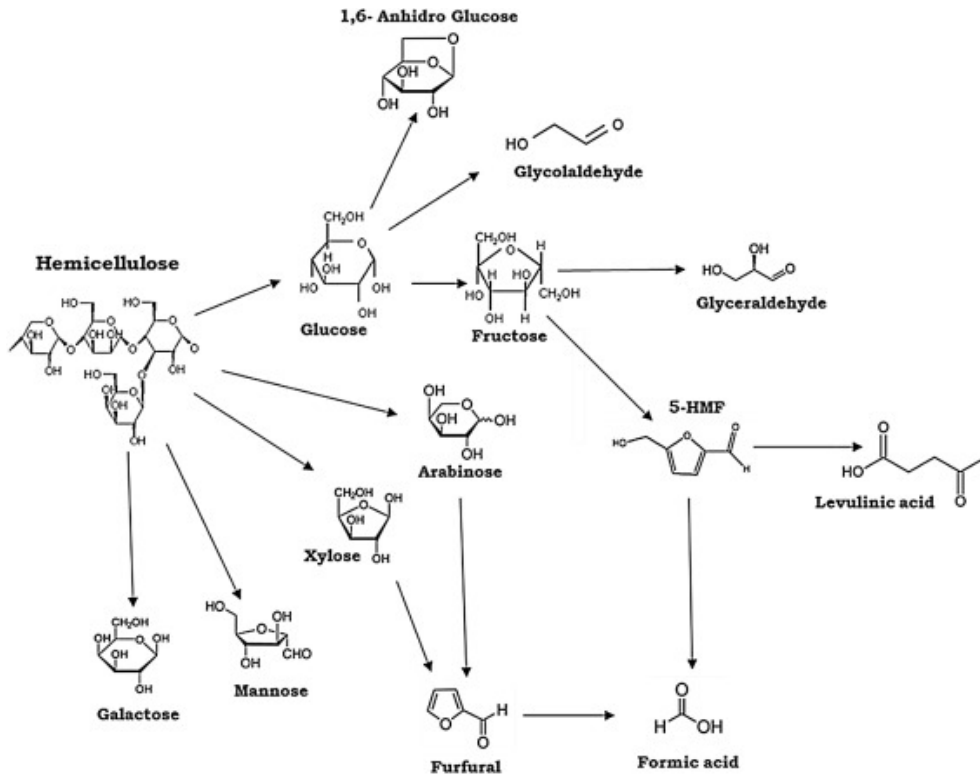


Fig.I.13: Reaction pathway for hemicellulose hydrolysis and formation of degradation products [41].

Research related to the transformation of these platform molecules is highly developed and enable to obtain a wide variety of alkanes, alkenes, alcohols, or complex esters, as illustrated in Fig.I.14 in case of Furfural.

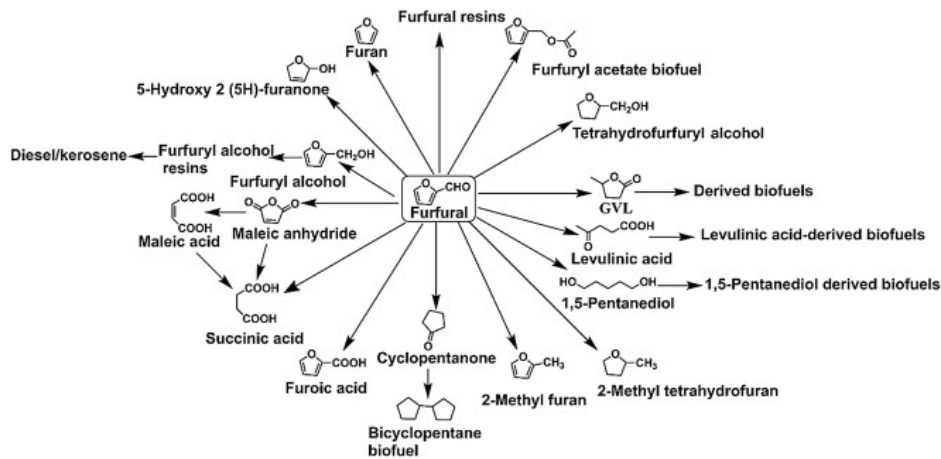


Fig.I.14: The pathways for the conversion of furfural as platform molecule into chemicals compounds of interest and fuels [42].

3.3.2. Properties of some cyclic ethers

Among the various compounds which can be obtained from bio-chemical platforms, the cyclic ethers as the furan and tetrahydrofuran family are arousing particular interest for their physical properties similar to transportation fossil fuels.

To illustrate that, the Table I.3 compares some properties of unsaturated cyclic ethers (furan, methyl-furan (MF), dimethyl-furan (DMF)) and saturated cyclic ethers (tetrahydrofuran (THF), methyl-tetrahydrofuran (MTHF) and dimethyl-tetrahydrofuran (DMTHF)) with those of ethanol (the most commercial biofuel), gasoline and diesel fuel.

	Chemical Formula	Oxygen content (Wt%)	Density (kg/l)	Boiling Point (K)	LHV (MJ/kg)	AIT (K)	RON/MON	CN
Furan	C ₄ H ₄ O	23.5	0.94 ^b	305.2 ^b	29.5 ^b	663 ^b	-	7 ^c
MF	C ₅ H ₆ O	19.5	0.91 ^b	336.0 ^b	30.4 ^b	-	131/- ^b	8.3 ^d
DMF	C ₆ H ₈ O	16.7	0.8 ^b	366.5 ^b	33.7 ^b	559 ^b	119/- ^b	10.9 ^e
THF	C ₄ H ₈ O	22.18	0.89 ^a	339.2 ^a	-	594 ^a	-	26.8 ^d
MTHF	C ₅ H ₁₀ O	18.57	0.85 ^a	353.4 ^a	32.0 ^a	543 ^a	86/72 ^a	20.5 ^d
DMTHF	C ₆ H ₁₂ O	15.97	0.83 ^a	364.1 ^a	-	-	82/- ^a	-
Ethanol	C ₂ H ₅ OH	34.8	0.79 ^c	351.6 ^c	26.8 ^c	763 ^c	120/99 ^c	5-8 ^c
Gasoline	C ₄ -C ₁₄	-	0.74 ^c	303-473 ^c	42.7 ^c	723 ^c	95/85 ^c	-
Diesel	C ₈ -C ₂₅	-	0.84 ^c	443-633 ^c	43.0 ^c	533 ^c	-	40-55 ^c

^aCollected from Tran et al.[44] ^bCollected from Xu et al.[45] ^cCollected from Ballerini et al [17]^d Collected from Kessler et al.[46] ^eCollected from Sudholt et al.[47]

Table.I.3: Properties of furan and THF derivatives, ethanol, gasoline, and diesel.

From the values shown in Table I.3, we can observe that furanic biofuel present a Lower Heating Value (LHV) higher than ethanol and closer to commercial fuels, especially the alkylates compounds (DMF and MTHF). The Auto Ignition Temperatures (AIT) of these biofuels are closer to that of diesel fuels suggesting a possible application in compression ignition engines due to also the high Cetane Number (CN) in particular for THF and MTHF.

A bibliographic review of the main work done on the combustion of the cyclic ethers belonging to the furan and tetrahydrofuran families is presented in the following sections.

3.3.3. Review of oxidation studies of furan and THF in the intermediate and high temperature range

3.3.3.1. Furans

Furan (F) and its main derivatives such as 2-methylfuran (MF) and 2,5-dimethylfuran (DMF) exist in liquid form at standard pressure and temperature conditions. They are cyclic unsaturated ethers (Fig.I.15).

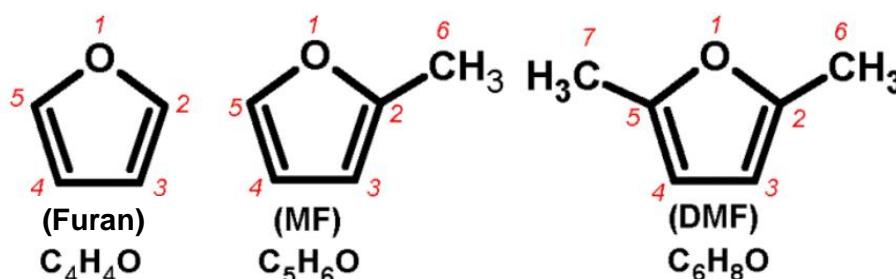


Fig.I.15 Molecular structure of furan (F), 2-methylfuran (MF), and 2,5-dimethylfuran (DMF) [48].

Furan derivatives (DMF, MF, and F) are representatives of the second-generation biofuels. Compared with bioethanol, they have higher heating values which are closer to that of gasoline (Table I.3).

Recently, the production methods of furan derivatives using agricultural lignocellulosic biomass have been developed by Zhao et al. [49], Mascal et al. [50], and Leshkov et al. [51]. These processes are based on the catalytic conversion of 5-hydroxy-methyl-furfural (HMF) [51] and furfural [52].

Different fundamental studies focused on the combustion characteristics of furan derivatives, including laminar burning velocities, laminar flame structures, ignition delay times, and kinetic studies. A summary of them is shown in Table I.4 in chronological order and by furanic compound.

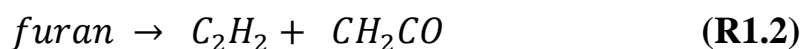
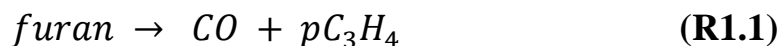
Fuel	ϕ	Reactor	Research	References
Furan, MF, DMF	pyrolysis	Flow reactor T=1050-1270 K	Fuel decomposition	Grela et al. [53] 1985
Furan	-	Jet-stirred reactor T=1000–1300	Fuel oxidation Species profiles	Thorton et al.[54] 1986
Furan	pyrolysis	Shock tube T=1050-1460 K	Fuel decomposition	Lifshitz et al.[55] 1986
Furan	pyrolysis	Shock tube T=1100-1700 K	Fuel decomposition Kinetics study	Organ et Mackie[56] 1991
Furan	pyrolysis	Shock tube T=1050-1460 K	Fuel decomposition	Fulle et al.[57] 1998
Furan	pyrolysis	Shock tube[56]	Kinetics study	Sendt et al.[58] 2000
Furan	pyrolysis	Flow reactor T=300-1700 K	Fuel decomposition	Vasiliou,et al[59] 2009
Furan	1.4, 1.8, 2.2	Premixed laminar flame P=35 Torr	Flame structure Kin. study	Tian et al [60] 2011
Furan	0.5, 1.0, 2.0	Shock tube T=1320–1880 K	In.delay time Kinetic study	Wei et al.[61] 2012
Furan	1.0, 1.7	Premixed laminar flame P=20,40mbar	Flame structure Kin. study	Liu et al. [62] 2014
Furan, MF, DMF			Review	Xu et al.[45] 2016
Furan	pyrolysis	Flow reactor T=1100-1600 K	Fuel decomposition Kinetics study	Cheng et al.[63] 2017
Furan, MF, DMF	0.5, 1.0, 2.0	Flow reactor T= 730–1170 K	Speices profiles Kinetics study	Tran et al.[6] 2017
MF	pyrolysis	Shock tube T=1100-1400K	Fuel decomposition Kinetics study	Lifshitz et al.[64] 1997
MF	0.8, 1.5	Premixed laminar flame P=30 Torr	Flame structure Kin. study	Wei et al.[65] 2012
MF	0.5, 1.0, 2.0	Shock tube-Flat flame T= 1200–1800 K	In.delay time Burn.velocity Kinetic study	Somers et al[66] 2013
MF			Quant. calculat. CBS-QB3	Davis et Sarathy[67] 2013
MF	0.25, 0.5, 1.0, 2.0	Shock tube high P T=1070 -1370K	In.delay time Kinetic study	Wei et al [68] 2013
MF			Quant. calculat. CBS-QB3	Somers et al [69] 2014

MF	1.0, 1.7	Premixed laminar flame P=20,40mbar	Flame structure Kin. study	Tran et al [70] 2013
MF	1.0	Shock tube T= 691–1006 K	In.delay time Kinetic study	Uygun et al [71] 2014
DMF	pyrolysis	Shock tube T=1070-1370K	Fuel decomposition Kinetics study	Lifshitz et al. [72] 1998
DMF			Quant. calculat. CBS-QB3	Simmie et al [73] 2009
DMF	2.0	Premixed laminar. flame P=4.0 kPa	Flame structure	Wu et al [74] 2009
DMF	0.9-1.5	Constant volume bomb P=1-7.5bar T=393K	Lam.burn. velocity	Wu et al[75]–[77] 2009-2011
DMF	pyrolysis	Flow reactor T=873-1098 K	Fuel decomposition Kinetics study	Djokic et al.[78] 2013
DMF			Quant. calculat. CBS-QB3	Sirjean et al [79],[80] 2013
DMF	0.5, 1.0, 1.5	Shock tube T= 1300–1831K P=1- 4 bar	In.delay time Kinetic study	Sirjean et al.[81] 2013
DMF	Pyrolysis 0.5, 1.0, 2.0	Shock tube T=820–1800 K P=1-80 bar Jet-stirred reactor T=770–1220 K Flat flame (heat flux method)	Fuel decomposition In.delay time Lam.burn. velocity Speices profiles Kinetics study	Somers et al.[82] 2013
DMF	1.0, 1.7	Premixed laminar. flame P=20,40mbar	Flame structure Kin. study	Togbe et al.[83] 2013
DMF	pyrolysis	Flow reactor T=873-1098 K	Fuel decomposition Kinetics study	Cheng et al.[84] 2014

Table 1.4: Literature studies on furan derivatives combustion and pyrolysis by considering experimental and numerical approaches.

By focusing on furan, which is produced during the oxidation and decomposition of all other furanic compounds, fourteen studies have been carried out on kinetic behavior of this unsaturated ether during oxidative and pyrolytic processes. Many studies have been considered the thermal decomposition of furan, but only four works were dedicated to its oxidation. Among these studies, all studies involve the pure fuel and only two are performed in flame condition.

The research on the experimental investigation on the thermal decomposition of furan has started relatively early. In the eighties, Grela et al. [53] and Lifshitz group [55], [64], [72] have studied the pyrolysis of F, MF and DMF. In particular, Lifshitz conducted a series of studies on the decomposition of F [55], MF [64] and DMF [72] using a shock tube coupled to a mass spectrometric chromatograph (GC/MS). During the thermal decomposition of furan ($T = 1050-1460$ K, $P = \sim 260-364$ kPa), CO, propyne (pC_3H_4), acetylene (C_2H_2) and ketene (CH_2CO) were identified as the major intermediate compounds while CH_4 , C_2H_4 , C_4H_2 , 1,3- C_4H_6 and C_6H_6 were detected as minor products. The authors have proposed two main routes for the decomposition of furan, the first one seeming to be the more relevant:



In 2000, Sendt et al. [58] obtained the thermochemical and kinetic parameters of several important reactions involved during furan decomposition. They proposed a detailed kinetic mechanism for furan pyrolysis. This mechanism has been validated by comparison with data obtained in pyrolysis conditions [56]. The authors found that a transfer of a hydrogen atom between the C2 and C3 positions of furan plays an important role in the decomposition of this compound finally giving reaction R1.1 as majority pathway and reaction R1.2 as minority pathway.

Ten years later, Tian et al. [60] performed the first study of furan oxidation in flame conditions. They investigated experimentally and numerically a F/O₂/Ar premixed laminar flames at low pressure ($P = 4.7$ kPa, $\phi = 1.4-2.2$). A Photo-Ionization Mass Spectrometer coupled with Molecular Beam sampling system (PI-MBMS) was used to determine the mole fraction profiles of species. They proposed a detailed kinetic mechanism for furan oxidation including 206 species and 1368 reactions. The mechanism considers species up to C₅ and with at least one oxygen in the molecules. The model was validated by comparison with their results obtained in flames and with pyrolysis results obtained in shock wave tube ($T = 1100-1700$ K, $P = 2017$ kPa) by Organ and Mackie [56] and ($T = 1533$ K, $P = 26$ kPa) by Fulle et al. [57]. A reasonable agreement has been reached between experiments and simulated results.

After the interesting results obtained by Tian et al. [60], other studies were conducted on furanic compounds oxidation in flame conditions. Indeed, in 2014, Nancy and Bielefeld groups conducted a series studies on the three “furan family” (F [62], MF [70] and DMF [83]). In furan study, Liu et al. [62] have investigated the chemical structure of two low-pressure premixed furan flames ($P=20,40\text{mbar}$, $\varphi = 1.0$ and 1.7) by using molecular-beam mass spectrometry and gas chromatography. The kinetics simulations were performed with a detailed mechanism with 305 species involved in 1472 reactions, based on the mechanism of DMF combustion developed by Sirjean et al. [81]. To optimize the numerical results for flame conditions, they have added and adjusted the furan sub-mechanism proposed by Tian et al [60], by updating some rate coefficients and the H-atom addition processes. A good general agreement between experimental and modeling results for the major combustion products as well as for many intermediate species was obtained. The comparison with Tian’s model shows that Liu’s model leads to better results for some species, due to the addition of some reaction pathways of F as well as to the use of different reactions base for the C_0 – C_2 species developed by Sarathy et al. [85]. From the reaction pathway analysis, it appears that furan is mainly consumed by H-addition on the C2 position of furan (the carbon atom bound to the oxygen atom) to form the dihydrofuryl-3 radical (C_4H_5O-3). The second important channel of consumption of furan is the OH-addition on the C-C bond forming acrolein (C_3H_4O) and the CHO radical. As example of the good agreement between experiment and simulated results using the mechanism, the profiles of some oxygenated species are reported in Fig.I.16.

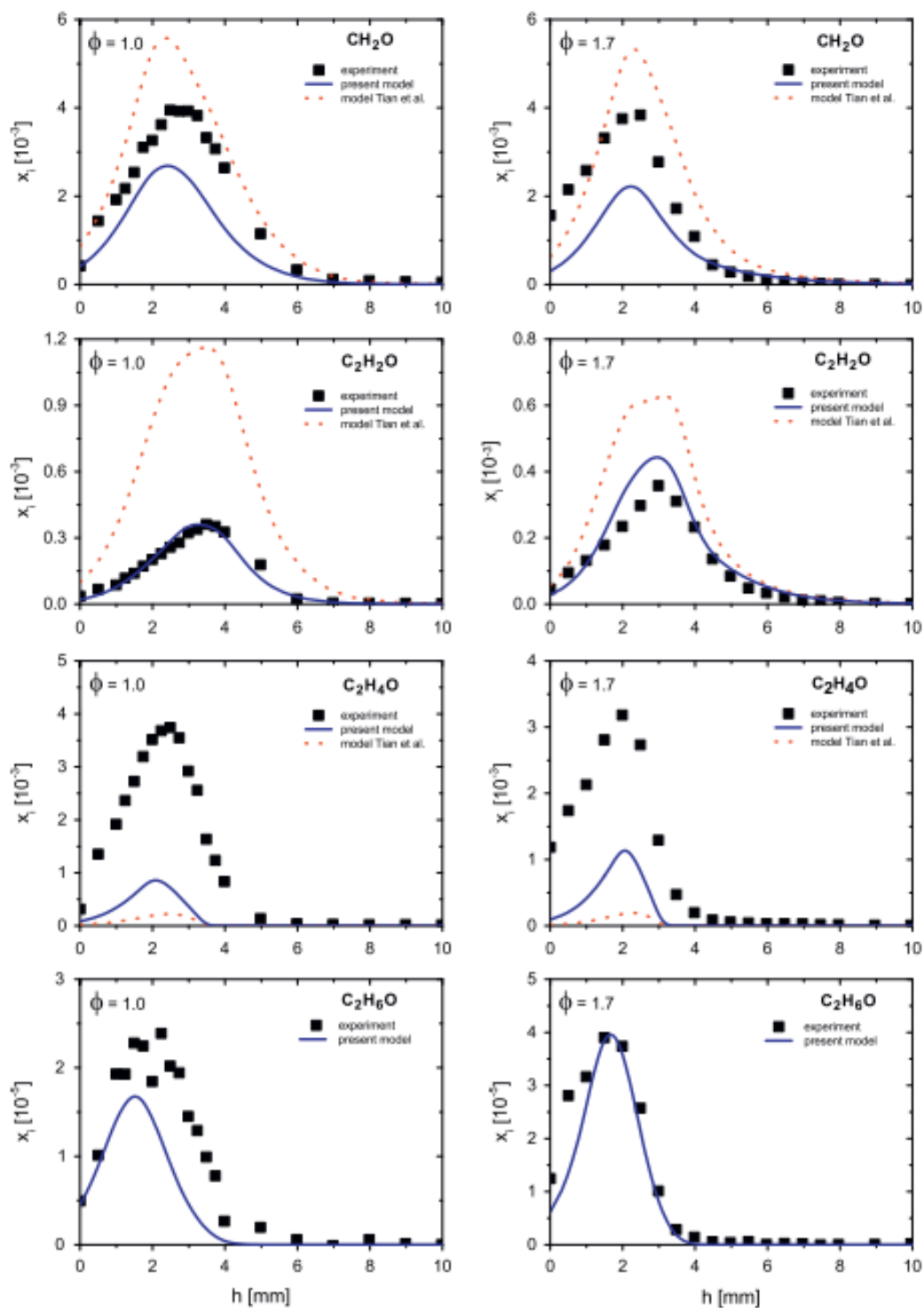


Fig.I.16: Mole fraction profiles of C_1 – C_2 oxygenated species. Symbols: experiment (EI-MBMS); lines: simulation; solid lines: Liu's model [62], dotted lines: model of Tian et al. [60]., except for C_2H_6O (simulation data were not available) [62].

Recently, Tran et al. [6] published an article on the experimental and modeling study of the Low-to-Moderate-Temperature (LMT) oxidation chemistry of furanic compounds. They report a dataset in the temperature range 730–1170 K for three

furanic fuels, 2,5-dimethylfuran (DMF), 2-methylfuran (MF), and furan (F), measured for different equivalence ratios ($\phi=0.5, 1.0$ and 2.0) in a flow reactor at 1bar. All three furanic fuels, especially DMF, produce several highly toxic oxygenated species including acrolein, methyl vinyl ketone, furfural, and phenol. These toxic species were found to be the products from the primary reactions of these fuels, and these trends could be explained satisfactorily by their model, pointing to some caution with regard to the potential emissions under LMT conditions. As example, the Fig.I.17 shows the maximum mole fractions of selected hazardous compounds from DMF, MF, and F oxidation.

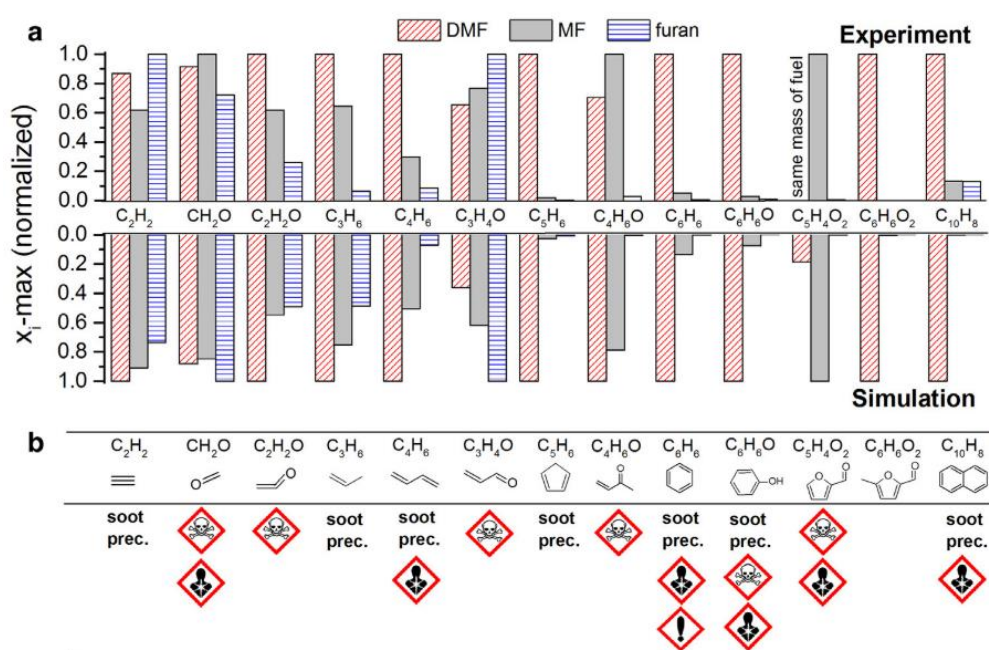


Fig.I.17. (a) Maximum mole fraction of selected hazardous compounds for DMF, MF, and F oxidation. Top: experiments at $\phi \sim 1$; bottom: LMT model predictions. For clarity, normalization by the highest value is performed, and mole fraction scales have been inverted for the simulations. (b) Structure of the respective main expected isomer and its pollutant potential. Hazard pictograms are based on the Globally Harmonized System of Classification and Labelling of Chemicals (GHS). Soot prec.: soot precursor [6].

The model includes detailed reactions subsets for HO_2 and O_2 addition to the two most important resonance-stabilized fuel radicals, 2-furylmethyl (MF-yl) and 5-methyl-2-furanylmethyl (DMF-yl). The kinetic data of these reactions subsets were computed using high-level theoretical calculations. Moreover, H-abstractions from MF and DMF by O_2 , is identified as a sensitive reaction class for the LMT oxidation of these fuels.

Some differences remain between experiment and modelling in the particular case of furan conversion. Some reactions which are very important in controlling the system reactivity of DMF and MF oxidation, i.e. the reactions of fuel radicals with HO₂, seem to have no importance for the furan conversion. From the Rate of Production (ROP) analysis it is highlighted the formation of furan during the oxidation of the other furanic compounds.

3.3.3.2. Tetrahydrofurans

Tetrahydrofuran (THF) and its derivatives (2-methyltetrahydrofuran (MTHF) and 2,5-dimethyltetrahydrofuran (DMTHF)) are cyclic saturated ethers which are liquid at standard temperature and pressure. The structure of these molecules is shown in Fig.I.18.

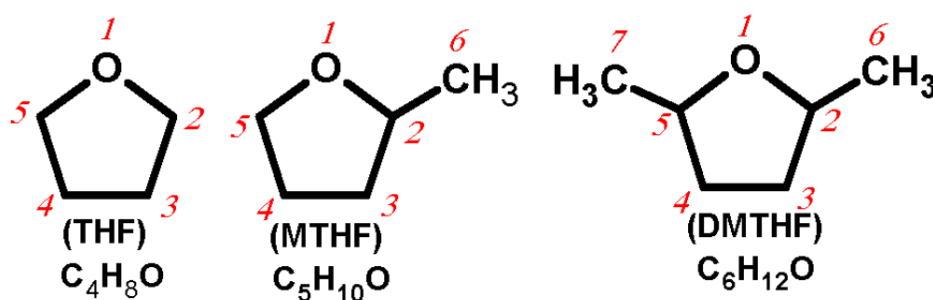


Fig.I.18 Molecular structure of tetrahydrofuran (THF), 2-methyltetrahydrofuran (MTHF), 2,5-dimethyltetrahydrofuran (DMTHF) [48].

Saturated cyclic ethers as tetrahydrofuran, 2-methyl-tetrahydrofuran and 2,5-dimethyl-tetrahydrofuran are possible candidates to become biofuel for internal combustion engine; thanks to their heating value (28.5-29.5 MJ/L), higher than that of ethanol (21.3 MJ/L) and closer than that to gasoline (31.6 MJ/L).

These compounds can be produced from lignocellulosic biomass through catalytic processes in high pressure conditions, which converts carbohydrates in THF derivatives, as reported by Yang and Sen [86] and summarized in Fig.I.19:

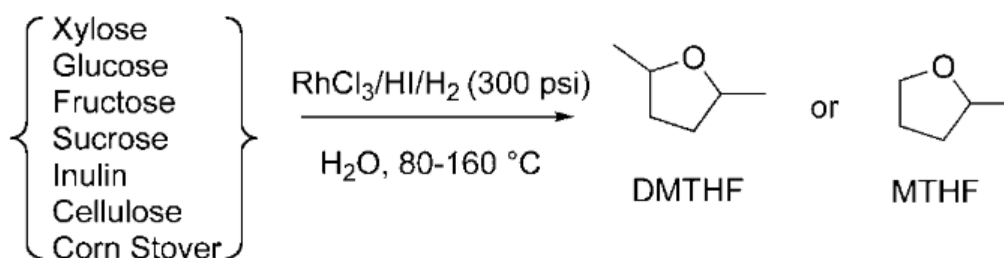


Fig.I.19 One-step transformation of carbohydrates and cellulosic biomass to tetrahydrofuran derivatives [86].

MTHF can be produced also through catalytic conversion of furfural, an important chemical platform for promising lignocellulosic biofuels [87], [88].

The MTHF has been approved by USDOE (United States Department of Energy) as a component of the "P-series" fuels for spark ignition engines [89]. This type of fuel was developed by Dr. Stephen Paul of Princeton University and it is a mixture of ethanol (25-40% by vol.), MTHF (20-35%), and hydrocarbons in $C \geq 5$ (25-40%), with the addition of butane (0-10 %) for the case of cold starting of the engine.

In addition, THF, its derivatives and other saturated cyclic ethers, have also been detected as intermediates formed from hydroperoxyalkyl radicals during combustion and ignition of $C > 4$ alkanes and alkenes [90]–[93].

Leppard [90]–[92] has shown that the chemistry of auto-ignition of higher alkanes involves the isomerization of peroxyalkyl radicals which form high concentrations of cyclic ethers (oxiranes, oxetanes, tetrahydrofurans and tetrahydropyrans). Among these cyclic ethers, substituted THFs are predominant. Subsequent reactions of these cyclic ethers can influence the overall chemical kinetic mechanisms of the oxidation of such alkanes [7].

For all the reasons described above, a better understanding of the combustion mechanism of fuel of the THF family is required. THF is well suited as a model molecule for studying the combustion chemistry of saturated cyclic ethers.

The Table I.5 presents the main works devoted to the pyrolysis and oxidation of THFs.

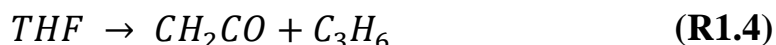
Fuel	ϕ	Reactor	Research	References
THF	pyrolysis	Heated reactor vessel T=802-842 K	Fuel decomposition	Klute et Walters[94] 1946
THF	pyrolysis	Heated reactor vessel T=819K	Fuel decomposition	Mcdonald et al.[95] 1951
THF	pyrolysis	Shock tube T=1050-1460 K	Fuel decomposition	Lifshitz et al.[96] 1986
THF	-	Heated reactor vessel T=493K	Fuel decomposition	Molera et al [97] 1988
THF	0.5-2	Shock tube T= 1000-1800 K Jet Stirred reactor T= 800-1100K	In.delay time Species profiles Kinetics study	Dagaut et al.[98] 1998
THF	1.0, 1.75	Premixed laminar flame P=2,3.3 kPa	Species profiles	Kasper et al.[99] 2011
THF	1	Shock tube T= 780-1100 K T= 691-1006K	In.delay time Kinetics study	Uygun et al.[71] 2014
THF			Quant. calculat. CBS-QB3	Verdicchio et al.[100] 2015
THF	0.7, 1.0, 1.3 0.5-2.0	Premixed laminar. flame P=6.7 kPa Shock tube T= 1300- 1700 K	Species profiles Burn.velocity In.delay time Kinetics study	Tran et al.[101] 2015
THF	0.5-2	Rapid compression machine T= 640-900K Jet stirred reactor 500 to 1000 K	In.delay time Species profiles	Vanhove et al.[102] 2015
THF			Quant. calculat. CBS-QB3	Lizardo et al. [103] 2016
THF			Quant. calculat. CBS-QB3 Kinetics study	Fenard et al.[7] 2017
MTHF	1.7	Premixed laminar flame P=4 kPa	Speices profiles	Moshammer et at.[104] 2013
MTHF	0.5-2	Rapid compression machine T= 639-878K Shock tube T= 880-1103 K	In.delay time Kinetics study	Tripathi et al.[105] 2017

MTHF	1	Rapid compression machine T= 640-900K	In.delay time Species profile Kinetics study	Fenard et al.[106] 2017
MTHF	Pyrolysis 0.7, 1.0, 1.3	Flow reactor T= 900–1100 K Premixed laminar Flame P=6.7 kPa	Fuel decomposition Species profile Burn.velocity Kinetics study	De Bruycker et al [107] 2017

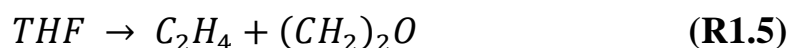
Table 1.5: Literature studies on THF derivatives combustion by considering experimental and numerical approaches.

As presented in Table 1.5, eleven studies have been carried out on kinetic behavior of THF during oxidative and pyrolytic processes. Among these studies, five study the oxidation of THF and only two are realized in flame conditions.

The interest on pyrolysis of THF started very early. Indeed, in 1946 Klute and Walters [94] studied for the first time the thermal decomposition of this saturated ether in heated reactor in the temperature range 802-842 K and the pressure range 6.7-40 kPa. Ethylene (C_2H_4) and CO have been detected with high concentrations. Acetaldehyde (CH_3CHO) and formaldehyde (CH_2O) have been identified as intermediates that play an important role in the decomposition of THF. These authors have suggested two main ways for THF decomposition:



More recently (1986), the Lifshitz team studied the thermal decomposition of THF using shock tube ($T = 1070-1530$ K, $P = 178-1018$ kPa) [96]. The analysis techniques used was gas chromatography with mass spectrometry detector. The authors suggested the main route for the decomposition of THF is:



Looking at the products, the first way was different from the one of Klute and Walters [94], which considers acetaldehyde instead of oxirane. Lifshitz et al. [96] found that

there is no isomerization between oxirane and acetaldehyde, but they proposed that CH_3CHO breaks down into CHO and CH_3 radicals in pyrolytic condition.

Ten years after the Lifshitz work, Dagaut et al. [98] proposed the first study on the oxidation of THF in 1998. They experimentally and numerically studied the ignition delay time and THF oxidation using respectively a shock tube ($T = 1000\text{-}1800\text{ K}$, $P = 200\text{-}500\text{ kPa}$, $\phi = 0.5\text{-}2$) and a jet stirred reactor ($T = 800\text{-}1100\text{ K}$, $P = 1000\text{ kPa}$, $\phi = 0.5\text{-}1$). The stable species and the intermediates such as C_2H_4 , C_3H_4 , C_3H_6 , $1\text{-C}_4\text{H}_8$, formaldehyde, acetaldehyde and propanal were measured by gas-chromatography. The more specific species 2,3- and 2,5-dihydrofurans were detected only in trace amounts. The authors proposed a detailed kinetic mechanism (71 species, 484 reactions) to describe the THF oxidation.

Later, in 2015, another study on the oxidation of THF was proposed by Vanhove et al.[102], in particular to investigate the low temperature oxidation and ignition of this biofuel through two distinct experimental devices: a Rapid Compression Machine (RCM) and a Jet-Stirred Reactor (JSR). Ignition delays of THF have been measured in RCM for pressures between 0.5 and 1.0 MPa, and core gas temperatures ranging from 640 to 900 K. They have shown the existence of two-stage ignitions at temperatures between 680 and 810K, the cool flame being clearly marked between 680 and 730 K. By sampling the reactive mixture during the ignition delay, they provided the evidence of the formation of $\text{C}_1\text{-C}_4$ aldehydes and alkenes, different cyclic ethers such as oxirane, methyloxirane, oxetane, furan, both isomers of dihydrofuran and 1,4-dioxene, as well as cyclopropanecarboxaldehyde. The oxidation of THF was also studied in a JSR, close to atmospheric pressure, at temperatures from 500 to 1100 K and at equivalence ratios from 0.5 to 2. They obtained mole fraction profiles, which indicate a significant low-temperature reactivity of THF, beginning at temperatures around 550 K. They observed also that the isomerization of 2,3-dihydrofuran can yield 2-butenal and cyclopropanecarboxaldehyde that subsequently isomerizes to 2-butenal.

Regarding the oxidation of THF in flame conditions, only two studies are available in literature until now. The first one to study THF in flames was Kasper et al [99] in 2011. They published a work on the identification and quantification of the chemical species produced in low-pressure premixed laminar $\text{THF/O}_2/\text{Ar}$ flames ($P = 2\text{-}3.3\text{ kPa}$, $\phi = 1\text{-}1.75$) using ionization or photo-ionization mass spectrometry combined with molecular beam sampling (PI-MBMS or EI-MBMS, respectively). About 60

intermediates radicals and stable species were detected. Based on the identified intermediates species, THF consumption pathways were also discussed. The data suggest the presence of γ -butyrolactone in the THF flames which can be interpreted as indirect evidence of the formation of hydroperoxides.

More recently, Tran et al. [101] studied laminar low-pressure premixed flame structure, atmospheric adiabatic laminar burning velocities, and high-pressure ignition delays. The structure of laminar premixed low-pressure (6.7 kPa) argon-diluted (78%) THF flames were studied at three equivalence ratios (0.7, 1.0 and 1.3) by using on-line gas chromatography analysis. During the low-pressure flame experiments, about 40 stable species were identified and quantified. Ethylene, propene, formaldehyde, acetaldehyde, and dihydrofurans were observed as important intermediates species. Aromatic compounds such as benzene were detected but in very low amounts. The adiabatic laminar burning velocities of THF–air mixtures were measured using the heat flux burner method at atmospheric pressure (initial temperatures from 298 to 398 K and equivalence ratios from 0.55 to 1.60). The ignition delays of THF–oxygen–argon mixtures were measured behind reflected shock waves (temperatures from 1300 to 1700 K, pressures around 8.5 atm, mixtures containing 0.25–1% of fuel for equivalence ratios in the 0.5–2.0 range). They proposed a kinetic model with 255 species in 1723 reactions for THF combustion which was developed using a combination of automatic generation (EXGAS), Evans–Polanyi correlations (for H-abstraction kinetic data), and theoretical calculations (for unimolecular initiation, H-abstraction and β -scission kinetic data). The model predicts correctly ignition delays obtained in shock tube, but overpredicts significantly the measured laminar burning velocities, for elevated temperatures especially. The influence of the initiation reactions by breaking C–C or C–O bonds, which was proposed in literature and had a significant impact under pyrolysis, has been found negligible under their studied conditions. As example, the experimental and simulated profiles for small oxygenated species are presented in Fig. I. 19.

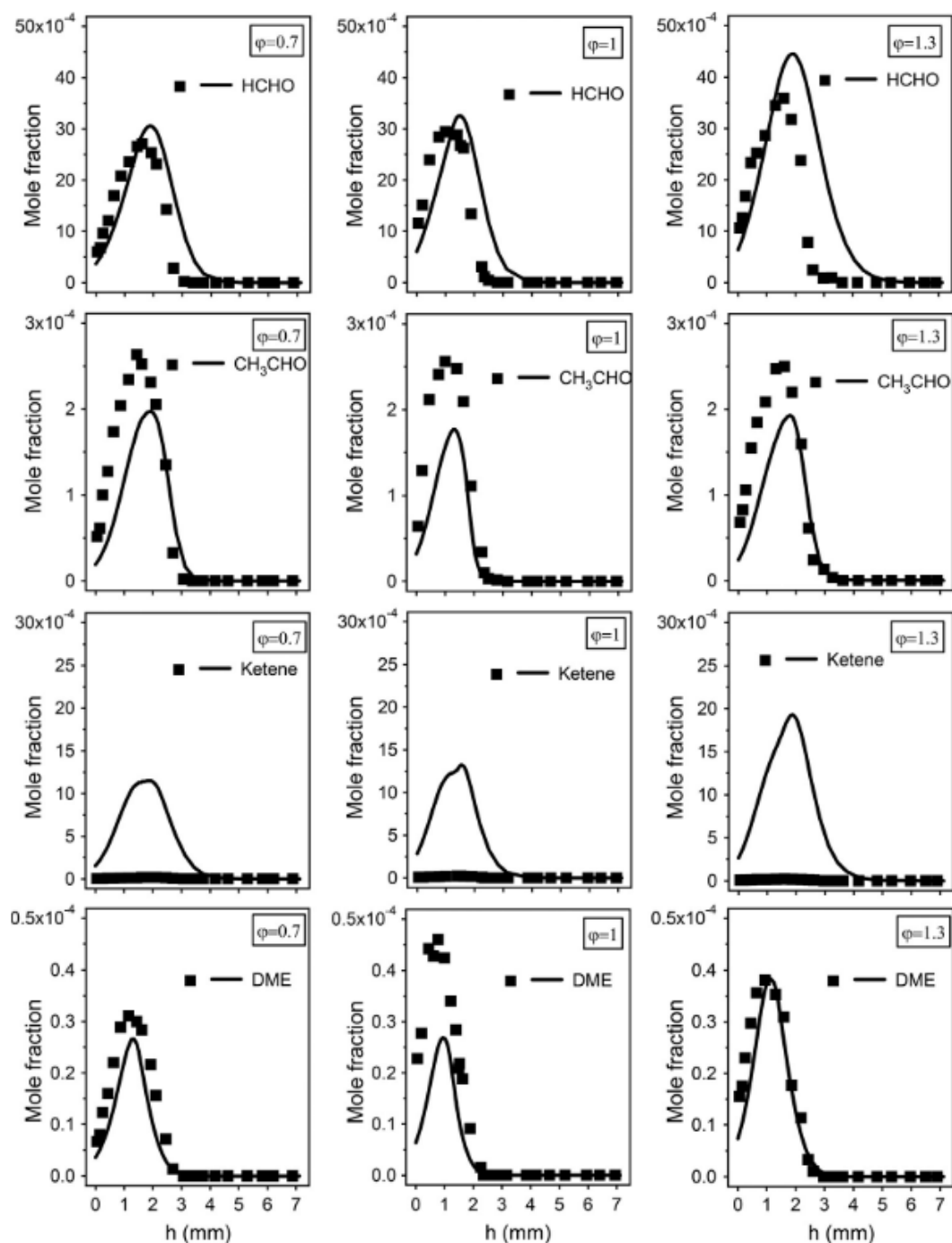


Fig.I.19 Mole fraction profiles of C_1 - C_2 oxygenated intermediates. Symbols: experiment; lines: simulation [101].

Last year, Fenard et al. [7] have proposed a detailed kinetic model for the low-temperature oxidation of THF. The thermochemical and kinetic data related to the most important elementary reactions involved in low temperature oxidation have been derived from ab initio calculations. The model contains 467 species and 2390 reactions. Simulations were performed and validated for measurements carried out

with different types of experimental setups: jet-stirred reactors (Vanhove et al. [102] and Dagaut et al. [98]), a rapid compression machine (Vanhove et al. [102]), shock tube experiments (Uygun et al. [71]), and low-pressure laminar flame structures (Tran et al [101]). Predictions from this model are overall in good agreement with this broad range of literature experimental measurements. The model explains the formation of most experimentally observed stable intermediates observed in JSR or RCM below 800 K. Fig.I.20 shows representative results for some oxygenated species performed in JSR.

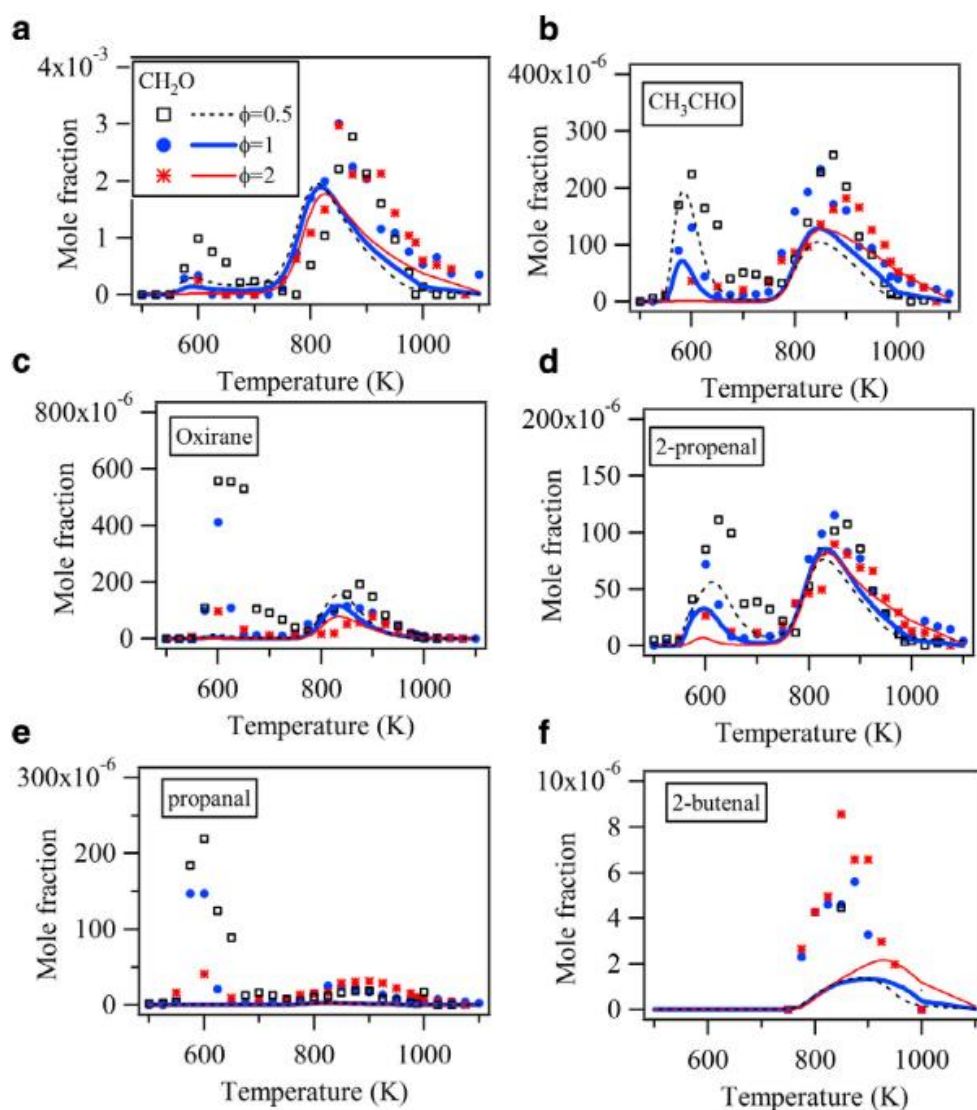


Fig.I.20. Comparison between simulated (lines) and experimental (symbols) mole fraction profiles for the oxygenated compounds produced during the oxidation of THF/O₂/He mixtures in a JSR at $p = 0.106$ MPa, $\tau = 2$ s and ϕ from 0.5 to 2 [7].

This literature study shows that for F and THF combustion, only few studies have been performed in flame conditions and as pure fuels. Derivates of these compounds will be used in engine in the future, thanks to their properties closer to commercial fuels, as indicated in the first part of this paragraph. As engine fuels, they will be blended with some other hydrocarbon fuels, to improve the engine performance.

4. Conclusion

In this chapter we have seen that combustion has an important place in modern society. The use of fossil fuels results in a significant increase in GHG emissions and air pollutants, and thus contributes to the greenhouse effect and induced global warming. Emissions of pollutants related to combustion processes also cause a lot of disturbances on the environment (photochemical pollution, acid rain, production of tropospheric ozone ...) and on humans (respiratory disorders, carcinogens ...).

One of the solutions to limit this contribution in the transport sector is the development of the biofuels. Some highlights of different generation of biofuels have been presented and in particular the lignocellulosic biofuels have been detailed.

Among this typology of biofuels, the compounds of the furan and THF families seem to be promising candidates, thanks to their properties comparable with fossil fuels.

A bibliography study on furan and THF derivates is presented, and we noticed that the studies on oxidation in flame conditions are very few and any studies consider some mixture of these compounds with other hydrocarbons.

As reported in several works on kinetics behavior of F and THF, different pollutants such as aldehydes or other toxic oxygenated compounds are formed during the combustion of these biofuels, which could affect the formation of nitrogen oxides, another important pollutant.

In the next chapter, a review of the NO formation mechanism and their interaction with biofuels in engine combustion are presented.

Chapter II: Nitrogen oxides chemistry

1. Mechanisms of formation of NO in combustion processes

Nitrogen oxides (NO_x) are formed in almost any combustion and some industrial processes (nitric acid production, fertilizer manufacturing, surface treatment, etc.), mostly as nitric oxide (NO) with smaller amounts of nitrogen dioxide (NO_2) and nitrous oxide (N_2O).

During combustion processes, the produced NO is converted to NO_2 in the presence of oxygen (from 0.5 to 10%). This reaction continues slowly in the atmosphere and explains the brown color of the polluted air layers located at a few hundred meters of altitude in some cities. NO_x are also involved in the formation of photochemical oxidants (as tropospheric ozone) and increase the greenhouse effect. Indeed N_2O has a global warming potential (GWP) [108] 298 times higher than CO_2 and about 9 times higher than CH_4 .

At the global scale, the main emitters of NO_x are road transport and large combustion plants. Volcanoes, thunderstorms and forest fires also contribute to NO_x emissions [109].

Five main NO formation mechanisms can be identified in combustion processes:

- Thermal-NO
- Prompt-NO
- Fuel-NO
- NO formation mechanism via N_2O
- NO formation mechanism via NNH

1.1. Thermal-NO mechanism

The first reaction scheme for formation of nitrogen monoxide NO from the molecular nitrogen of air at high temperature was proposed by Zeldovich [110]. The Zeldovich mechanism, or thermal-NO formation, is well established. The initiating step is the attack of an oxygen atom on the triple bond of N_2 :



This reaction has a high activation energy, about 75 kcal/mol [111] and is the limiting step in thermal-NO formation. Once formed, the nitrogen atom is rapidly oxidized to NO through reactions with OH or O₂:



The Zeldovich mechanism efficiency strongly depends on the temperature and on the concentration of O atoms and OH radicals. These three reversible reactions significantly contribute to the NO formation at high temperature (usually above 2000 K).

1.2. Prompt-NO mechanism

The mechanism initiated by the reaction of CH_{*i*}-radicals (n=0, 1, 2 or 3) with N₂ is termed prompt-NO ([8], [112], [113]) and was discovered by Fenimore [112] in 1971. Fenimore did the following observation by studying the formation of NO in hydrogen, carbon monoxide and various hydrocarbons flames stabilized on atmospheric and high-pressure burners. By plotting the NO mole fraction as a function of the distance above the burner (HAB), in hydrogen or carbon monoxide flames, the extrapolation of the NO values measured from the burned gases leads to a value of NO equal to 0 at burner surface (HAB=0). However, in hydrocarbon flames, this extrapolation at the burner surface indicates a positive value suggesting the presence of a NO quantity which can not be only explained by thermal NO.

For the CH radical, the initiation reaction is:



The radicals C₂ may also contribute to this mechanism according to the following initiation reaction:



Fenimore called this new NO formation route "Prompt-NO". In the same period, Barnun and Bauer studied the reactions between acetylene and elementary nitrogen atoms in a reflected shock tube. They followed spectrophotometrically the CN, HCN, and C₂ production rates [114]; one of the first measurements of these species during combustion process. Some years later, De Soete [115] confirmed that HCN is an important intermediate in NO formation pathway.

The term "Fenimore prompt-NO mechanism" was later proposed by Bowman [116] to avoid any confusion in the terminology when describing the NO formation at a faster rate than that calculated from the Zeldovich mechanism.

1.2.1. *The "CH + N₂ ⇌ products" reaction*

The Fenimore mechanism is the main source of NO formation in low temperature hydrocarbon flames (T <2000 K). The involved reactions are prevalent in the flame front and are sensitive to the equivalent ratio of fuel mixtures. Under these conditions, the formation of thermal-NO is negligible compared to that of prompt-NO due to the high presence of CH in the flame front and the low temperature.

Several studies have been carried out to determine the rate constant of reaction (R2.4a), for example by using a shock tube at elevated temperature (3000-4000K). This constant was determined by following the consumption of CH by laser absorption [117] or the formation of N atom by using atomic resonance absorption spectroscopy (ARAS) [118]. However, the reaction (R2.4a) is controversial, because it does not respect the rule of spin conservation. Indeed, the reactants (CH and N₂) are in a doublet potential energy surface, while the products (HCN and N) are in a quartet surface.

For three decades, measurements and complex theoretical calculations have been carried out to explain this spin forbidden reaction. Theoretical calculations focused on finding the correct surface crossing from the doublet to the quartet surface, since intersystem crossing is the limiting step for the rate constant calculation value [119].

In 2000 Moskaleva and Lin [113] were the first who solved the problem of the initiating reaction of the prompt-NO mechanism. By using theoretical chemistry calculations, they showed that the products of the initiation reaction were NCN + H:



Contrary to the reaction (R2.4a), this reaction (R2.4b) respects the spin conservation. The products (NCN and H) are, indeed, in a doublet potential energy surface. Moskaleva and Lin proposed also the following rate constant expression by using the Rice-Ramsperger-Kassel-Markus (RRKM) theory:

$$k_{[111]} = 2.22 \times 10^7 T^{1.48} \exp(-11760/T)$$

in cm³/mol.s, T is the temperature in K.

In order to validate this new pathway for prompt-NO, experimental measurement of NCN was needed.

Smith [121] was the first to detect NCN in low pressure methane flames, doped or not with NO (CH₄/O₂/N₂ and CH₄/NO/O₂/N₂) by Laser Induced Fluorescence (LIF).

A modelling study of NO formation in natural gas flames was performed by El Bakali et al [122]. They were the first to include the reaction R2.4b in the mechanism. They used the rate constant calculated by Moskaleva and Lin, but this led to an important underestimation (by more than a factor of 6) of the amount of prompt-NO in flames. In fact, the Moskaleva rate constant was in reasonable agreement with shock tube measurements, within the temperature range 2300–3800 K (see Fig.II.1), but much higher than the flame temperature range. In consequence El Bakali and coworkers proposed a new value of the rate constant to better fit with experiments:

$$k_{[120]} = 5.10 \times 10^{11} \exp(-13600/RT)$$

Vasudevan et al [123] were the first to measure NCN in shock tube by laser absorption. They re-examined the rate of reaction (R2.4b) by studying the consumption of CH radical. The obtained rate constant is closer to that given by Dean et al. [117]:

$$k_{[121]} = 6.03 \times 10^{12} \exp(-11150/T)$$

Following this discrepancy found by El Bakali and coworkers, Harding et al.[124] proposed a new value of the rate constant of reaction (R2.4b) using ab initio calculation methods:

$$k_{[122]} = 4.1 \times 10^8 T^{1.122} \exp(-8819/T)$$

This constant was determined by transition state theory calculations. This constant is in good agreement with the experimental value found by Vasudevan [123].

Fig II.1 reports the plot of the experimental measurements and theoretical calculations for the $\text{CH} + \text{N}_2 \rightleftharpoons \text{products}$ rate coefficient. It can be noticed that the major results are reported for a high temperature range as in case of shock tube studies.

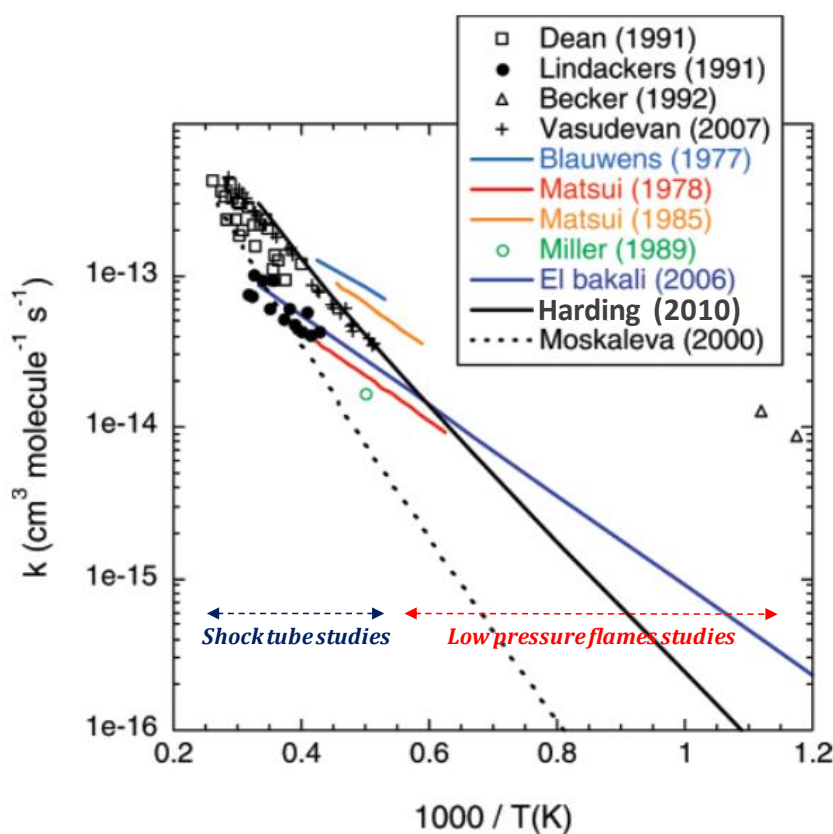


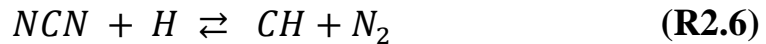
Fig. II.1: Plot of the experimental measurements and theoretical predictions for the $\text{CH} + \text{N}_2 \rightleftharpoons \text{products}$ rate constant. The black symbols denote direct experimental results, the colored lines and symbols denote modeling results, while the black solid and dashed lines denote the theoretical predictions [124].

Other NCN experimental measurements were also performed in flames. Sutton et al. [125] presented semi-quantitative measurements of the NCN intermediate in five low-pressure premixed CH₄/O₂/N₂ flames, ranging from fuel-lean to fuel-rich conditions. They found high correlations between the CH and NCN concentration peaks and the NCN peak and post-flame NO concentrations over all equivalence ratios.

Lamoureux et al. [126] were the first to quantitatively measure NCN in a low-pressure methane flame by combining Laser Induced Fluorescence (LIF) and Cavity Ring-Down Spectroscopy (CRDS) techniques.

1.2.2. Thermochemistry properties of NCN

The thermochemistry properties of cyanonitrene radical (NCN) are important to model prompt-NO formation. The value of the enthalpy of formation of the NCN radical is strongly correlated to the branching ratio of the reaction $\text{NCN} + \text{H} \rightleftharpoons$ products:



Reaction (R2.6) is the second most important reaction in the prompt-NO mechanism, according to sensitivity analysis [15, 17].

Goos et al. [128] proposed a value around $457.8 \pm 2.0 \text{ kJ mol}^{-1}$ based on a detailed analysis of available experimental and theoretical thermochemical data combined with two Active Thermochemical Tables (ATcT) analyses. Other previous modeling studies of prompt-NO have employed different values for $\Delta_f \text{H}^0_{298}(\text{NCN})$: Konnov [129] recommended the high value of $464.4 \text{ kJ mol}^{-1}$ from Bise and coworkers [130]. Recently, Lille group [8] found that the best agreement with flame measurements is obtained with an even lower $\Delta_f \text{H}^0_{298}(\text{NCN}) = 444.3 \text{ kJ mol}^{-1}$, as stated in [131].

1.2.3. NO modelling

Following the study of Moskaleva and Lin, El Bakali et al. [122] were the first ones who integrated reaction (R2.4b) in a prompt-NO sub-mechanism coupled to a detailed hydrocarbon oxidation mechanism GDFkin@3.0_NCN. It was validated against prompt-NO measurements in low pressure flames.

Sutton et al. [125] compared the experimental results of the NCN and CH, obtained in low-pressure premixed CH₄/O₂/N₂ flame, with numerical calculations using the GRI-Mech 3.0 and GDFkin 3.0 mechanisms modified with additional NCN formation and consumption reactions. Good agreement between calculations and experiments was found for NCN mole fraction profiles when using the modified mechanisms.

Konnov [129] modified his previous kinetic mechanism (Konnov0.6) to take into account the latest results and discussions regarding the formation of the prompt-NO. According to Konnov, the rate constant of (R2.4b) from Vasudevan et al. [123] overestimates the formation of NO in the burnt gases for atmospheric flames. Consequently, he adopted the rate constant derived from the experimental results of Dean et al. [117], obtained in shock tube.

Lamoureux et al. [127] have quantitatively measured CH, NO and NCN in CH₄/O₂/N₂ and C₂H₂/O₂/N₂ flames stabilized at low pressure. The authors have updated the GDFkin@3.0_NCN mechanism [122]. Good agreement was obtained between the mole fraction experimental profiles of these species and those simulated. They propose to slightly modify the rate constant value of reaction (R2.4b):

$$k_{[125]} 1.95 \times 10^{12} \exp(-16915/RT)$$

This value is closer to those proposed by Vasudevan et al. [123] and Harding et al. [124]. Fig. II.2 presents the new scheme of the prompt-NO mechanism proposed by Lamoureux and co-workers:

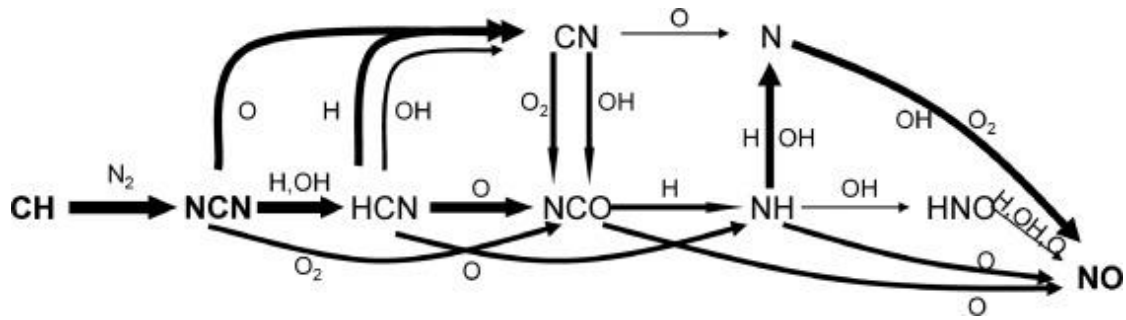


Fig. II.2: Scheme of the prompt-NO in the flame front of a rich $\text{CH}_4\text{-O}_2\text{-N}_2$ flame based on rate of production analysis with GDFkin@3.0_NCN mechanism [127].

The same authors (Lamoureux et al [8]) have recently updated the NO formation mechanism. In their new mechanism named NOMEcha2.0, the NCN chemistry has been revisited, notably by taking into account the thermodynamic data of the NCN radical. The rate constant value of the reaction R2.6 was modified based on the experimental results in shock tube of Faßheber et al. [132] and Dammeier et al [131]. They also introduced two new nitrogen species HNC and HNCO as well as the reaction route $\text{HCN} \rightarrow \text{HNC} \rightarrow \text{HNCO} \rightarrow \text{NH}_2 \rightarrow \text{NH} \rightarrow \text{NO}$. The new NOMEcha2.0 mechanism has been validated on CH, NO, NCN, NCO, CN and HCN species profiles measured quantitatively in low pressure $\text{CH}_4/\text{O}_2/\text{N}_2$ and $\text{C}_2\text{H}_2/\text{O}_2/\text{N}_2$ flames. It has also been validated on the experimental data obtained by Sutton et al. [125] in flames of C_1 to C_4 alkanes, on the HCN and NO profiles obtained by Miller et al. [133] in $\text{H}_2/\text{O}_2/\text{HCN}/\text{Ar}$ flames stabilized at low pressure, on the HCN species measured in a jet stirred reactor (JSR) by Dagaut et al. [134], and on HNCO measurements in a plug-flow reactor by Glaborg et al. [135]. Fig. II.3 shows the new reaction scheme so obtained in a stoichiometric $\text{CH}_4/\text{O}_2/\text{N}_2$ flame:

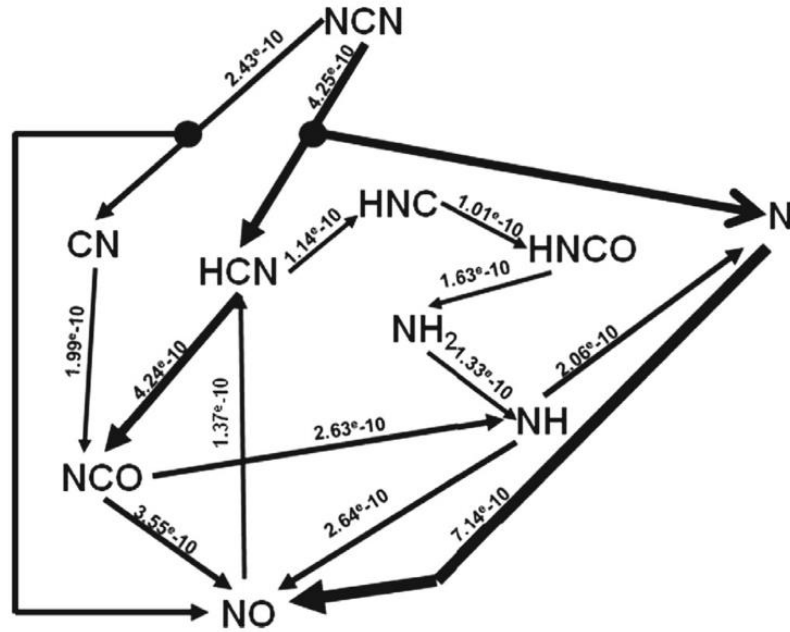


Fig.II. 3: Reaction pathways of prompt-NO formation considering the flow rates integrated along the vertical axis in the stoichiometric CH₄/O₂/N₂ flame [8].

1.3. Fuel-NO mechanism

The Fuel-NO mechanism describes the formation of NO from nitrogenous fuels such as fossil fuels, coals or fuels used for propellants in the aeronautical industry. These fuels can contain from 0.5 to 2% nitrogen by weight, mainly in pyridine (C₅H₅N) and pyrrole (C₄H₅N). This mechanism is initiated by a pyrolysis step of the nitrogen compounds in the fuel leading to the formation of hydrogen cyanide (HCN) and ammonia (NH₃). The carbon-nitrogen bonds have lower energy than the N₂ triple bond. This path is therefore easier and faster at low temperature than thermal-NO mechanism. The formation of fuel-NO from nitrogenous fuels depends on the temperature and the presence of oxygen (O, OH and O₂) in the combustion zone.

HCN and NH₃ are the key intermediate species for fuel-NO mechanism. Different works have been carried out on the oxidation chemistry of these compounds, especially for HCN. Most of these works were reviewed by Dagaut et al. [134] and recently the chemistry was re-examined by Glarborg and Marshall [136] who emphasized the role of the hydrogen isocyanide isomer HNC. The key issue in HCN chemistry is the selectivity towards forming other nitrogen species during oxidation,

The rate constant of the initiation reaction R2.8 has low activation energy ($E=58$ kcal mol) and is very sensitive to pressure. The formation of N_2O is thus favored under conditions of high pressure, moderate temperature, and fuel lean conditions.

1.5. NO formation mechanism via NNH

The possible NO formation mechanism via NNH is based on the addition of a hydrogen atom to the molecular nitrogen followed by an oxidation step leading to NO. It was proposed by Hayhurst and Hutchinson [139] based on the modelling work of Bozzeli and Dean [140]:



The NNH mechanism is most significant at slightly reducing condition and it is especially sensible to the temperature. Konnov et al. [141] showed that the formation of NO via NNH in a stirred reactor may be important in the case of a relatively short residence time (some ms) associated with particularly high temperatures (of the order of 2200 K). At low temperatures (1500-1900 K), this mechanism can be neglected regardless of the residence time.

2. Links between NO_x and oxygenated fuels

The use of biofuels allows a reduction of the dependence to petroleum-based fuels and should limit the increase of total amount of greenhouse gases in the atmosphere. Differences in chemical properties of added oxygenates such as cetane number, oxygen content, latent heat of vaporization, and low heating value can affect pollutant emissions.

Biodiesel, alcohols and ethers are widely studied in the literature and their performances are determined, neat or blended with fossil fuels, and in different engines conditions.

2.1. Biodiesel

Diesel engines are widely used for transportation and power generation, mainly due to their relatively high thermal efficiency. With the strict emission regulations, there is a great interest to develop engine combustion systems which offer high efficiency with reduced NO_x and smoke emissions.

Biodiesel is an interesting alternative to conventional diesel, because it does not require any modifications of the engine system. It can be defined as a mixture of alkyl esters of long chain fatty acids synthesized via trans-esterification of triglycerides [142] (Fig. II.6).

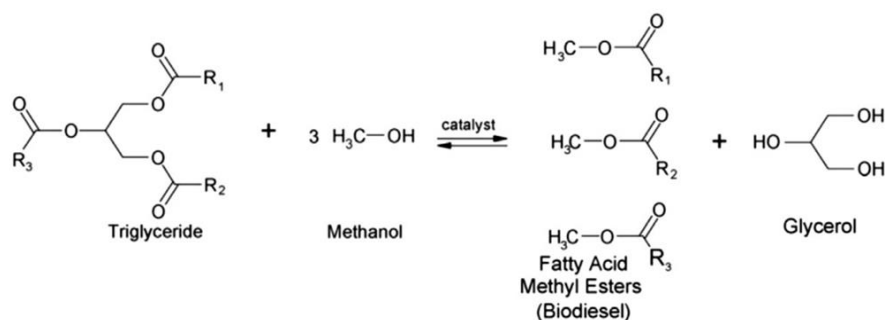


Fig.II.6: Transesterification reaction of triglycerides.[143].

Compared to conventional diesel fuels, biodiesel is generally found to reduce emissions of hydrocarbons (HC), carbon monoxide (CO), and particulate matter (PM)-

It increases however aldehydes and nitrogen oxides (NO_x) emissions [142], [144]–[146]. For example, Wu et al. [147] studied five methyl esters of different origins in a diesel engine and compared the oxidation of these esters with conventional diesel. The results of NO_x emissions for the five biodiesels are 10-23% higher than for diesel, as shown in Fig.II.7.

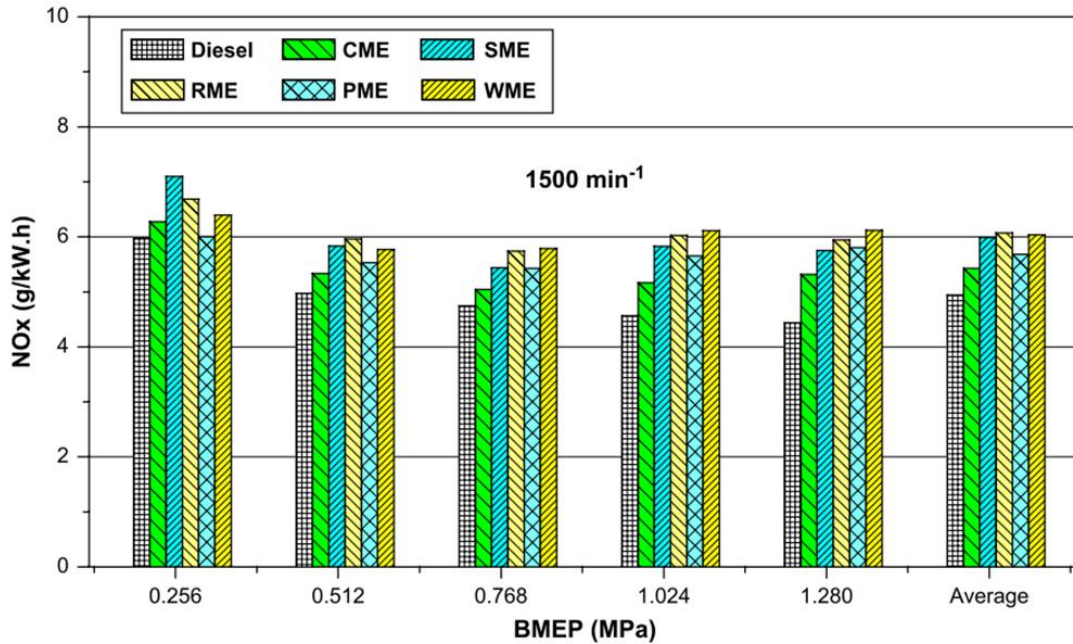


Fig. II.7: NO_x emissions in DI engine for five methyl esters (CME: cottonseed methyl ester, SME: soybean methyl ester, RME : rapeseed methyl ester, PME : palm oil methyl ester; WME: waste cooking oil methyl ester) and diesel [147]. BMEP = Brake Mean Effective Pressure.

In the literature it is shown that numerous factors contribute to NO_x emissions and their relative importance varies with engine technology and operating conditions. These emissions depend on injection timing, adiabatic flame temperature, radiative heat losses, engine technology and operating conditions.

Recent studies focused on the chemical characteristics of biodiesel, in particular on the degree of the fuel unsaturation [4]. The unsaturation of the oils and fatty acid methyl esters (FAME), i.e. biodiesels, is evaluated by using iodine number (IN), which takes into account the number of double bonds present in the esters carbon chain [5], [143].

Historically, iodine number (also known as iodine value) has been used to study the oxidative stability of fats and oils, since it indicates the propensity of the oil or fat to

polymerize and to form deposits [4]. It is expressed in grams of iodine which react with 100 g of biodiesel sample. Indeed, iodine reacts with the double bonds, present in biodiesel.

Iodine number is in connection with the cetane number (CN) and cold filter plugging point (CFPP), important parameters for diesel fuels. The CN gives information on the ignition quality or ability of fuel to auto-ignite quickly after being injected [142]. It is based on two compounds which are hexadecane with a CN of 100 and heptamethylnonane with a CN of 15. CN increases with increasing chain length and saturation of fatty acids. However, biodiesel has higher CN than conventional diesel fuel because of its higher oxygen content.

Cold filter plugging point (CFPP) is used as an indicator of low temperature operability of fuels. It indicates the temperature at which the test filter starts to plug due to fuel components that have started to gel or crystallize [142]. Fig. II.8 shows some examples of FAMES as a function of their unsaturation and compared with European standard for cetane number, iodine value and CFPP. The value of CN, IN and CFPP are shown in table II.1.

<i>FAME</i>	<i>IN (g I₂/100g)</i>	<i>CN</i>	<i>CFPP (°C)</i>
<i>Palm</i>	57	61	10
<i>Olive</i>	84	57	-6
<i>Almond</i>	92	57	-6
<i>Corn</i>	101	53	-12
<i>High Oleic Sunflower</i>	102	53	-6
<i>Rape</i>	109	55	-10
<i>Soybeans</i>	128	49	-5
<i>Sunflower</i>	132	50	-3
<i>Grape</i>	138	48	-6

Table II.1: Values of iodine number (IN), cetane number (CN) and CFPP for FAME used in Fig. II.8 [148].

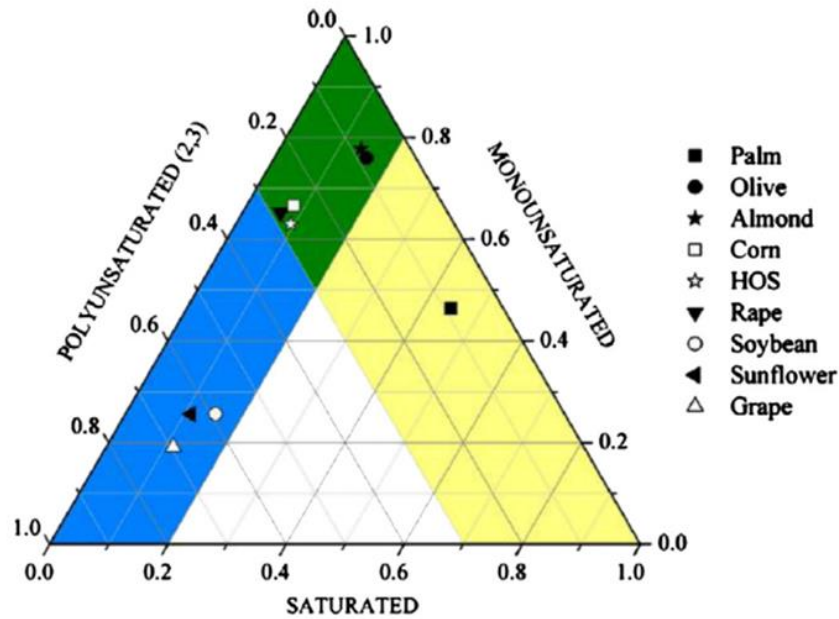


Fig. II.8: Biodiesel by saturated, mono-unsaturated, poly-unsaturated FAME and areas verifying the limits imposed by European standard EN 14214 for cetane number, iodine value, and CFPP; yellow (right): conformed cetane number and iodine value; blue (left): conformed CFPP; green (intersection): biodiesel that satisfies EN 14214 standard [148].

Several studies showed a strong relationship between NO_x emissions and iodine number. For example, Altun [3] observed that the biodiesel having the lowest iodine number had also the highest cetane number, lowest density and adiabatic flame temperature, which leads to a reduction of NO_x emissions. Additionally, the increase of unsaturation in biodiesel fuels produces higher NO_x emissions, smoke opacity, and lower HC emissions.

Love et al. [149] studied the effect of iodine number on NO_x formation in pre-vaporized laminar flames of biodiesels like canola methyl ester (CME), soy methyl ester (SME) and methyl stearate (MSt) to delineate the effects associated with fuel chemistry alone by eliminating parameters such as injection timing, atomization and droplet vaporization phenomena. It was observed that the NO concentration peak significantly increased with the iodine number indicating the existence of a strong correlation between the chemical structure of the neat biodiesel and NO_x formation. Furthermore, the observed variation of NO emission index with different fuels agreed with the observed trends in engine studies.

In a study realized by Cecrle et al [150], the cetane number, unsaturation percentage, density and H/C mole ratio were seemed to be significantly correlated with NO emissions. Also, the double carbon (C=C) bond in unsaturated biodiesel molecule released more energy when they were broken compared to a carbon hydrogen (C-H) bond, which in turn led to increased combustion temperature and pressure inside the chamber. This significantly results in an increased thermal-NO production. In addition, it has been mentioned that fuel unsaturation might also lead to increased oxidation of CH radicals during the premixed burn phase, promoting subsequent prompt-NO formation.

A fundamental study has been performed by Sylla et al. [151] on the impact of the methyl butanoate (MB) on NO formation in stoichiometric low pressure methane/MB flames. The species profiles were measured by coupling Laser Induced Fluorescence (LIF), Gas Chromatography (GC) and Fourier Transform Infrared Spectroscopy (IRTF). They found that MB oxidation promotes the formation of CH₃ radical in comparison to methane since it contributes to increase C₂ and C₃ species. In presence of MB, NO is consumed early in the flame front through reaction with HCO radical, which is formed from formaldehyde, an important intermediate during MB oxidation.

2.2. Alcohols and ethers

Alcohols are widely used in both compression and spark ignition engines. Indeed, their characteristics allow them to be used neat or blended with fossil fuels. The ether fuels, such as methyl tert-butyl ether (MTBE) and dimethyl ether (DME), are mainly used as additives at low blending ratio to enhance the octane number and oxygen content of gasoline.

The addition of alcohols and ether fuels to gasoline yields a complete combustion due to the higher oxygen content, and thereby leads to increased combustion efficiency and decreased engine emissions [152]. Awad et al. [152] have shown in their review that the use of butanol, methanol, ethanol, fusel oil (a by-product of alcohol production after fermentation during the distillation process), MTBE, and DME as fuels in SI engine reduce CO and NO_x emissions in comparison with gasoline combustion. On the other hand, the energy value of alcohol and ether fuels is approximately 30% lower

than gasoline. In addition, alcohols can be used as pure fuels in spark ignition engines, but some modifications to the engine are needed.

Yusri et al. [153] reviewed different works on the engine performance and exhaust emissions of first aliphatic alcohol family (methanol, ethanol, propanol and butanol) in compression and spark ignition engines. In diesel engine, they highlighted that NO_x emission decreases when binary alcohol/diesel blends are used due to higher vaporization of methanol, ethanol, propanol and butanol. In spark ignition engine, NO_x , CO, CO_2 and HC emissions are lower than in gasoline fuel when oxygenated blends are used.

The NO_x -emission-decreasing effect, observed by using short-chain alcohols-diesel blends, is also found for long-chain alcohols, such as pentanol and hexanol. These alcohols overcome disadvantages of short-chain alcohols such as the lower cetane number, lower density and viscosity. Suhaimi et al. [154] studied the engine performance of 2-ethyl-1-hexanol (2-EH)/ diesel, blended in different percentages. The blending of 2-EH with diesel fuel (DF) results to reduce NO_x emission over the entire load ranges.

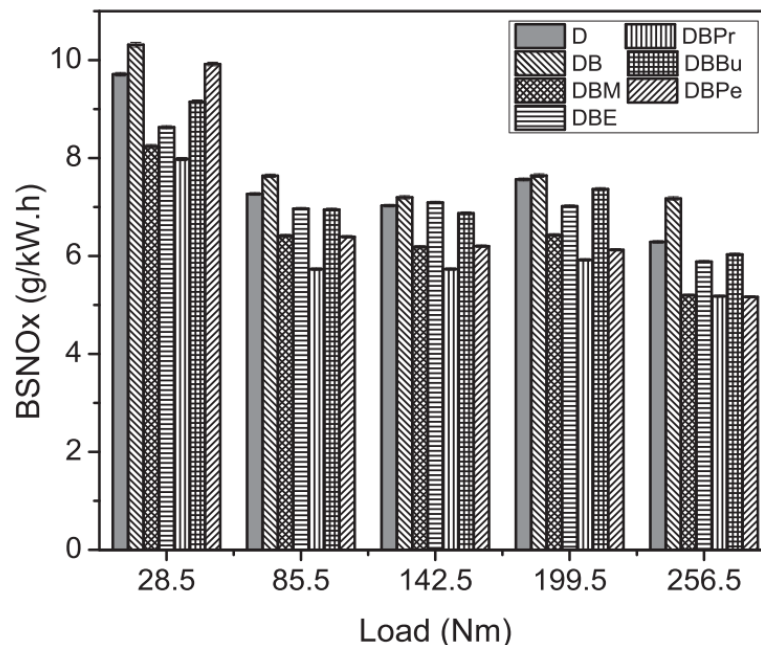


Fig. II.9: Variation of Brake Specific NO_x (BSNO_x) at different engine loads for diesel (D), waste cooking oil biodiesel (B), methanol (M), ethanol (E), 2- propanol (Pr), n-butanol (Bu) and n-pentanol (Pe) blended with diesel and biodiesel [155].

Alcohols are also used in blends with biodiesel and diesel to increase the oxygen content and reduce NO_x emission. Ghadikolaie et al. [155] studied seven fuels, including diesel (D), waste cooking oil biodiesel (B), methanol (M), ethanol (E), 2-propanol (Pr), n-butanol (Bu) and n-pentanol (Pe) used to produce six blended fuels, labelled as DB, DBM, DBE, DBPr, DBBu and DBPe respectively. Each blended fuel has the same oxygen content of 5.0% and very close carbon and hydrogen contents. The results, presented in Fig II.9, show that the presence of alcohols in the blends decreases NO_x emission with respect to biodiesel/diesel blend. The highest decrease is observed for 2-propanol (19.3%) because of the alcohol branch. As reported by Koivisto et al. [156], the increase in alcohol branch (from 1-Octanol to 3-Octanol or adding two methyl group branches to 3-Octanol to form 3, 7- Dimethyl-3-octanol) caused reduction in NO_x emissions due to the increase of ignition delay time and the decrease of the adiabatic flame temperature.

Recently, ethers and small carbonyl ester have attracted an increasing attention because of their high oxygen content. In particular, dimethyl carbonate (DMC) is primarily used as an oxygenated additive in diesel engine to reduce PM emissions [157]. DMC is considered as a 'green fuel' due to its non-toxic nature, rapid biodegradability and low bio-accumulation. It is a highly inflammable liquid which does not produce irritating or mutagenic effects by contact or inhalation. It is hydrophobic and miscible in diesel. [158]. The impact of DMC on NO_x formation has been evaluated by Kumar and coworkers [159]. They have screened different diesel-oxygenated blends for achieving simultaneous reduction of smoke and NO_x emission by testing 3 different oxygenated chemical function fuels: Diethyl ether (DEE, ether), Dimethyl carbonate (DMC, carbonyl ester) and Diglyme (DGM, glycol ether). DEE leads to the highest reduction of NO_x emission. In addition, this trend is observed for higher percentages of DEE blended, as seen in Fig. II.10. This may be due to the high latent heat of vaporation of DEE blends which leads to a reduction of the combustion temperature.

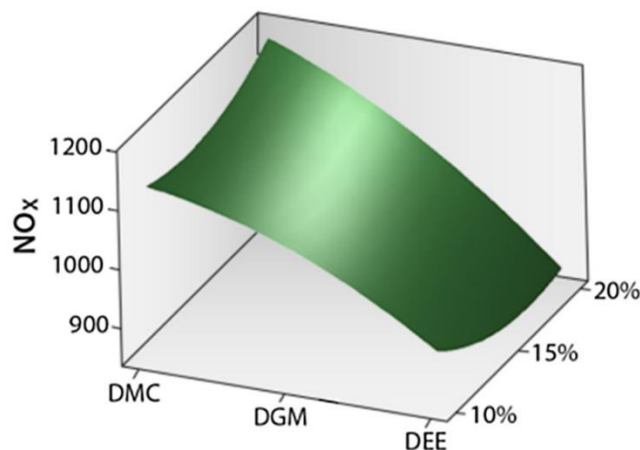


Fig. II.10: Response surface for combined effect of: Oxygenate type [Diethyl ether (DEE, ether), Dimethyl carbonate (DMC, carbonyl ester) and Diglyme (DGM, glycol ether)] and blends on NO_x emissions [159].

A fundamental study on the NO_x formation for other oxygenated species as ethyl acetate (EA) and methyl ethyl ketone (MEK), has been carried out by Lamoureux et al. [160]. This study was performed in seeded CH₄ / O₂ / N₂ low-pressure laminar flames as a function of the equivalence ratio. After improving the kinetic mechanism to accurately predict CH radical and NO mole fraction measured in flame by LIF and CRDS, they observed that CH peak decreased when MEK and EA replaced methane. This explains the decrease of NO in the burnt gases and indicates that NO is mainly produced according to the prompt-NO mechanism.

Recently another family of ethers, such as furan compounds, has taken the interest of researchers as alternative fuel for transportation, thanks to the new production methods from lignocellulosic compounds.

Furan derivatives (i.e., DMF - 2, 5-dimethylfuran, MF - 2-methylfuran, and furan), or tetrahydrofuran (THF) derivatives (i.e., DMTHF - 2, 5-dimethyltetrahydrofuran, MTHF - 2-methyltetrahydrofuran and THF), became attractive oxygenated fuels, due to their combustion properties comparable to those of commercial fuels. Few works have considered the performance of this new biofuels in real engine conditions, especially on pollutant emissions. Indeed, there are only some investigations on the combustion and emission of DMF in internal combustion engine. Xu et al. [161], [162] first investigated on the use of DMF as a biofuel in the engine. The experiments

highlighted that DMF has shorter combustion duration and higher combustion efficiency than gasoline. Some remarkable researches ([161] and [162]) also discussed the performance of the engine with DMF. Results showed that DMF also induced significant reduction in soot emissions. All these studies show that DMF is compatible with the existing combustion systems due to its analogous combustion properties to gasoline. Meanwhile, the studies highlight the competitiveness of DMF, but its high emission level of NO_x is a concern because of its high flame temperature.

On the other hand, MF has triggered only little interest. Wang and coworkers [165], tested a direct-injection spark-ignition (DISI) engine fueled with MF, compared to gasoline, ethanol and DMF. Although MF has a similar chemical structure to DMF, its combustion characteristics are significantly different. Results showed that MF produces 73% and 40% less HC emissions than gasoline and DMF respectively. This is mainly because of its high combustion temperature and high oxygen content. However, due to the high in-cylinder temperature, MF induces higher NO_x emissions. The maximum difference in NO_x emissions between MF and the other three fuels is at the lower load end where it has been shown that MF generates 82%, 281% and 40% more NO_x emissions than gasoline, ethanol and DMF, respectively.

At present, biofuels are most often used as additives for gasoline and diesel because of their inadequate yields and fuel supply infrastructures. For this reason, Wei et al. [166], studied the combustion characteristics and emissions of 10% MF gasoline (M10) blend fuel, examined in a single cylinder four-stroke SI engine. In particular, results of the regulated gas emissions highlighted the draw-back of higher NO_x productions for M10 due to its relatively high combustion temperature.

2-methylfuran (MF) was also studied blended with diesel (MD). In Xiao and coworkers study [167], combustion characteristics and emissions of a four-cylinder direct-injection compression-ignition (DICI) engine fueled with diesel–MF blends (DM) and pure diesel were investigated. Results showed that diesel–MF blends have different combustion performance from pure diesel. However, diesel–MF blends lead to higher NO_x emissions than pure diesel and the NO_x emissions are increased with the increase of MF fraction. The soot emissions from diesel–MF blends are significantly reduced compared to pure diesel.

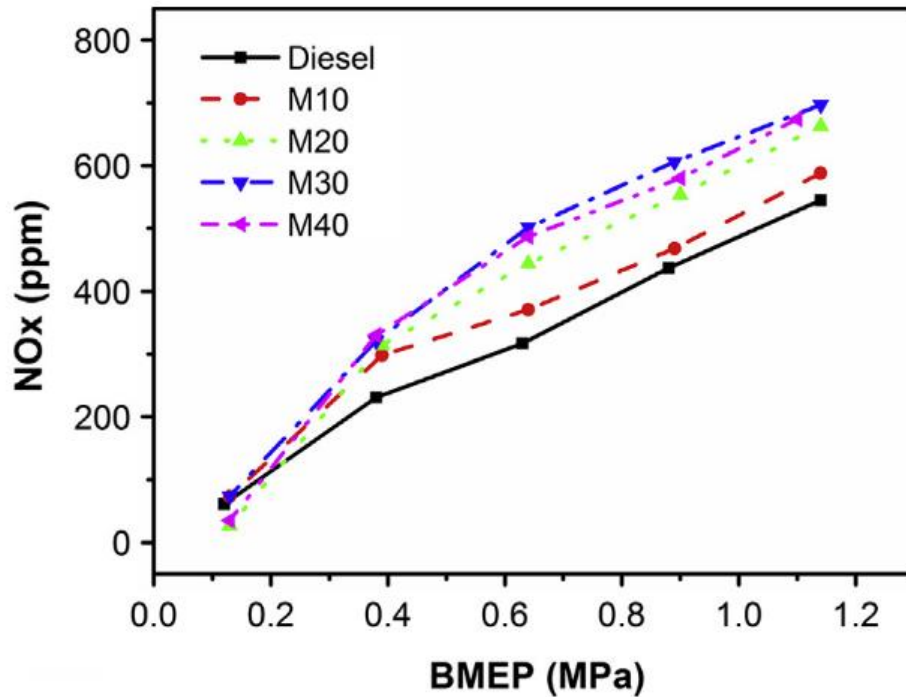


Fig.II.11. Variation of NO_x emissions with engine loads for different fuels (D=Diesel, M10=10%MF-D, M20=20%MF-D, M30=30%MF-D, M40=40%MF-D) [167].

As shown in Fig.II.11, NO_x emissions from the engine with diesel–MF blends are higher than that of pure diesel at medium and high loads and increase with the increase of MF fraction [167].

Another tested biofuel from cyclic ethers group is the 2-methyl-tetrahydrofuran (MTHF). In 1988, Rudolph and Thomas [168] comparatively analyzed pollutant emissions from a spark ignition engine running with gasoline blends with 10% liquid biofuels (methanol, ethanol, MTBE and MTHF). The results showed that the mixture containing 10% of MTHF has a power and emissions of CO, NO_x and unburned hydrocarbons almost similar to those of gasolines.

Among this studies, the unique fundamental study on the interaction between the NO_x and furanic compounds is the work of Alexandrino et al. [169], where the effect of the 2,5-DMF concentration on the NO conversion as well as on the 2,5-DMF conversion in the presence of NO were investigated. The experiments were performed in an isothermal quartz flow reactor at atmospheric pressure in the 800–1400 K temperature range. The NO conversion (initial concentration fixed at 900 ppm), at atmospheric pressure using 2,5-DMF, has been studied from pyrolytic to very fuel-lean conditions and by varying the inlet C/N ratio value, i.e., varying the initial concentration of 2,5-

DMF (100 and 300 ppm). Under the conditions of the work, 2,5-DMF is not seen to exert a negative influence on the NO emissions. However, a beneficial effect of adding 2,5-DMF is not observed either.

Apart from Alexandrino's [169] study on NO reburning, no fundamental study was performed on the furan's and THF's compounds to evaluate the effect of their oxidation on NO_x formation.

3. Conclusion

NO is one of the major pollutants emitted from combustion processes. It is formed according to different pathways: thermal-NO, prompt-NO, fuel-NO, NNH and N₂O mechanisms. Among these mechanisms, the prompt-NO directly depends on the oxidation of the fuel and its chemical characteristics.

To reduce the dependence to petroleum-based fuels and to limit the increase of total amount of greenhouse gases in the atmosphere, biofuels are an interesting alternative. Several studies show a strong relationship between NO_x emissions and chemical characteristics of biofuels, especially the degree of unsaturation, the ramification degree and the oxygen content. Much has been done in recent years to arrive at a more complete view of the problem, but the data are complex and do not lead to a single solution. A conclusion is that further work is required to better understand the kinetics behavior of the new biofuels on NO_x formation.

Regarding the furanic biofuels, the bibliography study shows that few studies are focused on these compounds to evaluate the NO_x emission in engine conditions and any study investigate the NO formation during the combustion of these promising biofuels.

In this context, this thesis work aims to investigate how the chemical differences between furan and tetrahydrofuran could affect the NO formation by focusing on prompt-NO mechanism. In the next chapter the experimental set up is detailed and the analytical techniques used to study the oxidation of F and THF in flame conditions are described.

Chapter III Operating set-up

This work aims to study the role of particular biofuels, i.e. furan and tetrahydrofuran, on the NO_x formation chemistry in flame conditions. To that purpose, we have associated two complementary approaches: the first one is an appropriate experimental set-up to establish a very detailed database able to characterize the influence of the biofuel oxidation on NO_x formation; the second one is a modelling step to evaluate kinetic schemes available in the literature to predict CH formation from biofuels oxidation. The experimental setup and the operating conditions used to obtain the database, and the simulation code used to characterize the kinetic behaviors of CH₄/biofuel/O₂/N₂ flames are presented in this chapter.

1. Introduction

Flames involve gas-phase reactions, globally exothermic, which are able to self-propagate via a chain-branching mechanism. Flame structure, i.e., the temperature and the concentration profiles of the chemical species in the reaction mixture, strongly depends on heat transfer, molecular transport processes, and chemical reactions.

The laminar premixed flame is a simple flame model for which the fuel and the oxidizer (usually air or oxygen) are premixed upstream the burner. Premixed laminar flames consist in a deflagration wave that propagates in a stationary gaseous mixture with a characteristic velocity, called the burning velocity. This kind of flames, i.e., the laminar premixed ones stabilized on a burner, can be considered as one-dimensional (flat), i.e., the flame structure evolves only along one preferential direction.

Following Fristrom and Westernberg [170], the laminar premixed flame consists in four distinct and specific regions (Fig. III.1), successively the unburned mixture, the preheating, the reactional and the burned gas zones.

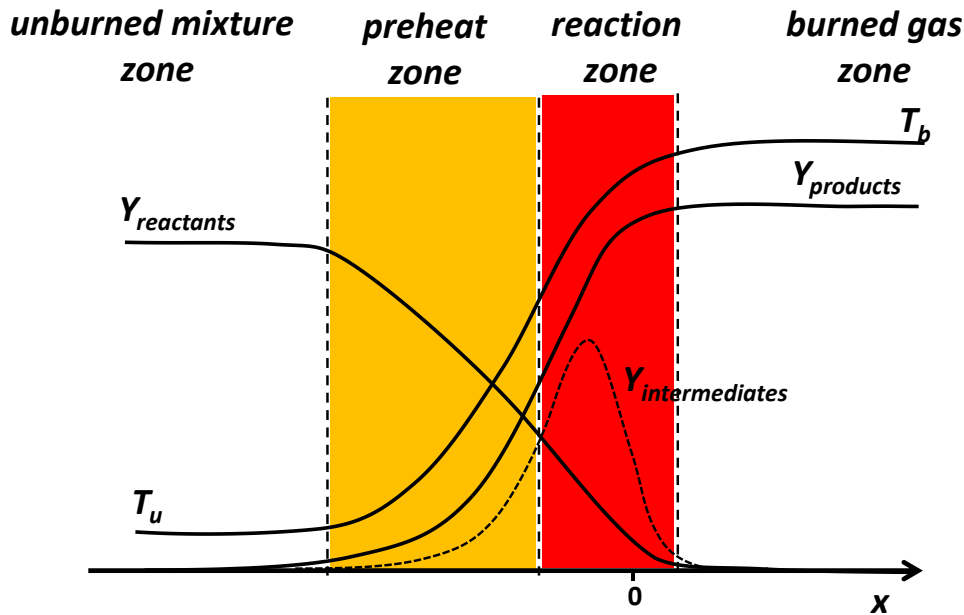


Fig. III.1: Classical chemical structure of premixed flame.

The experimental data obtained in a premixed flame, such as temperature and chemical species concentration evolutions as a function of the height above the burner (HAB), are highly useful for kinetic studies and more precisely for the development, optimization and validation of detailed kinetic mechanisms for fuel oxidation and/or pollutants formation.

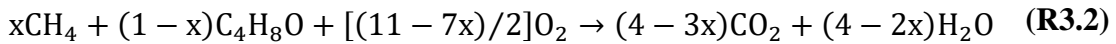
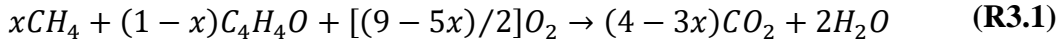
For this reason, we have selected laminar premixed flames to investigate the NO formation and its interaction with fuel oxidation, particularly with furan (F) and tetrahydrofuran (THF) oxidation.

The choice of working in low pressure conditions allows to benefit from a dilated reaction zone locked nearly a few millimeters from the burner surface and thus disposing of a better spatial resolution. These experimental conditions are suitable to the realization of a flame structure study with the experimental techniques used in this work.

2. The flames under investigation

In this work, six laminar premixed flames are studied to analyze the effect of the oxidation of biofuels, namely furan (F) and tetrahydrofuran (THF), on NO formation: a stoichiometric and a slightly-rich $\text{CH}_4/\text{O}_2/\text{N}_2$ flames, and biofuels/ $\text{CH}_4/\text{O}_2/\text{N}_2$ flames

are operating in similar conditions of equivalence ratio, pressure, total flow and dilution rate. The methane flames serve as reference to the results obtained in biofuels/CH₄/O₂/N₂ flames. According to the value of these key parameters, the gas flow rates of methane, oxygen and biofuels are calculated using the following global reactions for the methane (CH₄)/furan (C₄H₄O) flames (R3.1) and for the methane (CH₄)/tetrahydrofuran (C₄H₈O) flames (R3.2).



where x is the CH₄ relative mole fraction in the fuel mixture.

The equivalence ratio ϕ is defined as the ratio of the fuel-to-oxidant experimental ratio to the stoichiometric fuel-to-oxidant one:

$$\phi = \frac{\left(\text{Fuel/Oxid.}\right)_{exp.}}{\left(\text{Fuel/Oxid.}\right)_{stoich.}} \quad (3.1)$$

In equation 3.1, the index *stoich.* stands for stoichiometric conditions and the index *exp.* for experimental conditions. In our conditions, ϕ is calculated by the following equations that take into account oxygen from initial F in the equation 3.2, and THF in the equation 3.3, feeding the burner:

$$\phi = \frac{(9 - 5x)(\chi_{CH_4} + \chi_{C_4H_4O})}{2\chi_{O_2}} \quad (3.2)$$

$$\phi = \frac{(11 - 7x)(\chi_{CH_4} + \chi_{C_4H_8O})}{2\chi_{O_2}} \quad (3.3)$$

In these two relations, χ_{CH_4} , $\chi_{C_4H_4O}$, $\chi_{C_4H_8O}$, χ_{O_2} and χ_{N_2} are respectively the methane, F, THF, oxygen and nitrogen mole fraction in the gaseous mixture upstream

the burner. Table III.1 reports these flame conditions defined in standard conditions for temperature and pressure.

The first two flames reported in Table III.1 are our reference methane flames. The first one is in stoichiometric conditions (flame called M1.0), and the second one is moderately fuel-rich (flame called M1.2). The other four flames are stabilized by considering a fuel mixture of 50% F - 50% methane (called FM1.0 and FM1.2) or 50% THF - 50% methane (called THFM1.0 and THFM1.2). Their equivalence ratios are equal to those of reference methane flames.

Our choice for the operating conditions is justified from practical considerations (flame stability) and the need of using a nearly constant flame dilution and total flow rate. So, the choice has been made to work with a constant flow rate of 5 l/min in STP conditions, a dilution rate of about 70% (χ_{N_2}), and a constant pressure of 40 torr (5.333 kPa).

Flames	ϕ	χ_{N_2}	Flow sL/min					TOT
			O ₂	CH ₄	F	THF	N ₂	
M1.0	1.00	0.68	1.067	0.533	0	0	3.400	5.00
M1.2	1.20	0.66	1.063	0.638	0	0	3.300	5.00
FM1.0	1.00	0.70	1.147	0.176	0.176	0	3.500	5.00
FM1.2	1.20	0.70	1.096	0.202	0.202	0	3.500	5.00
THFM1.0	1.00	0.70	1.184	0.158	0	0.158	3.500	5.00
THFM1.2	1.20	0.70	1.136	0.182	0	0.182	3.500	5.00

Table III.1: Operating conditions for the CH₄/biofuel/O₂/N₂ flames. Flow rates are defined in STP conditions ($P=1$ bar and $T=273$ K).

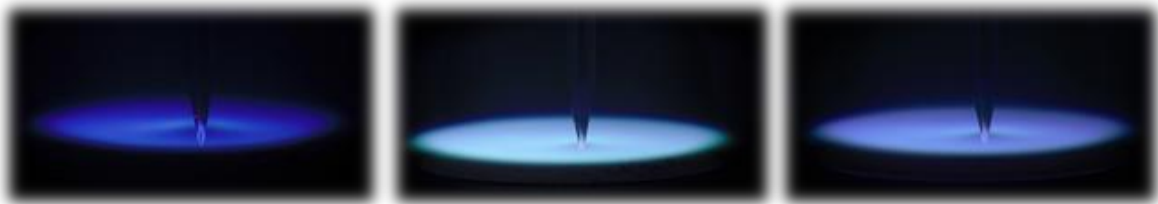


Fig. III.2: Picture of our three low-pressure stoichiometric flat flames: M1.0; FM1.0, THFM1.0.

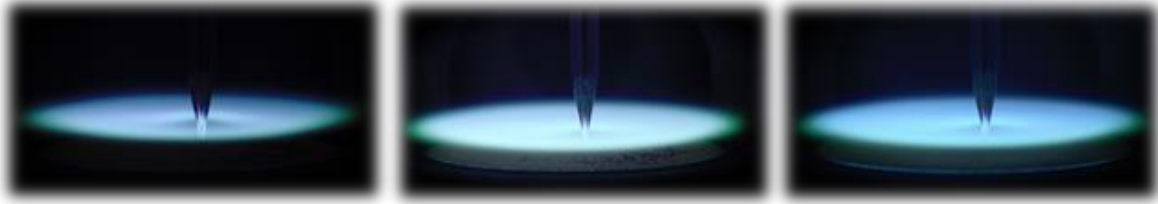


Fig. III.3: Picture of our three low-pressure moderately rich flat flames: M1.2; FM1.2; THFM1.2.

Fig. III.2 and Fig. III.3 present pictures of the six flames we have investigated in this work. They show the typical blue-violet luminosity of the stoichiometric flames and a stronger luminosity of the moderately rich flames. Different shades of flame color from blue to green are due to different chemiluminescence intensities from the electronically excited species CH^* (430 nm) and C_2^* (514 nm), respectively.

3. Experimental set-up

The experimental set-up is shown in Fig.III.4. It is mainly composed of the fuel-mixture feeding section, the burner and its low-pressure chamber, the Gas-Chromatographic (GC) analysis device and the laser diagnostics system. These two analytical techniques will be described in sections 4. and 5 respectively.

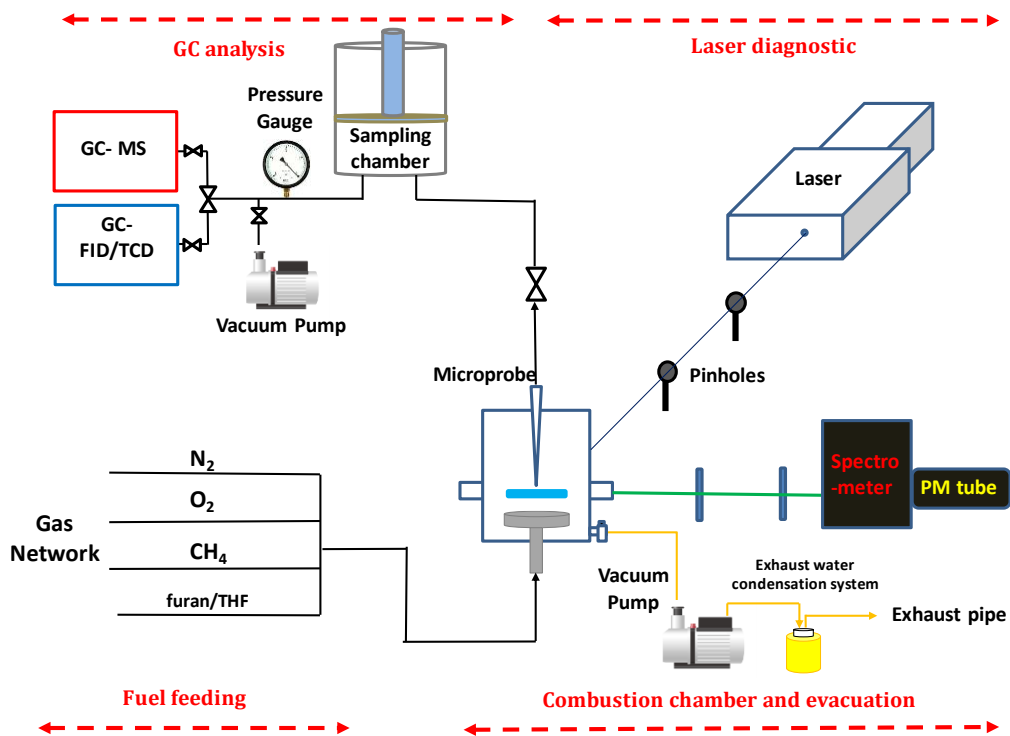


Fig.III.4: Global experimental set up.

3.1. Fuel feeding section

Gaseous compounds are delivered by the laboratory gas network and their purity is respectively 99.95% (identified impurities: C₂H₆ 200 ppm, N₂ 200 ppm, H₂ 20 ppm, CO₂ 10 ppm, O₂ 10 ppm) for methane, 99.995% (identified impurities: H₂O 3 ppm) for oxygen and 99.999% (identified impurities: O₂ 1 ppm) for nitrogen. The fuel premixed mixture is fed to the burner by steel and Teflon tubes connected to the mass flow controllers.

The volumetric flow rate of each gaseous compound is regulated by a Bronkhorst mass flow controller (MFC; F-201CV) characterized by a maximum flow rate of 1 L/min for CH₄, 2 L/min for O₂ and 5 L/min for N₂ in standard conditions.

Biofuels F (SIGMA-ALDRICH, purity $\geq 99.9\%$) and THF (SIGMA-ALDRICH, anhydrous, purity $\geq 99.9\%$, inhibitor-free), which are liquid at ambient temperature (boiling point 31.3°C and 66°C respectively at atmospheric pressure), are pre-vaporized before being mixed with the other gaseous components. Vaporization is obtained in a heated steel vessel and the volumetric gaseous flow rate is controlled by a specific heated MFC (Millipore VC-4901) before mixing with the methane/oxygen/nitrogen gas mixture. In our operating conditions, and because the needed amount of F is relatively low, it is not necessary to heat F (the vapor pressure in ambient conditions is sufficient to generate the needed flow rate). For this reason, the heated vessel system is switched off. In the case of THF, the vessel is warmed up to 40°C to enable the generation of the required flow rate to stabilize the flames. The heated MFC is warmed up to 60°C to avoid condensation of biofuels in cold zones of the feeding line. In the same way, from the evaporation vessel exit to the burner inlet, the system is heated at 60°C to prevent any condensation.

Fig.III.5 shows the fuel feeding section with gas connections, MFCs and liquid fuel vaporization system. The calibration procedure for the heated MFC is detailed in Annex A.

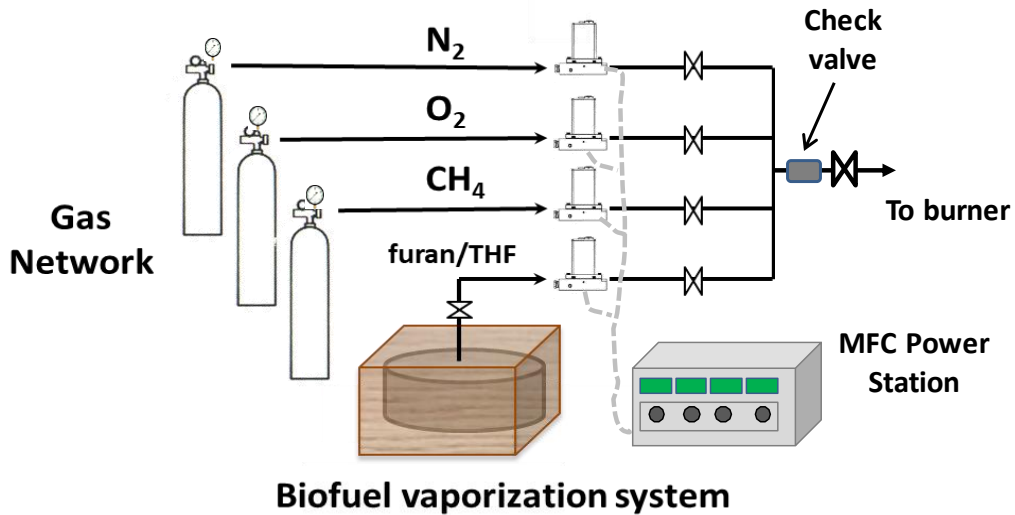


Fig.III.5: Fuel feeding section.

3.2. The burner and combustion chamber

The flat flame burner used to study the kinetic behaviors of $CH_4/O_2/N_2$ flames, seeded or not with biofuel, consists of a 6-cm-diameter bronze-porous-plate water-cooled McKenna burner (Holthuis & Associates; Fig.III.6).

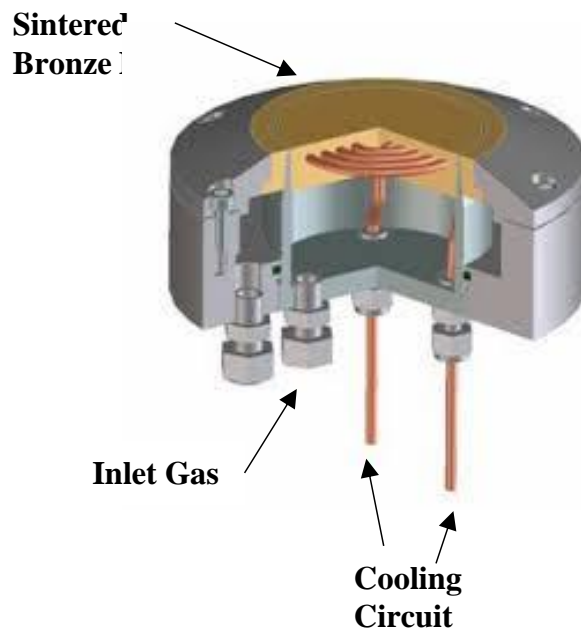


Fig. III.6: McKenna burner [171].

The burner is used to stabilize our six laminar premixed flat flames at low pressure (5.33 kPa-40 torr). The water-cooling system of the burner is set at 40°C to prevent

condensation of biofuel on the burner surface and to ensure constant reproducible conditions for flame stabilization.

The burner is inserted in a stainless-steel enclosure of 24 cm diameter and 30 cm height as shown in Fig. III.7. A water-cooling system, set at temperature 80°C, is connected to the top of the combustion chamber to ensure flame reproducibility day by day. The burner can be translated along the vertically axis to adjust the position of the probed volume with respect to the optical access windows for the laser diagnostics and the position of the microprobe for GC analysis. Burner position is controlled via a digital micrometric system allowing an accuracy of about 10 μm .

A vacuum pump (Leybold SOGEVAC SV25B) is used to obtain and maintain the selected pressure in the chamber. The pressure is controlled by an automatic device which consists of an electron-valve (Bronkhorst F-001, max flow rate 300 NL/h) and a pressure gauge (Tylan CDLD-21S12; 0-100 Torr), allowing to adjust and keep constant the pressure at 5.33 kPa (40 Torr) during all the measurements. The chamber design ensures a homogeneous and equally distributed vacuum pumping in the entire chamber, so that the flame is not disturbed. The exhaust gases, pumped from the combustion chamber, are sent to the evacuation system as shown in Fig.III.7. The system is composed of a PVC container of about 20 liters to favor the water and pump oil condensation, before sending the exhaust gas to vent.

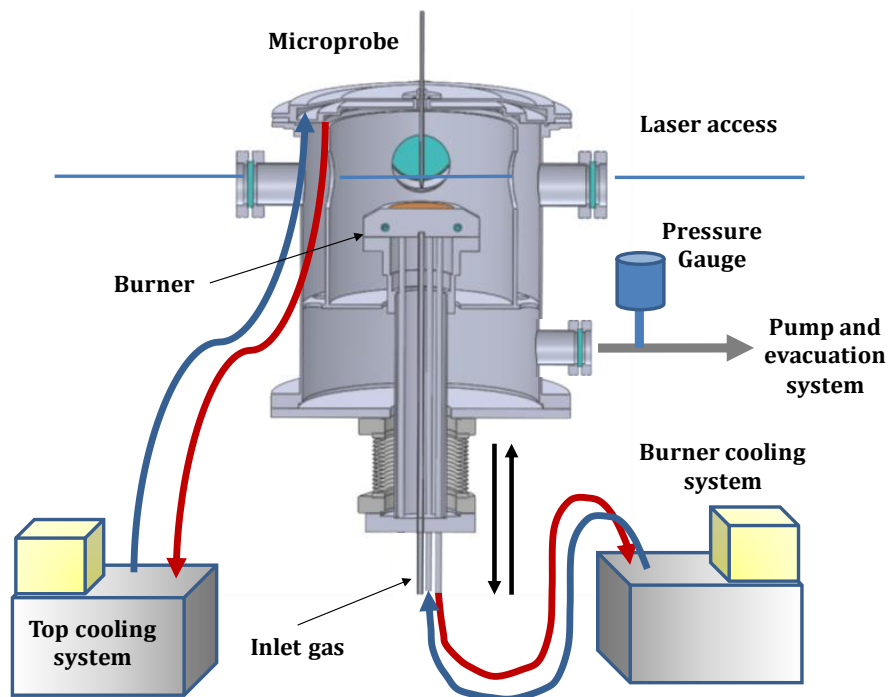


Fig.III.7: Burner enclosure.

4. Gas chromatography analysis set up

To realize flame structure analysis, gaseous samples can be collected at different HABs by using an appropriate quartz microprobe. Generally, to access to qualitative and quantitative information about stable chemical species present in the reactional mixture, these samples are analyzed by gas-chromatography, mass spectrometry and/or infrared spectroscopy. These techniques allow to establish detailed experimental databases by obtaining the profiles of the concentration evolution of stable chemical species, which are of interest to develop or validate detailed combustion kinetic mechanisms.

Gas Chromatography is an ex-situ technique which enables the separation of chemical species according to their respective affinity between a mobile phase (carrier gas) and a stationary phase (the chromatographic column).

In this work, the flame structure is studied by on-line gas chromatography analysis. As shown in Fig. III.4, the global experimental setup is composed of:

- The specific sampling system;
- A gas-chromatograph coupled with a mass spectrometer to identify the chemical species;
- A second gas-chromatograph coupled with a FID/TCD detector for their calibration/quantification.

4.1. The sampling system and the injection procedure

Fig. III.8 shows the GC analysis devices and more precisely the scheme of the sampling line. This mainly consists of a *quartz microprobe*, a *sampling-compression chamber*, a *vacuum pump* and a *pressure gauge*. From the burner enclosure, the flame gases are sampled by a *quartz microprobe* connected to the sampling chamber by an appropriate PFA-Teflon tube.

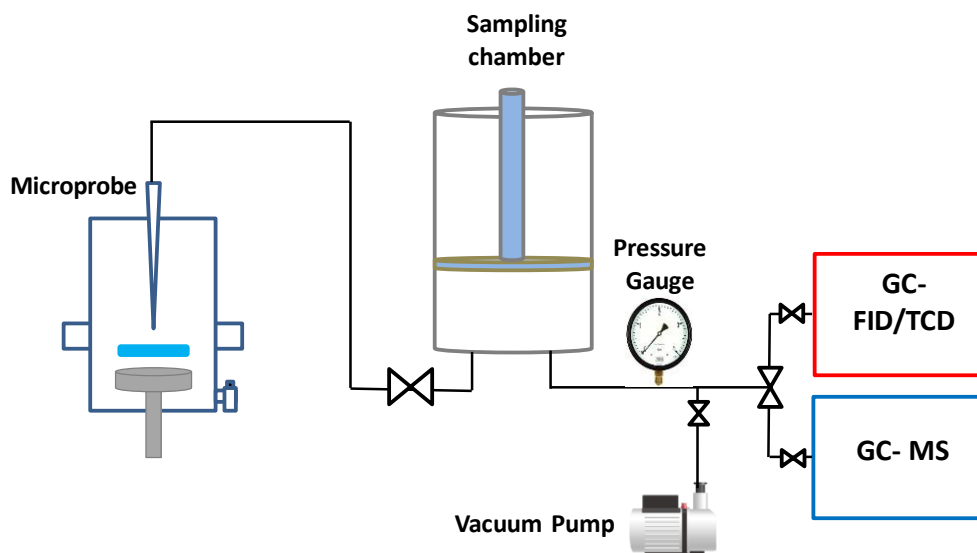


Fig.III.8: The sampling system for GC analysis.

An important volume of gas sample (V_1 about 2 L, piston in top position) at low pressure (10 Torr) is collected in a *sampling chamber* in which the initial pressure is null. After compression to about 300 Torr (piston in down position, compression factor of about 30), the gaseous sample is sent in the injection loop of the gas-chromatography device. This value of the sampling pressure allows, on one hand, to dispose of good injection conditions with respect to operating conditions of the GC device, and on the other hand to obtain a very good sensitivity for the GC analysis. The *sampling chamber* is composed of a stainless-steel cylinder equipped at each extremity with two removable flanges between which a compression piston is movable. The guiding and control of the translational movement of the piston are realized with a pneumatic jack. The sealing of the piston during the vertical displacement is ensured by EPDM rubber (Ethylene Propylene Diene Monomer) O-rings.

The temperature of the entire sampling system, from the microprobe to the sampling loop, is controlled with heating devices and regulated to a temperature of 80 °C to avoid any condensation problem.

The sampling procedure has to be realized as fast as possible to avoid the recombination of reactive species. For this reason, it is important to have a high pumping power for the sampling step to provide high vacuum condition in the microprobe and sampling chamber. The required vacuum is obtained using a rotary pump (Pfeiffer Vacuum Duo 20M, N₂-flow of 24 m³/h). The piston filling pressure

and the injection pressure are checked and measured using a capacitive pressure gauge (CERAVAC CTR 100 Oerlikon Leybold Vacuum, 0-1000 Torr). A valve makes possible to isolate the sampling system from the combustion chamber after the sampling step.

Probe sampling approaches are well-known to be intrusive methods that may thermally and hydro-dynamically disturb the reactive environment, as opposed to non-intrusive laser diagnostic techniques which do not induce such perturbations.

The state/quality of the probe walls and also its geometry, in particular the opening angle and the size of the orifice of the microprobe, can strongly influence the efficiency of the gas expansion during sampling step [172]. One disturbance can be the modification of the composition of the gaseous mixture sampled. These disturbances can be reduced by a rapid gas expansion by minimizing the pressure in the microprobe. Radical-molecule reactions, which have a high activation energy, can be "frozen" by this method. Nevertheless, recombination reactions between atoms and radicals can occur in the microprobe.

As mentioned above, disturbances can be also hydrodynamic and thermal (cooling) perturbations. These are however relatively weak in the case of a microprobe [173]. To minimize this perturbation, the choice of microprobe material is important. Quartz is the best candidate because it reduces thermal losses thanks to its low thermal conductivity. In the same way, its low coefficient of expansion allows the probe to keep the same geometry at any point in the flame, and its chemical inertness respects the representativeness of the gaseous sample.

Several studies on flames structures have used microprobes as sampling method. El Bakali [174] and Delfau [175] have shown that the shape of the microprobe can induce significant reactivity at the surface of the burner. To evaluate this eventuality, the concentration evolution profiles for reactants (here CH_4 , F, THF and O_2) may be compared by using different microprobe geometries. Lefort [176] suggests a qualitative explanation for this reactivity at the burner surface during microprobe sampling. The reactivity varies with the position of the microprobe in the flame. Indeed, when the microprobe is placed between the burner surface and the end of reaction zone, it is directly affected by the temperature gradient of the flame. A possible consequence is that species can react inside the probe as inside a flow reactor.

In order to choose the best microprobe shape and minimize the reactivity near the burner surface, two quartz microprobes have been tested. The first one (A) presents a needle-shaped geometry with an opening angle of 10° and an orifice diameter of $300\ \mu\text{m}$. The second microprobe (B) shows a conical geometry with an opening angle of 30° and an orifice diameter of $250\ \mu\text{m}$. A picture of the two microprobes is shown in Fig. III.9. To compare these two microprobes, the Fig. III.10 shows the effect of their respective shape on the CH_4 concentration profiles obtained by GC in the flame M1.0. To well interpret these results, it is important to specify that the initial CH_4 mole fraction is equal to 0.106.



Fig. III.9: The two microprobes tested for GC analysis: A - opening angle of 10° with an orifice diameter of $300\ \mu\text{m}$. B- opening angle of 30° with an orifice diameter of $250\ \mu\text{m}$.

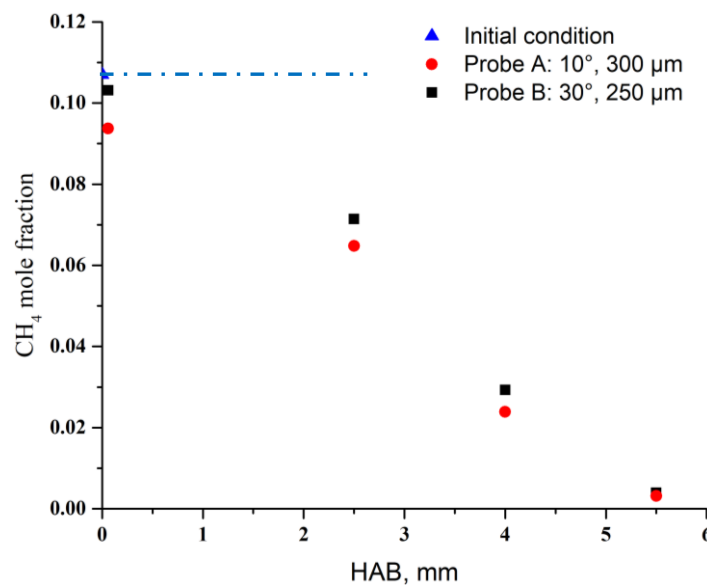


Fig.III.10: Illustration of the influence of the shape of the microprobe on the CH_4 profile in the reference flame M1.0.

At the burner surface the CH_4 mole fraction measured with microprobe B (orifice of 30°) is closer to 0.106. The probe A (10° opening angle) profile points out a significant consumption of CH_4 (near 12%) with respect to the initial condition. This difference between the CH_4 mole fraction measured with the two microprobes decreases when the distance from the burner increases. In conclusion, to minimize the microprobe reactivity the quartz probe B with the 30° opening angle has been selected for all GC analyses.

Another important parameter for the microprobe sampling step is the orifice diameter, since it affects the sampling time and can perturb the fluid-dynamics proper to the studied flames. To optimize the sampling conditions, the orifice of microprobe B has been progressively increased from $126\ \mu\text{m}$ to $250\ \mu\text{m}$ to reduce the sampling time. A CH_4 profile measurement in M1.0 flame has been performed to evaluate the potential effect of orifice dimension on flame structure analysis, as shown in Fig III.11.

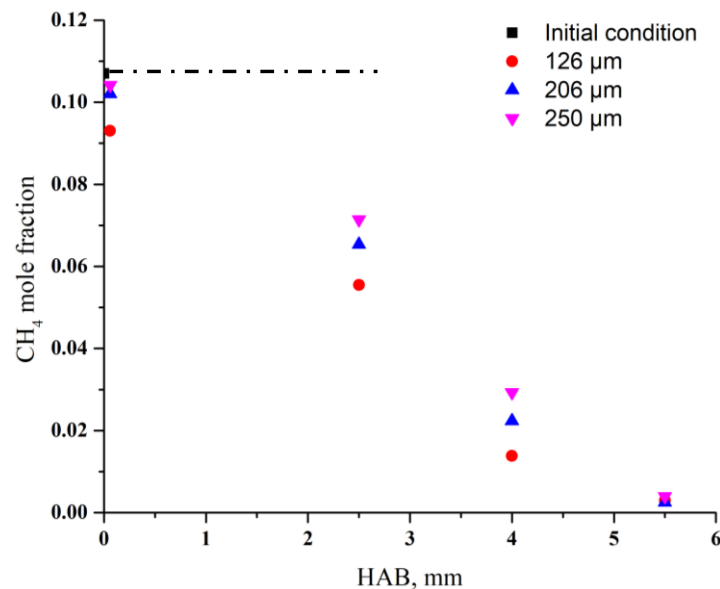


Fig. III.11: Influence of the size of the microprobe orifice on the CH_4 mole fraction profile in the M1.0 Flame.

It is observed that the reactivity of the microprobe at the burner surface seems to increase when the size of the orifice decreases; the more important effect is noticed for an orifice of $126\ \mu\text{m}$. This phenomenon could be explained by an increase of the residence time of the species inside the microprobe affected by the temperature gradient of the flame.

To ensure efficient pumping and to obtain a correctly stabilized flame, the microprobe with 30° opening angle and an orifice of 250 μm has finally been selected; this choice offers the better compromise between time sampling and reactivity problems.

Fig. III.12 shows a picture of the conical microprobe with 30° opening angle and an orifice of 250 μm inside the THFM1.2 Flame.

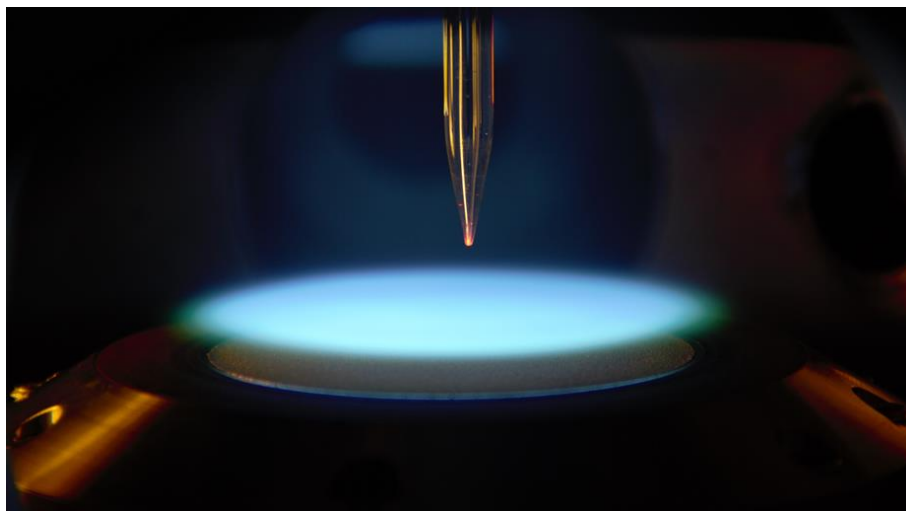


Fig. III.12: Sight of the microprobe B inside THFM1.2 Flame.

4.2. The MS–Gas-Chromatograph (GC/MS)

Gas Chromatography is an analytical technique that enables the separation of chemical species according to their respective affinity between the carrier gas and the chromatographic column. Depending on the temperature programming, the gas flow rates and the choice of the column, all the chemical species initially in the sample gas can be correctly separated. In that case, all of them are characterized by a specific time called the retention time. At the column exit, the chemical species can be measured and/or identified with an appropriate detector. Three detectors are used in this work: the Flame Ionization Detector (FID), the Thermal Conductivity Detector (TCD) and the Mass Spectrometry (MS).

A first chromatographic system (GC/MS) is coupled to a mass spectrometer (Agilent Technologies 5975C) for the identification of the hydrocarbon species measured in the CH₄/F/O₂/N₂ and CH₄/THF/O₂/N₂ flames.

The collected species are first separated using a Rt-QBond capillary column (30 m \times 0.25 mm \times 0.08mm, 100% divinylbenzene, Restek) with helium as carrier gas. After segregation along the column, the chemical species are ionized and mass-separated in a Quadrupole mass spectrometer (Fig.III.13). This detector consists in a tungsten or rhenium filament heated by an electric current to a temperature at which electrons are emitted. The electrons, used to fragment the molecules, are accelerated in a potential field to achieve a standardized energy of 70 eV, so that mass spectrum can be compared with numerical spectral libraries. High vacuum is maintained in the ion source to minimize reactions between the ions formed and other ions or radicals. The fragments resulting from the collision between the electrons and the chemical species are then separated according to their mass/charge ratio to generate a mass spectrum specific of this chemical species. Electron-impact spectra are highly structured and constitute a “fingerprinting” of the species for comparison with spectra of known compounds. In our case, the mass spectra of the analyzed species are compared to those of the NIST reference spectral library for identification [177].

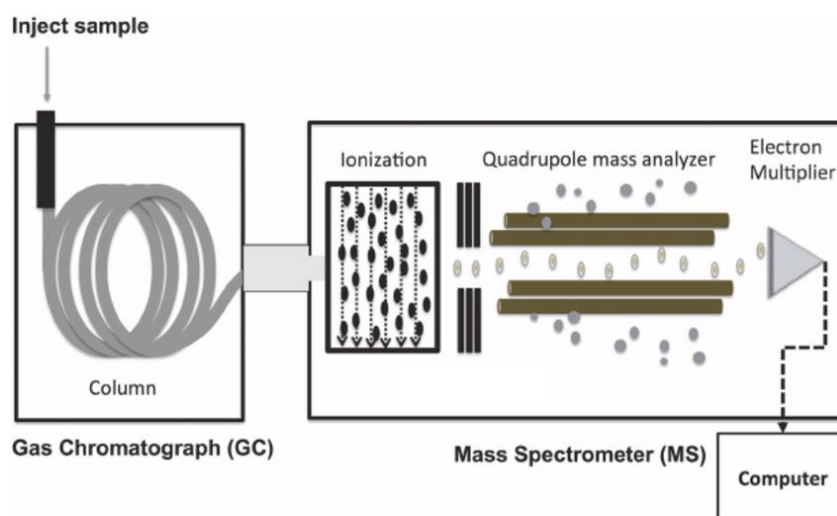


Fig. III.13: Schematic diagram of a gas chromatography quadrupole mass spectrometer (GC/MS) [178].

An example of the experimental mass spectrum of F (a) compared with the theoretical one (b) is shown in Fig.III.14.

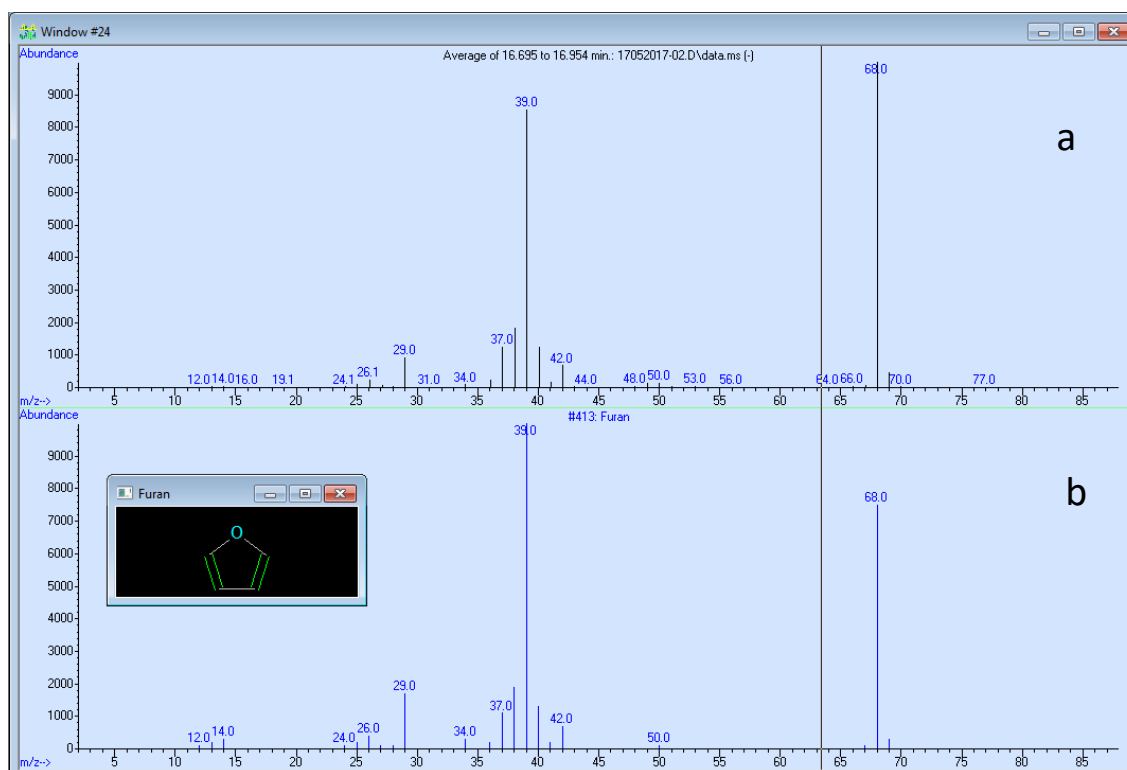


Fig. III.14: Furan typical mass spectrum ($m = 68.08$ au): comparison between experiment (a) and reference (b).

By mass spectra comparison, the GC/MS analysis allows to identify the species eluted from the gas chromatographic device. So, to assign a chemical compound to each chromatographic peak from analysis with GC/FID/TCD, we need to use the same capillary column and the same analysis programming for the two GC devices.

4.3. The FID/TCD -Gas-Chromatograph (GC/FID/TCD)

The second device (Perkin Elmer Clarus 580; Fig.III.14) is coupled with two detectors placed in parallel, a Thermal Conductivity Detector (TCD) and a Flame Ionization Detector (FID). This analysis system allows us to establish the relative evolution profiles of the stable chemical species detected in the flames, and, in a second step, to quantify them. A 10-port-gas-valve with diaphragm (Gas Sampling Valve, called GSV) equipped with 2 injection loops enables to simultaneously inject the gaseous samples in two different columns connected respectively to TCD and FID detectors. Fig. V.15 shows the different configurations of the gas chromatography device during the analysis process.

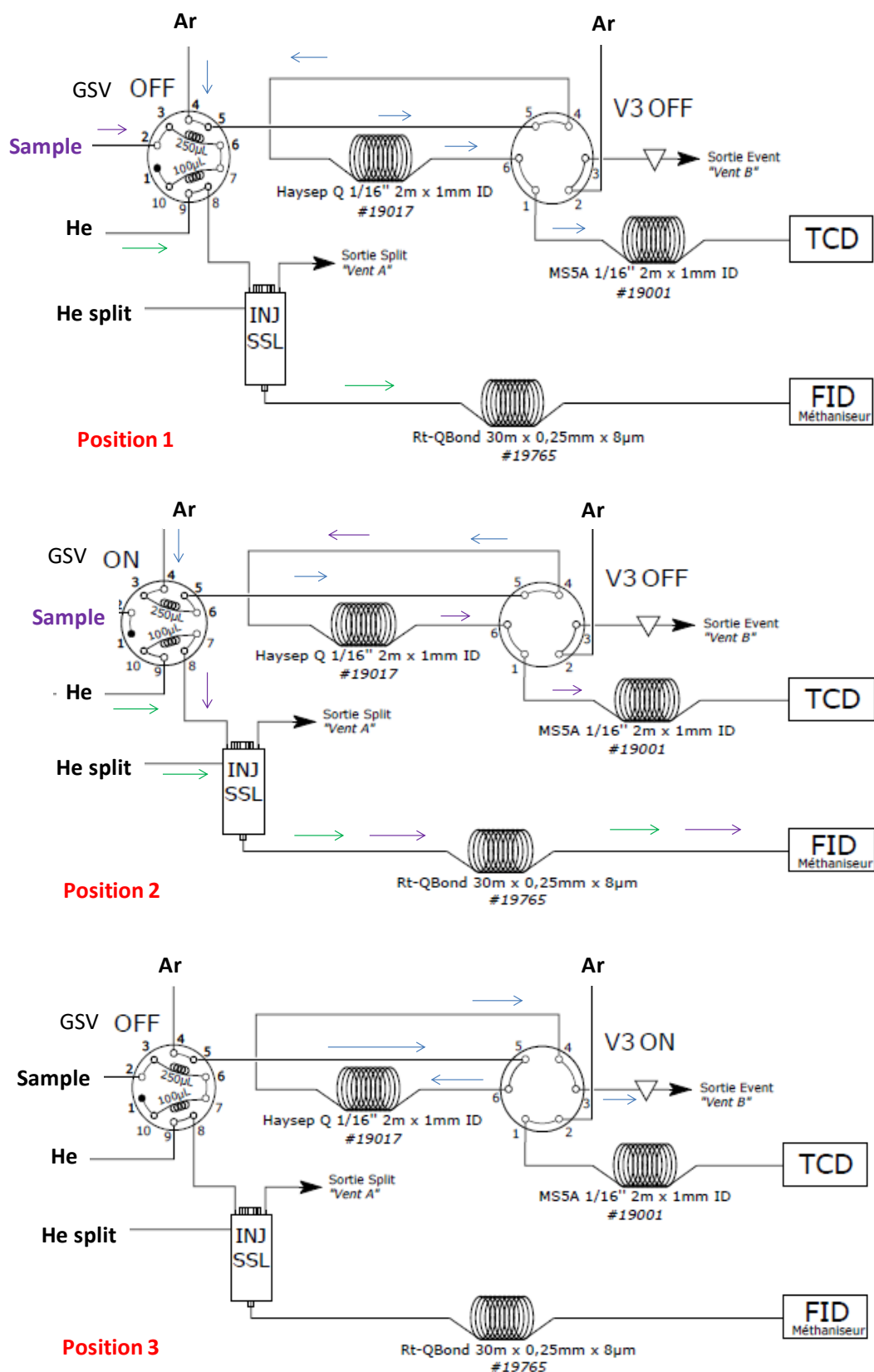


Fig. III.15: Scheme of analysis by FID/TCD/gas chromatography.

As shown in Fig.III.15, after compression, the gaseous sample is sent to the GSV valve to fill the two injections loop (Position 1). For the injection of gaseous samples

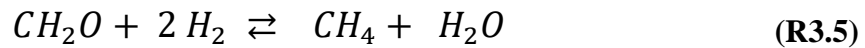
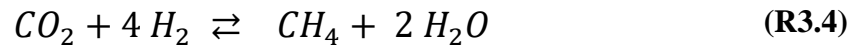
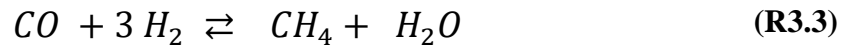
in the two columns, the GSV rotates to allow the passage of the carrier gases (Ar for the TCD line, and He for the FID line), which push the samples towards the two detector channels (Position 2). On the TCD line, the Haysep column allows to protect the molecular sieve (MS5A) from hydrocarbon contamination. Thus, when permanent gases are eluted from the Haysep column, the V3 valve turns in back-flash position to eluate hydrocarbons towards vent B (Position 3). After the analysis, both valves return in "Position 1" configuration.

So, the first loop of 250 μL allows the injection of the gaseous sample in the Haysep Q column for trapping hydrocarbons species, before entering in the micro-packed columns (molecular sieve MS5A 2m \times 1 mm) which is connected to the TCD detector. As mentioned above, the trapping column prevents hydrocarbons to contaminate molecular sieve, which could deteriorate rapidly. The two columns are separated by a 6-port-valve (V3) to allow switch in back-flush mode. Therefore, when valve V3 is ON, the Haysep Q column is isolated and traversed by the carrier gas in opposite side to vent the hydrocarbons. Note that Argon is used as carried gas for TCD channel. TCD detector works by having two parallel tubes both containing gas and heating coils. The gases are examined by comparing the heat loss rate from the heating coils into the gas. Normally one tube holds the carrier gas, used as reference gas, and the sample to be tested go through the other. Using this principle, a TCD senses the changes in the thermal conductivity of the column effluent and compares it to the one of the reference flow of carrier gas. This process is nondestructive for the sample but less sensitive respect to a FID detector. TCD enables to quantify permanent gases such as O_2 , H_2 and N_2 . The quantification limit is 50ppm.

The second loop of 250 μL injects the mixture to a capillary column Rt-QBond (30 m \times 0.25 mm \times 0.08mm, 100% divinylbenzene, Restek; the same column as the one used in the GC/MS device) directly connected to the FID detector to analyze hydrocarbons and oxygenated species. Helium is used as carried gas for the FID channel. A FID consists of a hydrogen/air flame and a collector plate. The effluent from the GC column passes through the flame, allowing the production of ions from organic compounds which are collected on an electrode. The resulting current is directly proportional to the hydrocarbon concentration in the gases and is detected by a suitable electrometer. The evolution of this current with the analysis time is called

chromatogram. The FID is extremely sensitive with a large dynamic range and the quantification limit is 1ppm.

In our device, the FID detector is coupled with a methanizer, a Nickel catalyst hydrogenating reactor, which converts CO, CO₂ and formaldehyde (HCHO) into methane (CH₄), according to the following reactions:



Regarding the methanizer device, differences in response factor between CH₄, CO, CO₂ and CH₂O are observed after FID detector, meaning that the conversion of CO, CO₂ and CH₂O in CH₄ is not complete and is affected by different efficiency of catalyzer for each compound. For this reason, all these compounds are calibrated directly without assuming the same response of CH₄.

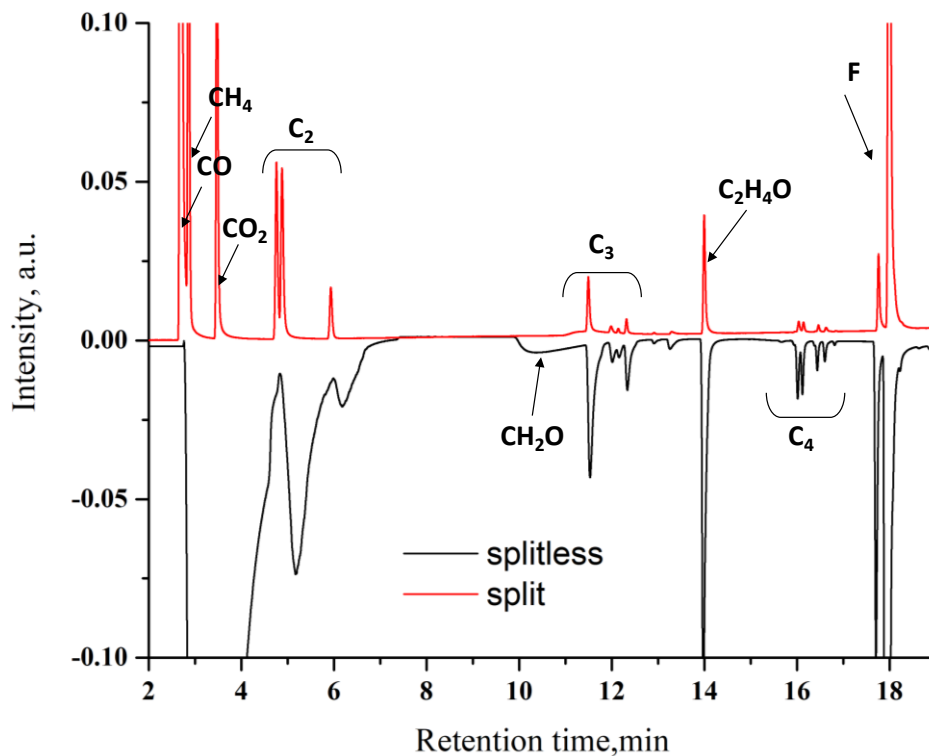


Fig. III.16: Chromatogram in split and splitless mode performed in FM1.0 flame at 1.8 mm

A splitter is located between the GSV valve and the Rt-QBond column to allow Split (diluted) /Splitless (concentrated) injection of gaseous samples. The Split injection mode avoids to overload the capillary column and allows a better peak resolution especially for abundant species such as the CO, CH₄, CO₂, F, THF, C₂ oxygenated and C₂-C₃ hydrocarbons. As example, the Fig.III.16 shows a comparison between a chromatogram performed in split mode and one performed in splitless mode 1.8 mm above the burner the in FM1.0 flame. We can observe how in splitless mode the peaks of CO, CH₄, CO₂ and C₂ hydrocarbons are completely undefined.

The signals from both detectors TCD and FID are archived and treated by the software EMPOWER to obtain retention time and area of each peak on each chromatogram. The retention time allows the identification of the chemical compounds, and the area of the peak is relative to its concentration. By determining the area of each species at different height above the burner (HAB), we obtain their relative concentration evolution. To obtain the absolute concentration profile as function of HAB, a calibration procedure for each species is adopted. This procedure will be detailed in the paragraph 1.2.1 of Chapter IV.

Several tests were performed to define the best analysis conditions based on the requirements to improve peak separation and analysis time. The parameters on which we have worked to reach these goals were especially the oven temperature programming and the split ratio.

The increase of the temperature leads to a decrease of the retention time of the analyzed species. This means a decrease of analysis time provided that the separation efficiency is not compromised. The choice to start with an isotherm at 40° for 5 min allows to elute with a satisfying resolution the peaks from the light gases O₂, N₂ and H₂ in TCD channel, and CH₄, CO, CO₂ in FID channel. To correctly elute the other compounds with high boiling point, we increase the temperature up to 240°C with a rate of 10°C/min, and hold this value for 3 min. With this temperature programming, we are able to correctly separate all species present in our flames.

In the same way, the split ratio affects the resolution quality of the peaks. Therefore, we have made the choice to use the split mode to analyze CO, CH₄, CO₂, furan, THF, light oxygenated compounds and hydrocarbons up to C₃, which are the more abundant

species in our flames. Different tests were performed to optimize the split ratio, and a flow value of 25 ml/min for the split is finally chosen. To analyze the other intermediate of the flames, the splitless mode has been used with satisfying results in terms of resolution and sensitivity (see Fig.III.16. for comparison of the two modes).

A summarized description of gas chromatographic analysis conditions is reported in table III.2.

Chromatograph	Perkin Elmer Clarus 580
Injection Loop (GSV)	2 loops V=250 μ L T _{GSV} =150°C
Injector FID	Split 25:1 ; (Split mode) Split 1:1 (Splitless mode) T=250°C
Time events V3	0 min.: OFF: trapping column and molecular sieve are in series 5 min.: ON: trapping column is isolated from molecular sieve 28.3 min: OFF: trapping column and molecular sieve are in series
Columns	Rt-QBond (capillary column) 30 m \times 0.25 mm \times 0.08mm, Vector gas: He Hayesep Q (column for trapping) 1/16" 2m \times 1 mm Vector gas: Ar MS5A (molecular sieve) 1/16" 2m \times 1 mm Vector gas: Ar
Flow	1ml/min FID channel 8,5 mL/min TCD channel
Oven temperature programming	40°C for 5.3min 10°C/min--->240°C 240°C for 3min
FID detector	T=400°C H ₂ =40mL/min Air=400 mL/min
TCD detector	T=120°C He (reference) =5mL/min

Table III.2: GC analysis conditions.

5. The laser diagnostics set-up

The experimental setup used to measure NO and CH profiles with Laser Induced Fluorescence (LIF) is illustrated in Fig. III.17. The monochromatic laser beam is sent to the burner enclosure using an appropriate optical set. Two pinholes are arranged to check that the laser axis is parallel to the burner surface and an attenuator controls the laser energy before that the beam meet the flame. The laser beam is adjusted before the enclosure's entrance by a rectangular slit of $600\ \mu\text{m} \times 300\ \mu\text{m}$. A photodiode positioned at the opposite window of the burner enclosure is used to check the laser energy variations. It also enables the triggering of the numerical oscilloscope.

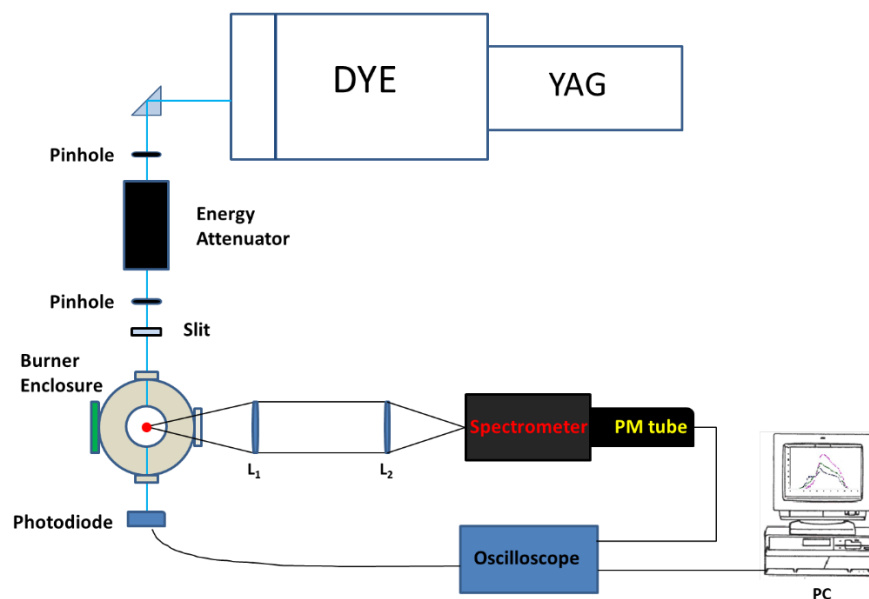


Fig.III.17: Laser Induced Fluorescence set up for NO et CH measurements.

The fluorescence signal is collected at 90° with respect to the laser beam and is focused on the slit of a spectrometer by a system of two lenses ($L_1=300\ \text{mm}$ and $L_2=200\ \text{mm}$). The spectrometer entrance slit is parallel to the excitation axis. The collection volume V is defined by the width (f_e) and height of the spectrometer entrance slit. Thanks to the lenses system, it is possible to obtain a magnifying factor (m.f) of 1.5, given by the followed relation: $\text{m.f.} = f_e/\text{sp} = L_1/L_2$. Considering this value and the width of the entrance slit, the spatial resolution (sp) is estimated to be about $0.300\ \text{mm}$ for NO ($f_e=0.2\text{mm}$) and 0.225 for CH ($f_e=0.15\text{mm}$). At the output of the spectrometer, the fluorescence signal is collected by a photomultiplier tube (PMT). Simultaneously with the laser intensity, the fluorescence signal is gathered and

averaged over 300 pulses and stored by a digital oscilloscope. A LabVIEW program is used to manage the acquisition of these different signals and partially process them.

5.1. The laser source: Nd-YAG/Dye laser

The laser source used in this work is a tunable dye laser (TDL Quantel 50) pumped by a Nd-YAG laser (Quantel YG 781 C10) with 10 ns pulses (10 Hz). The YAG laser emits a beam in the infrared at 1064 nm. Thanks to a frequency doubling system, a beam at 532 nm is generated. The doubling crystal is thermostatically controlled to limit the energy fluctuations due to temperature variations. A mechanical system enables to optimize its position (phase matching). The laser energy at 532 nm is around 470 mJ.

The dye laser is pumped by the 532 nm from the YAG laser. The pump beam is sent in the oscillator cavity to generate the laser beam in the visible spectral range according the dye used. Through an intra-cavity network, the required wavelength is selected manually or automatically. The laser beam is then amplified in order to have sufficient energy. A dye mixture (Rhodamine 590 and 610) is used to generate the fundamental wavelength at the oscillator output ($\lambda \approx 572$ nm). After the amplification phase, the radiation frequency is doubled, and then mixed with the residual infrared wavelength of the YAG through a crystal of beta borate of barium (BBO, non-linear optic crystal), to generate a UV beam at ~ 226 nm to excite NO molecules.

In the case of the CH excitation, the wavelength around 315 nm is provided by doubling the fundamental dye radiation after the amplification step.

A picture of dye laser is shown in Fig.III.18.

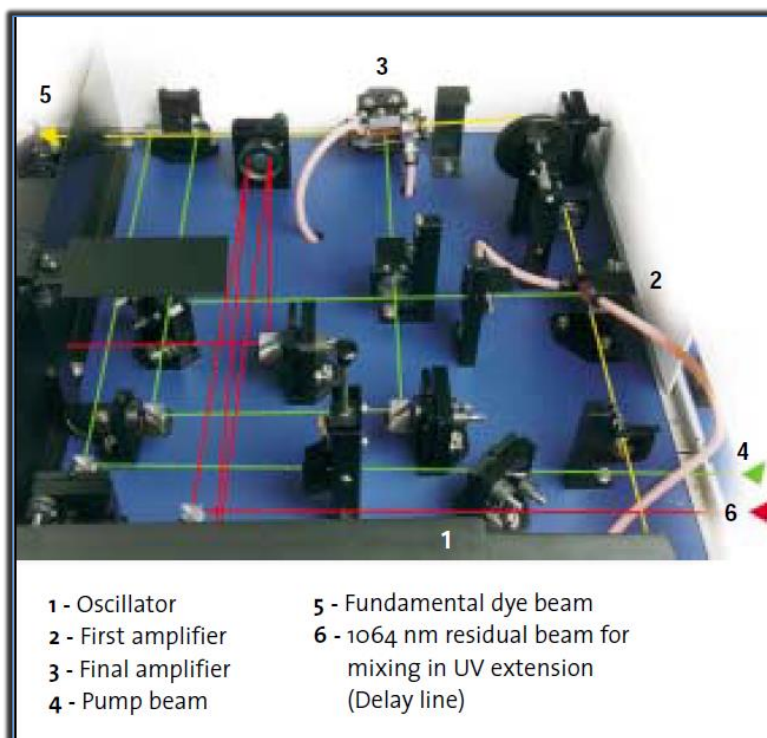


Fig.III 18 Dye Laser.

The position of each crystal (doubling and mixing) is optimized according to the incident wavelength via an automatic positioning system called "auto-tracking".

A system of four Pellin-Broca prisms (PB) placed at the output of the dye laser enables to separate the generated wavelengths (in the case of NO: 1064, 572, 286, and 226 nm), and select the desired excitation wavelength (~ 226 nm). The beam energy at the laser exit is around 1mJ.

For NO measurements and thanks to an attenuator, the energy of the beam is reduced to stay in the linear energy regime of LIF (around $70 \mu\text{J}$, see more details in chapter V).

In the case of CH measurements, the attenuator is not necessary because a pre-dissociate state is excited. Further details will be also provided in chapter V.

5.2. The collection signal system

The fluorescence signal is collected with an angle of 90° relative to the excitation laser beam. A Spectra Pro Imager spectrometer (Princeton Instruments Acton SP 2300) is used with a 300 mm focal length and 1200 lines/mm to enable the acquisition of

fluorescence spectra. It is also equipped with adjustable input and output slots from 0 to 3 mm in width by means of a micrometer screw. NO profiles are determined with an input slit of 0.2 mm in width and 10 mm in height, allowing to obtain a spatial resolution of 0.300 mm in flame thanks to a lenses system placed before the spectrometer. This spatial resolution is chosen according to the intensity of NO fluorescence signal and the number of points needed to determine the NO profile with an adequate spatial resolution in the flame. Thanks to the higher LIF signal intensity of CH species, the profiles are determined with an input slit of 0.15 mm in width, allowing to obtain a spatial resolution of 0.225 mm in flame. Because CH radicals are present in the reaction zone, we need accuracy in spatial resolution to correctly define its profile.

Photons transmitted by the spectrometer are collected by a photomultiplier (PM) located behind the spectrometer. During LIF measurements, a photomultiplier Philips XP2020Q is used, and is powered by a variable high voltage generator to obtain an adjustable amplification. The PM has a rising time of 1.5 ns. Its spectral response is described in Fig. III.19.

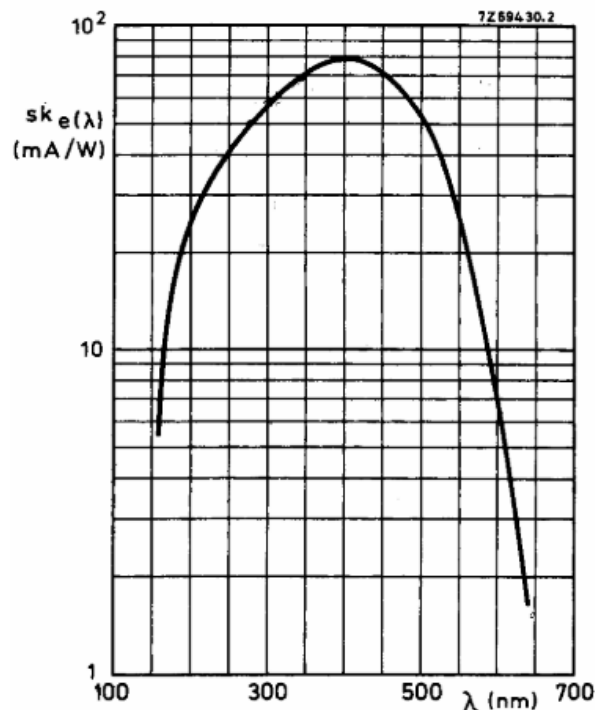


Fig. III.19 photomultiplier Philips XP2020Q spectral response.

The electrical signals from the PM are then transferred to a digital oscilloscope (LECROY 9354A, 8-bit, 500-MHz bandwidth, 1 GS/s sampling rate) for signal analysis.

6. Chemical kinetics modelling

In order to characterize the F and THF oxidation, and the prompt-NO formation in CH₄/F-THF/O₂/N₂ flames, we have decided to model the experimental data obtained with appropriate detailed chemical mechanisms available in the literature.

6.1. The numerical approach to characterize premixed laminar flames

To model a premixed laminar flame, the formulation of the problem considers the following set of conservation equations, as described by Smoke [179]:

- *Continuity equation*

$$\dot{M} = \rho u A \quad (3.4)$$

- *Energy conservation*

$$\dot{M} \frac{dT}{dx} - \frac{1}{c_p} \frac{d}{dx} \left(\lambda A \frac{dT}{dx} \right) + \frac{A}{c_p} \sum_{k=1}^k \rho Y_k V_k c_{pk} \frac{dT}{dx} + \frac{A}{c_p} \sum_{k=1}^k \dot{\omega}_k h_k W_k = 0 \quad (3.5)$$

- *Species conservation*

$$\dot{M} \frac{dY_k}{dx} + \frac{d}{dx} (A \rho Y_k V_k) + A \dot{\omega}_k W_k = 0 \quad (3.6)$$

- *Equation of state*

$$\rho = \frac{p \bar{M}}{RT} \quad (3.7)$$

With	\dot{M}	: mass flow (kg/s)
	ρ	: density (kg/m ³)
	u	: flow rate (m/s)
	A	: flame section surface (m ²)
	x	: spatial coordinate (m)
	c_p	: mixture heat capacity at constant p (kJ/(kg K))
	c_{pk}	: heat capacity at constant p of the species k (kJ/(kg K))

λ	: thermal conductivity of the mixture (kJ/(m*s*K))
T	: temperature (K)
Y_k	: mole fraction of species k
V_k	: diffusion rate of species k (m/s)
$\dot{\omega}_k$: net mole reaction rate of the species (Kmol/(m ² *s))
h_k	: enthalpy of species k (kJ/kg)
W_k	: molecular weight of the species k (kg/Kmol)
\bar{M}	: average molecular weight of the mixture (kg/Kmol)
p	: pressure (Pa/m ²)
R	: ideal gas constant (kJ/(kmol*K))
k	: generical chemical species

The inlet boundary conditions (x=0) are:

$$T(0) = T_{\text{burner}}$$

$$\dot{M}(0) = \dot{M}_0$$

$$Y_k^0 = Y_k^f - \frac{\rho Y_k V_k A}{\dot{M}}$$

The net chemical production rate $\dot{\omega}_k$ of each species k results from a competition between all the chemical reactions that involve this species.

For a burner stabilized flame, it is possible to not solve the energy equation with using a defined temperature profile. Using the experimental temperature profile allows to better represent the radiative heat losses which can occur in the real burner condition and also to avoid solving the energy equation, which increases the calculation time.

6.2. Calculation tools: Cantera

6.2.1. *Introduction*

In this work we have selected the Cantera software package as numerical solver for the equations previously presented.

Cantera is an open-source suite of object-oriented software tools for problems involving chemical kinetics, thermodynamics, and/or transport processes. It is currently used for applications including combustion, detonation, electrochemical

energy conversion and storage, fuel cells, batteries, aqueous electrolyte solutions, plasmas, and thin film deposition.

Cantera was originally written and developed by Prof. Dave Goodwin from California Institute of Technology [180]. It is written in C++ and can be used from both Python and MATLAB interfaces, or in applications written in C++ and Fortran 90. In this work, we choose to use the Python interface.

6.2.2. *Description of the Cantera software*

Cantera considers different reactor configurations such as plug flow reactors (PFR), continuously stirred tank reactor (CSTR), or some cases representative of real configuration as flames or catalytic reactors. It is possible also to solve multiphase mixture and surface chemistry problems.

Cantera solves the conservation equations for several types of configurations. It handles the computation of chemical processes using kinetic mechanisms provided by the user.

This software package includes a set of models for representing steady-state, quasi-one-dimensional reacting flows, which can be used to simulate common flames.

To solve a premixed laminar burner stabilized flame, we used the specific model *BurnerFlame.py* (Fig.III.20). This Python code required some input data files such as the kinetic mechanism in Cantera format (Mech.cti) and the experimental temperature profile (Exp_T_profile.dat). This last input data file is required if we decide to not solve the energy equation.

Cantera solver uses a Newton integration method to solve the equations. When the convergence is reached, the code returns an output data file with simulation results in xml format (Solution.xml). These variable values could be used as initial solution for a new calculation or to create some spreadsheet file which contains all the information required by the user such as the profiles of all the species involved in the reaction mechanism. From this output file it is possible to calculate the formation / consumption rates of the species to perform the analysis of the main reactional pathways. If the sensitivity analysis calculation has been performed, the normalized sensitivity coefficients could be also extracted from this file.

Fig.III.20 shows a schematic representation of Cantera analysis process.

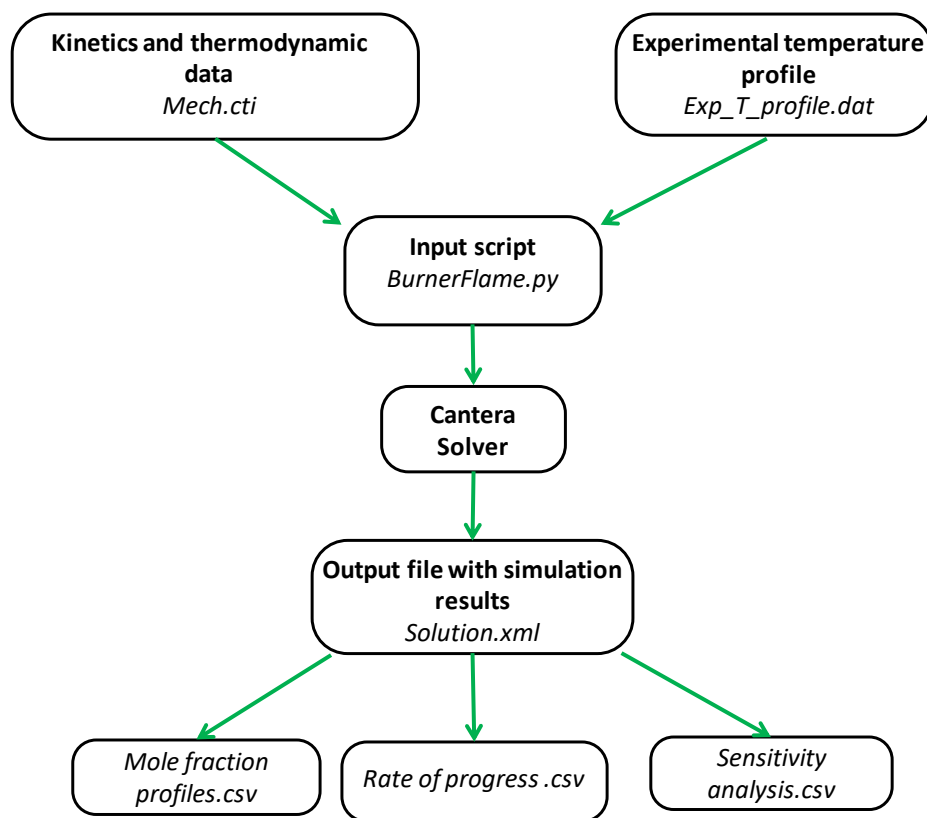


Fig.III.20. Architecture of Cantera simulation.

6.2.3. Kinetic mechanism in the Cantera format.

The software reads the detailed chemical mechanism in an external file with the extension “.cti” (i.e.: mech.cti in Fig.III.20), where the chemical reactions, the thermodynamic and transport data for each species are described.

The mechanism file contains all the information needed by Cantera to interpret the kinetic mechanism. This data file is written by respecting a specific syntax, which includes the entry parameters (called *entries*), i.e. reactions or species, and how these parameters have to be interpreted (called *directives*). It is composed of three main parts:

- some general information;
- the description of the chemical species involved in the mechanism;
- the set of chemical reactions.

In each one of those parts, specific information has to be defined. As example, Fig.III.21 presents the structure of the input file with kinetics and thermodynamic data.

In the first part (Part 1 in Fig.III.21), the reactional mixture is described by these main required followed fields:

- *name*: to identify the physical state of the medium;
- *elements*: declaration of all the chemical elements involved in the mechanism;
- *species*: the name of all the chemical species involved in the mechanism are declared;
- *reaction=all* : to consider all reactions in the mechanism;
- *transport*: about how consider the diffusion coefficients of the mixture.

As in many combustion simulations, we use an ideal gases mixture.

In the second part of this input file (Part 2 in Fig.III.21), all the species involved in the mechanism are specified by defining their thermodynamic and transport properties. Each species is described by the following fields:

- *name*: how the chemical compound is named;
- *atoms*: where the numbers and the chemical elements which form the species are defined;
- *thermo*: where polynomial coefficients to calculate the thermodynamic properties are listed;
- *transport*: this field is defined if the transport properties are required to resolve the problem and contain the parameters to define the transport properties.

About the thermodynamic properties mentioned before, they are defined from polynomial coefficients developed by the NASA "Chemical Equilibrium Program" [181]. The format introduces 2 sets of 7 coefficients ($a_{i,k}$) which allow the calculation of the thermodynamic properties for each species in two different temperature ranges: a low temperature range, generally between 300 K and an intermediate temperature close to 1000 K, and a high temperature range, between the same intermediate temperature and a higher temperature (3000 K or 5000 K for example).

The thermodynamic properties, such as heat capacity (C_p), enthalpy (H) and entropy (s), are thus calculated for each k species by using the following equations:

$$\frac{C_{p,k}}{R} = a_{1,k} + a_{2,k}T + a_{3,k}T^2 + a_{4,k}T^3 + a_{5,k}T^4 \quad (3.8)$$

$$\frac{H_k^0}{RT} = a_{1,k} + a_{2,k}\frac{T}{2} + a_{3,k}\frac{T^2}{3} + a_{4,k}\frac{T^3}{4} + a_{5,k}\frac{T^4}{5} + a_{6,k}\frac{1}{T} \quad (3.9)$$

$$\frac{S_k^0}{R} = a_{1,k} \ln T + a_{2,k}T + a_{3,k}\frac{T^2}{2} + a_{4,k}\frac{T^3}{3} + a_{5,k}\frac{T^4}{4} + a_{7,k} \quad (3.10)$$

The Gibbs energy G^0 can be calculated from H^0 and s^0 ($G^0 = H^0 - Ts^0$). Hence it is possible to calculate the equilibrium constants in function of the pressure (K_p) of each reversible reaction, as well as the rate constant of the inverse reactions.

$$\Delta G^0 = -RT \ln K_p \quad (3.11)$$

$$K_c = \frac{k_{for}}{k_{back}} = K_p \left(\frac{P}{RT} \right)^{\sum \nu_{prod} - \sum \nu_{reac}} \quad (3.12)$$

With: ν : stoichiometric coefficient

k_{for} : forward rate constant

k_{back} : backward rate constant

K_c : equilibrium constant

The transport properties required to include the molecular parameters of the species such as its geometry (atom, linear or nonlinear), the collisional diameter of Lennard-Jones, the potential of Lennard-Jones, the molecular dipole moment, the polarizability and the number of collisions resulting in rotational relaxation.

The third part (Part 3 in Fig.III.21) gathers all the reactions included in the chemical mechanism. The constant of the reaction rate is written according to the modified Arrhenius equation:

$$k_i = A \times T^n \times \exp\left(-\frac{E}{RT}\right) \quad (3.13)$$

which obeys to the law of mass action, with a rate coefficient that depends only on temperature. Each reaction has to be described by the following fields:

- *reaction equation*: the reaction equation determines the reactants and products in stoichiometric conditions. It can be taken into account the irreversibly (\Rightarrow) or reversibly (\Leftrightarrow) feature of the reaction.
- *Reaction rate*: for each reaction, three coefficients are taken into account to define the reaction rate constant. These coefficients correspond to the pre-exponential factor (A), the corrective coefficient of pre-exponential factor variation with the temperature (n), and the activation energy (E).

The uni-molecular and tri-molecular reactions depend on the pressure. For some reactions, in the low-pressure limit, a collision partner is needed to initiate the reaction. Then the “+ M” characters are added on either side of the equation symbolizing the 3rd body. The reaction is in low pressure limit and there is no high-pressure limit. This reaction is called `three_body_reaction` and an example of its syntax is showed in Part 3:

In a three-body reaction, different species may be more or less effective in acting as collision partner. These effects can be accounted for by defining a collision efficiency for each species, through the 'efficiencies' field.

However, when the reactions are in particular conditions to be between the low-pressure and the high-pressure limits, it is said that the reactions are in the "fall-off" zone and indicated as `falloff_reaction`. To represent this case, “+ M” is then enclosed in parentheses, and the constants k_f (reaction rate at the high-pressure limit) and k_{f0} (reaction rate at the low limit of pressure) are specified. So, several methods to represent the "fall-off" zone can be used. Two methods are considered, the Lindemann's theory and the Troe's formalism, which need to be specified in

falloff_reaction entry. An example of each syntax method is presented in Part 3 of Fig.III.21.:

The dependence on the pressure can also be expressed by considering different values of the rate constant for different ranges of pressure as shown in Fig.III.21

```

units(length='cm', time='s', quantity='mol', act_energy='cal/mol')
ideal_gas(name='gas',
  elements="N O C H Ar He",
  species=""J00cy(COCCC)    J00cy(CCOCC)    H00cy(COCCCJ)
           H00cy(COCCJC)   H00cy(COCJCC)   H00cy(CCJ0CC)
           H00cy(CCOCCJ)   H00cy(CCOCCJ)   0*cy(COCCC)
           .....
           C3H2          C3H2(S)         C3H2C
           H2CCC(S)      C3H30           C3H302H
           C2HCHO        CH3COCH20       C6H5CH3
           C6H5CH2       PC3H40H-2       SC3H40H
           SC3H50H       CH3CHCHO        C6H11
           AC4H700H      HOC4H6          CYC*CCOHC0
           HC(*O)OOH     cy(0)13cy(CCCOC) C*CCC(OJ)OOH""",
  reactions='all',
  transport='Mix',
  initial_state=state(temperature=300.0, pressure=OneAtm))

```

Part 1

```

# Species data
#-----
.....
species(name='C2H2OH',
  atoms='C:2 O:1 H:3',
  thermo=(NASA([300.00, 1000.00],
    [ 5.62397968E-01, 2.64598620E-02, -2.28453705E-05,
      9.14478695E-09, -1.06711936E-12, 1.48374643E+04,
      2.10439544E+01])),
    NASA([1000.00, 5000.00],
    [ 6.81339897E+00, 8.05827723E-03, -3.11728612E-06,
      5.54590896E-10, -3.71804255E-14, 1.31583034E+04,
      -1.09863525E+01])),
  transport=gas_transport(geom='nonlinear',
    diam=4.162,
    well_depth=224.7,

```

Part 2

```

# Reaction data
#-----
.....
reaction('CH2O + OH <=> HCO + H2O', [7.820000e+07, 1.63, -1055.0])

three_body_reaction('HCO + M <=> H + CO + M', [5.700000e+11, 0.66, 14870.0],
  efficiencies='H2:2.0 CH4:2.0 H2O:6.0 CO2:2.0 CO:1.5 C2H6:3.0')

falloff_reaction('CO + O (+ M) <=> CO2 (+ M)',
  kf=[1.362000e+10, 0.0, 2384.0],
  kf0=[1.173000e+24, -2.79, 4191.0],
  efficiencies='H2:2.0 AR:0.7 HE:0.7 CO2:3.6 CO:1.75 H2O:12.0')

# Reaction 745
falloff_reaction('CH2O + H (+ M) <=> CH2OH (+ M)',
  kf=[5.400000e+11, 0.454, 3600.0],
  kf0=[1.270000e+32, -4.82, 6530.0],
  efficiencies='H2:2.0 CH4:2.0 H2O:6.0 CO2:2.0 CO:1.5 C2H6:3.0',
  falloff=Troe(A=0.7187, T3=103.0, T1=1291.0, T2=4160.0))

pdep_arrhenius('CH3 + OH <=> CH2(S) + H2O',
  [(0.01, 'atm'), 4.936000e+14, -0.669, -445.8],
  [(0.1, 'atm'), 1.207000e+15, -0.778, -175.6],
  [(1.0, 'atm'), 5.282000e+17, -1.518, 1772.0],
  [(10.0, 'atm'), 4.788000e+23, -3.155, 7003.0],
  [(100.0, 'atm'), 8.433000e+19, -1.962, 8244.0])
.....

```

Part 3

Fig. III.21 Structure of the input file with kinetic and thermodynamic data.

6.2.4. *Premixed laminar burner-stabilized flame code.*

The script and the set of commands to perform a Cantera simulation considers different parts, as shown in Fig.III.22. A parameters section (Part 1) is dedicated to specify all the initial boundary conditions such as the initial mole fraction of the fuel, oxygen and nitrogen, the temperature at the burner surface (t_{burner}), the pressure (p) and the mass flow rate at burner (\dot{m}).

To solve the equations, Cantera needs to discretize the domain. For this reason, the width of flame and the criteria which define the grid are specified in this section.

Then, the “gas” python function is created (Part 2) by specifying its initial state and its chemical, thermodynamic and transport properties by importing the data file “chem_mech_file.cti”.

After, it is necessary to create the “flame”, detailed in Part 3 of Fig.22. “BurnerFlame” is a burner-stabilized, premixed flat flame defined by gas phase, width of the flame and the mass flow rate, previously specified. In our case, the experimental temperature profile is imposed.

The criteria for the solver are detailed in the Part 4.

The solver uses a Newton integration method. In order to improve the solutions convergence, firstly the flame is solved with mixture – averaged transport properties and then considering multicomponent transport properties. At the end of this part, the xml output file is generated.

The last part of the script contains the instruction to save the results in a csv file (Part 5).

```

# parameter values
p = 0.0526 * ct.one_atm
tburner = 443.428
mdot = 0.03626 # kg.m-2.s-1
reactants = 'CH4:0.1067, O2:0.2133, N2:0.6800'

width = 0.025 # m

loglevel = 1
refine_grid = True

```

Part 1

```

chem_mech_file = mech_name + '.cti'

gas = ct.Solution(chem_mech_file)

gas.TPX = tburner, p, reactants

```

Part 2

```

f = ct.BurnerFlame(gas=gas, width=width)

f.burner.mdot = mdot

zloc, tvalues = np.genfromtxt('M1.0_T_profile_by_LIF.dat', delimiter=',', comments='#').T
zloc /= max(zloc)

f.flame.set_fixed_temp_profile(zloc, tvalues)

f.show_solution()

f.energy_enabled = False #False

```

Part 3

```

f.transport_model = 'Mix'
f.set_refine_criteria(ratio=3.0, slope=0.3, curve=1)
f.solve(loglevel, refine_grid)

xml_file_name = 'M1.0_flame_fixed_T_'+mech_name+'.xml'
f.save(xml_file_name, 'mixav',
       'solution with mixture-averaged transport')

print('\n\n switching to multicomponent transport...\n\n')
f.transport_model = 'Multi'

f.set_refine_criteria(ratio=3.0, slope=0.1, curve=0.2)
f.solve(loglevel, refine_grid)

f.save(xml_file_name, 'multi',
       'solution with multicomponent transport')

```

Part 4

```

# write the velocity, temperature, density, and mole fractions to a CSV file
csv_file_name = 'M1.0_flame_fixed_T_'+mech_name+'.csv'
f.write_csv(csv_file_name, quiet=False)
f.show_stats()

```

Part 5

Fig. III.22 Script and the set of commands to perform a Cantera simulation of a burner stabilized flame.

7. Conclusion

In this chapter we have presented the procedure to study the role of some particular biofuels, i.e. furan (F) and tetrahydrofuran (THF), on the NO_x formation chemistry.

In order to achieve this goal, six CH₄/F/THF/O₂/N₂ flames have been defined to be studied by experimental and numerical approaches. In this way, the experimental study is performed by using two different, but complementary techniques described in this chapter.

The mole fraction profiles of the stable chemical species in the flames are obtained by gas chromatography analysis. Laser Induced fluorescence is used to perform the CH and NO mole fraction profiles and the temperature profiles in flame.

The numerical approach consists of modelling the flames experimentally studied to evaluate the impact of the biofuel oxidation on NO formation. To model the experimental results, the software Cantera has been chosen and described.

Main GC analysis results are presented in the next chapter compared with the modelling results; whereas the NO and CH results obtained by LIF are presented in chapter V.

Chapter IV Study of fuel oxidation

In this chapter, the study of furan (F) and tetrahydrofuran (THF) oxidation in $\text{CH}_4/\text{F}/\text{THF}/\text{O}_2/\text{N}_2$ premixed laminar flames stabilized in low pressure conditions is presented.

In the first part, complementing the previous chapter, the experimental procedure implemented to obtain the species mole fraction results by GC is detailed.

Secondly, we present the two detailed kinetic mechanisms available in the literature dedicated to the oxidation of F and THF. After this presentation, we compare our experimental results with the modelled ones, and discuss about this comparison to evaluate their ability to predict the oxidation of the investigated fuels in our experimental conditions.

1. Experimental

1.1. Identification of the chemical species

The chemical compounds are identified by GC/MS, as already described in chapter III. Indeed, by comparing mass spectra of the analyzed species to those of the NIST library, it is possible to identify most of the chemical species measured in the flames. When this identification is uncertain, for example in case of the presence of isomers in the gaseous sample (species for which mass spectra are very similar), other criteria are adopted to valid the identification. As example, for cis and trans isomers or similar compounds, as C_4 compounds (isobutene, 1-butene, 1,3-butadiene), polarity and boiling temperature can be used to understand and validate their elution order.

In this work, six $\text{CH}_4/\text{F}/\text{THF}/\text{O}_2/\text{N}_2$ flames have been studied to evaluate the impact of F and THF oxidation on NO formation. The use of GC systems has allowed the identification of 65 stable chemicals:

- 15 in methane flames;
- 46 in furan doped flames. Among them, 15 are present in CH_4 flames and 31 species are related to the F oxidation;

- 49 in THF doped flames. Among them, 15 are in common with CH_4 oxidation and 34 species are related to the THF oxidation, whose 17 are formed in both biofuels oxidation.

To illustrate the difference of kinetic behavior in the $\text{CH}_4/\text{F}/\text{O}_2/\text{N}_2$ and $\text{CH}_4/\text{THF}/\text{O}_2/\text{N}_2$ flames, the Fig.IV.1 presents a zoom of the GC/FID chromatograms measured in these two flames at the same height above the burner in splitless mode (see paragraph 4.3 chapter III).

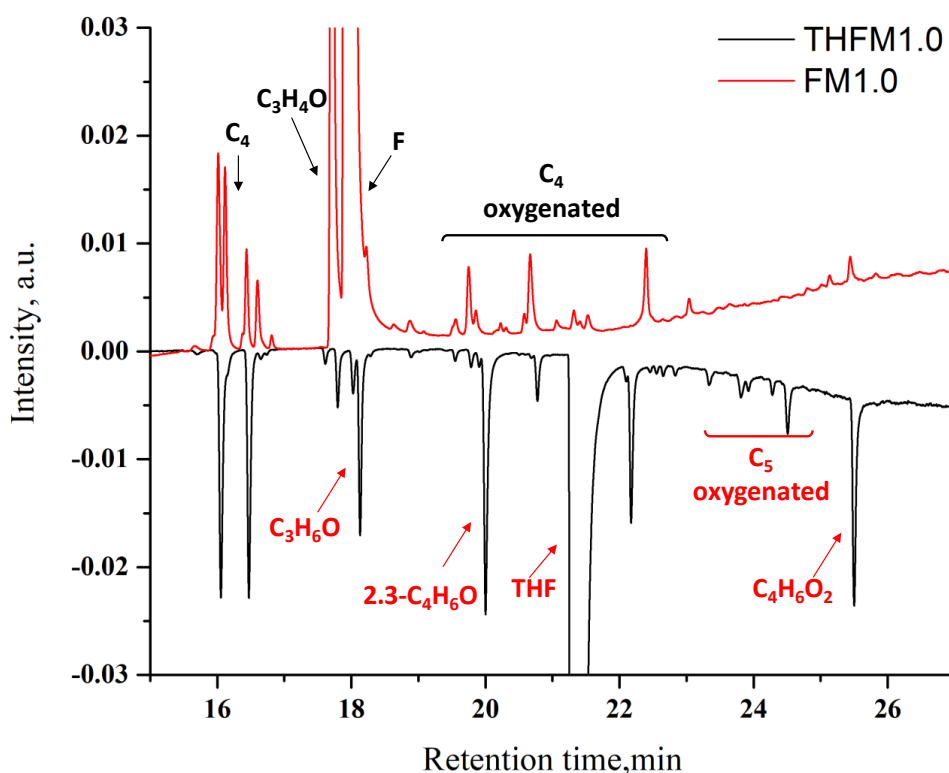


Fig.IV.1 Comparison of the GC-FID chromatograms obtained in the two FM1.0 and THFM1.0 flames 1.8mm above the burner in splitless mode.

Note that in the furan flames, the two isomers ($\text{C}_3\text{H}_6\text{O}$), propanal and acetone, are not evaluated because their peaks are covered by fuel peak. In the case of THF flames, the peak of these three species are well separated due to the low concentration of F in THF flames.

1.2. Determination of species mole fractions

The relative evolution profiles of each species present in the flames and measured by GC, were calibrated in absolute concentration (mole fraction) using four distinct procedures depending on the nature of the species considered.

1.2.1. *Calibration methods*

The mole fraction χ_i of a species (i) is related to the detector sensitivity (α_i), the species peak area (A_i) obtained on the chromatogram and the injection pressure (P_{inj}) of the gaseous sample in the chromatographic analysis device:

$$\chi_i = \frac{A_i}{\alpha_i P_{inj}} \quad (4.1)$$

The sensitivity factor (α_i) depends on the analyzed species, the characteristics of the chromatographic column, the GC operating parameters and the injection procedure.

Calibration procedure consists to determine the sensibility coefficient (α_i) (also called response factor) of the (i) chemical species mainly by using standard mixtures of known concentrations.

To determine the response factor, different methods have been used according to the chemical species:

- Methane, furan and tetrahydrofuran are calibrated by injection of fresh mixture of the six flames feeding;
- Major products (CO, CO₂, O₂, H₂, N₂) and light hydrocarbons (C₂-C₄) are calibrated using commercial gaseous standard mixtures (Air Products, uncertainty on mole fraction ± 0.5 -2%);
- All other intermediate liquid species at ambient temperature were quantified by preparing gas mixtures in storage flasks using the partial pressure method;
- Formaldehyde is specifically calibrated using aqueous solutions of formaldehyde and acetaldehyde. This procedure is detailed in the following section;

- For the species which are not calibrated directly by the previous methods, the response factor is determined using effective carbon number method [182].

An example of calibration curve is shown in the Fig.IV.2 in the case of acrolein. This calibration curve is obtained using two gaseous mixtures of acrolein in nitrogen at known mole fraction. These mixtures were prepared by using partial pressure method.

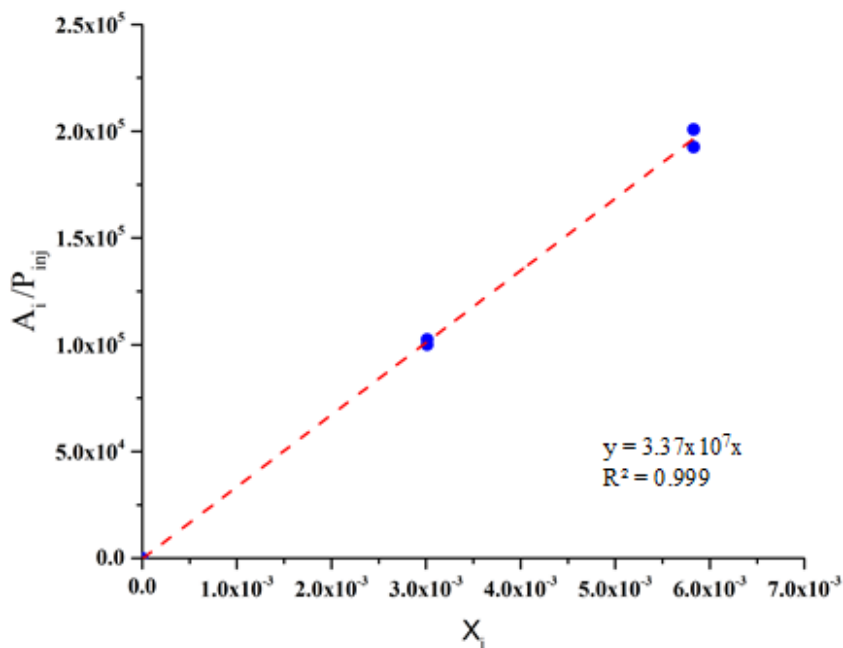


Fig. IV.2: Example of a calibration curve for acrolein.

1.2.2. Formaldehyde calibration

Formaldehyde (CH_2O) is an important indoor air pollutant and the source of oxidizing agents in the atmosphere. It is encountered in many manufacturing processes such as fermentation and in the production of adhesives, fireproofing agents and urea-formaldehyde foam.

CH_2O is an important oxygenated pollutant also in combustion processes. It is one of the major products of low temperature hydrocarbons oxidation [183], [184] and it is formed also during the oxidation of biofuels [70], [185]. Hence, it is important to be able to quantify this compound to correctly validate the detail kinetic mechanisms.

Formaldehyde polymerizes rapidly and combines with water to produce methylene glycol. Formaldehyde can be analyzed by different analytical techniques such as

colorimetry or High-Performance Liquid Chromatography (HPLC); unfortunately, these methods cannot be used to analyze this aldehyde in the gas phase. On the other hand, formaldehyde can be detected in gas phase by Fourier-Transform InfraRed spectroscopy (FTIR) and Gas-Chromatography (GC).

By using GC analysis, we can measure formaldehyde with a FID detector coupled with a nickel catalyst-methanizer, and with Mass-Spectrometer detector (MS). Thermal Conductivity Detector (TCD) also enables to detect CH_2O but only in high concentration due to the low sensitivity of this detector for this compound. Anyway, an absolute calibration of the measurements obtained with these different techniques is required to quantify formaldehyde in gas phase.

Due to the toxicity of formaldehyde and its propensity to polymerize in presence of water, it is difficult to manipulate formaldehyde in gas phase. In this work, we propose a new method for a direct calibration of formaldehyde based on the preparation of a CH_2O aqueous solution with the addition of an internal standard already calibrated in gas phase by methods described previously.

1.2.2.1. Preparation of the solution

Commercial aqueous solutions of formaldehyde are available but mainly in high concentration condition (such as formalin which is a saturated aqueous solution with 40% by volume of CH_2O). For concentrations less than 5 mol%, CH_2O is usually in aqueous solution in its hydrated form (methylene glycol). As the CH_2O concentration increases, the methylene glycol leads to the formation of oligomers [186]. To prevent the polymerization process, methanol may be added (10-12% by volume) as stabilizer. However, methanol reacts with formaldehyde in liquid phase to form hemi-formal which affects the volatility of the formaldehyde in solution [187].

As described in the thesis of Oancea [188] and Delcroix [189], it is possible to prepare aqueous solution of formaldehyde up to CH_2O mole fraction of 10% without methanol. By following authors' recommendations, we have prepared aqueous solutions containing 1% by volume of formaldehyde by the depolymerization of paraformaldehyde in deionized water [190]. Deionized water was produced with an

Aquadem EFP2010 which supplies water with a peak resistivity of 18 MΩcm. The appropriate amounts of paraformaldehyde (Sigma-Aldrich, powder, 95%) and deionized water to prepare about 100 ml of solution are heated around 373 K until complete dissolution of the paraformaldehyde. To favor paraformaldehyde depolymerization, a small amount of sodium hydroxide solution (0.1 M) is added to the mixture.

After cooling at ambient temperature, the formaldehyde solutions are weighed again, and the necessary amount of deionized water is added to compensate the loss of water for evaporation.

1.2.2.2. Addition of internal standard

To link an analysis in liquid phase by direct injection of the solution in GC with another one realized in gas phase, we need to add a compound as internal standard in the liquid solution, which can be analyzed with both methods.

An internal standard is a chemical substance that is added in a known amount to the samples which contains the analyte of interest. The relationship between the two signals obtained from the analysis of the solution (analyte / internal standard) is then used to obtain the concentration of the analyte from the internal standard calibration curve [177].

Acetaldehyde (C₂H₄O) is the best candidate as internal standard for formaldehyde solution. It is a liquid aldehyde at ambient temperature with a chemical structure close to formaldehyde; it is miscible in all proportions with water [191] and it can be easily calibrated in gas phase with GC device by preparing gas mixtures using the partial pressure method.

In aqueous solution of formaldehyde at ambient temperature, we add acetaldehyde in the same range of concentration. The CH₂O-C₂H₄O-H₂O solution is weighed again, and the final mole fraction of each compound is then calculated.

Acetaldehyde has a boiling point of 20.2 °C. Therefore, to avoid any change of the liquid composition and to reduce its volatility, the final solution is cooled down to around 5°C in an ice /water vessel.

The cold solution is injected several times in the GC device by using a syringe and by using the same GC method as the one for gaseous samples analysis. To illustrate this calibration procedure, the Fig.IV.3 shows the interesting zone of the chromatogram resulting from the analysis of the liquid solution.

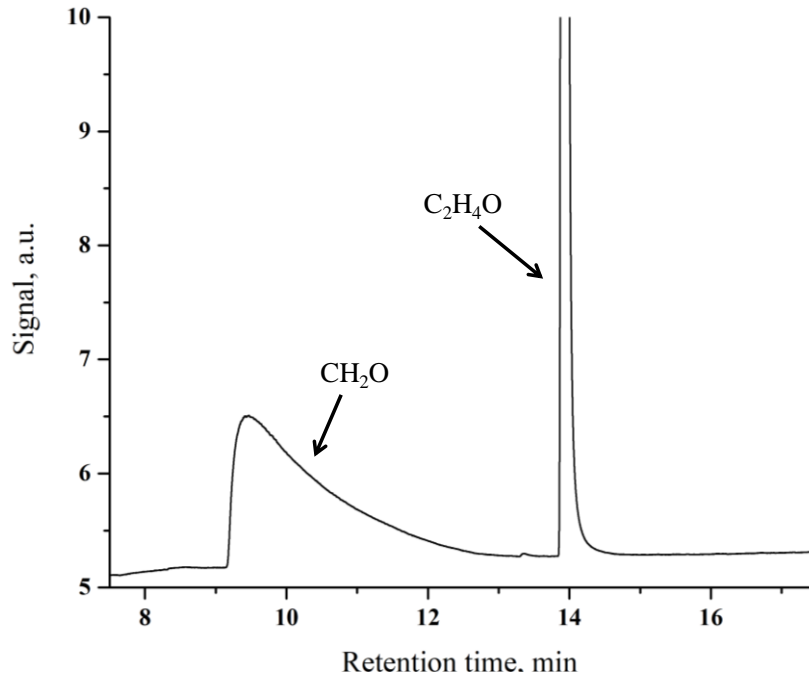


Fig.IV.3 Zoom of the CH₂O-C₂H₄O-H₂O liquid solution analysis chromatogram.

For the liquid sample, the response factor is defined to be the ratio of the peak area (A_i) to the mole fraction of the species (i) (χ_i). By considering the response factors respectively for formaldehyde ($\alpha_{liq}^{CH_2O}$) and acetaldehyde ($\alpha_{liq}^{C_2H_4O}$):

$$\alpha_{liq}^{CH_2O} = \frac{A_{CH_2O}}{\chi_{CH_2O}} \quad (4.1)$$

$$\alpha_{liq}^{C_2H_4O} = \frac{A_{C_2H_4O}}{\chi_{C_2H_4O}} \quad (4.2)$$

We can formulate that the ratio F between the two response factors in liquid phase:

$$F = \frac{\alpha_{liq}^{CH_2O}}{\alpha_{liq}^{C_2H_4O}} \quad (4.3)$$

Then assuming that the ratio is not affected by the phase of the injection sample and knowing the response factor in gas phase of acetaldehyde $\alpha_{gas}^{C_2H_4O}$, it becomes possible to determine the response factor of formaldehyde in the gas phase:

$$\alpha_{gas}^{CH_2O} = F \times \alpha_{gas}^{C_2H_4O} \quad (4.4)$$

For a better accuracy, the value of F ratio is averaged on several injections of CH₂O-C₂H₄O-H₂O solutions.

1.3. H₂O calculation

To determine the mole fraction profile of water (H₂O), we have considered the balances in carbon (C) and hydrogen (H). Indeed, at a position (HAB index) in the flame, the hydrogen/carbon ratio (H/C) must have the same value as the initial mixture at burner surface (IN index).

$$\left[\frac{\sum_k n_k(C)\chi_k}{\sum_k n_k(H)\chi_k} \right]_{IN} = \left[\frac{\sum_k n_k(C)\chi_k}{\sum_k n_k(H)\chi_k} \right]_{HAB} \quad (4.5)$$

With: χ_k = mole fraction of species k.

$n_k(A)$ = number of atoms C or H in the compound k.

By considering this relation, the mole fraction of H₂O can be calculated for all the position above the burner in the six flames by the following equation:

$$\left[\frac{\sum_k n_k(C)\chi_k}{\sum_k n_k(H)\chi_k} \right]_{IN} = \left[\frac{\sum_k n_k(C)\chi_k}{\sum_{k \neq H_2O} (n_k(H)\chi_k) + 2\chi_{H_2O}} \right]_{HAB} \quad (4.6)$$

$$[\chi_{H_2O}]_{HAB} = \frac{1}{2} \left(\frac{[\sum_k n_k(C)\chi_k]_{HAB}}{[\sum_k n_k(C)\chi_k]_{IN}} - \left[\sum_{k \neq H_2O} n_k(H)\chi_k \right]_{HAB} \right) \quad (4.7)$$

The mole fraction profiles of H₂O obtained in each flame are presented in paragraph 2 of this chapter.

1.4. Main GC results

For the six CH₄/F/THF/O₂/N₂ studied flames, the determination of the mole fraction profiles of each species was performed two times, starting from the burned gases to the burner surface. After the calibration procedure, we have obtained the absolute mole fraction profile of all the species detected in our flames, except H₂O. The mole fraction profiles of H₂O in flames are calculated by using the atomic balance ratio C/H. Implicitly, we have assumed that most of the species containing C and H atoms in flame have been quantified. We neglected the presence of atoms and radicals like H, O and OH which are assumed to be not relevant for the C/H ratio (because not measured). After the calculation of H₂O profiles, we proceeded to add up the mole fraction of all quantified species including water ($\sum_k \chi_k$), and this at each HAB. Then, we normalize for the sum of mole fractions in order to respect the condition $\sum_i \chi_i = 1$ and then the conservation of each element (C, H, O).

Despite the similar structure of these two biofuels, the saturation or unsaturation of the molecule entails a different kinetic behavior during the oxidation of F and THF, as shown the various compounds detected.

In furan flames, the formation of hydrocarbon species is enhanced with respect to THF flames. Indeed, during the oxidation of this unsaturated ether 24 hydrocarbons species are produced against 18 for THF. In particular, the formation of dienes and alkynes is enhanced with respect to THF oxidation. Low concentration of benzene and of other PAH precursors such as cyclopentadiene and 1,3-butadiene are detected.

Concerning the oxygenated species, these compounds are formed in large amount during THF oxidation. Indeed, in THF oxidation 21 oxygenated species are formed, compared to 18 in F. We detected very toxic aldehydes such as acrolein, methacrolein, crotonaldehyde, cyclopropanecarboxaldehyde, valeraldehyde, ... In particular, in THF flames the formation of ethers such as the dihydrofuran isomers and methyl-oxirane is enhanced.

Among the oxygenated species, we detected also some species typical of low temperature oxidation such as butanedial, methyl oxirane and dioxene. methyl-oxirane was detected with respect to the oxirane, which is important in THF oxidation [7].

This may be another example of synergy between the methane and THF due to the high concentration of CH_3 radical issued in methane oxidation.

As reported by Fenard et al. [7], butanedial is formed during THF oxidation in the low temperature range from the 2-tetrahydrofuranyl radical. This species was observed also by Vanhove et al. [102] in Rapid Compression Machine (RCM). The same authors observed also the dioxene and methyl-oxirane in their RCM.

The profiles of all species detected in this study and a table with the maximum of their mole fraction are reported in Annex C.

1.5. Error estimation

The quality of the comparison between experimental results and modelled ones depends among others on the accuracy of the measurements. Therefore, it is important to evaluate the uncertainties associated with these experimental results in order to estimate the accuracy of the models.

For the six $\text{CH}_4/\text{F}/\text{THF}/\text{O}_2/\text{N}_2$ studied flames, the determination of the mole fraction profiles of each species was performed two times. The comparison of the two series of measurements for all the species is characterized by a very good reproducibility ($\pm 1.5\%$) for the six flames.

By considering all the elements constituting the experimental device, it is certain that the potential sources of error are numerous. For example, it can be considered that the accuracy of the composition of the gas mixture sent to the burner is directly related to the accuracy of the mass flow controllers ($\pm 0.5\%$). The calibration of the chemical species in absolute mole fraction constitutes also an important source of errors: accuracy of the composition of the standard mixtures, stability of the detector between the different calibration step, accuracy of the gas quantity injected into the GC devices, etc... Another source of errors is directly related to the analysis systems used. Several factors can be implicated in this case: errors in the interpretation of the results (integration of peaks $\pm 2\%$), uncertainty in standard mixtures ($\pm 2\%$), gas injection pressure ($\pm 0.5\%$), temporal resolution of GC signal, etc...

Finally, by taking into account all these parameters, we estimate that the global uncertainties on the experimental measurements by GC are $\pm 5\%$ on the mole fractions of the major species and $\pm 10\%$ on minor species.

2. Modelling

In the second part of this chapter, we present the numerical approach used to model the experimental results we obtained. For that, we have chosen to test two detailed kinetic mechanisms available in the literature and dedicated to the oxidation of F and THF.

About furan combustion, the first to study the oxidation of this lignocellulosic biofuel in flame conditions was Tian et al. [60] in 2011. They investigated experimentally and numerically the premixed laminar F/O₂/Ar flames at low pressure ($P = 4.7$ kPa, $\phi = 1.4$ - 2.2) and proposed a detailed kinetic mechanism including 206 species involved in 1368 reactions. This mechanism was validated by comparison with their experimental results obtained in flame and with pyrolysis results obtained in shock wave. A reasonable agreement has been reached between experiments and modelling. The Tian model is moreover an important theoretical basis for further modeling work on furan oxidation, such as Wei et al [61] or the series of studies conducted by Nancy's and Bielefeld's groups on the oxidation of three furans: F [62], MF [70] and DMF [83].

Recently, Tran et al. [6] have published an article on the experimental and modelling study of the low- to moderate-temperature oxidation chemistry, which is the results of a continuous development from their previous studies ([62], [70] and [82]) for the high and low temperature oxidation of DMF, MF, and F in low-pressure flames.

About THF, the first to present a kinetic mechanism for the oxidation of this biofuel was Dagaut et al. [98] in 1998, who studied experimentally and numerically the ignition delay time and THF oxidation using respectively a shock tube and a jet stirred reactor. The authors proposed a detailed kinetic mechanism including 71 species involved in 484 reactions. More recently (2015) Tran et al.[101] proposed a new kinetic mechanism for THF oxidation, based on the experimental studies of laminar low-pressure premixed flame, atmospheric adiabatic laminar burning velocities, and high-pressure ignition delay times. The model predicts correctly the ignition delay

times obtained in shock tube conditions, but overpredicts significantly the measured laminar burning velocities, in particular in high temperature range.

Recently, Fenard et al. [7] have proposed the first detailed kinetic model for the low-temperature oxidation of THF. Thermochemical and kinetic data related to the most important elementary reactions have been derived from ab initio calculations. This mechanism contains an upgraded version of the Tran model [101] for high-temperature conditions.

2.1. The Tran mechanism

Tran et al. [6] report the first dataset in the 730–1170 K temperature range for three furanic fuels, 2,5-dimethylfuran (DMF), 2-methylfuran (MF), and F. The low temperature oxidation of the three fuels was investigated in a laminar flow reactor at 1 bar for 9 fuel/O₂/Ar mixtures, and for three equivalence ratios ($\phi \sim 0.5$, ~ 1.0 , ~ 2.0). The flow reactor was coupled to an Electron Ionization Molecular-Beam Mass Spectrometer (EI-MBMS) to measure stable and labile species. In their previous studies ([62], [70], and [82]), a kinetic model was developed from [79] to predict High-Temperature (HT) oxidation of DMF, MF, and F in low-pressure flames. The model was extended to include the reactions of gasoline surrogate mixtures (toluene, n-heptane, iso-octane) and Polycyclic Aromatic Hydrocarbons (PAH) up to C₁₆ [192] and was called the "HT model". In [6], they extend this HT model by including reactions concerning the Low-moderate temperature (LMT) oxidation of the furanic fuels.

The final chemical mechanism includes 3145 elementary reactions involving 524 chemical species and is optimized for LMT and HT oxidation of F, MF, and DMF. It is composed by two parts, an HT model developed in the previous work ([62], [70], [82], and [190]) and upgraded in this one, and a LMT model expressly developed in this last work by Tran et coworkers. In this thesis we used the global mechanism (HT+LMT models) to compare our experimental results and in the following section it will be named Tran mechanism.

The model was evaluated in the case of the LMT experiments, performed in flow reactor, as well as selected data sets taken from the literature: JSR data for DMF at 10

bar [82], measurements in a flow reactor for MF at 1 bar [193], and earlier results for furan studies in JSR condition at 1 bar [54]. Global properties in the LMT regime include validation for shock tube ignition delay times for DMF at 20 and 80 bar [82], and RCM ignition delay times of MF at 16 and 30 bar [194]. The HT range has been validated with low-pressure flame experiments of DMF, MF, and F ([62], [70], and [82]), and shock tube ignition delay times at 1.2–16 bar [195]. For all these experimental conditions, a satisfactory agreement is observed between literature experiments and predictions with the new LMT model.

The most important developments in the LMT oxidation include theoretical calculations of the rate coefficients for the following set of reactions: H-abstractions from the lateral methyl groups of DMF and MF by O_2 and reactions of the resonance-stabilized fuel radicals 2-furylmethyl (MF-yl) and 5-methyl-2-furanylmethyl (DMF-yl) with HO_2 and O_2 . They propose the resulting Arrhenius expressions (in cm^3 , mol, s, cal units) for the reactions:



A preliminary analysis indicated that OH-addition to the furan ring largely contributed to the consumption of DMF, MF, and F. Moreover, potential products of this process such as acrolein (C_3H_4O) and methyl vinyl ketone (C_4H_6O) were experimentally detected in large amounts. In addition, the kinetic data for H-abstractions from F by OH has been updated with the theoretical calculations from Mousavipour et al [196].

The experimental results show an increasing dependence of the fuel conversion (from F to DMF) on equivalence ratio. This trend seems to be linked to the number of lateral methyl groups in the fuel and depends on the bimolecular initiation reaction with O_2 for DMF and MF conversion. These reactions seem less important for furan conversion.

In all experimental conditions evaluated, the Tran mechanism presents a globally good agreement with measurements. As example, Fig.IV.4. presents the comparison of the simulated mole fraction profiles performed with Tran model and the experimental data of Liu et al [62] obtained in low pressure flames of $F/O_2/Ar$.

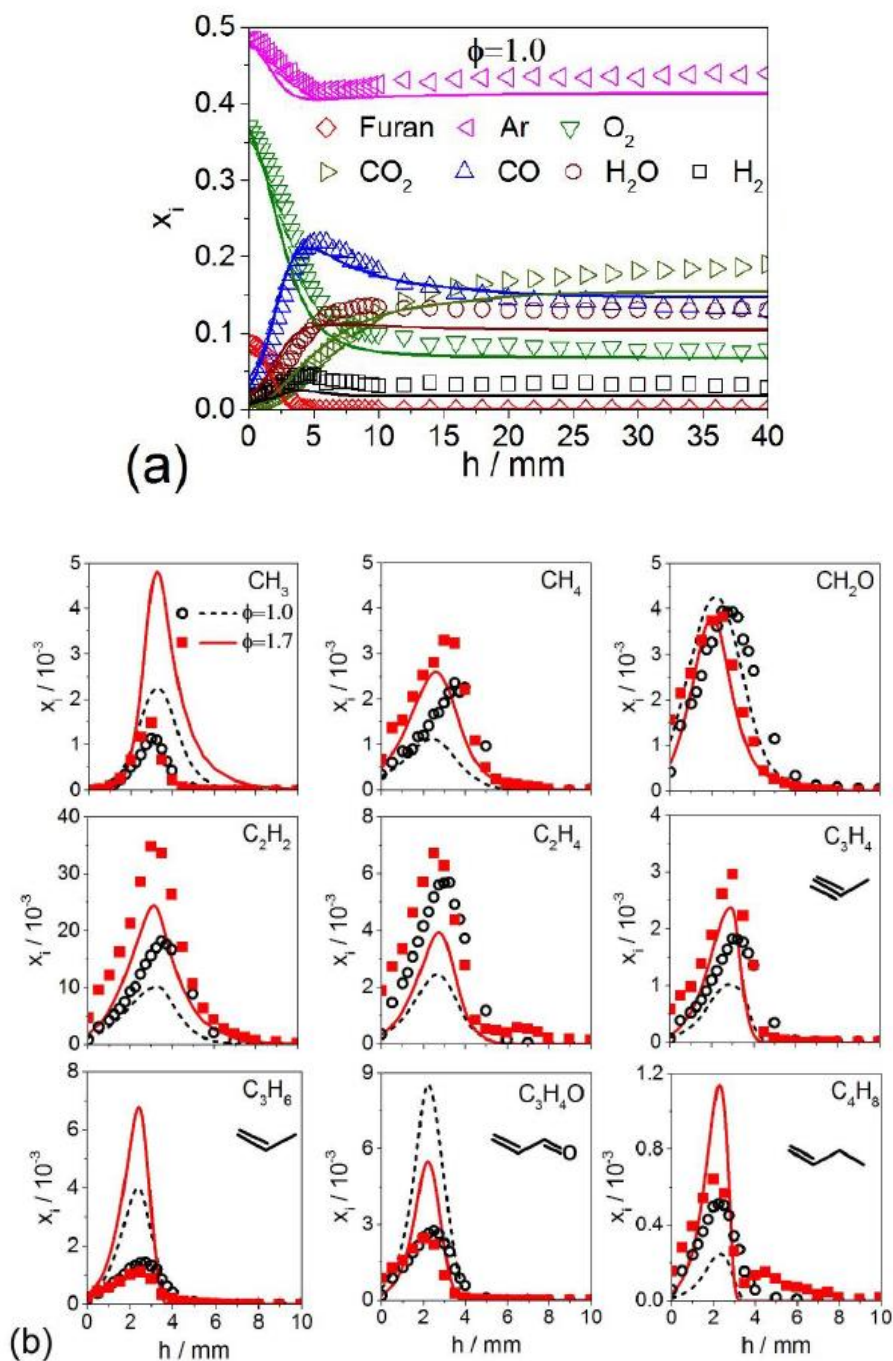


Fig.IV.4. Main species (a) and selected fuel-destruction intermediates (b) in a low-pressure premixed flame $F/O_2/Ar$. Symbols: experiments at $\phi=1.0$, from Liu et al. [62]; lines: Tran model. Figures are from the supplementary materials of Tran et al.[6].

From rate of productions (ROP) analysis (Fig IV.5), the authors have pointed out that the OH-additions to the ring is particularly important, especially for F at low temperature. This higher importance of OH-addition for F compared to MF and DMF mainly results from the slow H-abstractions reaction for F. The mole fraction of acrolein as the main product from OH-addition reaction to the furan ring was seen to

increase at lower temperatures than those of formaldehyde (CH_2O) and acetylene (C_2H_2) which are representative of the H-addition reaction.

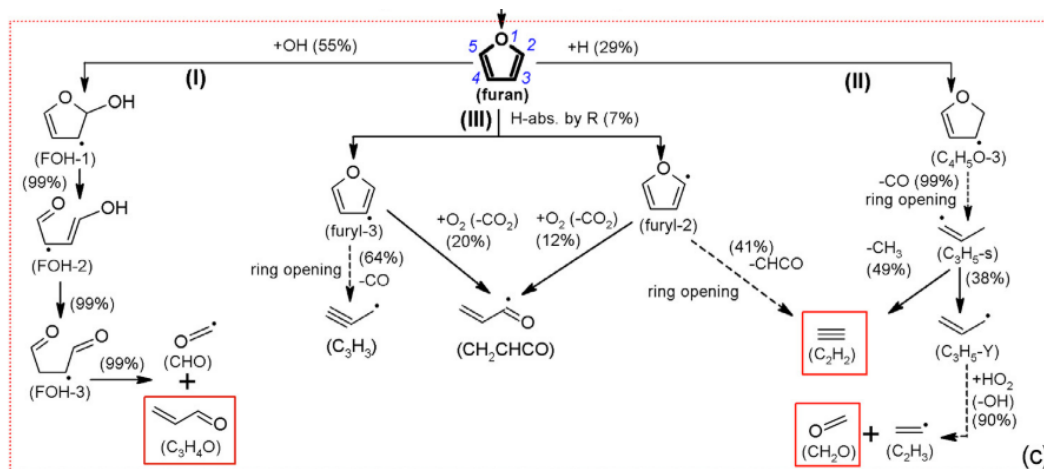


Fig.IV.5. Reaction pathway (ROP) analysis for the consumption of F in flame condition at $\phi \sim 1$ using the Tran model. Percentages are the relative rates of consumption determined in the 900–950 K temperature range. Primary stable intermediates are highlighted by solid boxes; they were also detected in the experiment. Dashed arrows represent the product(s) of a series of radical reactions [6].

For CH_2O and acetaldehyde ($\text{C}_2\text{H}_4\text{O}$), some different trends are observed between experiments and modelling. In F oxidation, the effect of equivalence ratio on CH_2O formation seems not to be significant. The lack of lateral methyl groups limits the role of abstraction reactions and this might be the reason for this small dependence on the equivalence ratio.

The HT part of the model contains also a sub-mechanism of THF oxidation from Tran et al. [101] and Verdicchio et al. [100].

This study represents the most complete and upgraded kinetic mechanism for F oxidation available in the literature. It was validated in different conditions including low pressure flames, but only for pure fuel.

2.2. The Fenard mechanism

Fenard et al. [7] recently proposed a new model for THF oxidation in low temperature conditions. This model is built on the validated high-temperature THF oxidation model of Tran et al. [101], which has been extended using results from high-level theoretical calculations for the important low-temperature reactions.

The model (named Fenard mechanism in the following) contains 467 species involved in 2390 reactions and was validated through the experimental data obtained by Vanhove et al. [102] in RCM and jet-stirred reactor, by Uygun et al. [71] in shock tube conditions, as well as the measurements reported by Dagaut et al. [98] and Tran et al. [101].

The structure of the kinetic model consists of a C₀-C₄ base from Metcalfe et al. [197], a high-temperature sub-mechanism upgraded from the scheme proposed by Tran et al. [101], and a sub-mechanism for the low-temperature oxidation of THF.

The original mechanism [101] was based on theoretical calculation for reactions of THF [100] and tetrahydro-furyl radicals. Because these reactions play an important role for temperatures higher than 1200 K, the rate parameters for the unimolecular decompositions of THF, which lead to the formation of products through H-shift and ring opening, were updated. Different other adjustments on rate parameters have been taken into account to upgrade the model in low temperature conditions.

The low-temperature sub-mechanism was developed using a similar structure as the one usually considered for the low-temperature mechanism of alkanes [183], i.e. including the oxidation pathways typically observed at temperatures between 550 and 750 K.

Fig.IV.6 presents a comparison between simulated and experimental mole fraction profiles of species sampled in stoichiometric THF flames. The simulations are performed with the Fenard model with the THF low-temperature oxidation sub-mechanism and are compared with the mechanism at high temperature proposed by Tran et al.[101]. The agreement for the flame results is satisfactory, even slightly better in some cases than that of Tran et al.[101].

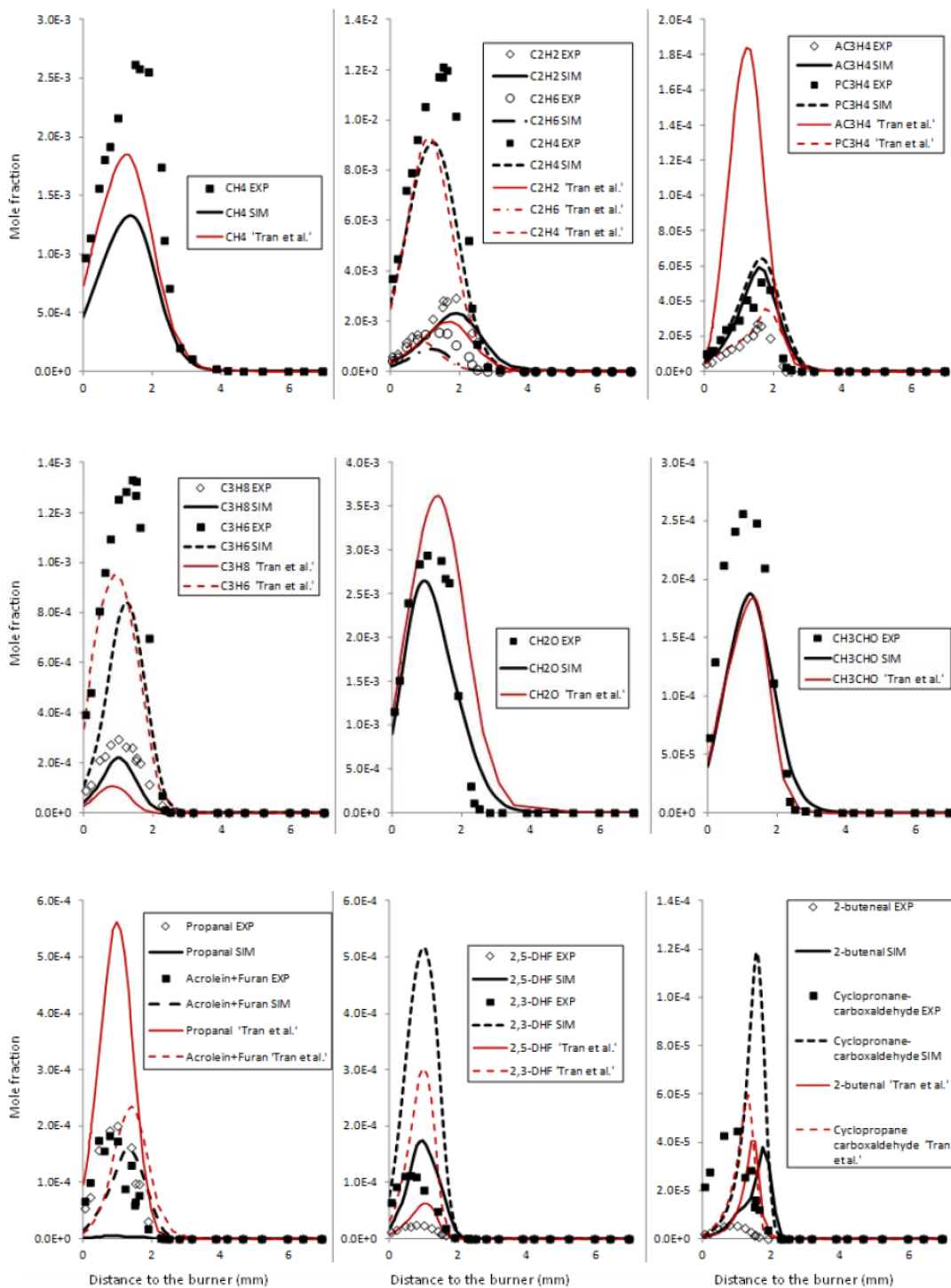


Fig.IV.6. Simulations of the mole fraction profiles of species sampled in stoichiometric THF flames [101]. Black lines: simulations performed with the Fenard model. Red lines: simulations with the model developed by Tran et al. [101]. Image from supplementary material of Fenard et al. [7].

Fig. IV.6 shows that the mole fraction profiles of C₂–C₃ hydrocarbons, such as CH₄, C₂H₆, C₂H₄, C₂H₂, C₃H₆ and C₃H₈ are fairly well predicted with Fenard kinetic

scheme. Propene is mostly formed by the sequence THF \Rightarrow 2-tetrahydrofuranyl radical \Rightarrow butan-1-al-4-yl \Rightarrow n-C₃H₇(+CO) \Rightarrow n-C₃H₇O₂ \Rightarrow C₃H₆(+HO₂). This sequence remains the main formation pathway of propene even at higher temperatures.

Regarding oxygenated intermediates, the predicted mole fraction profiles of formaldehyde, acetaldehyde, and acrolein (2-propenal) are globally in good agreement with the experimental data.

The comparison show that the predicted mole fraction profiles of the cyclic products produced during THF oxidation are in good agreement with the experimental results in all the temperature range. This is especially the case of unsaturated compounds such as 2,3-dihydrofuran and 2,5-dihydrofuran. The model is also able to very correctly predict the mole fraction profile of F.

Cyclopropanecarboxaldehyde is mostly formed by the isomerization of 2,3-dihydrofuran. Its mole fraction profile is therefore also fairly well reproduced in the low temperature simulations but overestimated at high temperature. Except for DHFs, dioxene is the most important experimentally detected product deriving from 3-tetrahydrofuranyl radical.

The Fenard mechanism represents the most recent and updated chemical kinetics model for the oxidation of THF present in the literature. It is validated in different conditions including low pressure flames, but only in case of pure fuel. We have used this model, and the Tran model, to simulate our flames filled with a mixture of methane and biofuels (F and THF).

2.3. Experimental - modelling comparison

In this part, we discuss about the comparison of our experimental results obtained in the CH₄/F/THF/O₂/N₂ flames, with the simulated ones by using two detailed kinetic schemes, Tran and Fenard with their associated thermodynamic and transport data.

To be more representative, the experimental temperature profile is introduced as input to the Cantera “BurnerFlame” modeling code for all calculations. Note that for methane and THF doped flame, the experimental temperature profiles have not been

modified or corrected before being introduced as input data, meaning that no modification has been introduced to take into account an eventual shift induced by microprobe perturbation. The experimental temperature profiles are obtained by using in situ NO-LIF thermometry (see the annex B). Because the experimental temperature measurements have not been performed in furan flames at the time of this manuscript is written, we used the ones obtained in the THFM1.2 flame. The choice of the THFM1.2 temperature profile has been made by comparing the simulated temperature profiles of all flames performed in adiabatic conditions. This comparison shows that the THFM1.2 adiabatic temperature profile is the closer profile to the ones calculated for furan doped flames in same conditions.

In the next section the comparison between the experimental and simulated profiles is presented. Firstly, the comparison experiments/modelling is presented for the reactants, main stable species, C₂-C₃ hydrocarbons and oxygenated species in methane flames. We used these flames to test the ability to predict the methane oxidation of these two kinetic schemes. Then, the comparison for F and THF flames are presented through the reactants, main products and C₂ intermediates in the two equivalence ratio conditions. Finally, the kinetic behaviors of the two biofuels are compared by showing the C₃-C₄ hydrocarbons and main oxygenated species formed in both biofuels combustion at a selected equivalence ratio condition. All the experimental and simulated results are presented in the annex C.

However, it must be noted that certain intermediate species were measured during this study but were not taken into consideration by the different models tested. Table IV.1 presents all the chemical species measured in CH₄/F/THF/O₂/N₂ flames and involved or not in the two kinetic schemes.

Name	Formula	Calibration	Experiments			Modelling	
			M	FM	THFM	Fenard	Tran
Carbon Monoxide	CO	CSM	✓	✓	✓	✓	✓
Methane	CH ₄	FGM	✓	✓	✓	✓	✓
Carbon Dioxide	CO ₂	CSM	✓	✓	✓	✓	✓
Ethylene	C ₂ H ₄	CSM	✓	✓	✓	✓	✓
Acetylene	C ₂ H ₂	CSM	✓	✓	✓	✓	✓
Ethane	C ₂ H ₆	CSM	✓	✓	✓	✓	✓
Formaldehyde	CH ₂ O	LSIS	✓	✓	✓	✓	✓
Propene	C ₃ H ₆	CSM	✓	✓	✓	✓	✓
Propane	C ₃ H ₈	CSM	✓	✓	✓	✓	✓
Allene	aC ₃ H ₄	CSM		✓	✓	✓	✓
Propyne	pC ₃ H ₄	CSM		✓	✓	✓	✓
Dimethyl ether	C ₂ H ₆ O	PP	✓	✓	✓	✓	✓
Methyl alcohol	CH ₃ OH	PP	✓	✓	✓	✓	✓
Acetaldehyde	C ₂ H ₄ O	PP	✓	✓	✓	✓	✓
Isobutane	iC ₄ H ₁₀	CSM		✓	✓	✓	✓
Isobutene	iC ₄ H ₈	CSM		✓	✓	✓	✓
1-butene	1-C ₄ H ₈	CSM		✓	✓	✓	✓
1.3-butadiene	1.3-C ₄ H ₆	CSM		✓	✓	✓	✓
1.2 butadiene	1.2-C ₄ H ₆	CSM		✓		✓	✓
Trans-2-butene	2-C ₄ H ₈	CSM		✓		✓	✓
Cis-2-butene	2-C ₄ H ₈	CSM		✓	✓	✓	✓
Butane	C ₄ H ₁₀	ECN			✓	✓	✓
Methoxyethane	C ₃ H ₈ O	ECN			✓		
2-butyne	2-C ₄ H ₆	ECN		✓		✓	✓
Propylene Oxide	C ₃ H ₆ O	PP			✓	✓	
Acrolein	C ₃ H ₄ O	PP		✓	✓	✓	✓
Furan	C ₄ H ₄ O	FGM		✓	✓	✓	✓
Propanal	C ₃ H ₆ O	PP			✓	✓	✓
Acetone	C ₃ H ₆ O	PP			✓	✓	✓
Iso-pentane	i-C ₅ H ₁₂	ECN		✓			
1-butene-3-methyl	C ₅ H ₁₀	ECN		✓	✓		
1-butene-2-methyl	C ₅ H ₁₀	ECN		✓			
Ethyl-Cyclopropane	C ₅ H ₁₀	ECN			✓		
1.3-cyclopentadiene	C ₅ H ₆	ECN		✓		✓	✓
2-pentene	C ₅ H ₁₀	CSM		✓	✓		✓
Allylic alcohol	C ₃ H ₆ O	PP		✓	✓		
2,3 -dihydrofuran	C ₄ H ₆ O	PP			✓	✓	✓
Trans-1.3-pentadiene	C ₅ H ₈	ECN		✓			✓
Cis-1.3-pentadiene	C ₅ H ₈	ECN		✓			✓
Isobutenal	C ₄ H ₆ O	PP		✓			
1-propanol	C ₃ H ₈ O	ECN			✓		
Isobutanal	C ₃ H ₈ O	PP		✓	✓		
2.5-dihydrofuran	C ₄ H ₆ O	PP			✓	✓	✓
Methyl vinyl ketone	C ₄ H ₆ O	PP		✓		✓	✓
Tetrahydrofuran	C ₄ H ₈ O	FGM			✓	✓	✓

Furan 2 methyl	C ₅ H ₆ O	PP		✓			✓
Butanal	C ₄ H ₈ O	ECN		✓		✓	✓
Furan-3-methyl	C ₅ H ₆ O	PP		✓			
Cyclopropanacarboxaldehyde	C ₄ H ₆ O	ECN			✓	✓	✓
2-butenal	C ₄ H ₆ O	PP		✓	✓	✓	✓
1-hexene	C ₆ H ₁₂	PP			✓		✓
Hexane	C ₆ H ₁₄	PP			✓		
Benzene	C ₆ H ₆	CSM	✓			✓	✓
2-methyl-tetrahydrofran	C ₅ H ₁₀ O	PP			✓		
3-methyl-tetrahydrofran	C ₅ H ₁₀ O	PP			✓		
4-Pentenal	C ₅ H ₈ O	ECN			✓		✓
Pentanal	C ₅ H ₁₀ O	PP			✓		
1.3-dioxene	C ₄ H ₆ O ₂	ECN			✓	✓	
2-pentenale	C ₅ H ₈ O	ECN		✓			
Butanedial	C ₄ H ₆ O ₂	ECN		✓	✓	✓	
Hydrogen (TCD)	H ₂	CSM	✓	✓	✓	✓	✓
Oxygen (TCD)	O ₂	CSM	✓	✓	✓	✓	✓
Nitrogen (TCD)	N ₂	CSM	✓	✓	✓	✓	✓

Table IV.1 Summary of all the species involved in the experiments and detailed chemical mechanisms. (Calibration: CSM=Commercial Standard Mixture, FGM= Fresh Gas Mixture, LSIS=Liquid Solution Internal Standard, PP= Partial Pressure, ECN= Equivalent Carbon Number)

2.3.1. Study of the methane flames

The Tran and Fenard mechanisms previously presented have been firstly used to simulate the low-pressure premixed methane/air flames. This first experiments/modelling comparison aims to evaluate the ability of these two kinetic schemes to correctly predict methane oxidation in stoichiometric and slightly rich conditions. In all the following figures, symbols are used for experiments and lines represents modelling, blue for Tran mechanism and red for Fenard model.

2.3.1.1. Fuel and major species

The comparisons of the experimental and modeled profiles obtained for major species in the case of M1.0 and M1.2 methane flames are presented in Fig. IV.7 and Fig. IV.8.

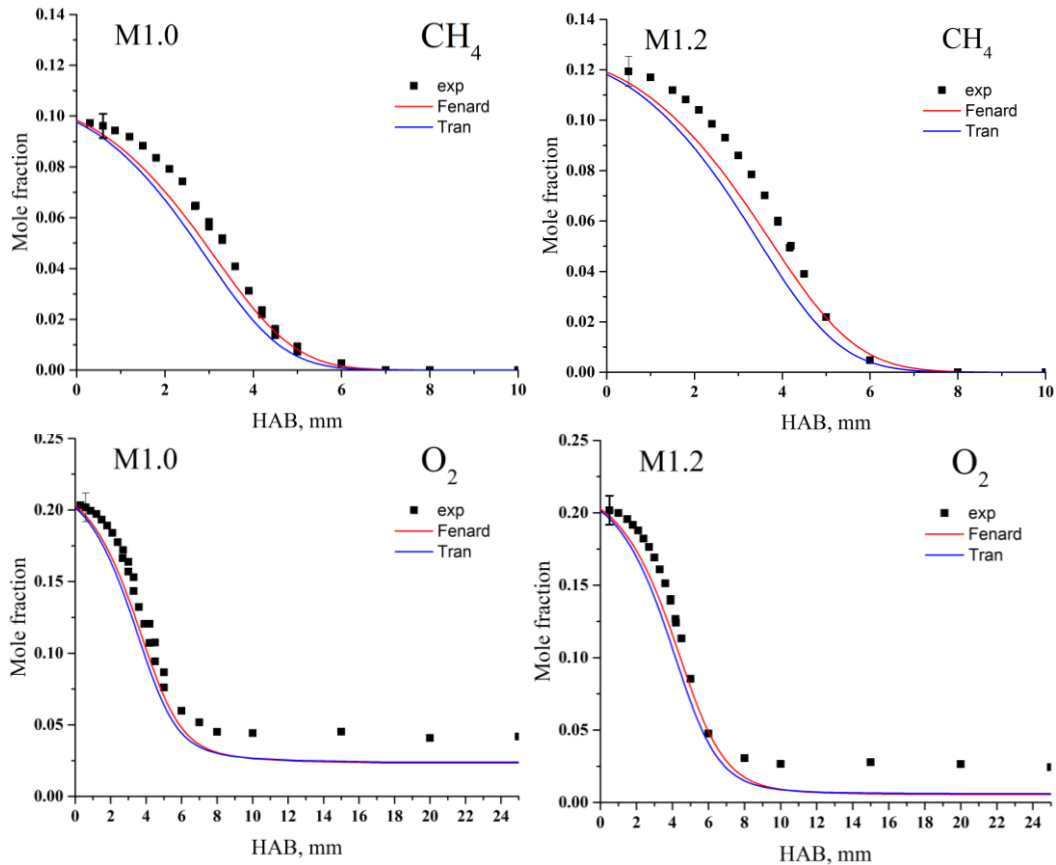


Fig.IV 7: Comparison between experimental and modelled mole fraction profiles for O_2 and CH_4 in M1.0 and M1.2 flames.

The consumption of methane and oxygen is well predicted by both models and for both equivalence ratios. Nevertheless, a disagreement is observed in the burnt gases for O_2 . Indeed, modelling systematically underpredicts the residual mole fraction of this compound in both methane flames.

Carbon monoxide (CO) and dioxide (CO_2) are well predicted by both models. However, models tend to slightly overestimate by 10% the CO mole fraction in burnt gases. While for CO_2 , there is a good agreement especially in rich condition for both models.

In the case of water (H_2O) and hydrogen (H_2), the experiment-modeling agreement is quite satisfactory even if the simulated profiles are shifted with respect to the experimental profiles.

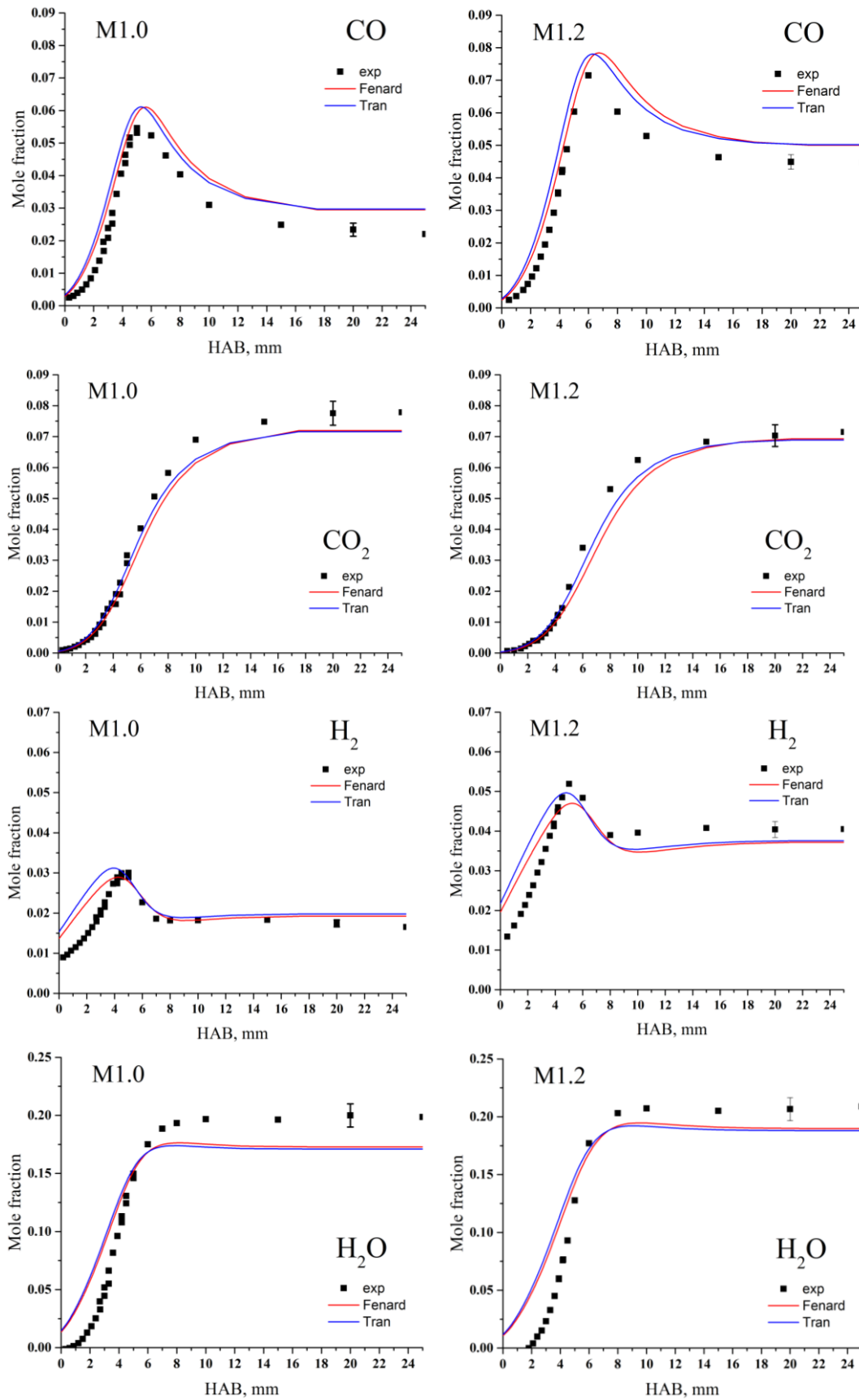


Fig.IV 8: Comparison between experimental and modeled mole fraction profiles for major species in M1.0 and M1.2 flames.

2.3.1.2. Intermediate species C₂-C₃

In Fig.IV.9 are presented the results for C₂ hydrocarbons: acetylene (C₂H₂), ethylene (C₂H₄) and ethane (C₂H₆). Among these species, ethane is the most abundant C₂ species and its experimental maximum is 1.1×10^{-3} and 2.0×10^{-3} in stoichiometric and rich conditions respectively.

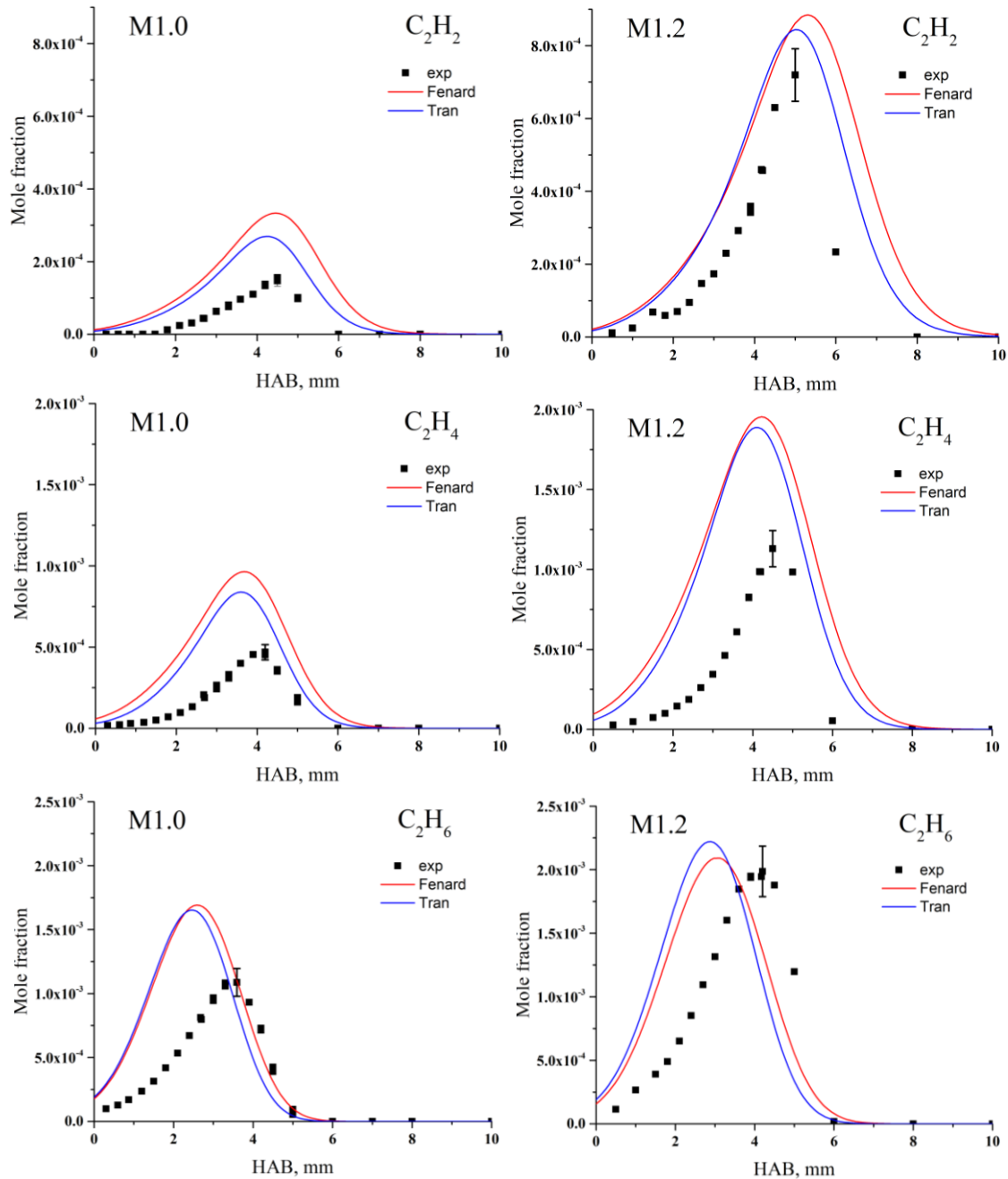


Fig.IV.9: Comparison between experimental and modeled mole fraction profiles for C₂ species in M1.0 and M1.2 flames.

Acetylene (C_2H_2) in stoichiometric flame is overestimated by about 30%; a better agreement is found in rich condition. Ethylene (C_2H_4) is overestimated at both equivalence ratio conditions by nearly 40%. In the case of ethane (C_2H_6), the simulated profiles are shifted back with respect to the experimental ones in both conditions; nevertheless, the absolute simulated value is quite similar to the experimental one in rich condition; while in stoichiometric condition, the simulated value is overestimated by 30%.

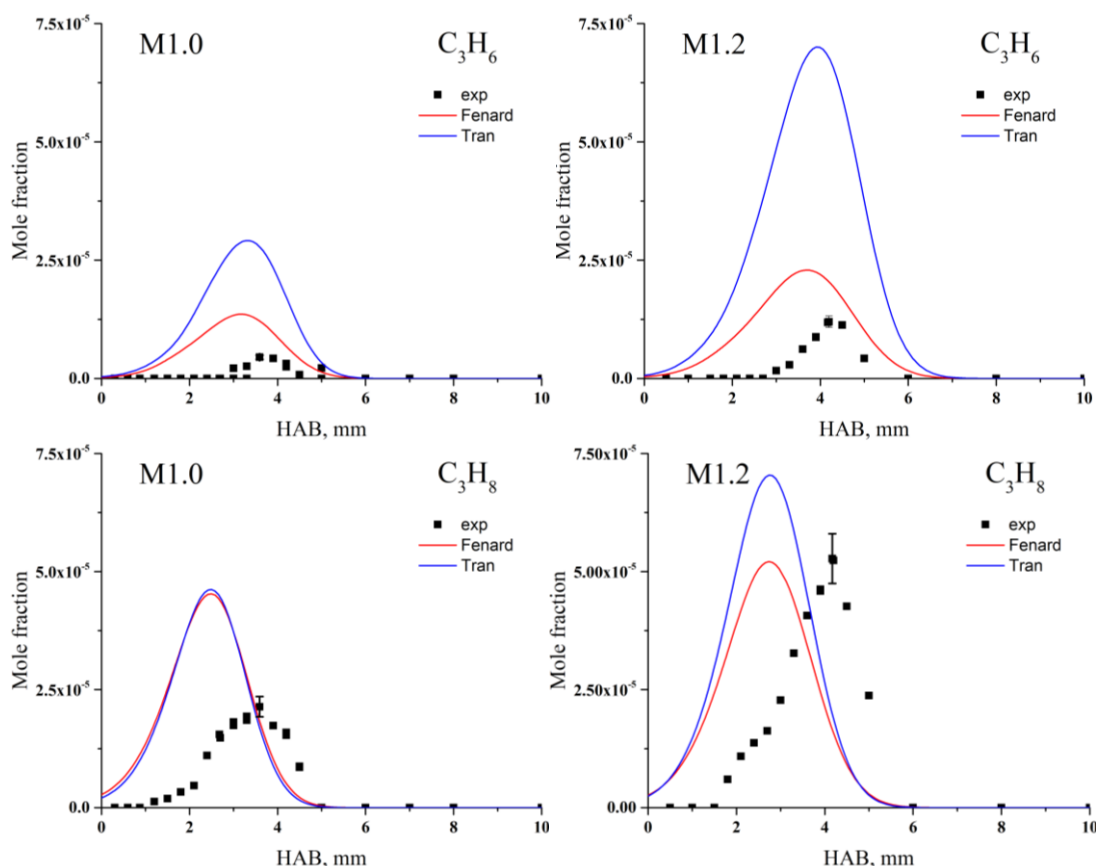


Fig.IV.10: Comparison between experimental and modeled mole fraction profiles for C_3 species in M1.0 and M1.2 flames.

By considering the C_3 hydrocarbons (Fig.IV.10), the only species detected in methane flames are propane (C_3H_8) and propene (C_3H_6). Propane presents the higher experimental mole fraction maximum with 2.2×10^{-5} and 5.3×10^{-5} in stoichiometric and rich flame respectively. Experimental and simulated results are not in good agreement. In stoichiometric flame, both mechanisms overestimate the propane mole fraction by about 40%; in rich flame, the calculated mole fraction is close to the experimental one. In both equivalence ratios the C_3H_8 peak mole fraction is slightly shifted. In the case

of propene, Fenard predictions are in better agreement with experiments; on the contrary Tran strongly overestimates the peak mole fraction by a factor up to 5.

2.3.1.3. Oxygenated intermediates

Formaldehyde (CH_2O), acetaldehyde (CH_3CHO), dimethyl ether (DME) and methanol (CH_3OH) are the only oxygenated species detected in the two methane/ O_2/N_2 flames. Formaldehyde is the most abundant oxygenated species with an experimental peak mole fraction of 7.9×10^{-4} in the stoichiometric flame, and 9.5×10^{-4} in the rich flame.

As shown in Fig.IV.11, both models seem to well predict the acetaldehyde mole fraction evolution, and a global good agreement is observed too for formaldehyde. In the case of CH_2O , the calculations overpredict the peak mole fraction in the two methane flames, the trend being more pronounced in the stoichiometric flame. Regarding methanol, the two kinetic schemes predict well its peak mole fraction, but a strong disagreement is found for the shape of the profile, the modeled ones being very closer to the burner by comparing with the experimental ones. A nearly same conclusion can be made for DME; moreover, the Fenard model overestimates the peak mole fraction by a factor of 2, while Tran presents a disagreement of only 30%. The increase of equivalence ratio does not seem to affect the oxygenated species except for acetaldehyde, species for which we can observe a slight increase in rich condition.

Fenard and Tran models predict quite well the mole fraction profile of the species in the methane flames, even if they have not been developed for this purpose. Results are in good agreement also with the increase of equivalence ratio. Therefore, we can continue the study the experiments/modelling comparison by focusing on F and THF doped methane flames.

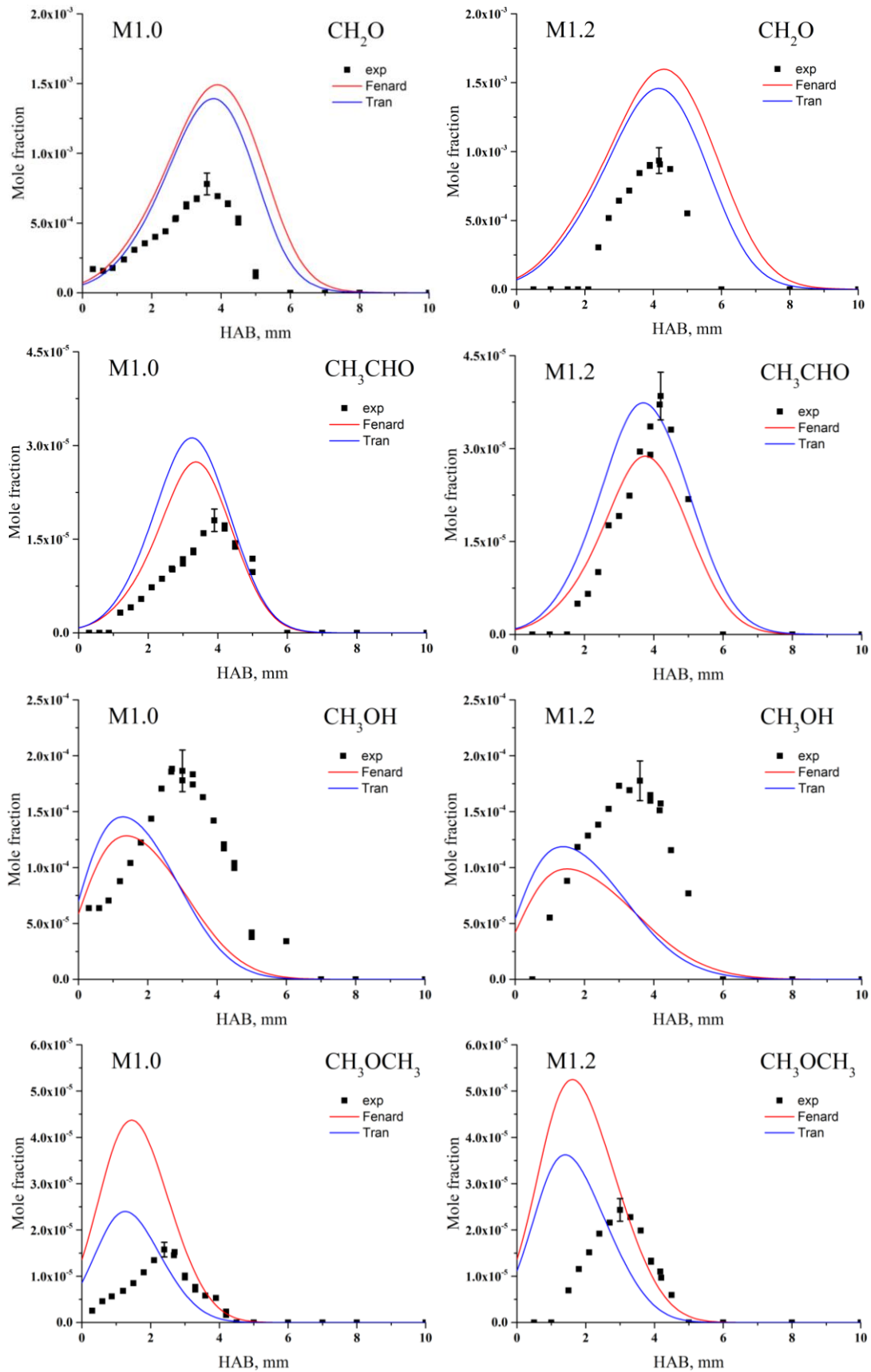


Fig.IV.11: Comparison between experimental and modelled mole fraction profiles for oxygenated intermediates in M1.0 and M1.2 flames.

2.3.2. Study of the furan flames

The following sections present the comparison of experimental and simulated mole fraction profiles of the main stable species up to C₂ hydrocarbons for the two 50%CH₄/50%Furan/O₂/N₂ premixed flames in stoichiometric and rich condition ($\phi=1.2$), FM1.0 and FM1.2, respectively.

C₃-C₄ species and the oxygenated intermediates will be presented in the section 2.3.4 and compared with the same species obtained in THF flames. Indeed, this comparison should allow to highlight the main differences involved during the oxidation of these two biofuels.

2.3.2.1. Fuel and major species

The comparison of the experimental and modeled profiles obtained in the case of methane flames seeded with furan (FM1.0 and FM1.2) are presented in Fig. IV.12 and Fig. IV.13.

Fig.IV.12 shows the reactant profiles, methane (CH₄), furan (C₄H₄O) and O₂. The first observation we can make is that the simulated profiles are shifted with respect to the experimental profiles. This effect is probably due to the preliminary temperature profile used for the simulation (see paragraph 2.3). We note the same trend for CH₄ even if the phenomenon is less pronounced. A good agreement is found for O₂ with the same behavior in the burnt gases as the one observed in CH₄/O₂/N₂ flames.

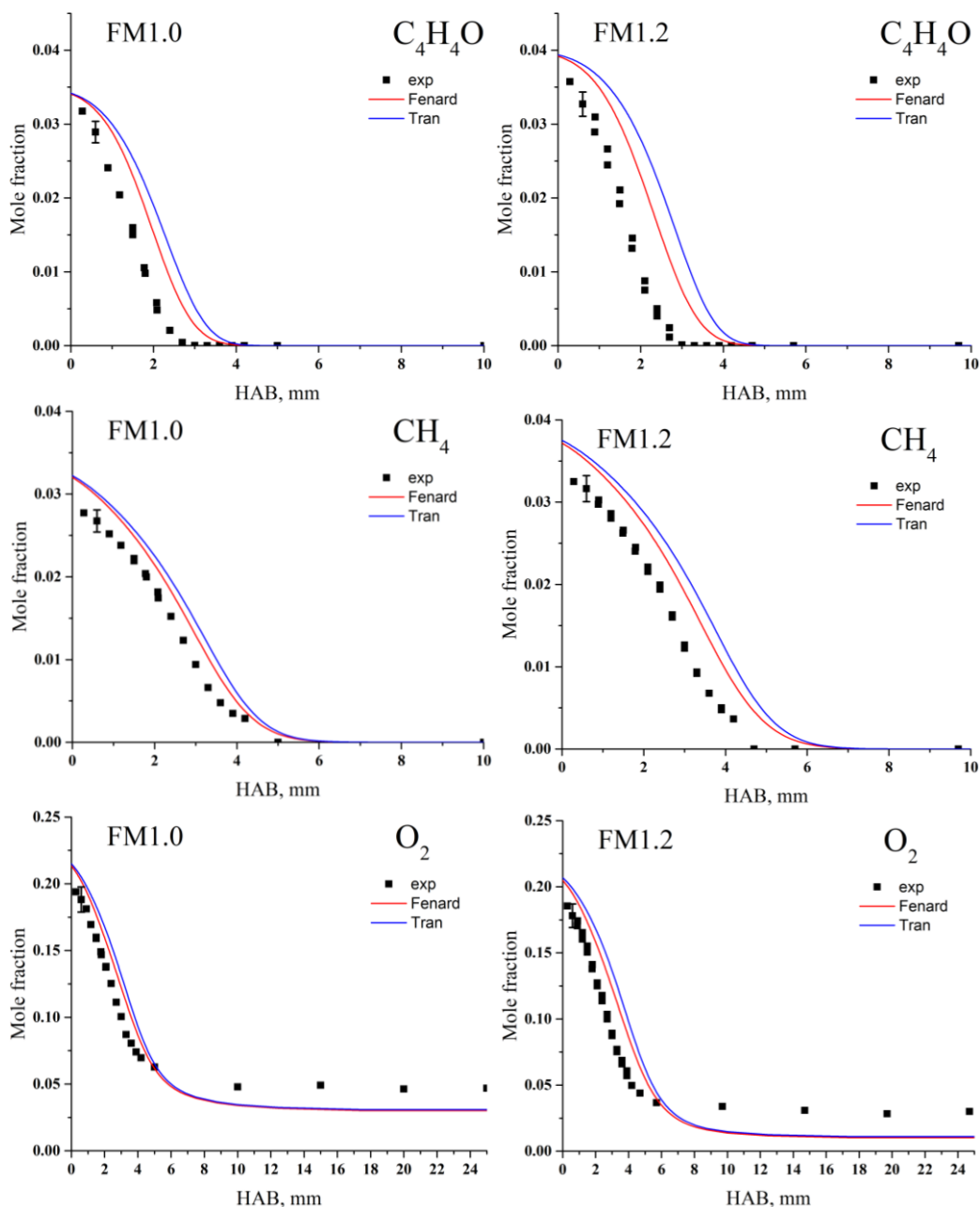


Fig.IV.12: Comparison between experimental and modelled mole fraction profiles for F, CH₄ and O₂ in FM1.0 and FM1.2 flames.

Fig.IV.13 presents the comparison experiment/modelling for the major stable species. Globally both models are in good agreement with the experimental profiles and describe well the impact of the increase of equivalence ratio. CO and CO₂ species are well predicted by the two models, except that the simulated profiles are slightly shifted towards burnt gases. In case of molecular hydrogen, both models underestimate the burnt gases mole fraction in rich condition by about 20%. H₂O simulated profiles are in good agreement with the experimental ones.

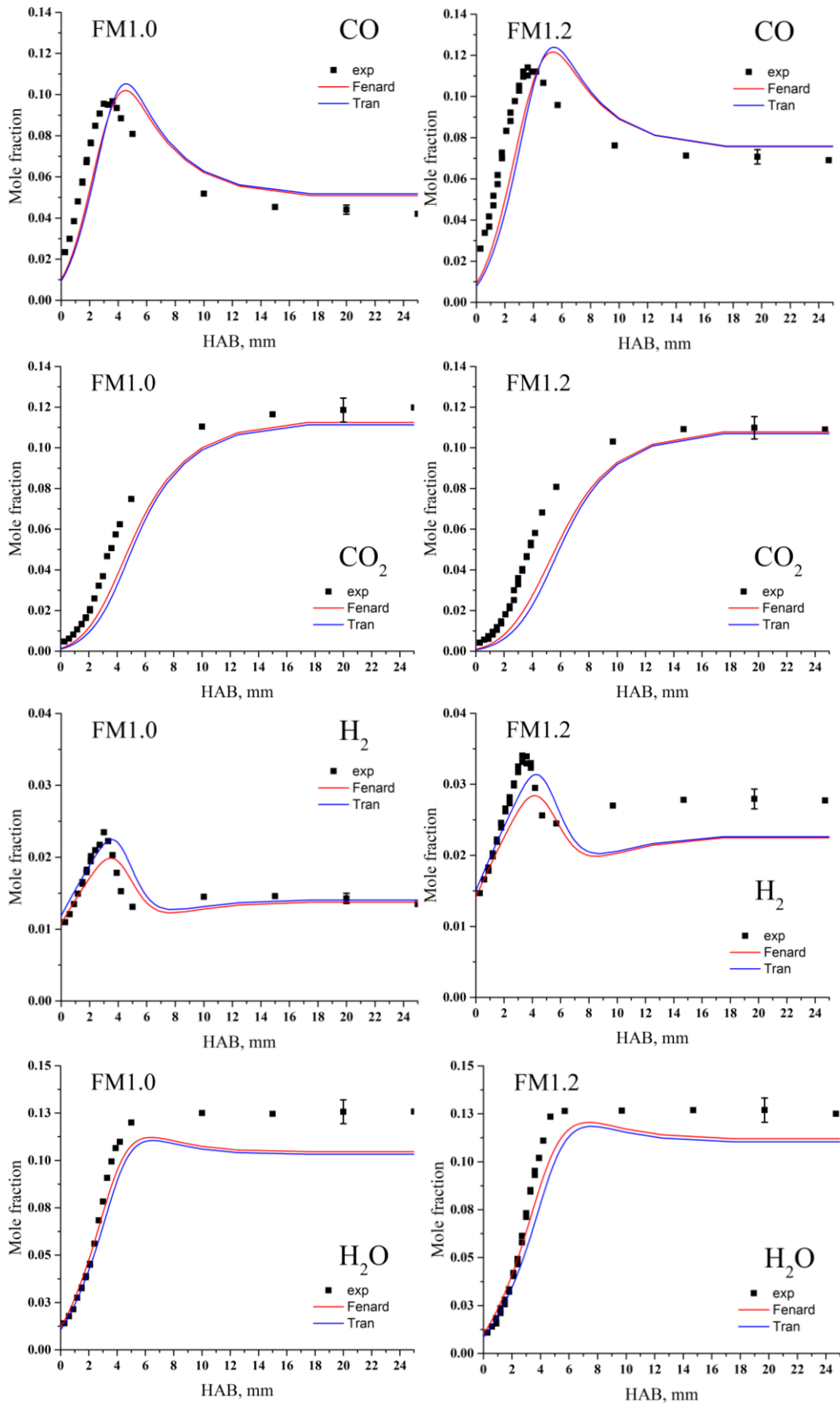


Fig.IV.13: Comparison between experimental and modelled mole fraction profiles for major species in FM1.0 and FM1.2 flames.

2.3.2.2. C₂ intermediates

Fig.IV.14 shows the results for experimental and simulated mole fraction profiles of C₂ hydrocarbons: acetylene (C₂H₂), ethylene (C₂H₄) and ethane (C₂H₆). These species are affected by the equivalence ratio variation and are some of the major species produced during the oxidation of F and THF. Among them, the most abundant species is clearly C₂H₂ with an experimental peak mole fraction of 6.3×10^{-3} in stoichiometric condition, and 1.0×10^{-2} in rich condition. This species is directly produced from main fuel decomposition route [62].

In the case of methane, both Tran and Fenard mechanisms predict in comparable way all the C₂ mole fraction profiles. In the CH₄/F/O₂/N₂ flames, the trend of both predictions is different. Globally Fenard mechanism well reproduces the production of C₂H₂ and C₂H₆ in stoichiometric and rich conditions. However, we can observe that the consumption of acetylene is shifted towards the burnt gases in comparison with the experimental profiles. Concerning C₂H₂ and C₂H₆, Tran mechanism underestimates their peak mole fraction by a factor up to 3 in both equivalence ratio conditions. Concerning ethylene (C₂H₄), Tran and Fenard underestimate the experimental profiles in stoichiometric and rich conditions by a factor of 1.5 and 3 respectively. In the case of these species also, the simulated peak mole fraction is shifted towards the burnt gases with respect to the experimental profiles. It is important to remind that the Fenard mechanism was specifically developed for THF oxidation.

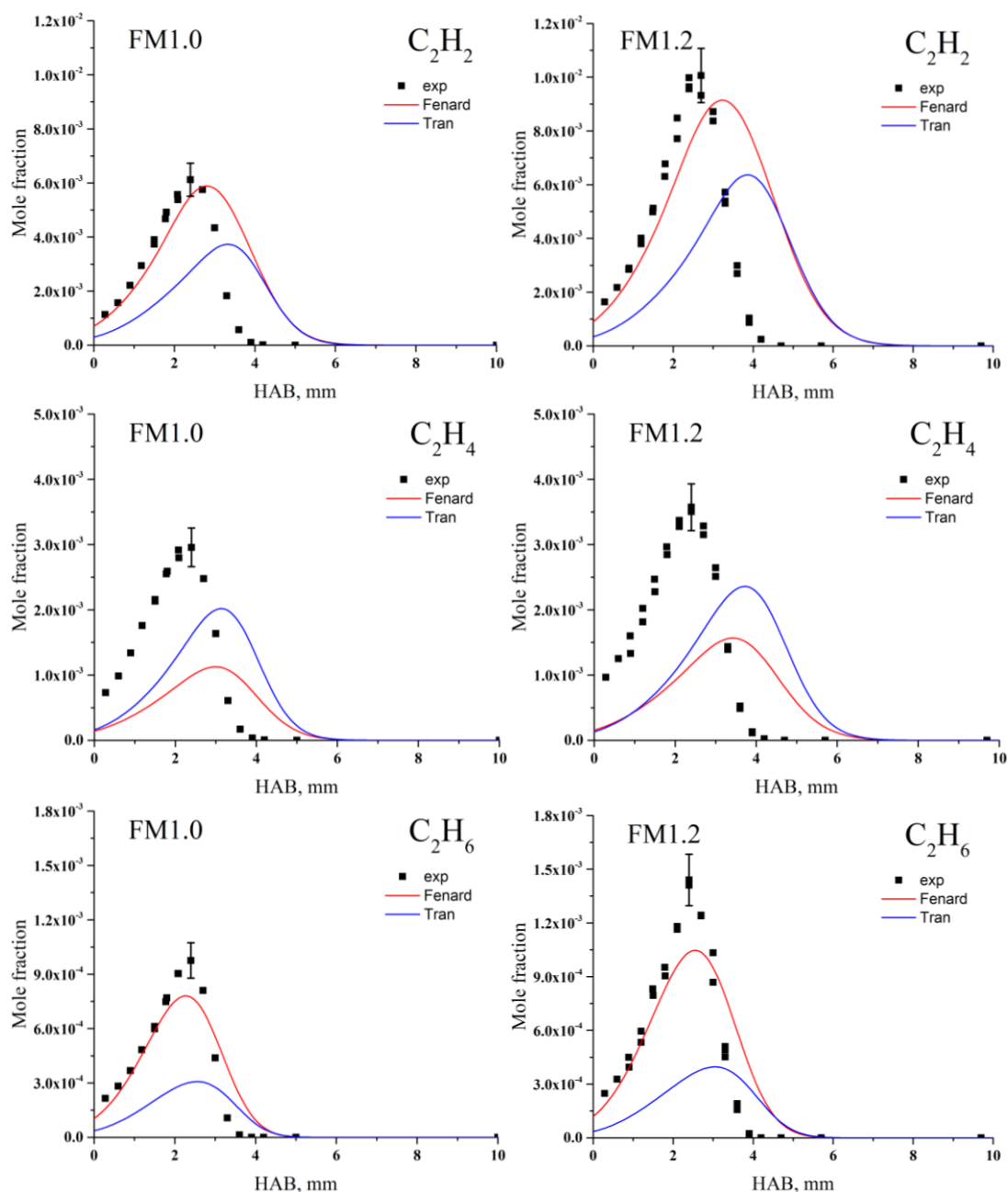


Fig.IV.14: Comparison between experimental and modelled mole fraction profiles for C_2 intermediates in FM1.0 and FM1.2 flames.

2.3.3. Study of the THF flames

In this section, we present the comparison between experimental and simulated profiles using the Tran and Fenard mechanisms for the 50%CH₄/50%THF/O₂/N₂ flames in stoichiometric and rich conditions, named THFM1.0 and THFM1.2 respectively.

2.3.3.1. Fuel and major species

Fig. IV.15 and Fig.IV.16 show the results for reactants and major species measured during the oxidation of methane/THF flames.

Both mechanisms correctly predict the mole fraction profiles of CH₄, THF (C₄H₈O) and O₂ in both equivalence ratio conditions. As previously observed for methane and methane/furan flames, the models underestimate the O₂ mole fraction in the burnt gases. This phenomenon was also observed in THF flames by Tran et al.[101].

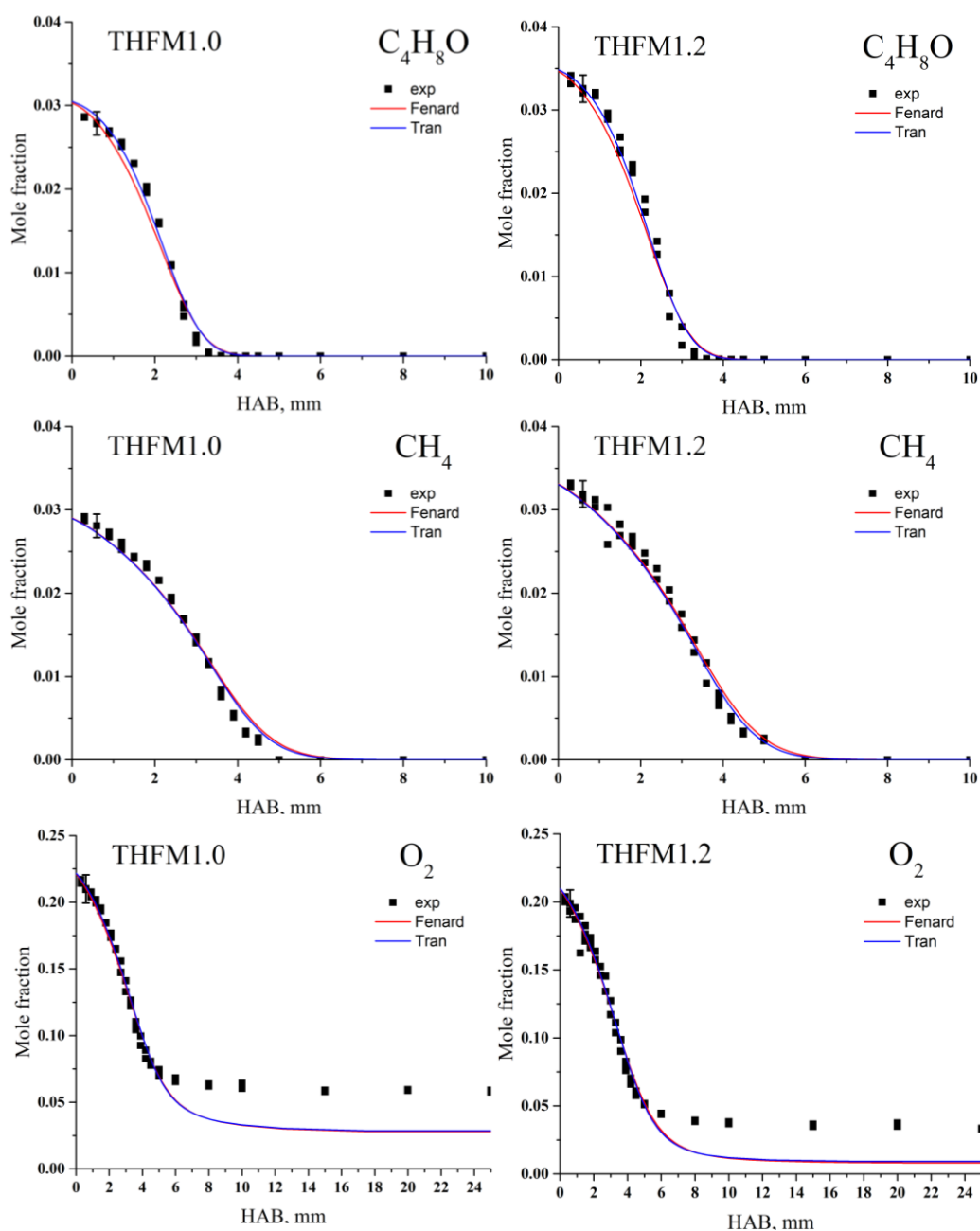


Fig.IV.15: Comparison between experimental and modeled mole fraction profiles for THF, CH₄ and O₂ in THFM1.0 and THFM1.2 flames.

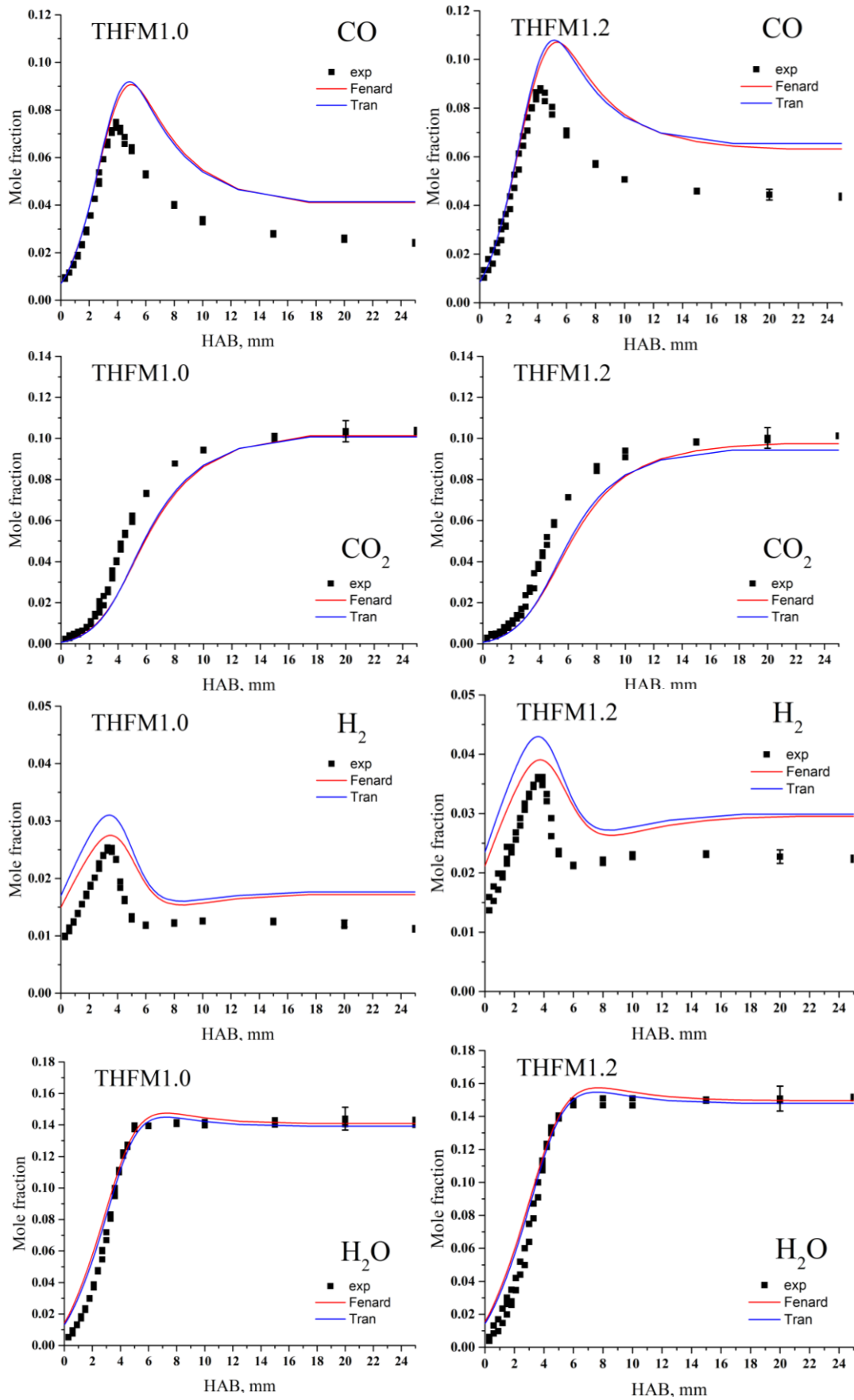


Fig.IV.16: Comparison between experimental and modelled mole fraction profiles for major species in THFM1.0 and THFM1.2 flames.

Regarding stable species such as CO, CO₂, H₂ and H₂O, we can observe that both mechanisms predict in the same way the experimental profiles. CO₂ and H₂O simulated profiles are in good agreement with the experimental ones in both flames. The calculated profiles for CO and H₂ are overestimated by about 10% and 25% respectively.

2.3.3.2. C₂ Intermediates

The comparison between experimental and predicted profiles for C₂ intermediate species is presented in Fig.IV.17. Among these species, the ethylene (C₂H₄) formation is strongly enhanced in the presence of THF compared to methane and methane/furan flames. In our flames the peak mole fraction values reaches 8.2×10^{-3} in THFM1.0 and 9.8×10^{-3} in THFM1.2 flames.

Globally for all the C₂ intermediate species, we can observe a good agreement between the simulated mole fraction profiles and the experimental ones in both conditions of equivalence ratio. However, Fenard mechanism slightly better predicts the C₂ species in both conditions with respect to Tran mechanism.

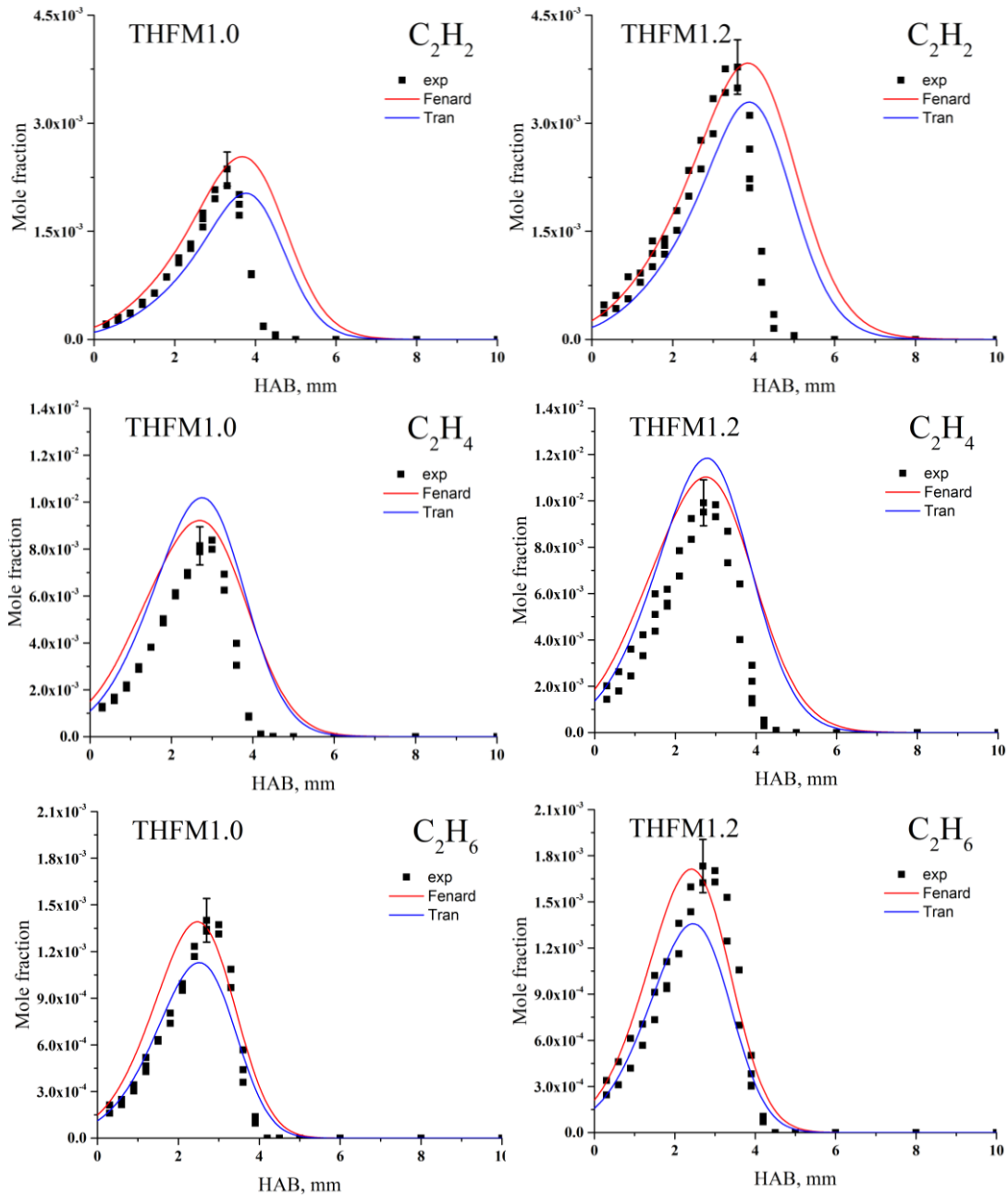


Fig.IV.17: Comparison between experimental and modelled mole fraction profiles for C_2 species in THFM1.0 and THFM1.2 flames.

2.3.4. Comparison F-THF: C_3 - C_4 and oxygenated intermediates

To evaluate the main differences between the flames methane/F and methane/THF, we have compared the results of simulated and experimental mole fraction profiles of particular species produced during the oxidation of both biofuels. We present here only the results for stoichiometric flames (FM1.0 and THFM1.0), but the same

behavior has been found in rich condition. For more details, all species profiles are presented in annex C.

2.3.4.1. C₃-C₄ hydrocarbon intermediates

Fig.IV.18 and Fig.IV.19 present the experiment/modelling comparison for C₃ and some selected C₄ hydrocarbon species respectively. Globally, Fenard mechanism predictions are in better agreement with the experiment profiles with respect to Tran mechanism. By considering the sum of the mole fractions of C₃ species in F and THF flames, we can notice that propene is the most abundant species among the C₃ hydrocarbons, with a contribution to the total amount of C₃ of 65 % in FM1.0 flame and 79 % in THFM1.0 flame. The higher amount of propene among C₃ intermediates in methane/furan flames is not consistent with the observations from Liu et al [62] in furan flames, where they find propyne as the most abundant C₃. An explanation could be that a higher concentration of radicals may be produced from methane oxidation and then may promote the recombination reactions allowing propene formation. About propyne and allene, we can observe that the ratio between the two isomers C₃H₄ is quite similar in both flames, respectively 3.0 and 2.7 in FM1.0 and THFM1.0 flames.

We can observe that both mechanisms underestimate propane (C₃H₈) peak mole fraction in FM1.0 flame by a factor of 7 for Tran, and 1.7 for Fenard. In THFM1.0 flame the underestimation is about a factor of 2 and 3 respectively for Tran and Fenard mechanism.

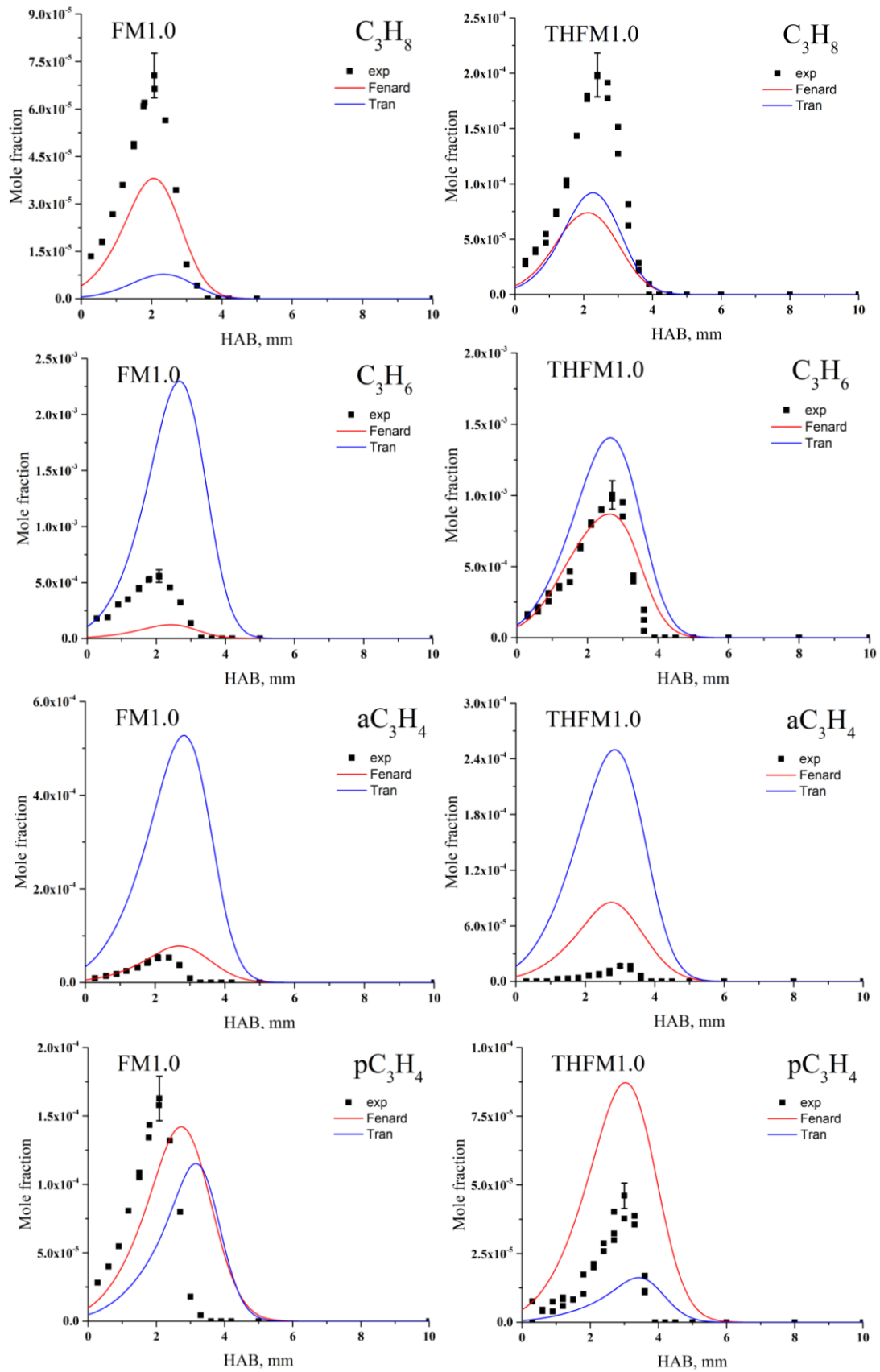


Fig.IV.18: Comparison between experimental and modelled mole fraction profiles for C_3 intermediates in FM1.0 and THFM1.0 flames.

In the case of propene (C_3H_6), the mole fraction profile is well predicted by Fenard mechanism during THF oxidation, but is underestimated by a factor of 5 in F oxidation. On the other hand, Tran mechanism overestimates the C_3H_6 peak mole fraction in methane flames seeded with F and THF flames by a factor of about 4.6 and 1.5 respectively. The C_3H_4 isomers (allene and propyne) are predicted in different ways by both mechanisms. By using Tran model, allene is overestimated by a factor of near 16 and 25 in F and THF seeded flames respectively. In contrast, the predictions from Fenard models are closer to experimental ones in both flames. Propyne simulated profile by Fenard mechanism in methane/furan flames is closer to experimental data than with Tran mechanism, for which we observe a shift of the peak mole fraction toward the burnt gases. In the methane/THF flames, the propyne peak mole fraction is overestimated by using Fenard mechanism and underestimated with Tran mechanism by a factor 2 in both cases.

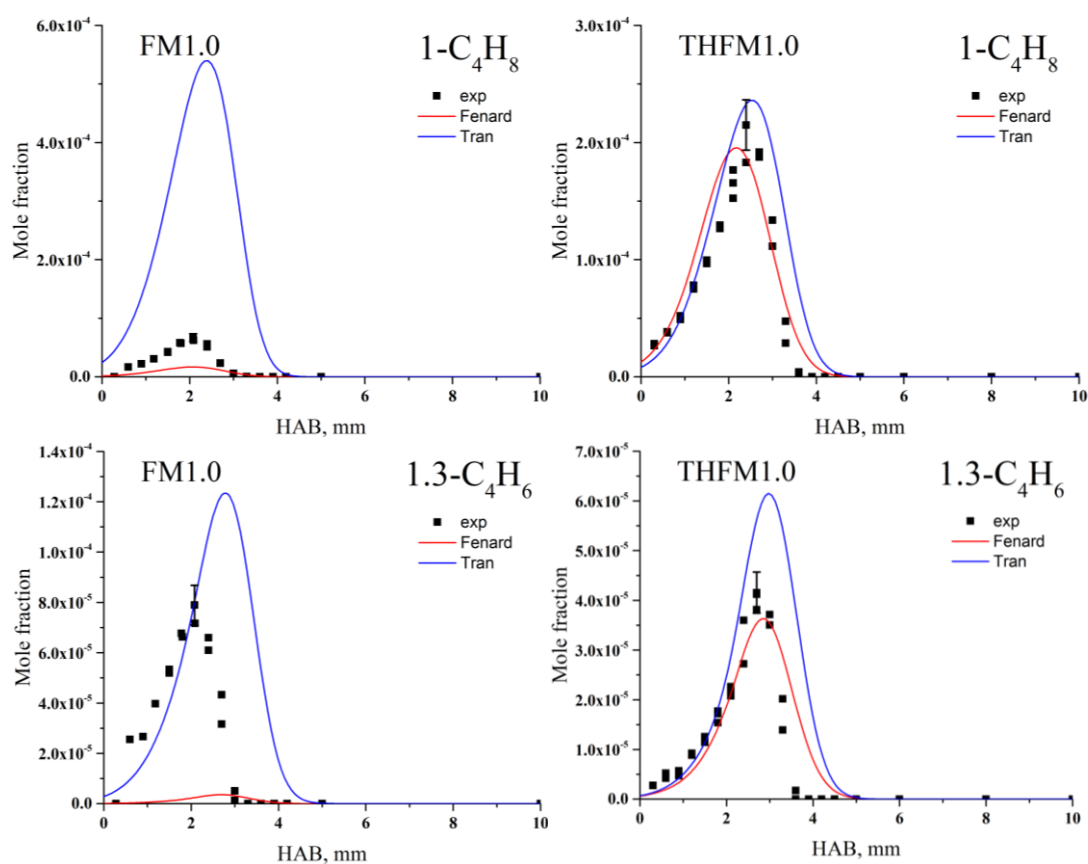


Fig.IV.19: Comparison between experimental and modelled mole fraction profiles for C_4 intermediates in FM1.0 and THFM1.0 flames.

Regarding the C_4 intermediates (1-butene – $1-C_4H_8$, 1,3-butadiene- $1,3-C_4H_6$), the most abundant species is the 1,3 butadiene in methane/F flames with a peak mole fraction of

8.1×10^{-5} , and 1-butene in the case of methane/THF with 2.1×10^{-4} . We can observe that the simulated profiles are not in good agreement with experimental data except for 1-butene and 1,3-butadiene in methane/THF flame. In furan flames, 1-butene and 1,3-butadiene are overestimated by Tran's mechanism by a factor of 8 and 1.5 respectively, whereas the Fenard model strongly underpredicts these species by a factor 2 and a factor 16, respectively.

2.3.4.2. Oxygenated species

In F and THF flames we detected an elevated amount of oxygenated species in particular aldehydes and ethers, but also ketones and alcohols. Some of these species are specific of the oxidation of F or THF, but others are produced during the oxidation of both biofuels such as acetaldehyde, propanal, isobutanal, dimethyl ether, acetone or allylic alcohol.

The Fig.IV.20 shows the results for some selected oxygenated species, in particular aldehydes such as formaldehyde (CH_2O), acetaldehyde (CH_3CHO), acrolein ($\text{C}_3\text{H}_4\text{O}$) and 2-butenal ($\text{C}_4\text{H}_6\text{O}$), which we can find in both biofuels flames.

In $\text{CH}_4/\text{F}/\text{O}_2/\text{N}_2$ flames, acetaldehyde and formaldehyde are the most abundant oxygenated compounds with a peak mole fraction of 2.1×10^{-3} at 1.6 mm and 2.2×10^{-3} at 2 mm respectively. In the case of methane/THF flames, the most abundant oxygenated species is formaldehyde and, in this flame, the $\text{CH}_2\text{O}/\text{CH}_3\text{CHO}$ ratio is around 8, similar to the value reported by Tran et al. [101].

Results show that in the case of formaldehyde (CH_2O), both mechanisms are in good agreement with experimental data. This small aldehyde is known to be an important intermediate species involved during THF oxidation.

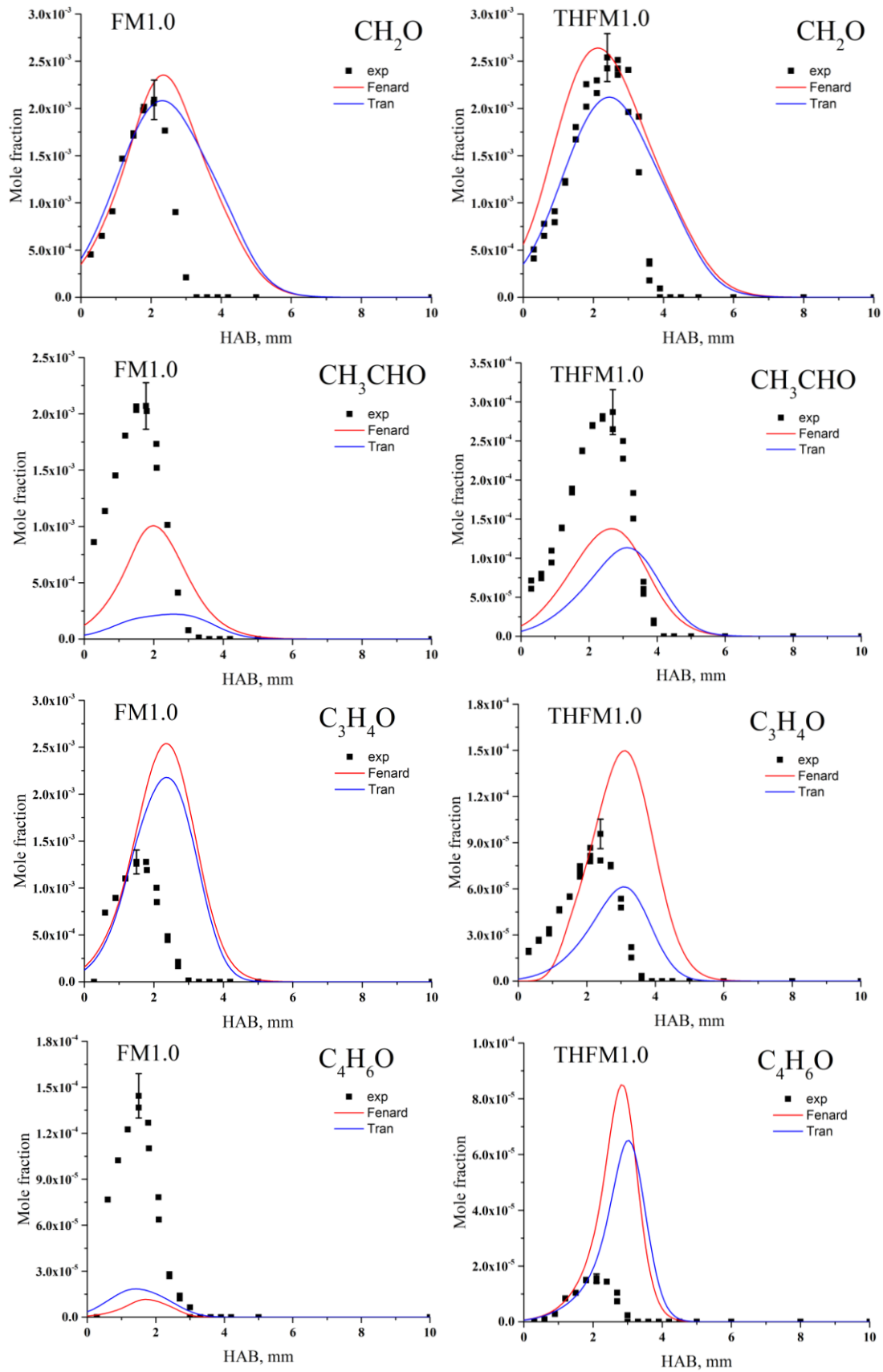


Fig.IV.20: Comparison between experimental and modelled mole fraction profiles for selected oxygenated species in FM1.0 and THFM1.0 flames.

For acetaldehyde (CH_3CHO) which is enhanced during F oxidation, the peak mole fraction in methane/F flames is underestimated with Tran model by a factor of near 20, and with Fenard mechanism by a factor of 2. In methane/THF flame, this underestimation is nearly the same value for both models and is around a factor of 2. Note that in previous work on furanic fuels oxidation ([5], [62], [70], [82], and [190]), the high formation of acetaldehyde during F combustion has been experimentally noticed. The inability of the kinetic scheme to reproduce this behavior is probably due to a missing reaction pathway in the furan sub-mechanism which can lead to acetaldehyde production.

Acrolein ($\text{C}_3\text{H}_4\text{O}$) is another important oxygenated intermediate, especially during F oxidation. In fact, its formation is enhanced in F flames with respect to THF ones. In the case of methane/furan flame, both models overpredict the peak mole fraction of acrolein by about a factor of 1.7. In methane/THF flame, Fenard mechanism overestimates the experimental data by a factor of 1.5. On the other hand, Tran model underestimates the acrolein peak mole fraction by a factor of 1.6.

2-butenal is strongly underestimated in methane/furan flame by both models; in methane/THF flame this oxygenated intermediate is over estimated by a factor of near 4 by both mechanisms.

2.4. Summary of the comparison experiments/modelling results

The six $\text{CH}_4/\text{F}/\text{THF}/\text{O}_2/\text{N}_2$ flames experimentally analyzed were modelled using two different kinetic mechanisms developed for the oxidation of F and THF, Tran (Tran et al [6]) and Fenard ([7]) respectively.

This work enables to test these two kinetic models available in the literature with experimental data acquired on the $\text{CH}_4/\text{F}/\text{THF}/\text{O}_2/\text{N}_2$ flames. The comparison of the modeling results usually leads to a satisfactory agreement with the experimental profiles measured in flames. Overall, the consumption of reactants and the formation of the products of combustion are correctly predicted by the different models. Concerning the hydrocarbon and oxygenated intermediates, divergences remain for some of these species. It is noticed that both mechanisms have been developed for pure fuels only.

From this comparison, the Fenard mechanism appears to better reproduce the experimental results for F and THF flames.

3. Conclusion

In this chapter the study of the furan (F) and tetrahydrofuran (THF) oxidation in CH₄/Furan/THF/O₂/N₂ premixed laminar flames stabilized in low pressure conditions is presented.

In the first part, complementing the previous chapter, the experimental procedure implemented to obtain the mole fraction results is detailed. In particular, a new method to calibrate formaldehyde is developed.

Sixty-five species were identified and quantified in the six examined flames. Among them, aldehydes (formaldehyde, acetaldehyde, acrolein, 2-butenal, propanal, cyclopropanecarboxaldehyde, ...) and PAH Precursors (acetylene, propene, propyne, allene, 1,3-butadiene) were some of the most important intermediate species. The chemical nature and the quantity of these pollutants are very sensitive to the fuel mixture.

Secondly, we present the two detailed kinetic mechanisms available in the literature dedicated to the oxidation of F and THF. The comparison of the modelling results carried out using the Cantera code usually leads to a satisfactory agreement with the experimental profiles measured in our flames. However, divergences remain for some hydrocarbon and oxygenated intermediates, which may have an influence for the prediction of prompt-NO.

In the Chapter V the ability of these models to predict the CH radical mole fraction profiles (key species for the prompt-NO mechanism) will be evaluated.

Chapter V: Determination of NO and CH profiles by laser diagnostics

Laser-induced fluorescence (LIF) is one of the most widely used laser spectroscopic techniques for probing minor species concentrations during combustion. It also allows the determination of flame temperature. The method is based on the measurement of the spontaneously emitted light from a molecule after its excitation to an excited state by absorption of the laser radiation. Usually, LIF is performed in the ultraviolet-visible spectral region to excite electronic transitions of the molecules of interest.

LIF enables to detect in situ at ppm and even sub-ppm levels the concentration of radicals, atoms and molecules in flames. Moreover, LIF offers high spatial resolution, providing reliable data in regions of steep gradients. Hence, LIF gives detailed information on the flame structure. In addition, LIF offers high selectivity, low background signal and a relatively simple experimental implementation in comparison with other laser spectroscopic techniques, such as CARS [198]. In addition to these advantages, and particularly over traditional probe methods, LIF is in principle non-intrusive. However, the interpretation of the LIF signal for measurement of temperature and species concentration is not straightforward and requires detailed knowledge of collisional processes. This often necessitates additional calibration methods for the quantitative measurements of the species concentrations.

In this chapter, the determination of NO and CH concentrations by laser induced fluorescence in CH₄/F/THF/O₂/N₂ low-pressure flames is presented.

1. General theory of linear LIF

Quantum mechanics describes the discrete energy levels occupied by molecules and atoms. The energy of a molecule can be decomposed as $E = hc[T(n) + G(v'') + F(J'')]$, where $T_e(n)$, $G(v'')$ and $F(J'')$ are respectively the electronic, vibrational and rotational energy (cm⁻¹) and depend on the rotational quantum number J'' and the vibrational quantum number v'' . Molecules may also have varying degrees

of electronic configurations. However, at temperatures typical of combustion processes, most of the molecules reside in the ground electronic state.

By measuring the relative population of the molecules in several of the vibrational-rotational states, it is possible to deduce the temperature of the system. On the other hand, by making an absolute measurement of the population in any given state, and knowing the temperature, it is possible to deduce the total species concentration [198].

Indeed, vibrational and rotational state populations are distributed according to Boltzmann statistics that is a function of the temperature.

The Boltzmann factor, i.e. the fraction of molecules for a given vibrational-rotational ground state which depends on the rotational quantum number J'' , on the vibrational quantum number v'' at the ground state and on the temperature T , is expressed by:

$$f_b = \frac{N^{n''v''J''}}{N_{tot}} = \frac{(2J'' + 1)}{Q_e Q_r(T) Q_v(T)} \exp\left(-\frac{hc((T_e(n) + G(v'') + F(J'')))}{k_b T}\right) \quad (5.1)$$

where Q_e , $Q_r(T)$ and $Q_v(T)$ are the partition functions respectively electronic, rotational and vibrational, c is the light speed, k_b is the Boltzmann constant, h Planck constant.

The population of the molecules on a given state J'', v'', n'' ($N^{n''v''J''}$) can be measured by Laser Induced Fluorescence (LIF). LIF consists to measure the spontaneous radiation emitted by the molecule after its excitation on an excited energy level (J', v', n') by absorption of laser radiation.

The energy collected by the excited species during the absorption process may be released by spontaneous emission (fluorescence), stimulated emission and collisional processes (electronic quenching and rotational and vibrational energy transfers such as RET and VET).

If the incident wavelength does not correspond to the absorbing transition of the molecule, the only process affecting the incident light is the scattering (Rayleigh scattering and Spontaneous Raman scattering).

A simplified two-energy level model is used to explain the LIF method. It consists first in exciting the selected species on a higher electronic state by absorption of laser

radiation. The frequency of this radiation is tuned on a specific rovibronic transition of the studied species, thus allowing the criterion of selectivity of the method. The most important processes involved in LIF are absorption, stimulated emission, spontaneous emission and collisional energy transfers. They can be evaluated by the rates of each process, as expressed in Fig V.1.

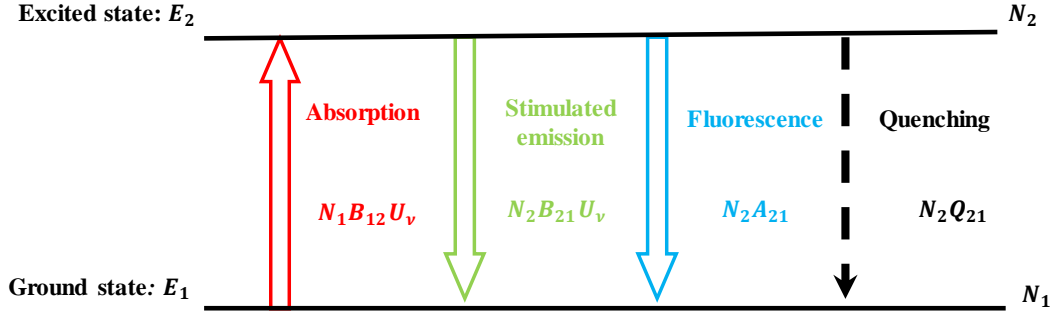


Fig. V.1: Simplified two-level model for laser induced fluorescence. N_1 and N_2 stand for the populations of respectively the ground and excited state.

The rates of the absorption and stimulated emission (s^{-1}) (b_{12} and b_{21}) are related to the Einstein coefficient of absorption and stimulated emission respectively, B ($J^{-1} s^{-1} m^{-3}$), through the relations:

$$b = B * U_\nu \quad (5.2)$$

$$g_1 B_{12} = g_2 B_{21} \quad (5.3)$$

where U_ν is the spectral laser energy density at the frequency ν ($J s m^{-3}$) and g_1 and g_2 are the degeneracy of 1 and 2 levels respectively.

The spontaneous emission, i.e. fluorescence, corresponds to the radiation emitted spontaneously by the excited molecules during their radiative relaxation towards the lower energy levels. The probability of spontaneous emission is represented by the Einstein emission coefficient A_{21} (s^{-1}).

The transfer of energy to the ground state by collision with other collision partners present in the medium (electronic quenching, Q (s^{-1})) is a non-radiative de-excitation phenomenon.

The stimulated emission represents the process of relaxation of the excited molecules towards the fundamental level simultaneously with the absorption of the incident photons. This emission is coherent with the exciting laser beam and it occurs on the laser axis.

In addition to spontaneous and stimulated emissions and quenching, other processes may also occur from the excited state, i.e., photo-ionization (W_{ion} , s^{-1}) or pre-dissociation (P_k , s^{-1}). These two latter processes are not considered into the approach of the two-energy levels model.

The temporal variation of the population of the molecules of total concentration N , between the initial state (1) and the excited state (2) is given by the following equations:

$$\frac{dN_1}{dt} = \dot{N}_1 = -N_1 B_{12} U_\nu + N_2 (B_{21} U_\nu + A_{21} + Q_{21}) \quad (5.4)$$

$$\frac{dN_2}{dt} = \dot{N}_2 = N_1 B_{12} U_\nu - N_2 (B_{21} U_\nu + A_{21} + Q_{21}) \quad (5.5)$$

The population conservation leads to:

$$N_1^\circ = N_1 + N_2 \quad (5.6)$$

where N_1° (molecules/m³) is the population of level (1) prior to laser excitation ($t = 0$).

By solving the population balance for the molecules in the excited state, with the initial condition N_1° and the hypothesis that the population in the initial excited state N_2° is negligible, the population of molecules in the excited state as a function of time is given by:

$$N_2(t) = B_{12} U_\nu N_1^\circ \tau_p (1 - e^{-t/\tau_p}) \quad (5.7)$$

$$\tau_p = \frac{1}{B_{12} U_\nu + B_{21} U_\nu + A_{21} + Q_{21}} \quad (5.8)$$

τ_p is called the *pumping time* and it represents a characteristic time of the processes involved during LIF, which depends on the different contributions: absorption, stimulated emission, spontaneous emission and quenching. Fig.V.2 shows the induced evolution of the excited state population as function of time.

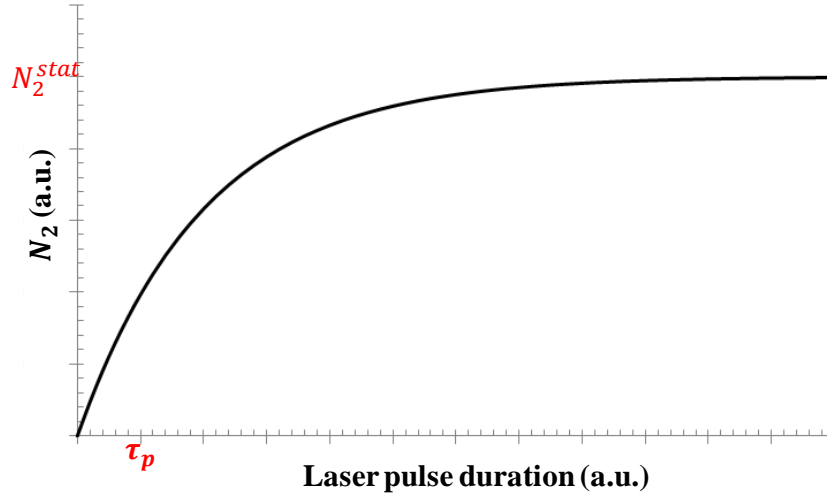


Fig V.2: Evolution of the excited state population as function of time when two-levels model is considered.

For $t \ll \tau_p$, the upper level population $N_2(t)$ initially builds up linearly with time and does not depend on the quenching rate:

$$N_2(t) = B_{12}U_\nu N_1^\circ t \quad (5.9)$$

For time values $t \gg \tau_p$, a steady state value of $N_2(t)$ is reached ($\frac{dN_2}{dt} = 0$), and is given by:

$$N_2(t) = N_1^\circ B_{12}U_\nu \tau_p = N_2^{stat} \quad (5.10)$$

and rearranging:

$$N_2^{stat} = N_1^\circ \frac{B_{12}}{B_{12}+B_{21}} \frac{1}{1+\frac{A_{21}+Q_{21}}{(B_{12}+B_{21})U_\nu}} \quad (5.11)$$

or alternatively:

$$N_2^{stat} = N_1^{\circ} \frac{B_{12}}{B_{12}+B_{21}} \frac{1}{1+\frac{U_v^{sat}}{U_v}} \quad (5.12)$$

where the quantity U_v^{sat} is defined as the following ratio:

$$U_v^{sat} = \frac{(A_{21}+Q_{21})}{B_{12}+B_{21}} \quad (5.13)$$

N_2^{stat} as a function of ratio $\frac{U_v^{sat}}{U_v}$ evidences two energy regimes.

At low laser excitation intensities ($U_v \ll U_v^{sat}$), the upper level population simplifies to:

$$N_2^{stat} = N_1^{\circ} B_{12} U_v \frac{1}{(A_{21}+Q_{21})} \quad (5.14)$$

The LIF process is said to be in the *linear regime of excitation* because N_2 varies linearly with the spectral laser energy density (so the input laser intensity).

If the intensity of the laser is increased until $U_v \gg U_v^{sat}$, this regime is called *saturated energy regime*, and the upper level population reaches the value N_2^{sat} :

$$N_2^{sat} = N_1^{\circ} \frac{B_{12}}{B_{12}+B_{21}} \quad (5.15)$$

The N_2^{sat} becomes independent on both the laser intensity and the collisional quenching rate. This regime appears ideal because the saturation maximizes the upper level population. Actually, this condition is difficult to archive because of the spatial inhomogeneities of the laser beam (the central zone is much more intense than the other edges) and the imperfect temporal shape of the laser pulse (the laser pulse is not a perfect top-hat). Fig.V.3 shows the evolution of the excited steady state population as a function of the spectral laser energy density.

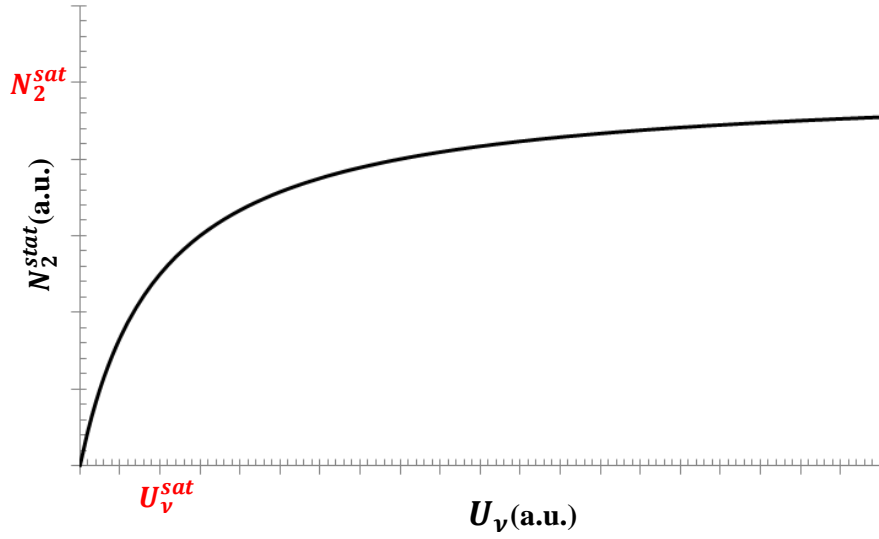


Fig.3: Evolution of the excited steady state population as a function of the spectral laser energy density.

2. Fluorescence signal

The fluorescence signal (S_{LIF}) designates the number of photons emitted by spontaneous emission and collected in a solid angle Ω from a collection volume V . If N_2 respects the number of excited molecules after the laser absorption, we have:

$$S_{LIF} = \frac{V\Omega}{4\pi} N_2 A_{12} \quad (5.16)$$

Then to related N_2 to N_1° we use one of the previous equations (5.9-5.15). In case of the linear and stationary regime of fluorescence, replacing N_2 by its value (eq. 5.14) into eq 5.16 leads to:

$$S_{LIF} = \frac{GV\Omega}{4\pi} N_1^\circ B_{12} U_v \frac{A_{21}}{A_{21}+Q_{21}} \quad (5.17)$$

The ratio $\frac{A_{21}}{A_{21}+Q_{21}}$ is the number of molecules which transfers between two levels by spontaneous emission with respect to the total number of returns (radiative or collisional). It is named the *fluorescence quantum yield* Φ .

As shown in equation (5.1), the number of molecules in a specific rotational level J'' , v'' is related to the total number of molecules through the Boltzmann expression:

$$N_1^{\circ} = N_{tot} f_B(J'', v'', T) = N_{J'', v''} \quad (5.18)$$

where $f_B(J'', v'', T)$ is the Boltzmann factor.

Finally, the expression of the fluorescence signal in the linear regime of excitation is:

$$S_{LIF} = \frac{GV\Omega}{4\pi} N_{tot} f_b(J'', v'', T) B_{12} U_{\nu} \frac{A_{21}}{A_{21} + Q_{21}} \quad (5.19)$$

In practice the spectroscopic selection rules authorize several radiation emissions issued from a given excited rotational level J' : $\Delta J = J' - J'' = 0, +1, -1$.

In addition, the processes of RET and VET contribute to transfer part of the excited molecules on the neighboring levels. Each populated level is the source of three other radiations. Therefore, the emission spectrum is much more complex than in a simplified two-level model. In practice, the fluorescence spectrum is collected in a given spectral bandwidth $\Delta\lambda_{coll}$. As long as the laser pumping is weak (i.e. $N_2 \ll N_1^{\circ}$), the fluorescence signal remains proportional to the population $N_{J'', v''}$ and the energy density:

$$S_{LIF} = \frac{GV\Omega}{4\pi} N_{J'', v''}^{\circ} B_{J'' J'} U_{\nu} \Phi \quad (5.20)$$

Where Φ is the effective fluorescence quantum yield which considers the emission occurring $\Delta\lambda_{coll}$.

3. NO concentration determination in flame

In this study, relative NO profiles have been determined by LIF in the linear regime of fluorescence. The calibration was performed by seeding a known concentration of NO in a reference flame. The procedure is described below.

3.1. NO measurements in flames by LIF: bibliography study

Nitric oxide is a diatomic molecule and its spectroscopic properties are well known. Several excitation-detection schemes commonly used in flames are listed in the Table V.1.

<i>Flames</i>	<i>Excitation</i>	<i>Detection</i>	<i>Signal Calibration</i>	<i>References</i>
CH₄/O₂/N₂ P=30, 70, 120 torr	A-X(0,0) Q ₁ (17)	A-X (0,1) A-X (0,2)	NO doping	[199]
CH₄/O₂/N₂ P=40 torr	A-X(0,0) Q ₁ (26)	A-X (0,2)	NO doping	[200]
CH₄/O₂/N₂ P=1-14.6 atm	A-X(0,0) Q ₂ (27)	A-X (0,1)	NO doping	[201]
CH₄/O₂/N₂ + CH₃Cl/CH₂Cl₂ P=40 torr	A-X(0,0) Q ₁ (26)	A-X (0,2)	NO doping	[202]
CH₄/O₂/N₂ P=25-30 torr	A-X(0,0) P ₂ (19)	A-X (0,2)	NO doping	[203]
CH₄/O₂/N₂ P=33 torr	A-X(0,0) Q ₂ (27)	A-X (0,2)	NO doping + CRDS	[204]
CH₄/EA/MEC/O₂/N₂ P=40 torr	A-X(0,0) Q ₂ (27)/ Q ₁ (23)	A-X (0,2)	NO doping	[160]
CH₄/O₂/N₂ P=40-75 torr	A-X(0,0) Q ₁ (16)	A-X (0,3)	NO doping	[205]
H₂-N₂O/N₂ P=0.81 atm	A-X(0,0) Q ₁ (26)	A-X (0,1)	FTIR spectroscopy	[206]
CH₄/air/NH₃ P=1 atm	A-X(0,0) Q ₂ (27)	A-X (0,1)	NO doping	[207]
CH₄/O₂/N₂ Co flow	A-X(0,0) Q ₁ (16)	A-X (0,3)	NO doping	[208]
CH₄/MB/O₂/N₂ P=40 torr	A-X(0,0) Q ₂ (27)	A-X (0,2)	NO doping	[209]

Table V.1: Literature studies on NO detection by LIF in flames. A-X (i,j) represents the vibrational band on which the fluorescence of the molecules is excited or collected with i= the vibrational level of the upper state and j=the vibrational level of the lower state.(CRDS Cavity Ring-Down Spectroscopy, FTIR Fourier Transform InfraRed, EA=ethyl acetate, MEC=methyl ethyl ketone, MB= methyl butanoate)

Excitation of NO typically occurs by means of a specific rovibronic transition within the A-X (0,0) band of NO molecule at ~226 nm. Detection of the fluorescence from one or more of the higher-order bands, A-X (0,1), A-X (0,2) or A-X (0,3), is used to avoid Rayleigh scattering within the A-X (0,0) band. Rayleigh scattering occurs at the

same wavelength as the incoming light. Unfortunately, even if Rayleigh scattering is avoided, other interferences such as fluorescence from secondary species have to be accounted for to obtain quantitative LIF measurements of NO.

The $B^3\Sigma_u^- - X^3\Sigma_g^-$ Schumann-Runge system of O_2 (175-535 nm) represents a source of potential interference with NO fluorescence because of spectral coincidences of its hot-band spectrum with that of NO. Indeed, at high temperature the O_2 molecules are redistributed among a large range of rotational and vibrational levels in the ground state. This leads to overlapping of O_2 and NO spectra, causing residual background interferences. Partridge et al. [210] and Thomsen et al. [201] studied these O_2 interferences in lean premixed $CH_4/O_2/N_2$ and $CH_4/O_2/Ar$ flames, between 1-6 atm and 1-14.6 atm, respectively. They proposed to excite NO on the $Q_2(27)$ transition of the A-X (0,0) band (~225.6 nm), because this line is intense, isolated and weakly dependent on temperature in the range of flame temperatures [211]. Thomsen et al. [201] proposed to collect the transitions of the A-X (0,1) band with a detection window of 2.7 nm width centered at 235.7 nm. In this case, the majority of the NO fluorescence is collected neglecting the O_2 fluorescence signal (~233.5nm) and the N_2 Stokes-Raman signal (~238 nm) bracketing the A-X (0,1) band of NO. Moreover, authors proposed to measure LIF signal on resonance, mode "ON" (~225.6 nm), and without resonance, mode "OFF" (~225.5 nm). Interference-corrected LIF signal corresponds to the difference between these two measurements ("ON-OFF").

Desgroux et al. [202] used "ON-OFF" signal correction method to study $CH_4/O_2/N_2$ flames seeded with CH_3Cl and CH_2Cl_2 at $P=40$ Torr. They probed NO by using LIF in the linear regime of energy by exciting, on resonance, the $Q_1(26)$ transition (~225.4 nm) of A-X (0,0) band, which is well isolated from NO adjacent lines and has a little temperature dependence. Although the $Q_1(26)$ line is not coincident with O_2 , they observed O_2 contribution in lean flames. OFF signal was measured around 224 nm. Fluorescence was collected on A-X (0,2) band to avoid interference with Raman scattering of secondary species and photolytic effects from chlorinated species.

Lamoureux et al. [160] measured NO fluorescence in $CH_4/O_2/N_2$ premixed laminar flames, containing various amounts of methyl ethyl ketone (MEK) and ethyl acetate (EA) at low pressure. NO-LIF measurements were performed by excitation of the A-X (0,0) band on the lines $Q_2(23)$ and $Q_2(27)$ near 225.6 nm. The fluorescence collection

was achieved using the A-X (0,2) band with a bandwidth of 8 nm. Unfortunately, the excitation range is possibly disturbed by O₂ Schumann-Runge bands. Caution was taken to prevent this background signal by recording the OFF-resonance signals. However, authors noted that Q₂(27) line has a Boltzmann fraction less dependent on the temperature than that of the Q₂(23). The NO mole fraction was quantitatively determined by measuring the LIF signal in the reference flame seeded with different known amounts of NO added to the premixed gases (0-600 ppm of NO). Very small amount was added to avoid reburning process, following a previous study by Berg et al. [203].

3.2. Excitation and collection bands selection

The transition to excite NO should be intense, isolated and should originate from an energy level, whose population is weakly dependent on the temperature in the range of interest. The Q₂(27) transition of the A-X (0,0) band at 225.58 nm fits these criteria especially concerning the constancy of the Boltzmann factor (f_B) with the flame temperature, as shown in Fig V.4 (variation of only about 20% in the 900-2300K temperature range).

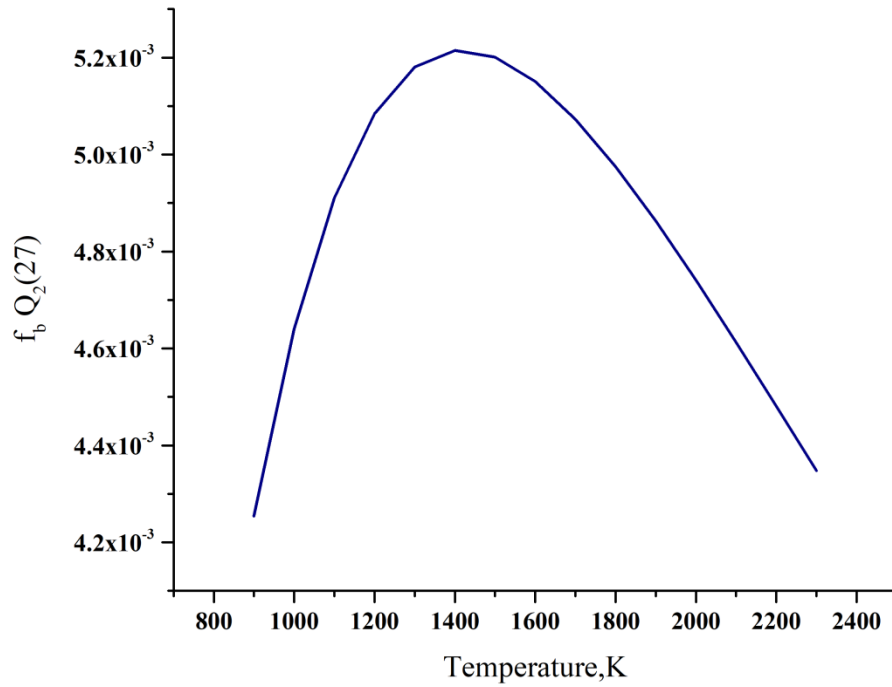


Fig.V.4: Variation of the Boltzmann factor of level ($J''=26.5$ $N''=27$) involved in the $Q_2(27)$ transition with the temperature. The values of the partition functions and energies necessary for the calculation of the Boltzmann factor are taken from Gillette [212] and Reisel [211].

Fig.V.5 shows the experimental LIF excitation spectrum, i.e., the evolution of the fluorescence signal with laser excitation wavelength in the A-X (0,0) band that we obtained in flame M1.0 (Table III.1).

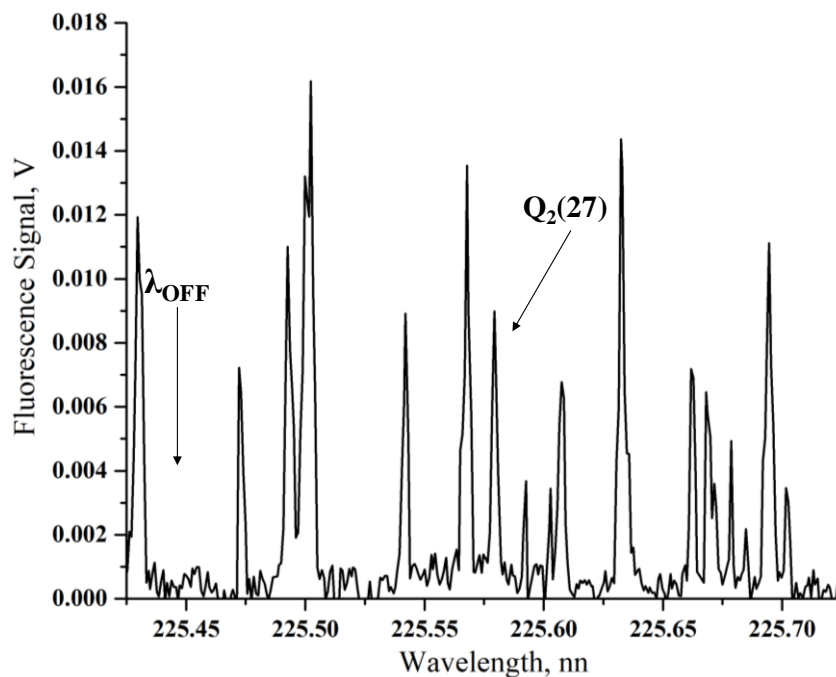


Fig. V.5: Experimental NO LIF excitation spectrum performed in flame M1.0.

Fig. V.5 also shows the excited transition $Q_2(27)$ and the non-resonance wavelength, where the OFF measurement of the signal is performed (λ_{OFF}). This wavelength is chosen near the $Q_2(27)$ transition to minimize the laser energy deviation, at 225.45 nm where NO absorption is negligible.

LIF is used in the linear regime of fluorescence. Fig.V.6 reports the variation of the fluorescence signal as function of the photodiode signal, i.e. the energy of the laser. Fig.V.6 clearly shows the linear regime of fluorescence up to 0.09 V, corresponding to 80 μ J of laser energy.

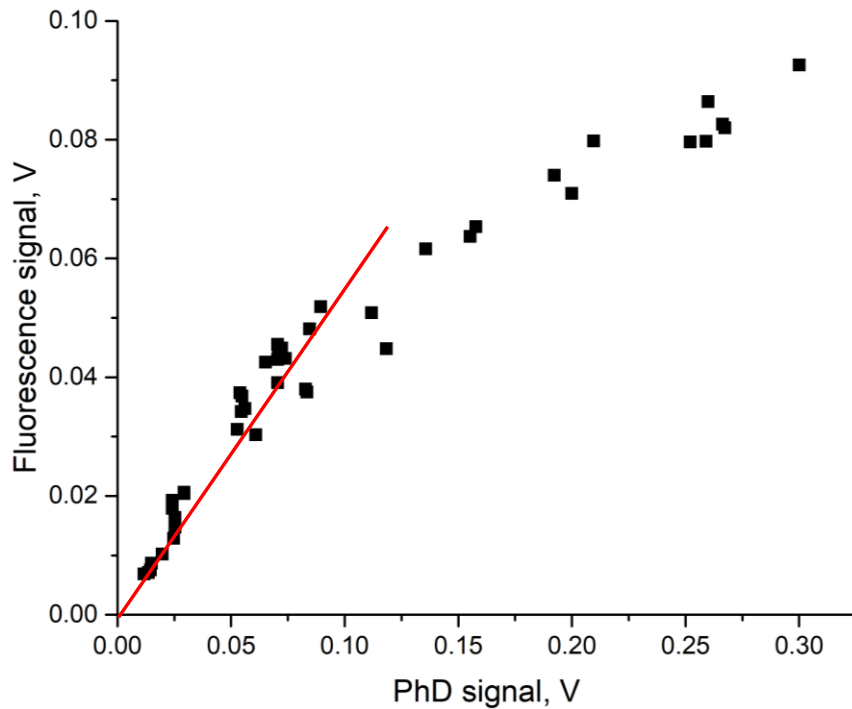


Fig.V.6: The variation of the fluorescence signal vs photodiode signal in flame M1.0.

The fluorescence signal is collected on the A-X (0,2) band with a spectral bandwidth of 7.4 nm centered at 247 nm. Fig.V.7 shows the typical fluorescence spectrum of NO in the range 220-260 nm, experimentally detected in flame M1.0. This spectrum is detectable for height above the burner (HAB) from 1 mm (Fig.V.7 is detected at HAB= 20 mm).

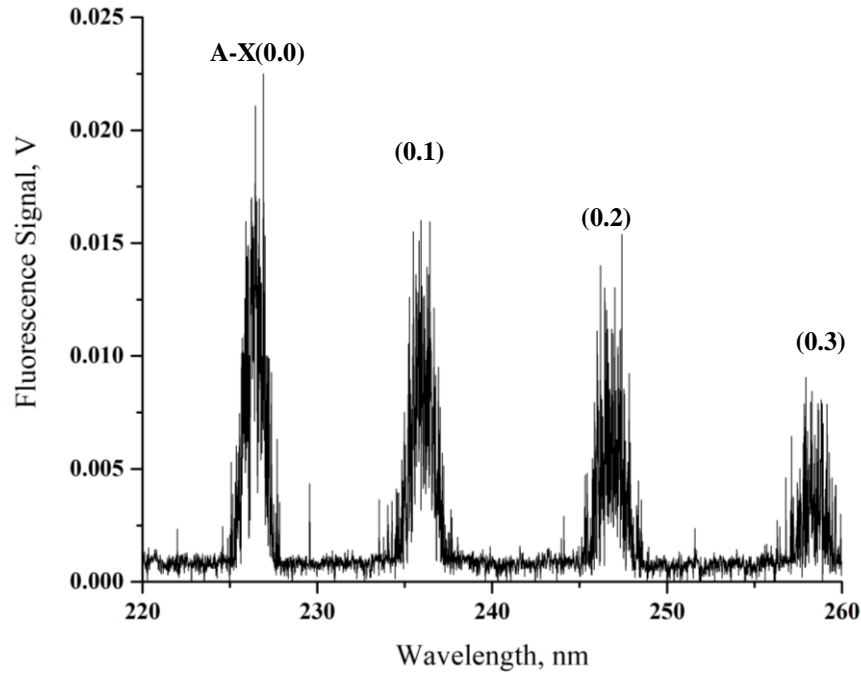


Fig.V.7: Experimental NO fluorescence spectrum in flame M1.0 at HAB= 20 mm.

3.3. Determination of the quenching rate

For NO concentration profiles, it is important to take into account the variation of the fluorescence quantum yield $\frac{A_{21}}{A_{21}+Q_{21}}$ as a function of the height above the burner. It is possible to obtain experimentally the quenching rate Q from the temporal decay of the fluorescence signal. Using the fluorescence two-energy level model, at the end of the laser pulse, the fluorescence signal decrease is expressed by:

$$dN_2/dt = -N_2(A_{21} + Q_{21}) \quad (5.21)$$

where N_2 is the rotational population of the excited level E_2 (m^{-3}), A_{21} is the Einstein coefficient of spontaneous emission (s^{-1}) and Q_{21} is the Quenching rate (s^{-1}).

By solving equation (5.20), we obtain:

$$\ln N_2 = -(A_{21} + Q_{21})t + C \quad (5.22)$$

The term $(A_{21} + Q_{21})$ corresponds to the slope of the straight line $\ln(N_2)=f(t)$ [213]. Fig. V.8 reports the $(A+Q)$ values (which has been calculated from the exponential fluorescence temporal decay) as function of the HAB for M1.0 for three different sets

of measurements. We observe a decrease of (A+Q) value at low HAB, while in the burned gas region, i.e., between 8 and 25 mm, the (A+Q) term is constant. The variation of (A+Q) along the flame is due to changes in the chemical composition along the flame and to collisional cross section variation with temperature.

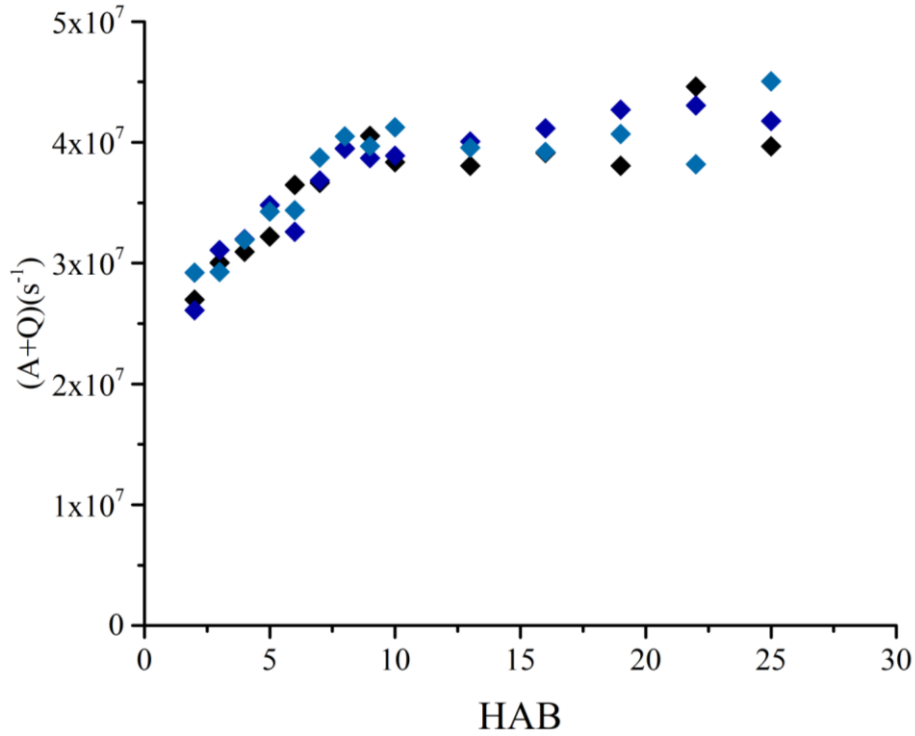


Fig. V.8: (A+Q) profile in M1.0 flame for three data sets.

Table V.2 shows the (A+Q) values determined, with the procedure above reported, in the burnt gases region of the six examined flames.

Flame	(A+Q) (s ⁻¹)	
<i>M1.0</i>	4.07x10 ⁷	± 4.2%
<i>M1.2</i>	4.12x10 ⁷	± 4.1%
<i>FMI.0</i>	3.87x10 ⁷	± 4.7%
<i>FMI.2</i>	3.89x10 ⁷	± 3.2%
<i>THFM1.0</i>	4.53x10 ⁷	± 4.6%
<i>THFM1.2</i>	4.52x10 ⁷	± 3.0%

Table V.2: (A+Q) in the burned gases of the six CH₄/F-THF/O₂/N₂ flames.

The A+Q value in the M1.0 flame is about 10% lower than the value previously reported in similar flames (El Merhubi's thesis [214]). The main value of (A+Q) in the six flames is 4.17x10⁷ s⁻¹. The standard deviation (7%) is slightly larger than the

standard deviation measured in each flame, while the standard deviation of the fluorescence signal is about 3-5%. The impact of the quenching variation is known to be decreasing by measuring the LIF signal at its temporal peak, i.e. a prompt detection before achievement of the collisional processes. In the following, NO profiles have been detected at the peak of the LIF signal and have not been corrected for (A+Q) variations.

3.4. Determination of the profile of NO relative population

LIF measurements are performed “ON” resonance with the $Q_2(27)$ transition of the band A-X (0,0) at 225.58 nm and “OFF” resonance at 225.45 nm.

3.4.1. Raw LIF profile determination

“ON” and “OFF” signals are averaged over 400 laser shots. Fig. V.9 shows “ON” and “OFF” profiles for flame M1.0. The “OFF” signal profile is approximately constant along the position in the flame and accounts for the flame emission and electronic background noise. Raw NO fluorescence signal is obtained by subtraction of the “OFF” signal from the “ON” [160].

For each studied flame, the NO fluorescence profiles are measured three times from the burned gases (25 mm) close to the burner surface (0.2 mm). For each flame the three raw LIF profiles are averaged. Measurements show a good data reproducibility.

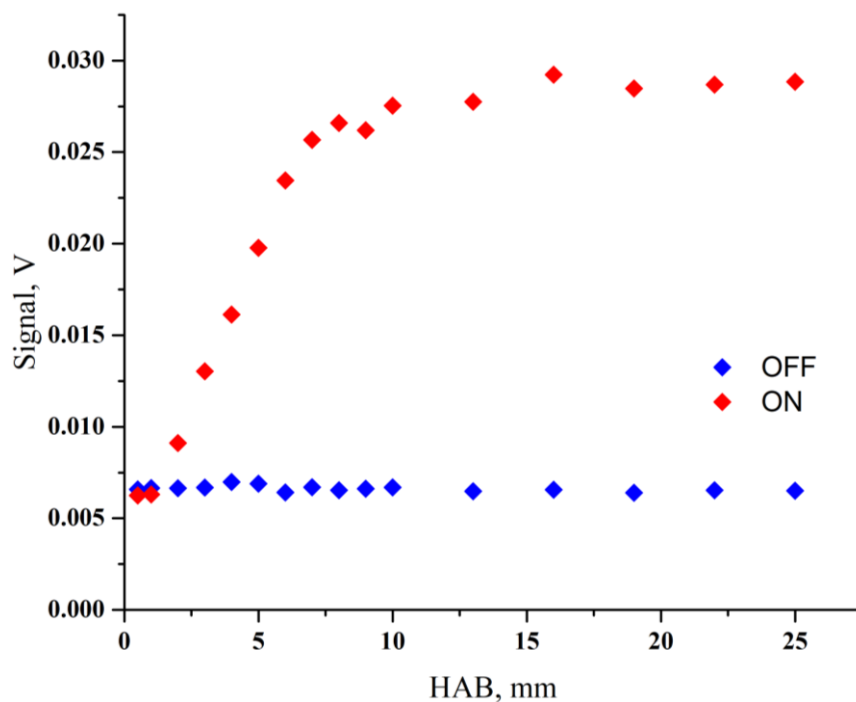


Fig.V.9: “ON” and “OFF” signals for flame M1.0.

3.4.2. Corrections of fluorescence signal

To obtain the concentration of NO molecules (N_{NO}) from the fluorescence signal (S_{LIF}), we need to take into account different factors as reported in the equation (5.18):

$$S_{LIF} = \frac{GV\Omega}{4\pi} N_{NO} f_b(J'', v'', T) B_{12} U_v \Phi \quad (5.20)$$

The signals “ON” and “OFF” at each flame position are divided by the energy of the laser during the acquisition (photodiode signal) to correct for the laser energy fluctuations. Raw NO fluorescence signal is then obtained by subtracting the already corrected “OFF” signal from the “ON” signal.

Moreover, from certain distance from the burner down to the burner surface, signal needs to be corrected for the solid angle occlusion caused by the small size of collection windows. The correction factor is given by the following relation based on geometrical considerations:

$$Corr(x) = \frac{S_{max}}{S'(x)} = \frac{\pi R_2^2}{\left[\pi - \cos^{-1}\left(\frac{x}{r}\right) \right] \left(\frac{l_2 R_1}{l_1} \right)^2 + \left(\frac{l_2 x}{r} \right)^2 \sqrt{\left(R_1 \frac{l_2}{l_1} \right)^2 - \left(\frac{l_2 x}{r} \right)^2}} \quad (5.23)$$

where S_{max} is the full surface of the solid angle and $S'(x)$ is the perturbed surface of the solid angle at the distance x above the burner, r (42.5 mm) is the full geometrical burner radius, R_1 (16 mm) is the enclosure windows radius, R_2 (20.87 mm) is the lens radius, l_1 (230 mm) is the distance between the burner center to the enclosure window, l_2 (300 mm) is the distance between the burner center to the lens. Fig.V.10 shows a geometrical scheme showing the different parameters involved in the correction factor.

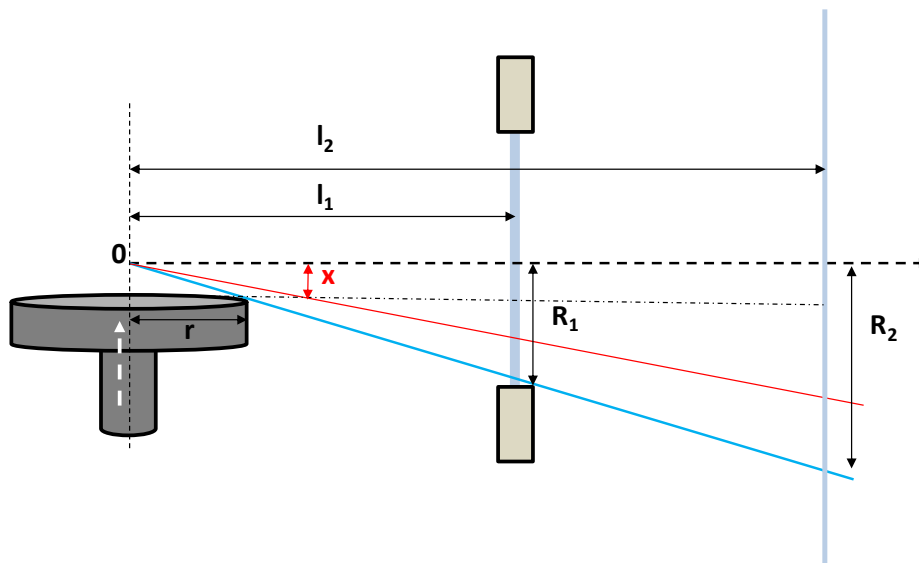


Fig.V.10: Geometrical scheme for solid angle correction.

With the above reported values for the geometrical characteristics of our experimental set-up, the solid angle correction is applied from 2.96 mm down to the burner surface. In case of NO, this region corresponds to the beginning of NO formation profile; therefore, the correction is not sizeable for methane flames, but its effect is more appreciable for biofuels doped flames because the reaction zones are more attached to the burner surface. Fig V.11 shows the tendency of the correction with the HAB and Fig. V.12 shows the effect of solid angle correction in flame FM1.2.

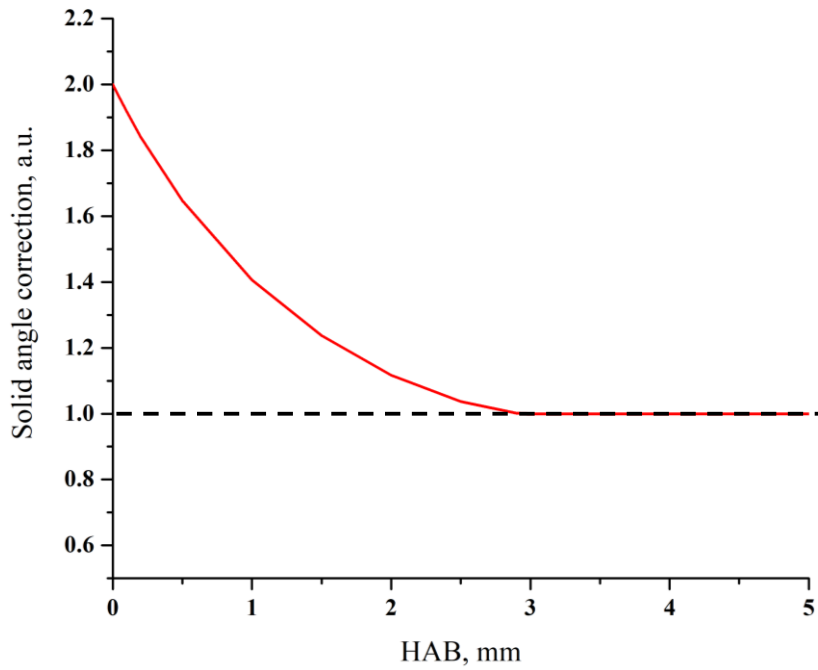


Fig.V.11: Solid angle correction in flame FM1.2.

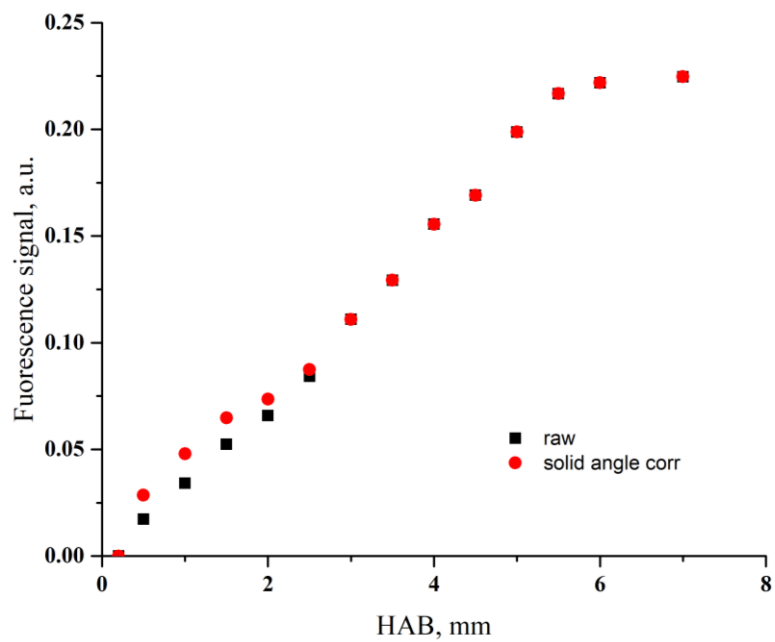


Fig.V.12: Comparison between the LIF raw profile and LIF profile after solid angle correction in flame FM1.2.

Knowing the temperature profile and the associated Boltzmann factor (see Fig.V.4), it is possible to correct the fluorescence signal profile by these terms and finally to obtain the NO relative concentration profile (N_{NO_tot}).

Fig.V.13 reports the comparison between the raw data (ON-OFF signals) and the data corrected for the temperature, the Boltzmann factor, solid angle and laser energy fluctuations.

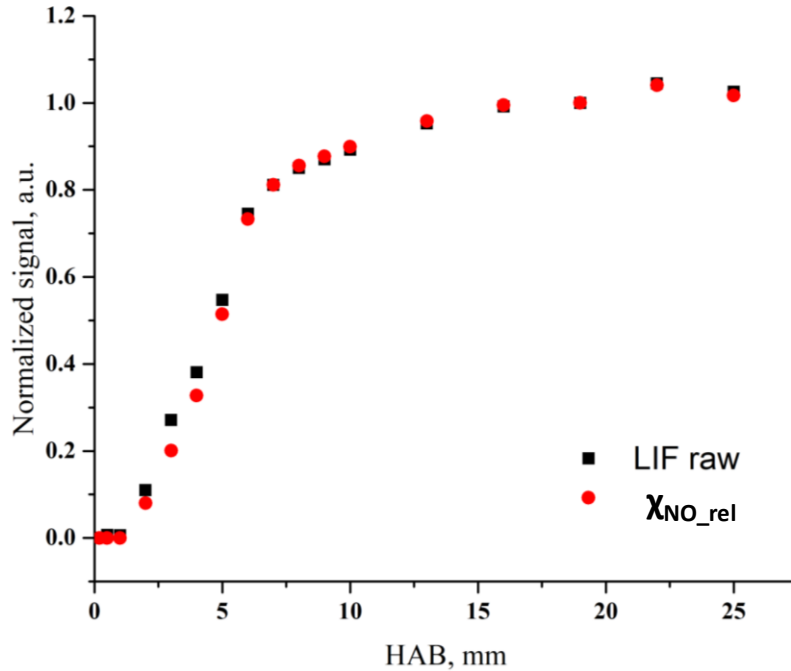


Fig.V.13: Comparison between the raw data (ON-OFF signals) and the data corrected for the temperature, the Boltzmann factor, solid angle and laser energy fluctuations in Flame M1.0.

3.4.3. Furan absorption: specific correction of LIF signal for FM1.0 and FM1.2 flames

Furan absorbs light in the spectral region between 210 and 232 nm, as shown in Fig. V.14. Consequently, at excitation wavelength around 226 nm, it is possible to have laser light absorption in the flame zone where the furan concentration is relatively high (the flame region close to the burner). Furan absorption does not affect the fluorescence collection, because it is detected at 247 nm.

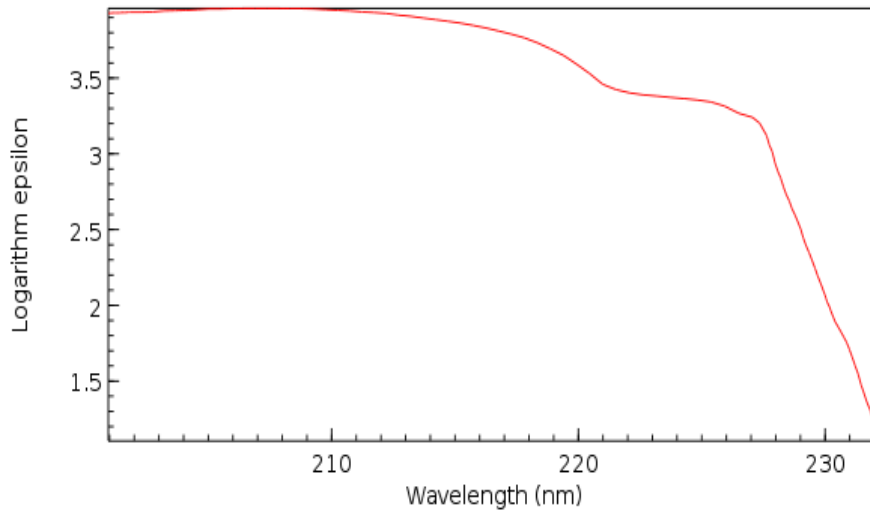


Fig.V.14: Furan UV-vis absorption spectrum [215], *epsilon* is the molar extinction coefficient.

To illustrate this perturbation with furan, Fig.V.15 shows the reduction of the transmitted laser energy, collected with a photodiode in the stoichiometric furan flame (FM1.0) with respect to the stoichiometric methane flame (M1.0). The energy decrease starts around 3 mm corresponding to the flame front of flame FM1.0.

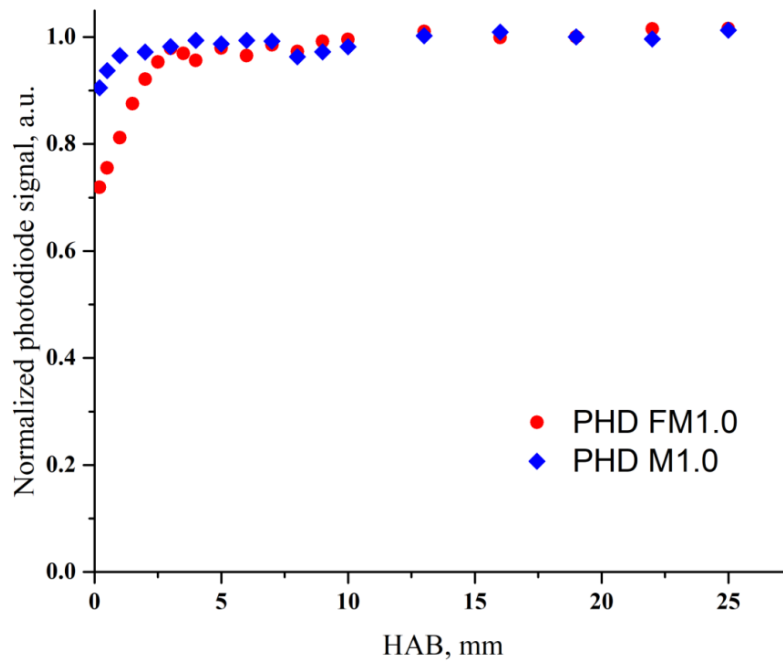


Fig. V.15: Profiles of the transmitted energy measured by a photodiode placed after the burner for M1.0 and FM1.0 flames.

As shown in the equation 5.18, the link between the fluorescence signal (S_{LIF}) and the relative population of NO (N_{NO}) also depends on the laser transmitted energy (U_v). Hence it is important to evaluate the local energy of the laser effectively involved in the collection volume. The following procedure is implemented in order to correct the LIF profiles for laser energy attenuation due to furan absorption.

By considering a homogeneous distribution of the species along the laser direction, it is possible to determine the laser intensity at the center of the burner, knowing the energy of the laser before and after entering the flame. Using the Beer-Lambert Law, we obtain:

$$I(z) = I_0(\lambda)10^{-\varepsilon_\lambda l C(z)} \quad (5.24)$$

where z is the vertical coordinate, $I(z)$ is the laser intensity collected by the photodiode, I_0 is the intensity before the flame, ε_λ is the molar extinction coefficient ($l \text{ mol}^{-1} \text{ cm}^{-1}$), $C(z)$ is the concentration (mol l^{-1}) and l is the path length (cm).

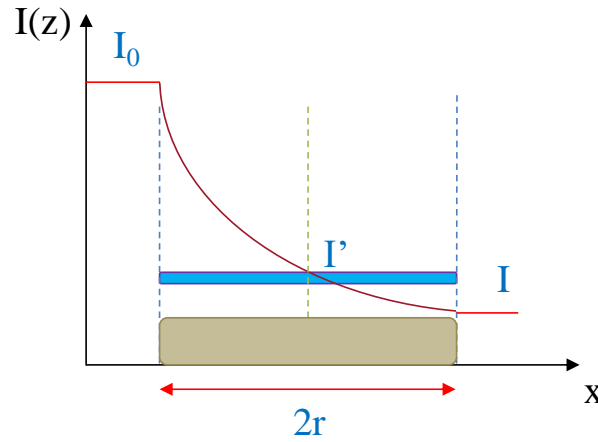


Fig. V.16: Schematic evolution of the laser intensity along the flame.

As shown in Fig.V.16, to evaluate the transmitted laser intensity along the burner axis in our case, we can use the following expressions:

$$I = I_0(\lambda)10^{-\varepsilon_\lambda 2r C} \quad (5.25)$$

$$I' = I_0(\lambda)10^{-\varepsilon_\lambda r C} \quad (5.26)$$

Where r is the burner radius and I' is the laser intensity at the burner axis. From (5.24) and (5.25), the laser intensity I' is:

$$I' = (I_0 * I)^{1/2} \quad (5.27)$$

Fig.V.17 shows the profile of I and I' along the flame FM1.0.

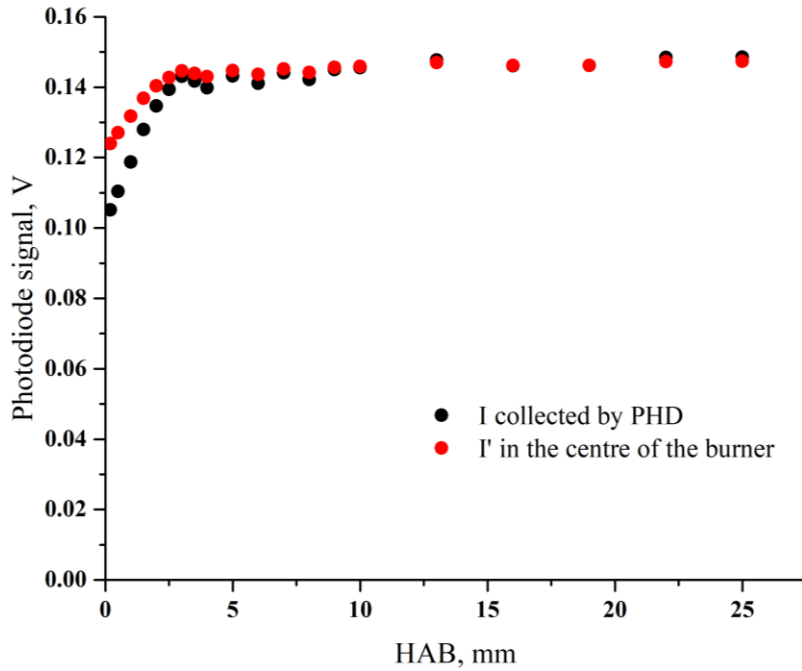


Fig.V.17: Profiles of the transmitted energy measured by a photodiode placed after the burner (I) and the after correction for furan absorption on the burner axis (I') for flame FM1.0.

Fig.V.17 clearly shows that the laser energy that excites the molecules in the collection volume, i.e., on the burner axis, is attenuated by the presence of furan molecules up to about 3 mm. Consequently, in this zone, we should correct the fluorescence signal for this effect.

The correction procedure used in the furan flames is the same as that detailed in section 3.4.2.

3.5. Linking procedure between the flames

The relation between the measured fluorescence signal and the concentration of NO molecules (equation 5.18) contains parameters which are difficult to determine ($G\Omega V$ factor, spectral energy density $U\nu$). Therefore, the absolute determination of the NO mole fraction profiles in flames requires a calibration with other techniques. Different techniques are reported in the literature to calibrate NO LIF signals: Cavity ring-down spectroscopy (CRDS) [216] or NO doping ([149], [158], [199], and [201]).

The method based on the seeding of a known amount of NO is simple and has a very good precision. It is commonly used in several laboratories ([149], [158], [199], and [201]).

Calibration is realized in two steps: firstly, the NO LIF signals collected in the burnt gases of the investigating flames, is compared with the LIF signal obtained in a reference flame; secondly the fresh gases of the reference flame ($\text{CH}_4/\text{O}_2/\text{N}_2$) are seeded with a known mole fraction of NO.

The comparison step between the flames is done in the burned gases at 19 mm with respect to the burner surface. The link between the flames and the reference flame (M1.0, stoichiometric methane flame) is obtained by alternatively measuring the LIF signals, corrected by the laser energy variations in each flame, according to the following procedure:

$$S_{LIF}^{reference} \rightarrow S_{LIF}^{Flame\ i} \rightarrow S_{LIF}^{reference} \rightarrow S_{LIF}^{Flame\ i} \rightarrow S_{LIF}^{reference} \rightarrow \dots$$

This step is repeated several times and the signal is detected in the “ON” and “OFF” modes, averaged over 400 laser shots in order to determine the $\frac{S_{LIF}^{Flame}}{S_{LIF}^{reference}}$ ratios.

These ratios are directly proportional to the ratios of the molecular populations in the ground state $\frac{N_{J^{flame}}}{N_{J^{reference}}}$, assuming negligible the impact of the quenching variation in the different flames (see Table V.3).

<i>Flames Ratio</i>	$\frac{S_{LIF}^{Flame}}{S_{LIF}^{reference}}$	
<i>M1.2</i>	2.22	± 3.14%
<i>FM1.0</i>	1.27	± 3.13%
<i>FM1.2</i>	2.45	± 3.83%
<i>THFM1.0</i>	0.74	± 3.58%
<i>THFM1.2</i>	1.31	± 3.44%

Table V.3: Fluorescence signal ratio.

Afterwards, the ratios are corrected for the Boltzmann factor variation to obtain the concentration ratios:

$$\frac{N_{tot\,flame}}{N_{tot\,reference}} = \frac{N_{J''\,flame}}{N_{J''\,reference}} \times \frac{f_{B\,reference}}{f_{B\,flame}} \quad (5.28)$$

Finally, mole fraction ratios between the reference flame and the other flames are obtained by considering the temperature variations in the flames that affect the molecular concentrations:

$$\frac{\chi_{flame}}{\chi_{reference}} = \frac{N_{tot\,flame}}{N_{tot\,reference}} \times \frac{T_{flame}}{T_{reference}} \quad (5.29)$$

Knowing the temperature, the Boltzmann factor of the Q₂(27) transition has been evaluated using the partition functions and the rovibrational energies reported by Gillette [22] and Reisel [18].

The values of $\frac{\chi_{flame}}{\chi_{reference}}$ and their relative standard deviations are reported in Table

V.4. By considering the uncertainties of the “linking procedure” and the temperature measurements, the precision of the mole fraction ratios is estimated to be 5%.

<i>Flames Ratio</i>	$\frac{\chi_{flame}}{\chi_{reference}} \pm 5\%$
<i>M1.0</i>	1.00
<i>M1.2</i>	2.33
<i>FM1.0</i>	1.24
<i>FM1.2</i>	2.39
<i>THFM1.0</i>	0.69
<i>THFM1.2</i>	1.28

Table V.4: NO mole fraction ratios at 19 mm in the six flames with respect to the reference flame.

3.6. NO doping method calibration

After the linking procedure, it is necessary to determine the absolute mole fraction of the reference flame. This is performed by seeding the reference flame with a known, but small, amount of NO from a standard mixture. Calibration measurements are performed at 19 mm above the burner, a location where the NO concentration profile reaches a plateau value. This measurement is performed by detecting the NO LIF signal in the burnt gases adding progressively a known quantity of NO in the fresh mixture. A commercial mixture of NO in N₂ ($2 \times 10^{-3} \pm 0.001$) is used in this study. The total flux of N₂ in the flame is maintained constant by substituting the N₂ flux of the reacting mixture with the flux of the commercial mixture of NO in N₂. The amount of added NO should not modify the chemistry of the flame with NO reburning effects. Indeed, it was shown that up to 600 ppm of NO could be added to N₂ without reburning [203]. In this work, the NO added to the reference flame varies from 0 to 40 ppm (on the basis of literature data we expect the various flames to produce mole fraction of NO not far from these values).

The detected LIF signal is proportional to the total mole fraction of NO (χ_{native} or $\chi_{added} + \chi_{native}$):

$$\chi_{native} \approx \left(\frac{S_{LIF}^{ON}}{PhD_{ON}} - \frac{S_{LIF}^{OFF}}{PhD_{OFF}} \right)_{native} \quad (5.30)$$

$$\chi_{added} + \chi_{native} \approx \left(\frac{S_{LIF}^{ON}}{PhD_{ON}} - \frac{S_{LIF}^{OFF}}{PhD_{OFF}} \right)_{tot} \quad (5.31)$$

and by the ratio of these two equations:

$$Y = \frac{\left(\frac{S_{LIF}^{ON}}{PhD_{ON}} - \frac{S_{LIF}^{OFF}}{PhD_{OFF}} \right)_{tot}}{\left(\frac{S_{LIF}^{ON}}{PhD_{ON}} - \frac{S_{LIF}^{OFF}}{PhD_{OFF}} \right)_{native}} - 1 = \frac{1}{\chi_{native}} * \chi_{added} \quad (5.32)$$

Afterwards, tracing Y as a function of χ_{added} , a straight line is obtained as shown in Fig.V.18. The inverse of the slope is the NO absolute mole fraction in the reference unseeded flame (χ_{native}).

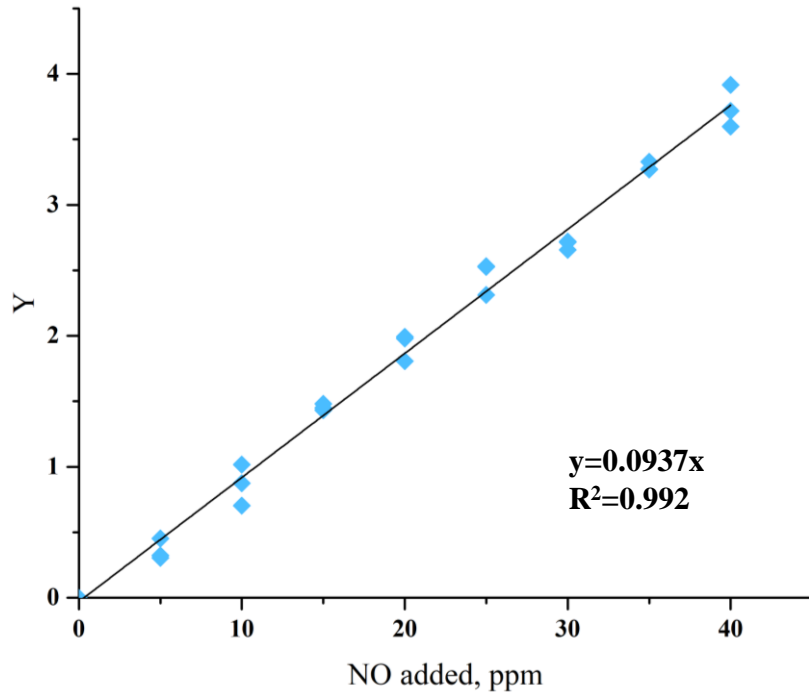


Fig.V.18: Calibration curve obtained in Flame1, HAB=19 mm

With this method, the NO mole fraction obtained in the reference flame at 19 mm is 10.67 ppm with a relative standard deviation of 3.08%. Knowing this value and the mole fraction ratios of Table V.3, the NO mole fraction of each flame is calculated at 19 mm. By considering the uncertainties of the calibration mixture and of the

experimental measurements, the precision of the calibration step is estimated to be $\pm 10\%$. Globally, the uncertainty of the NO mole fraction profiles is estimated to be around 15%.

The NO mole fractions calculated via this method at 19 mm in each studied flame are reported in Table V.5.

<i>Flames</i>	$\chi_{NO}(\text{ppm}) \pm 15\%$
<i>M1.0</i>	10.67
<i>M1.2</i>	24.90
<i>FM1.0</i>	13.27
<i>FM1.2</i>	25.58
<i>THFM1.0</i>	7.38
<i>THFM1.2</i>	13.73

Table V.5: NO mole fractions of investigated flames at 19 mm.

3.7. NO mole fraction profiles

NO mole fraction profiles are shown in Fig.V.19, V.20 and V.21 for the methane (Flame M1.0 and M1.2), furan-doped flames (Flame FM1.0 and FM1.2) and THF doped flames (Flame THFM1.0 and THFM1.2), respectively.

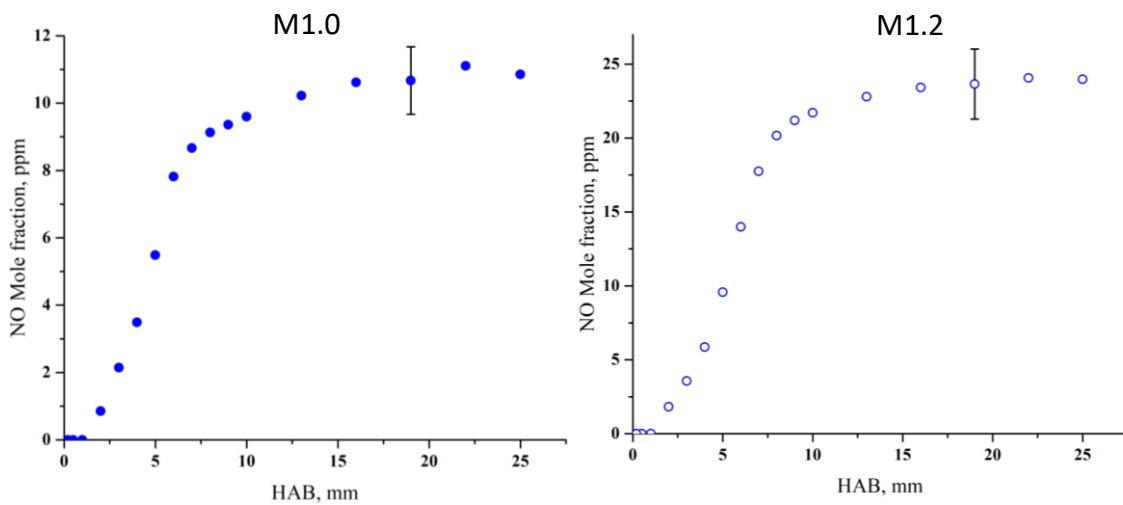


Fig.V.19: Mole fraction profiles of NO in the methane flames

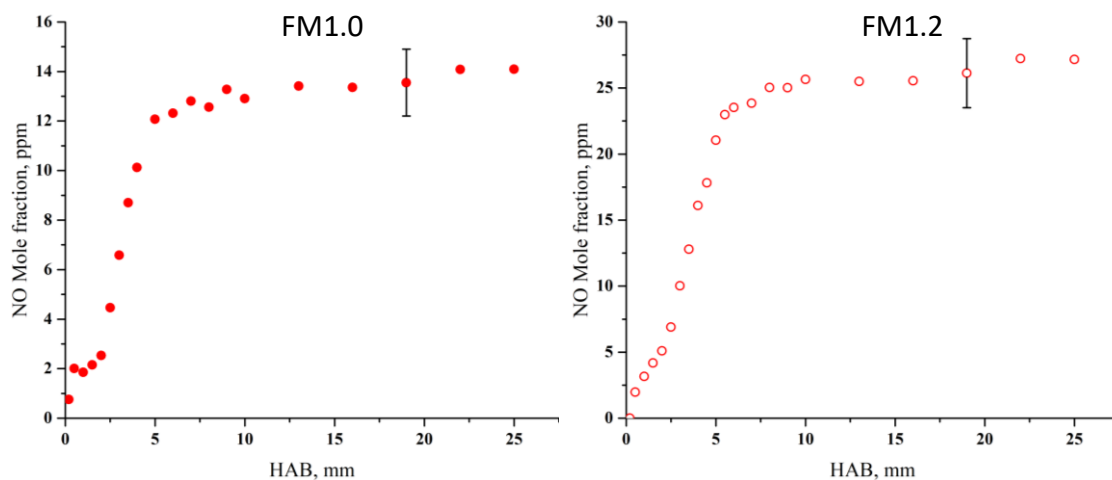


Fig.V.20: Mole fraction profiles of NO in the furan flames.

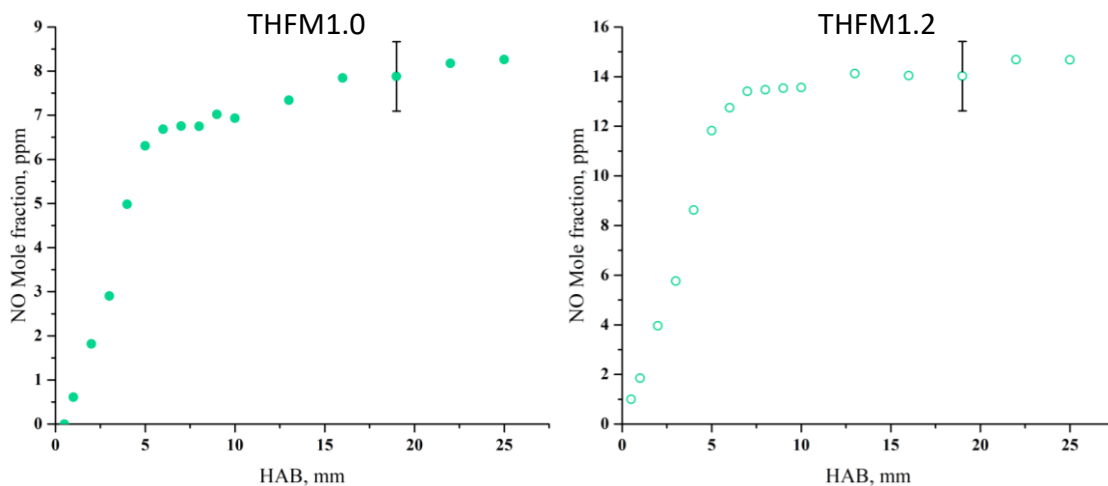


Fig.V.21: Mole fraction profiles of NO in the THF flames.

The experimental results of NO mole fraction will be discussed in section 5 of this chapter.

4. CH concentration determination in flame

The detection of the CH radical in the flames is very important since this intermediate species defines the flame front and is a "key" species involved in the prompt-NO mechanism. Due to its very low concentration in the reaction zone of the flame, CH detection is possible only with sensitive techniques, such as laser diagnostic techniques.

In this work, CH mole fraction profiles were measured using Laser Induced Fluorescence (LIF) and calibrated using a reference CH value previously obtained by Cavity Ring-Down Spectroscopy (CRDS).

4.1. CH Spectroscopy

The molecular bands of CH spectrum are observed in the combustion of hydrocarbons and in electrical discharges where carbon and hydrogen are present. Also, they are observed in the absorption spectrum of solar, stellar and interstellar atmospheres. The emission spectrum of CH in the visible and near-ultraviolet regions consists of three band systems: the transition $A^2 \Delta - X^2 \Pi$ around 430 nm, the transition $B^2 \Sigma^- - X^2 \Pi$ around 390 nm and the transition $C^2 \Sigma^+ - X^2 \Pi$ around 315 nm, where $X^2 \Pi$ is the ground state of the molecule and $A^2 \Delta$, $B^2 \Sigma^-$, $C^2 \Sigma^+$ are the excited states. Fig.V.22 shows the potential curves of the lowest excited electronic states of CH radicals [217].

The astronomical observations comprise the $A^2 \Delta$, $B^2 \Sigma^-$, $C^2 \Sigma^+$ systems, which were studied in detail by Herzberg and Johns [218], who also discovered the higher lying electronic states D, E and F. From these laboratory measurements it was concluded that the C state and higher rotation-vibration levels of the B state were subject to pre-dissociation effects.

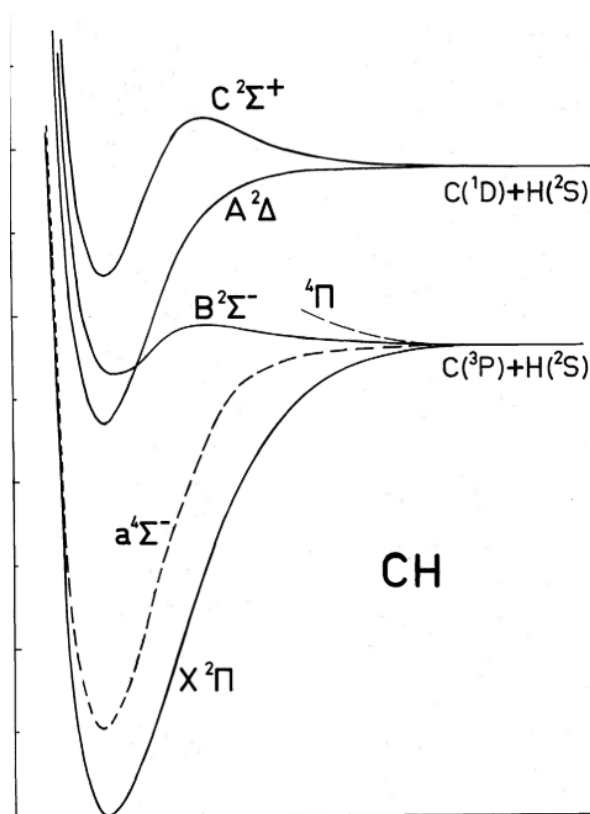


Fig.V. 22: Potential curves of the lowest excited electronic states in CH [217].

The phenomenon of predissociation occurs when the excitation of a molecule on an excited level leads to its dissociation. The excitation energy is less than the dissociation limit. This can occur when the potential energy curve of the upper state crosses the curve of a repulsive state, so that the two states have equal energy at some internuclear distance. This allows the possibility of a non-radiative transition to the repulsive state. This phenomenon can compete with fluorescence emission, where a scheme of this phenomenon is shown in Fig.V.23.

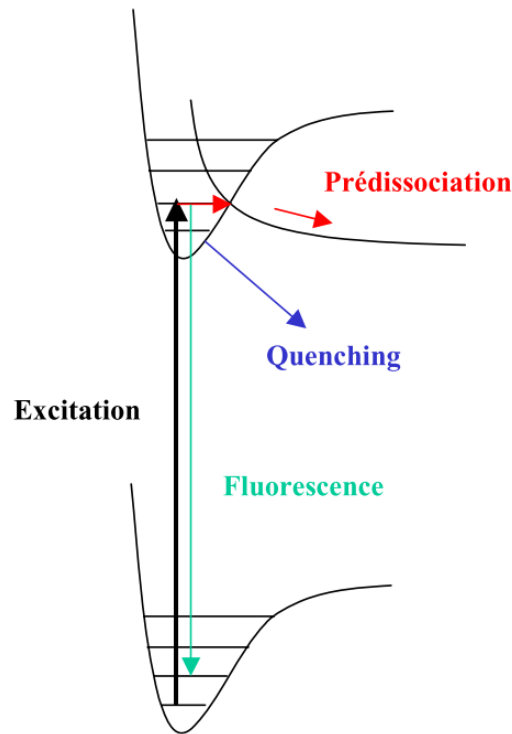


Fig.V.23: Predissociation phenomenon scheme.[216].

An additional de-excitation term needs to be added to the fluorescence quantum yield Φ . This coefficient, linked to the nature of the excited state and called the *predissociation rate* P (s^{-1}), quantifies the probability with which the molecules on an excited state of energy pass on the continuum of the neighboring electronic level of the same energy. The fluorescence quantum yield is then expressed by the relation:

$$\Phi = \frac{A}{A + Q + P} \quad (5.33)$$

where A is the Einstein coefficient for spontaneous emission and Q is the quenching rate.

Contrary to quenching, the predissociation rate is an intrinsic parameter of the molecule. This rate is not affected by temperature, pressure and collision partners, but varying with the excited level involved.

The fluorescence quantum yield of the predissociated states is low because the additional inclusion of the predissociation rate P in the denominator.

Ortiz and Campos [219] calculated the predissociation lifetime of the CH band C–X (0,0) and obtained a value between 8 and 21 ns as a function of the rotational quantum

number leading to a predissociation rates ranging from 4×10^7 to $11 \times 10^7 \text{ s}^{-1}$. This value indicates that the C state is nearly predissociated. Consequently, it remains possible to measure a fluorescence signal with a satisfying efficiency. The P value in the C ($v' = 0$) state has the same order of magnitude as the quenching rate, determined for diatomic molecules in our flames (see paragraph 3.3 of this chapter). This leads to the fact that the fluorescence signal is less dependent on the possible quenching variations during the CH LIF measurements.

4.2. Selection of the excitation/detection scheme for CH measurements.

As previously mentioned, CH is an important radical species; its spectroscopic properties have been well studied in the past for different applications. The Table V.6 summarizes several examples of CH detection in flames and indicates the used excitation/detection schemes.

<i>Flames</i>	<i>Excitation</i>	<i>Detection</i>	<i>Signal Calibration</i>	<i>References</i>
CH₄/O₂ P= 20 Torr	A-X (0,0) R(10) $\lambda=425\text{nm}$	A-X (0,0) Q branch $\lambda=431\text{nm}$		[220]
CH₄/O₂/N₂ Diffusion flame P=1 atm	A-X (0,0) R(7) $\lambda=426.8\text{nm}$	A-X (0,0) $\lambda_{\text{on}}=426.77\text{nm}$ $\lambda_{\text{off}}=426.67\text{nm}$	Rayleigh scattering	[221]
CH₄/O₂/N₂ P=40 Torr	A-X (0,0) R ₁ (9) $\lambda=425\text{nm}$	A-X (0,0) Q branch $\lambda=431\text{nm}$		[222]
CH₄/O₂/N₂ Diffusion flame P=1 atm	C-X (0,0) P ₁ (8) $\lambda=316.7\text{nm}$	A-X (0,0) Q branch $\lambda=430\text{nm}$	CRDS	[223]
CH₄/O₂ P= 8 Torr P= 1 atm	B-X (0,0) and (1,1), (1,0)	B-X (0,0) and (1,1), (0,1)		[224]
CH₄/O₂/N₂ P=25-30Torr	A-X (0,0) $\lambda=435.4\text{nm}$	A-X (0,0) $\lambda=431\text{nm}$	LIF/Rayleigh	[225]
CH₄/O₂/N₂ Diffusion flame P=1 atm	C-X (0,0) P ₁ (10) $\lambda=317.3\text{nm}$	C-X (0,0) Q branch $\lambda=314.4\text{nm}$	CRDS	[226]

CH₄/O₂/N₂ Counter-flow- Diffusion flame P=1, 3,6, 9, 12 atm	A-X (0,0) Q ₁ (10) λ=431.5nm	A-X (0,0) λ=430nm	CRDS	[227]
CH₄/EA/MEC/ O₂/N₂ P=40 torr	C-X (0,0) P ₁ (10) / P ₂ (10) λ=317.3nm	C-X (0, 0) Q branch λ=314.7nm	CRDS	[160]
CH₄/O₂/N₂ C₂H₂/O₂/N₂ P=40 Torr	C-X (0,0) P ₁ (8) / P ₂ (8) λ=316.7nm	C-X (0, 0) Q branch λ=314.7nm	CRDS	[127], [228]
CH₄/MB/O₂/N₂ P=40 torr	C-X (0,0) P ₂ (8) λ=316.75nm	C-X (0, 0) Q branch λ=315nm	CRDS	[151]

Table V.6: Literature studies on CH detection by LIF in flames. The excitation-detection schemes are also reported. (CRDS Cavity Ring-Down Spectroscopy)

The choice of an excitation / detection scheme depends on the flame conditions, the pressure and the confinement. Luque et al. [224] published an article presenting a synthesis of the different excitation / detection schemes with their advantages and disadvantages. Most of the measurements of CH have been performed using the A and B states; but the measurements are confronted to disturbances due to the Rayleigh scattering and to the natural emission of the flame. These aspects are crucial as CH is a minor species leading to a low intensity fluorescence signal

Luque et al. [224] have shown that the choice of the predissociated state of CH could partially overcome these problems. They showed that the excitation of the level $v' = 1$, $N' = 8$ of the predissociated state B is suitable for quantitative measurements of CH at atmospheric pressure. In a previous study, Hirano et al. [229] have performed CH 2D imaging and showed the feasibility of detecting CH by exciting the electronic state C at 312 nm. They then detect the fluorescence according to the A-X transition (430 nm), the A state being populated after electron energy transfer (EET). This same team then obtained instantaneous images of CH in an atmospheric turbulent flame using the C-X excitation band (1,0) at 290 nm and detection of the C-X band (1,1) at 315 nm [230].

Carter and co-workers [231] currently used the C-X band to perform CH imaging measurements in the flame front zone of a turbulent, premixed methane-air Bunsen

flame. They used high-speed planar laser-induced fluorescence (PLIF) of the CH radical involving the excitation and detection of the CH radical via the $C^2\Sigma^+ - X^2\Pi$ ($v'=0, v''=0$) band and leading to single shot images with satisfying signal to noise ratio. In a recent article, Carter's group [232] has used simultaneous particle image velocimetry (PIV) and planar laser-induced fluorescence (PLIF) utilizing R-branch transitions at 310.690 nm in the C-X (0,0) band at a 10-kHz repetition-rate in a turbulent premixed flame.

At PC2A laboratory, CH-LIF measurements have been performed using the predissociative $C^2\Sigma^+ - X^2\Pi$ state near 315 nm, according to an excitation/detection firstly proposed by Mercier [223] and Moreau [226] in diffusion flames. In her thesis, Laure Pillier [216] used the doublet $P_1(10)/P_2(10)$ excitation line of the C-X (0-0) transition, located at 317.2 nm, and collected the fluorescence of the Q branch (314.3-314.65 nm) of this same transition to study laminar premixed $CH_4/C_2H_6/C_3H_8/O_2/N_2$ flames stabilized on a porous burner at 30 Torr. The transition was chosen because it is intense and has a Boltzmann fraction relatively temperature-insensitive within the temperature range of interest. However, the double transition $P_1(10)/P_2(10)$ is not well separated and this characteristic is very important for the calibration procedure by CRDS.

The simulated emission spectrum of C-X (0-0) band is reported in Fig. V.24 showing the Q branch, the $P_2(8)$ and the $P_2(10)$ transitions.

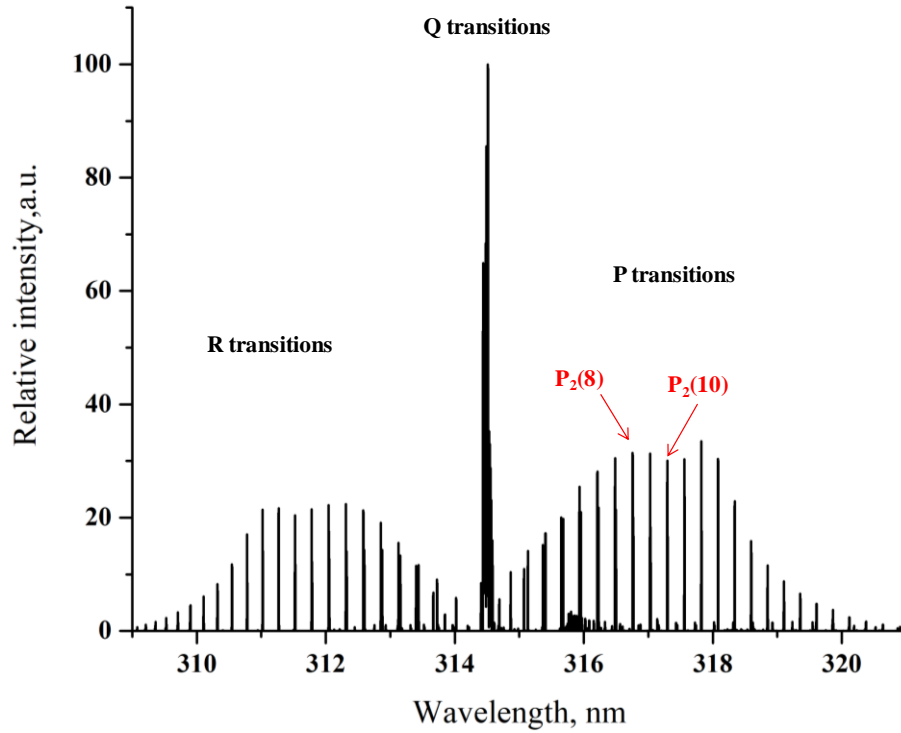


Fig.V.24: Simulated emission spectrum of CH C-X (0,0) band at $T=1800\text{K}$ and $P=40\text{Torr}$ by LIFBASE [233].

In this thesis, the well isolated $P_2(8)$ transition of the band C-X(0,0) at 316.7 nm was selected to determine the CH concentration profiles because of the relative constancy of the Boltzmann factor (f_B). In Fig.V.25 the Boltzmann factor is reported for this transition as function of the flame temperature.

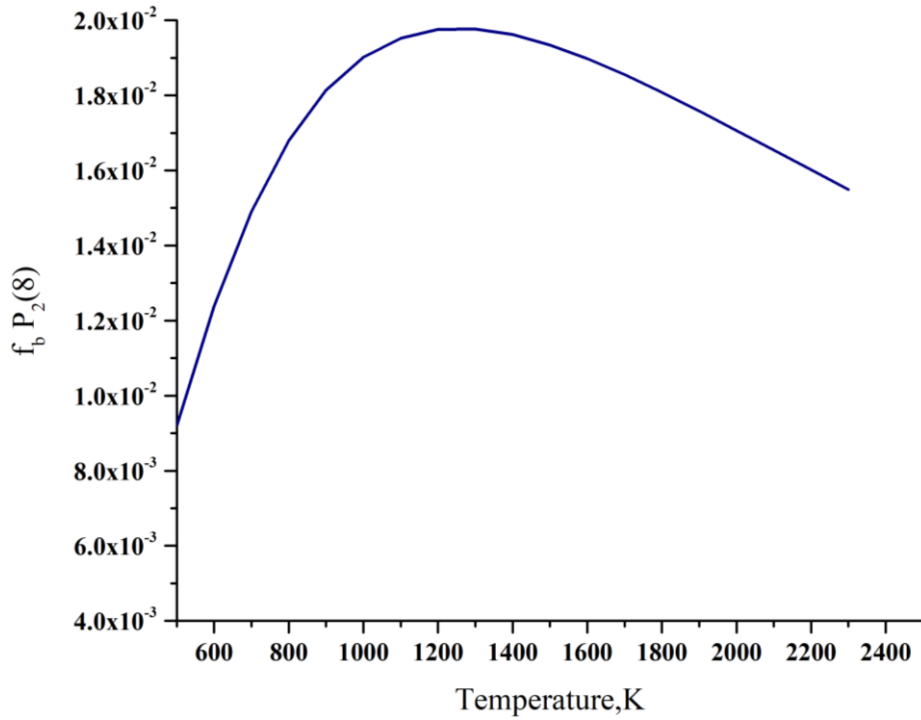


Fig.V.25: Variation of the Boltzmann factor for $N''=8$ involved in the $P_2(8)$ transition as function of the temperature.

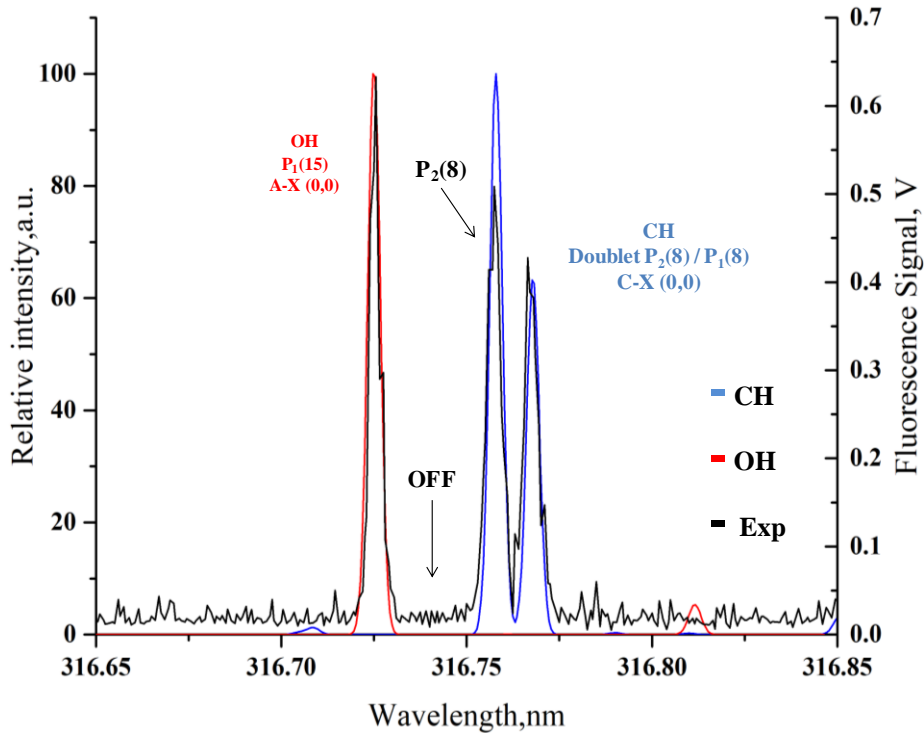


Fig. 26: Experimental CH LIF excitation spectrum and simulated LIF excitation spectra of CH and OH species at $T=1800\text{K}$ and $P=40\text{Torr}$ by LIFBASE [233].

Fig.V.26 shows the experimental LIF excitation spectrum, i.e., the evolution of the fluorescence signal with laser excitation wavelength, obtained in the reaction zone of

the M1.0 flame and the comparison with the simulated spectra of OH and CH. The different transitions have been identified using LIFBASE simulation, such as the doublet $P_1(8)/P_2(8)$ and the interfering transition $P_1(15)$ on the band A-X (0,0) of OH. The excited transition $P_2(8)$ of the band C-X (0,0) at 316.78 nm, identified on this figure, is well separated from the $P_1(8)$ and from the OH interferences.

Fig.V.26 also shows the non-resonance wavelength at 316.745 nm, where the OFF measurement is performed. This wavelength is chosen near the $P_2(8)$ transition to minimize the laser energy deviation. It is interference-free with OH fluorescence.

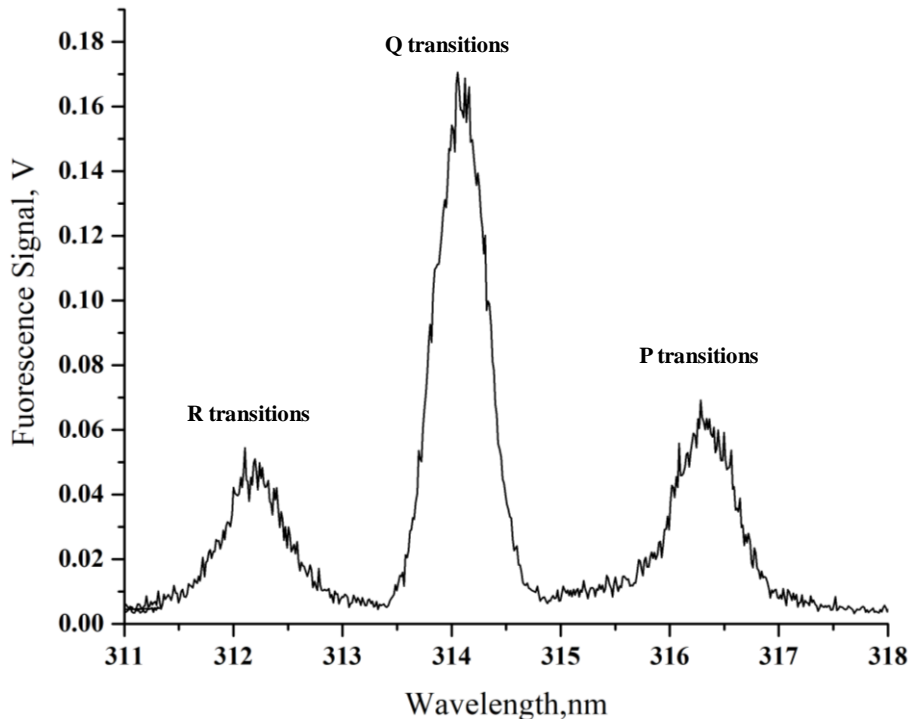


Fig.V.27: Experimental CH fluorescence spectrum in the flame M1.0.

Fig. V.27 shows the experimental CH fluorescence spectrum in the M1.0 flame. The Q transitions represent about the 50% of the emitted fluorescence. As reported by Moreau [226], this property constitutes an advantage to collect the CH fluorescence with a high efficiency and without the impact of scattering or flame emission. The entire Q-branch of C-X (0,0) band is collected with a narrow bandwidth of 1.6 nm by the spectrometer. Because of the value of the predissociative rate [30], CH measurements at low pressure are weakly affected by quenching variation.

4.3. Determination of the CH relative profiles

To obtain the CH relative population profiles, LIF measurements are performed “ON” resonance with the $P_2(8)$ transition at 316.78 nm and “OFF” resonance at 316.745 nm.

4.3.1. Relative CH profile in each flame

“ON” and “OFF” signals are averaged on 300 laser shots. As example, Fig. V.28 shows “ON” and “OFF” profiles obtained for M1.0 flame. The “OFF” signal profile is approximately constant along the height of the flame and accounts for interferences eventually induced by the laser. CH fluorescence signal is obtained by subtraction of the “OFF” signal from the “ON”.

For each studied flame, the CH fluorescence profiles are measured three times in the reaction zone between 0.5 and 8 mm. Measurements show good data reproducibility better than 3%.

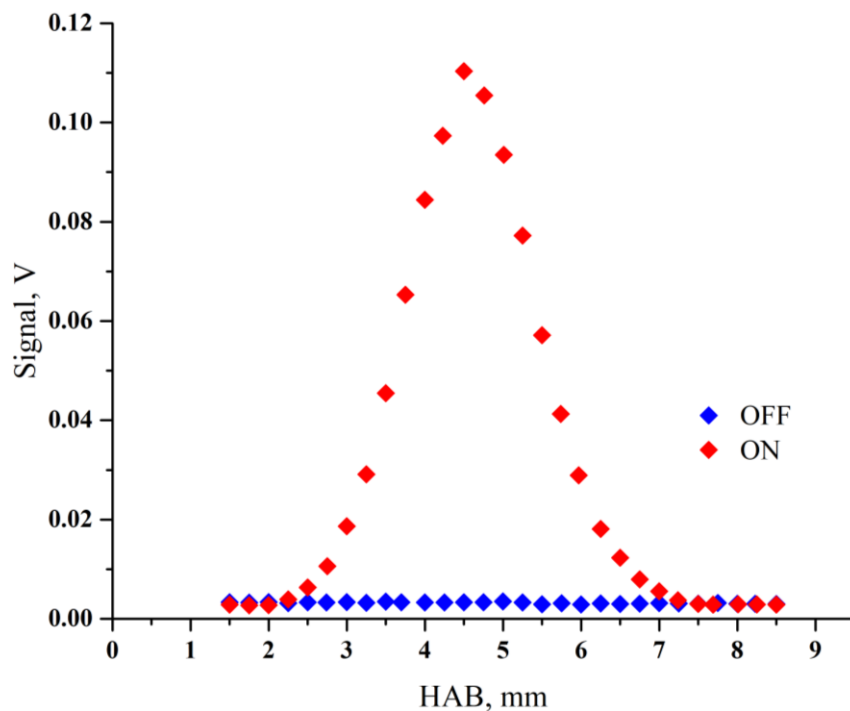


Fig. V.28: “ON” and “OFF” CH signals for flame M1.0.

As already presented for NO measurements (paragraph 3.4.2), to obtain the concentration of CH molecules (N_{CH}) from the fluorescence signal (S_{LIF}), we need to take into account different factors as reported in the equation (5.34).

$$S_{LIF} = \frac{GV\Omega}{4\pi} N_{CH} f_b(J'', v'', T) B_{12} U_\nu \frac{A_{21}}{A_{21} + Q_{21} + P} \quad (5.34)$$

Moreover, as shown for the NO measurements, the collection solid angle Ω decreases due to the geometrical configuration of the system. The correction factor is given by the equation (5.22) and it is applied from 2.96 mm down to the burner surface. This correction is important for CH detection because, the CH profile is in the reaction zone, closer than NO species to burner surface.

After this correction, we obtain the profiles of the relative rotational population $N_{j''}$ for CH radical in the flame. Fig.V.29 reports the comparison between the raw data (ON-OFF signals) and the CH $N_{j''}$ profiles in flame FM1.0.

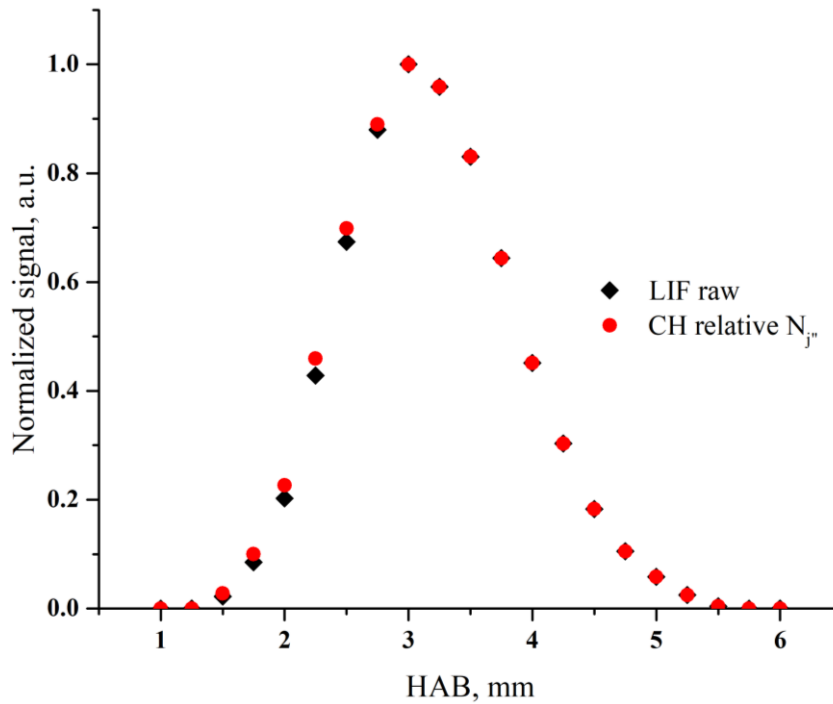


Fig.V.29: Comparison between the raw data (ON-OFF signals) and the CH $N_{j''}$ profiles in flame FM1.0.

4.3.2. Linking procedure between the flames

Similarly to the procedure performed for NO (see paragraph 3.5), the “linking procedure between the flames” is performed at the peak of CH profiles of each flame and is obtained by alternatively measuring CH LIF signals.

This step is repeated several times and the signal is detected in “ON” and “OFF” modes, averaged on 300 laser shots in order to determine $\frac{S_{LIF}^{Flame}}{S_{LIF}^{reference}}$ ratios.

These ratios are directly proportional to the ratios of the rotational populations in the ground states $\frac{N_{J^{flame}}}{N_{J^{reference}}}$. The impact of the quenching variation is negligible because of the predissociation feature of the excited level. Table V.7 shows the results of the linking procedure:

<i>Flames Ratio</i>	$\frac{N_{J^{flame}}}{N_{J^{reference}}}$	
<i>M1.2</i>	1.64	± 1.97%
<i>FMI.0</i>	1.16	± 1.17%
<i>FMI.2</i>	1.91	± 1.27%
<i>THFM1.0</i>	0.83	± 1.57%
<i>THFM1.2</i>	1.38	± 2.26%

Table V.7: CH relative rotational population ratio for the five flames with respect to the reference flame M1.0

4.3.3. LIF signal calibration: Cavity ring down spectroscopy

The relation between the measured fluorescence signals and the concentration of CH molecules (equation 5.34) contains parameters which are difficult to determine (GΩV factor, spectral energy density U_ν). Therefore, CH mole fraction profiles in flames is obtained by calibration with other techniques such as cavity ring-down spectroscopy (CRDS) ([125], [214], and [224]) or Rayleigh scattering ([219] and [223]). The calibration procedure is performed in a particular flame, called “calibration flame”. In this study, the absolute calibration of the CH fluorescence signal is performed in a flame in which the absolute CH rotational population was previously determined by Cavity ring-down spectroscopy (CRDS).

CRDS is an absorption measurement technique with excellent sensitivity. It is used to quantitatively measure minority species in many environments. This technique surpasses, by several orders of magnitude in sensitivity, other conventional absorption techniques since its principle is based on the measurement of the decay rate of the

intensity of the photons trapped between two highly reflective mirrors (constituting the optical cavity), instead of measuring the attenuation of the intensity of these photons crossing an absorbing medium.

Further details on the application of CRDS to the measurement of CH radicals can be found in the theses of Mercier [234] or Pillier [216].

The calibration flame in which CH population was determined by CRDS is a stoichiometric methane flame at 40 Torr, already studied in our lab and reported in the work of Lamoureux et al. ([7], [125], and [226]). The composition of the calibration flame is reported in Table V.8.

Flames	ϕ	χ_{N_2}	Flow sL/min			
			O_2	CH_4	N_2	TOT
<i>Calibration Flame</i>	1.00	0.69	0.960	0.480	3.350	4.790

Table V.8: Volumetric flow in standard condition ($P=1\text{atm}$, $T=0^\circ\text{C}$) in the CH calibration flame.

This flame shows a peak of CH mole fraction profile equal to 6 ppm, which corresponds to an absolute rotational population of 2.225×10^{10} molecules m^{-3} . This value has been obtained by “linking procedure between the flames”, with a rich methane flame reported in the articles from PC2A team ([125] and [226]), where the CRDS absorption measurements has been performed around the transition $P_2(8)$.

We have first applied an additional “linking procedure” between the reference flame (M1.0, stoichiometric methane flame) and the calibration flame in order to determine the ratio of their rotational populations. We obtained $N_{\text{CH}} = 2.6 \times 10^{10}$ molecules cm^{-3} in M1.0.

Then, the ratios determined in Table V.9 have been induced to determine the value of $N_{j''}$ in all the flame as shown in Table V.9.

<i>Flames</i>	$N_{J''}$ ($\#/cm^3$)
<i>M1.0</i>	2.614×10^{10}
<i>M1.2</i>	4.287×10^{10}
<i>FM1.0</i>	3.036×10^{10}
<i>FM1.2</i>	4.984×10^{10}
<i>THFM1.0</i>	3.610×10^{10}
<i>THFM1.2</i>	2.614×10^{10}

Table V.8: CH peak rotational population for the six flames.

The link between the rotational population ($N_{J''}^{CH}$) and the mole fraction (χ_{CH}) at each position of the flame is represented by the following equation:

$$\chi_{CH} = N_{J''}^{CH} \frac{T}{f_b(J'', v'', T)} \frac{k_b}{P} \quad (5.33)$$

where P is the pressure in Torr and k_b is the Boltzmann constant which can be expressed by the ratio $\frac{R}{N_A}$, where R is Ideal gas constant ($cm^3 \text{ Torr K}^{-1} \text{ mol}^{-1}$) and N_A is the Avogadro number (mol^{-1}).

Knowing the temperature profiles (preliminary profiles are in Annex B), we obtain the CH mole fraction profile for the six CH₄/F-THF/O₂/N₂ investigated flames. By considering the uncertainties of the CRDS calibration procedure, the “linking procedure between the flames” with our flames and the temperature measurements, the precision on the mole fraction values is estimated to be $\pm 15\%$.

The mole fraction values at the peak of CH profiles are shown in Table V.10:

<i>Flames Ratio</i>	$\chi_{CH} \pm 15\%$
<i>M1.0</i>	$5.38 \cdot 10^{-6}$
<i>M1.2</i>	$9.35 \cdot 10^{-6}$
<i>FM1.0</i>	$5.49 \cdot 10^{-6}$
<i>FM1.2</i>	$9.73 \cdot 10^{-6}$
<i>THFM1.0</i>	$3.96 \cdot 10^{-6}$
<i>THFM1.2</i>	$7.17 \cdot 10^{-6}$

Table V.10: Mole fractions at the peak of CH profiles for the six CH₄/F/THF/O₂/N₂ flame.

4.4. CH mole fraction profiles

The CH mole fraction profiles we obtained are shown in Fig.V.30, V.31 and V.32 for the methane (Flame M1.0 and M1.2), furan-doped flames (Flame FM1.0 and FM1.2) and THF doped flames (Flame THFM1.0 and THFM1.2), respectively.

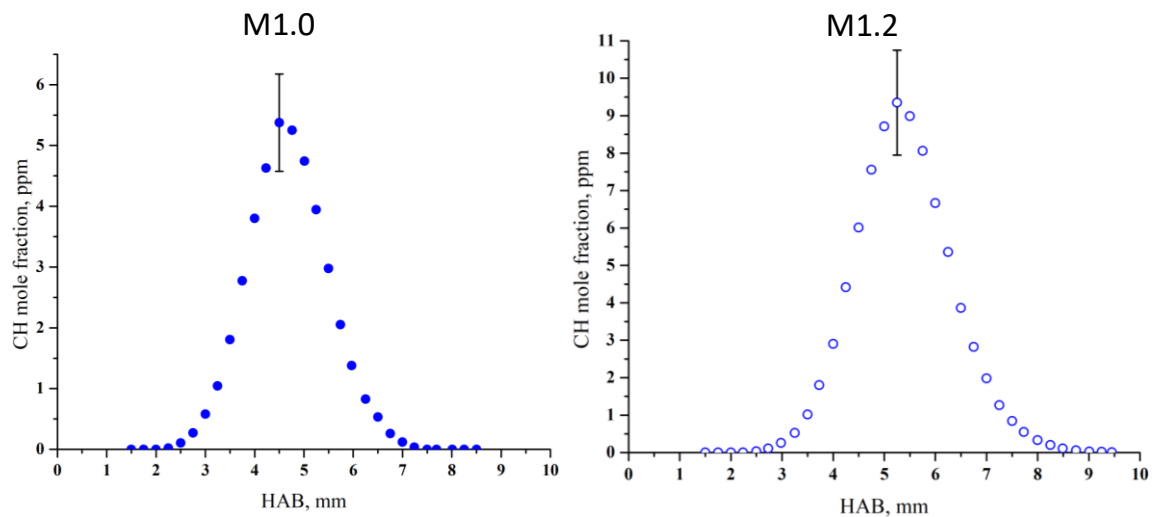


Fig.V.30: Mole fraction profiles of CH in the furan flames.

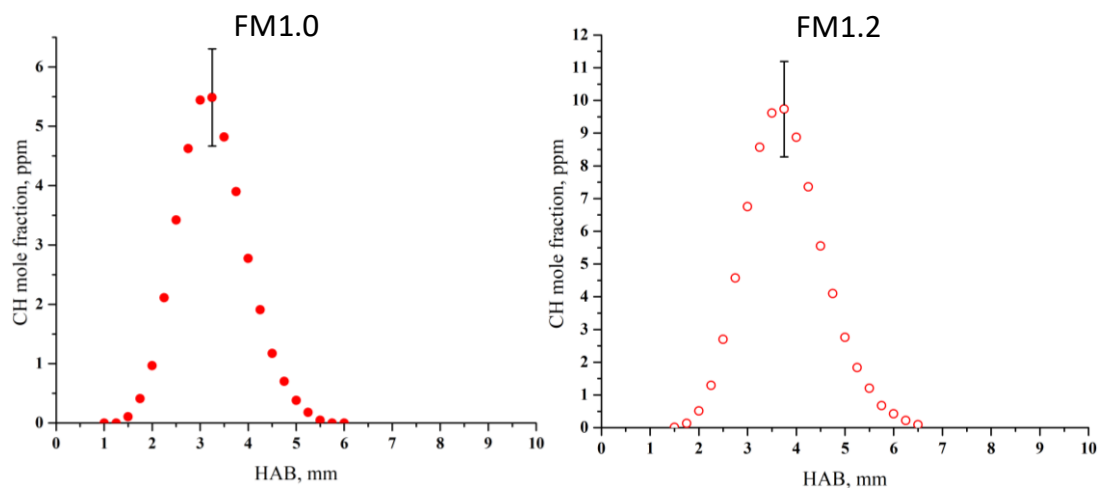


Fig.V.31: Mole fraction profiles of CH in the furan flames.

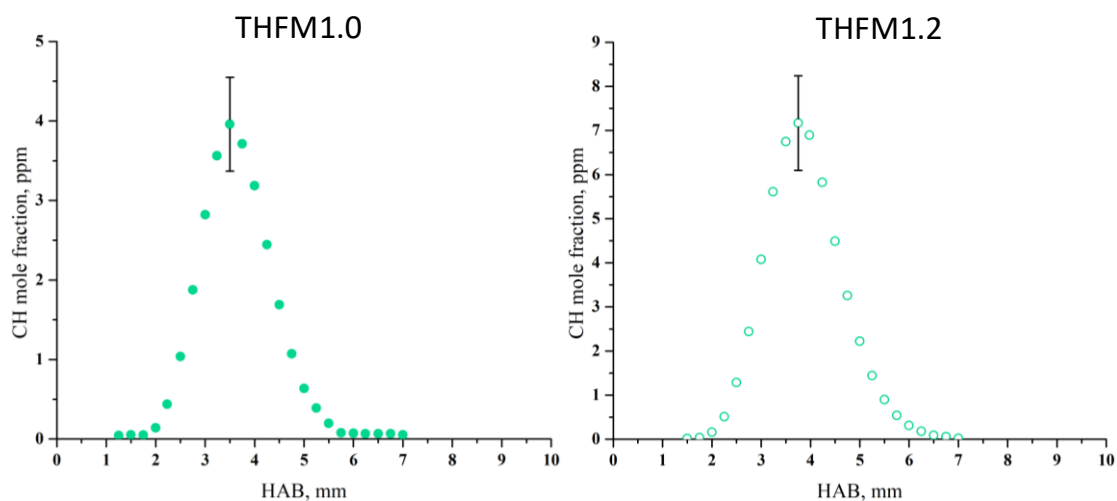


Fig.V.32: Mole fraction profiles of CH in the THF flames.

The experimental results of CH mole fraction profiles will be discussed along with NO in the next paragraph.

5. Results and discussion

In this section we discuss the results obtained for the CH and NO mole fractions profiles. At first, we discuss the effect of increasing the equivalence ratio on these species and then the behavior of the two different biofuels will be examined. In the last part, the CH experimental results will be compared with simulated profiles obtained by using the two same detailed kinetic mechanisms as in Chapter IV.

5.1. Equivalence ratio effect

The experimental CH and NO mole fraction profiles are shown in Fig.V.33, V.34 and V.35 for the methane (Flame M1.0 and M1.2), furan-doped flames (Flame FM1.0 and FM1.2) and THF doped flames (Flame THFM1.0 and THFM1.2), respectively.

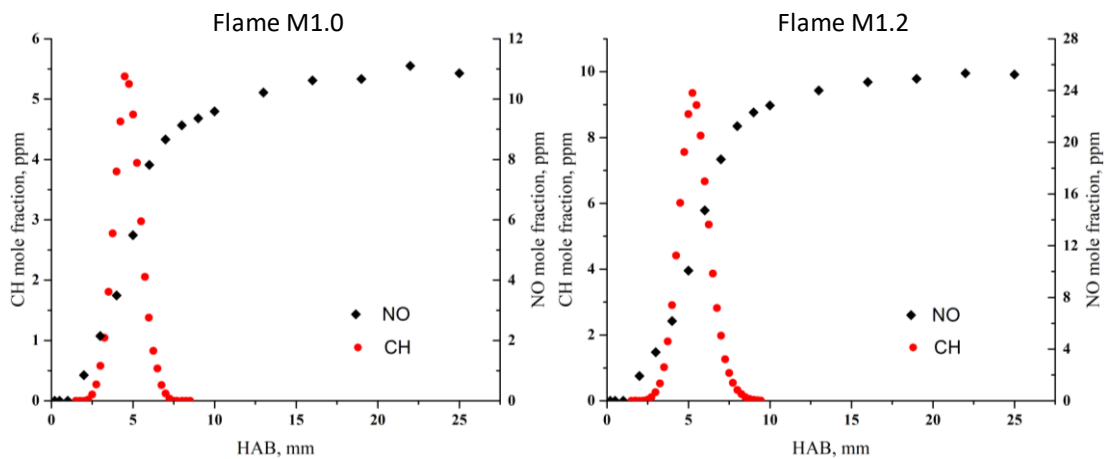


Fig.V.33: Mole fraction profiles of CH and NO in the methane flames

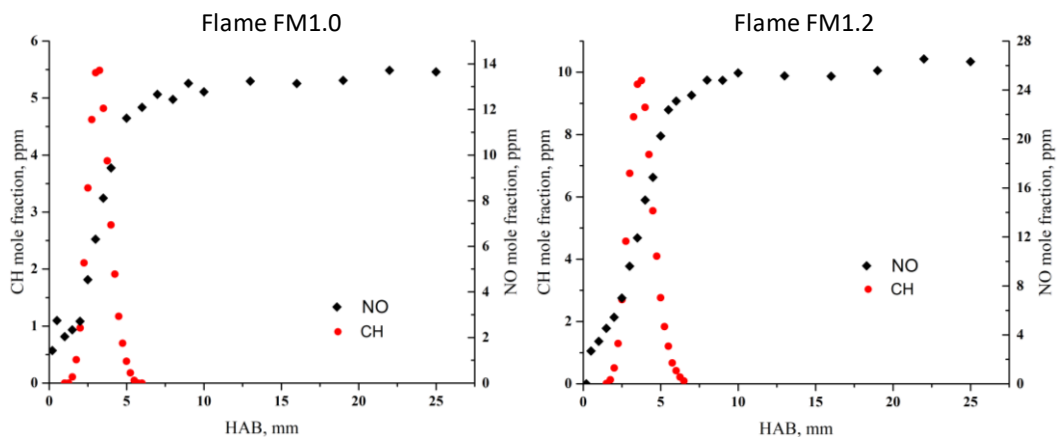


Fig.V.34: Mole fraction profiles of CH and NO in the furan doped flames.

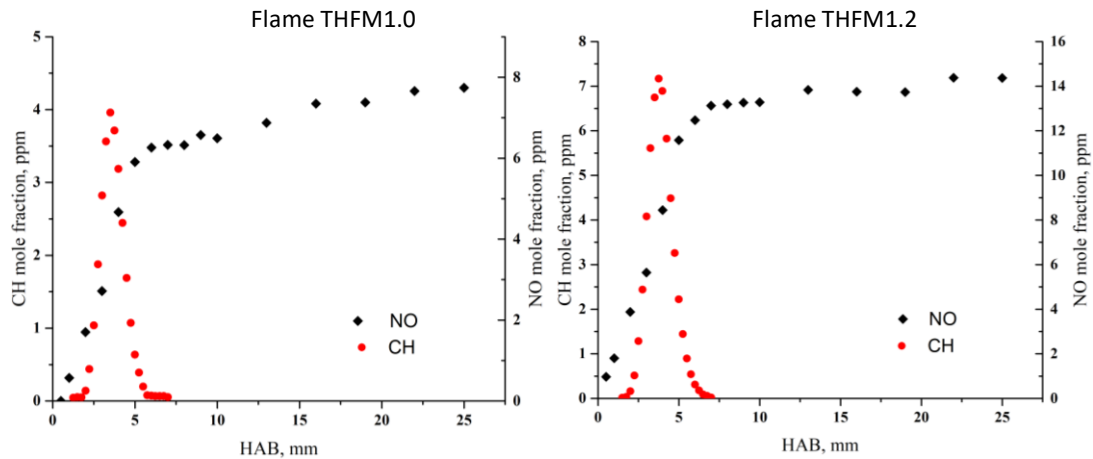


Fig.V.35: Mole fraction profiles of CH and NO in the THF doped flames

According to the prompt-NO mechanism, NO is formed in the flame front area where the CH radical is present. For each flame, the NO profile is constant in the burned gases zone indicating negligible contribution of the thermal-NO mechanism. Nevertheless, it is also noteworthy that the NO production starts upstream from the CH radical onset, as previously shown in several works ([125], [201], and [233]). The interpretation of this observation is not yet elucidated and required a modelling investigation.

Globally, the results show that the increase in the equivalence ratio corresponds to an increase in the mole fractions of both species. In particular, the increase of CH between the stoichiometric and the rich conditions corresponds to 74% for the methane flames, 77% for the doped furan flames and 81% for the doped THF flames. It is worth mentioning that these values are very close to each other.

Also in the case of NO we observe an increase between the stoichiometric and the rich conditions in the burnt gases. In particular, the mole fraction in rich conditions is 2.33 times higher than in stoichiometric conditions for methane flames, 1.92 for flames with furan and 1.86 for flames with THF.

A convenient way to link the NO behavior with that of its expected precursor is to report the NO mole fraction in the burned gases as a function of the CH at their peak locations, as shown in Fig.V.36. As references, we reported the results for NO and CH experimental mole fractions in low-pressure laminar premixed flames for different oxygenated biofuels: methyl butanoate [151], methyl-ethyl-ketone (MEK) and ethyl acetate (EA) [160]; and also for hydrocarbons C₁-C₃ ([125], [201], [202], [223], and

[226]). A modeling study performed in these flames reported in the literature, has shown that NO is formed through the prompt-NO mechanism. Despite the different flame conditions (fuel, pressure, equivalence ratio, nitrogen dilution), it is noteworthy that NO and CH mole fractions depend on each other, nearly linearly.

In this context, we can notice that the NO and CH mole fractions of the THF flames are of the same order of magnitude as the ones measured in previous oxygenated flames. On the other hand, the flames seeded with furan are close to the alkane flames. We can observe also that in acetylene flames the NO and CH mole fractions are nearly twofold higher with respect to the other fuels, but the linear relationship is still noticed. A last point to note is that in all these experiments, different equivalence ratios have been considered.

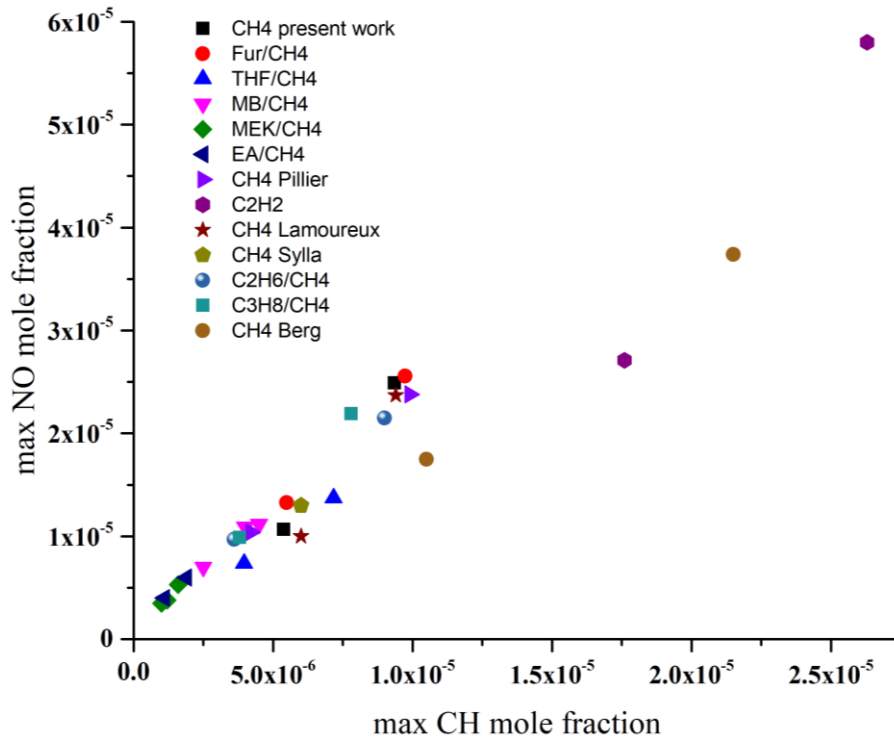


Fig.V.36: NO density in the burned gas as a function of the CH peak values for different flames stabilized at 40 Torr. Experimental data (at $P = 33$ Torr) after Pillier et al. [204] are reported with labels “CH₄Pillier”, “C₂H₆/CH₄”, “C₃H₈/CH₄”. Experimental data (at $P = 40$ Torr) after Sylla et al. [151] are reported with labels “MB/CH₄” and “CH₄ Sylla”. Experimental data (at $P = 40$ Torr) after Lamoureux et al. [127], [160], [228] are reported with labels “MEK/CH₄”, “EA/CH₄”, “C₂H₂”, “CH₄ Lamoureux”. Experimental data (at $P = 25$ -30 Torr) after Berg et al. [203], [225] are reported with labels “CH₄ Berg”.

5.2. Fuel effect.

The comparison of CH and NO mole fraction profiles obtained with the different fuel conditions at the same equivalence ratio are presented in Fig.V.37 for stoichiometric flames and in Fig.V.38 for rich flames.

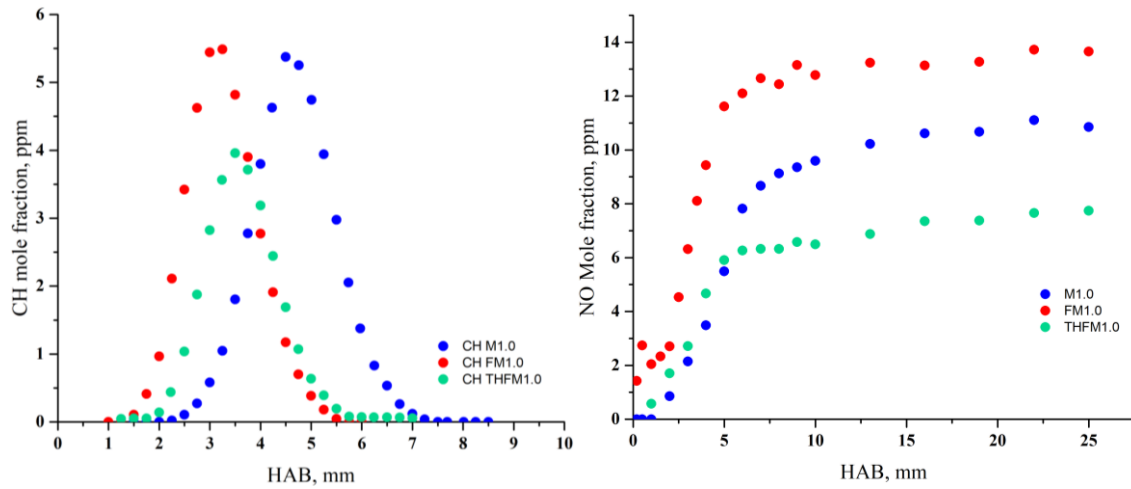


Fig.V.37: Mole fraction profiles of CH and NO for the three stoichiometric flames.

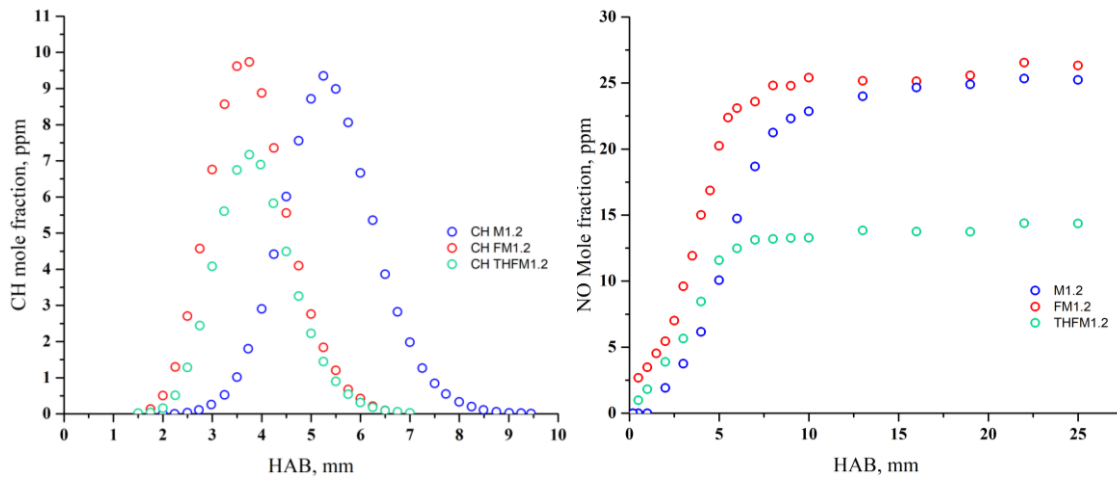


Fig.V.38: Mole fraction profiles of CH and NO in the three rich flames.

The results show that the presence of furan increases the peak of CH mole fraction with respect to methane flames. In furan flames we observe an increase of CH value in both conditions of equivalent ratio, about 2% at $\phi=1$ and 4% at $\phi=1.2$. Concomitantly an increase of NO about 24.4% in stoichiometric conditions and about only 2.7% in rich conditions is observed.

For THF flames, instead, we observe an important decrease of the CH peak values with respect to the methane and F/CH₄ flames in both conditions. In stoichiometric

THF flame, THFM1.0, we observe a reduction of CH mole fraction of 26.3% and in rich flame THFM1.2 23.3% with respect to the methane flames in the same equivalent ratio conditions. In the case of NO, a decrease is observed in the burned gases by 30.8% in stoichiometric conditions and 44.8% in rich conditions with respect to methane flames.

We can observe also that the gradient zone of the NO profiles of biofuels flames is closer to the burner surface, especially for the furan case. This is consistent with the closer stabilization of the flame observed with biofuels, notably because of their higher burning velocity with respect to methane [236].

To understand these different behaviors of these biofuels of the formation of CH and NO, we need first to investigate the kinetic formation of CH in these flames.

5.2.1. Methane flames

The CH radical is well known to be produced through the sequence $\text{CH}_3 \rightarrow {}^1\text{CH}_2 \rightarrow {}^3\text{CH}_2 \rightarrow \text{CH}$ in all hydrocarbon flames. CH_3 is the first intermediate species in methane flame [127]. In case of $\text{CH}_4/\text{O}_2/\text{N}_2$ flame, four reactions are involved in the CH_3 formation:



Then, CH_3 yields CH_2O , ${}^1\text{CH}_2$, C_2H_6 and in a less extent C_3H_6 . Indeed, the main intermediates in methane flames are ethane and formaldehyde as shown in the chromatographic results (paragraph 2.3.1.2 and 2.3.1.3 of chapter IV). Through the reaction (R.5.5) $\text{CH}_3 + \text{OH} = {}^1\text{CH}_2 + \text{H}_2\text{O}$, CH_3 leads to CH_2 singlet formation. From the kinetic analysis performed in acetylene and methane flame by Lamoureux et al [127], we can estimate that about 90% of the CH radicals are produced from ${}^3\text{CH}_2$ radicals and less than 10% are directly formed from ${}^1\text{CH}_2$ radicals in both flames. Generally, the singlet ${}^1\text{CH}_2$ radicals are rapidly converted to the ground state in the triplet state

$^3\text{CH}_2$ in each hydrocarbon and after $^3\text{CH}_2$ is converted in CH. When CH is formed, the prompt-NO mechanism can start.

5.2.2. Furan flames

As shown in Fig.V.37-38, the CH and NO mole fraction in the doped furan flames are slightly higher than those in methane. When methane is replaced by furan from flame M1.0 (C/O = 0.25) to flame FM1.0 (C/O = 0.36), the total number of C-atoms increases and in the same way the C/O ratio, while the total fuel flow decreases as shown in Table V.11:

Flames	ϕ	C/O	Fuel sL/min
M1.0	1.0	0.25	0.536
M1.2	1.2	0.29	0.640
FM1.0	1.0	0.36	0.353
FM1.2	1.2	0.42	0.404
THFM1.0	1.0	0.31	0.316
THFM1.2	1.2	0.37	0.364

Table V.11: Equivalence ratio, C/O ratio and fuel flow conditions for the six studied flames.

By observing the experimental flame structures obtained for the six $\text{CH}_4/\text{F}/\text{THF}/\text{O}_2/\text{N}_2$ flames, we can notice that in methane-furan flames, the mole fractions of acetylene is higher than that in the pure methane flames and in methane-THF flames. The formation of CH in acetylene flames is already studied by Lamoureux et al. ([125] and [226]). They observed that in rich and stoichiometric acetylene flames at low pressure, the formation of CH and consequently the prompt-NO formation is enhanced, because of the high presence of ketylenyl radicals (HCCO), which is the first intermediate species from the C_2H_2 oxidation ([237], [238]).

As reported by Park et al.[237], acetylene is mostly consumed through reactions with O:





They highlighted the importance of reaction R5.6 as dominant acetylene consumption path.). They also pointed out the importance of the reaction yielding $^1\text{CH}_2$:



This was confirmed by Shen et al. [239] which studied acetylene flames at elevated pressure.

Ketene $\text{C}_2\text{H}_2\text{O}$ is also linked to ketylenyl radicals from the following reaction:



The formation of this species is enhanced in furan oxidation at higher temperature, through the unimolecular decomposition of furan (R5.10 furan = $\text{C}_2\text{H}_2 + \text{C}_2\text{H}_2\text{O}$), as reported by Tian et al [60]. In furan oxidation, ketene is formed also at lower temperature by following the reactions [62]:



Therefore, the concentration of HCCO radicals in doped furan flames should be important.

The $^1\text{CH}_2$ radicals are produced from HCCO and CH_3 , where HCCO is the first intermediate species from the C_2H_2 oxidation, as already mentioned, and whereas CH_3 is the first intermediate species in methane flame [127]. In presence of acetylene, CH formation follows the typical sequence $^1\text{CH}_2 \rightarrow ^3\text{CH}_2 \rightarrow \text{CH}$ for hydrocarbon flames. However, the propensity to produce CH is different during acetylene and methane oxidation. Indeed, according to the literature ([125] and [226]), about 90% of the consumption of the $^3\text{CH}_2$ radicals yields CH radicals in presence of acetylene, but only about 10% of the $^3\text{CH}_2$ radicals give CH in methane flames, where $^3\text{CH}_2$ yields mainly to CH_2O and C_2H_6 . Therefore, a relevant presence of HCCO produced by acetylene and ketene in furan oxidation can explain the increase of CH formation in these flames.

HCCO radicals can also be consumed by the reaction:



This reaction pathway leads to the formation of C₂O radicals which can interact with N₂ via the reaction proposed by Williams and Fleming ([240], [241]):



This can be considered as another route for prompt-NO formation.

Regarding HCCO, it should be taken into account the direct interaction with NO through the following reaction which was shown to be important in NO-reburning processes ([242]):



For this reaction, Dagaut et al ([242]) showed that in presence of C₂H₂, NO-reburning is favored in comparison to other hydrocarbons. The products of reaction HCCO + NO may be HCNO + CO or HCN + CO₂. Tokmakov et al. [243] calculated the total rate constant of the reaction HCCO + NO, and the branching ratio between both reactions as function of temperature, showing that the second reaction prevails in the full temperature range (300–3000 K).

The interaction between NO and furanic compounds was studied also by Alexandrino et al.[169] where the decomposition of 2,5-dimethylfuran in presence of NO was investigated in flow reactor. NO-reburning was investigated in the presence of high NO concentration (900 ppm). The NO reburning was highlighted for NO mole fraction higher than 500 ppm by Berg et al [203] also in stoichiometric flames.

To conclude, HCCO could have a double effect on prompt-NO. On one side it promotes the CH and NO formation by prompt-NO mechanism, and on the other side, it may react with NO, also in stoichiometric condition, to favorite NO-reburning. These two competitive reactional pathways may explain the fact that the formation of CH, and consequently NO, does not totally correspond to the relevant present of C-atoms in furan/methane flames.

This analysis based on literature comparison gives some hypothetical explanations of the kinetics behavior of furan in prompt-NO formation. The confirmation of these hypotheses on the role of ketylenyl radicals on prompt-NO formation requires complementary modelling analysis.

5.2.3. THF flames

In THF flames, we observe a significant decrease of CH peak mole fraction in both conditions of equivalence ratio with respect to methane and methane-furan flames. The same observations hold with NO. The decrease of NO is directly induced by its link with CH through the prompt-NO mechanism.

Methane substitution by THF in our flames leads to a CH₄ decrease in the premixed gases and could partially explain the observed CH radical diminution. However, the added THF is expected to produce CH radicals also.

In our flame conditions, when methane is replaced by THF from flame M1.0 (C/O = 0.25) to flame THFM1.0 (C/O = 0.31), the total number of C-atoms increases, while the total fuel flow decreases, as already seen in case of furan/methane flames. The relative behavior of CH-peak value in these flames reflects the impact of THF in the fuel flow rate. However, because of THF, an increase of the CH mole fraction is also expected due to the increase of the total number of C-atoms in flames. Methane and THF may produce CH₃ radicals with different efficiencies, which then is converted into CH radicals according to the C₁ route. As it occurs for methane, the formation of CH₂ from CH₃ in THF oxidation could be in competition with the formaldehyde (CH₂O) formation. Due to the high concentration of CH₂O we observed in THF flames (see paragraph 2.3.4.2 in Chapter IV), an explanation of the decrease of CH peak mole fraction in THF flames could be linked to the promoted formation of formaldehyde with respect to CH₂ radicals. Consequently, NO formation, mainly due to the prompt-NO mechanism, decreases when methane is replaced by THF.

We can observe that for THF, the decrease of NO mole fraction in burnt gases is more pronounced than the decrease of CH peak mole fraction. This effect is more evident in rich conditions than in stoichiometric conditions. One explanation could be the implication of oxygenated species (such as CH₂O) to the reburning processes. Indeed, CH₂O formation is enhanced in THF oxidation with respect to methane oxidation. According to the literature [151], CH₂O can form HCO radicals, also earlier in the flame front, through the two following reactions:



However, HCO could react with NO, also closer to the burner surface, according to the reaction:



The importance of this reaction was previously mentioned by Alzueta et al.[244].

From our experimental observations, formaldehyde formation during furan oxidation is comparable to those during THF oxidation. This can suggest that the reburning process favored in presence of HCO radicals may also have an effect in furan-methane flames.

The presented analysis gives some interesting tracks, which need further confirmation notably using the rate of production (ROP) analysis, which will be performed as further analysis.

5.3. Comparison between experimental and numerical results for CH

CH mole fraction profiles measured by LIF are compared with modelling in Fig.V.39, V.40 and V.41 for the methane (Flame M1.0 and M1.2), furan-doped flames (Flame FM1.0 and FM1.2) and THF-doped flames (Flame THFM1.0 and THFM1.2), respectively. Simulations were performed by using the kinetic mechanisms detailed in chapter 4 and proposed by Tran et al.[6] and Fenard et al. [7], called in this work Tran and Fenard, respectively.

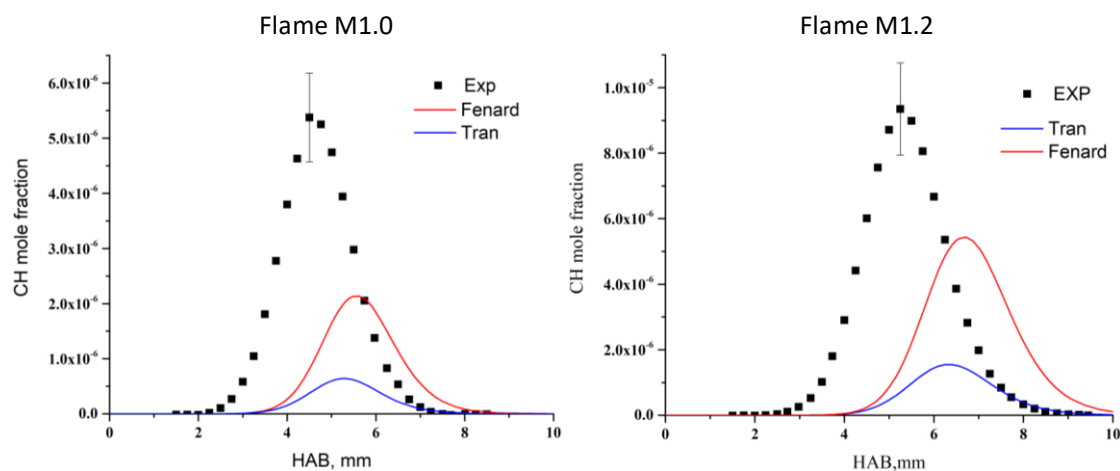


Fig.V.39: CH profiles measured by LIF in M1.0 and M1.2 methane flames. Comparison with the simulated ones by using TRAN [6] and FENARD [7].

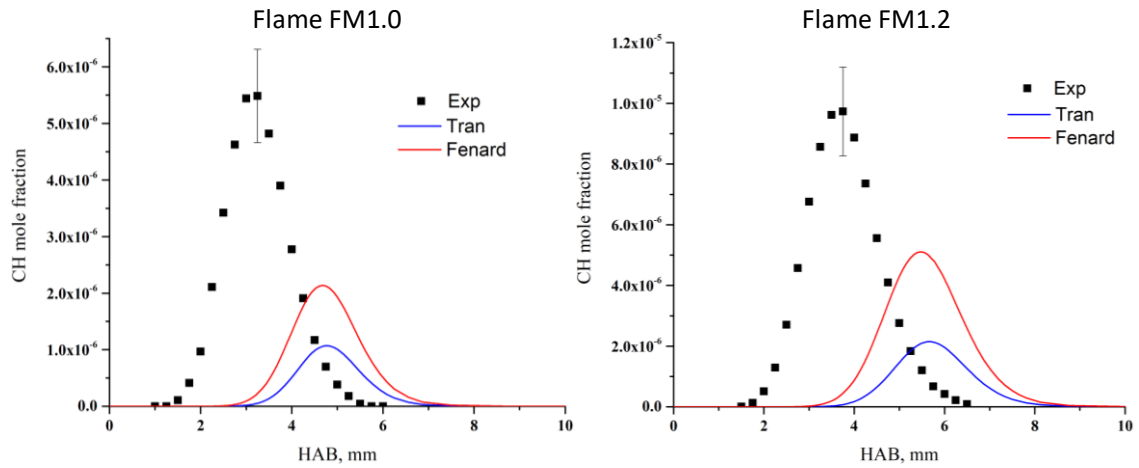


Fig.V.40: CH profiles measured by LIF in FM1.0 and FM1.2, furan doped flames.

Comparison with the simulated ones by using TRAN [6] and FENARD [7]

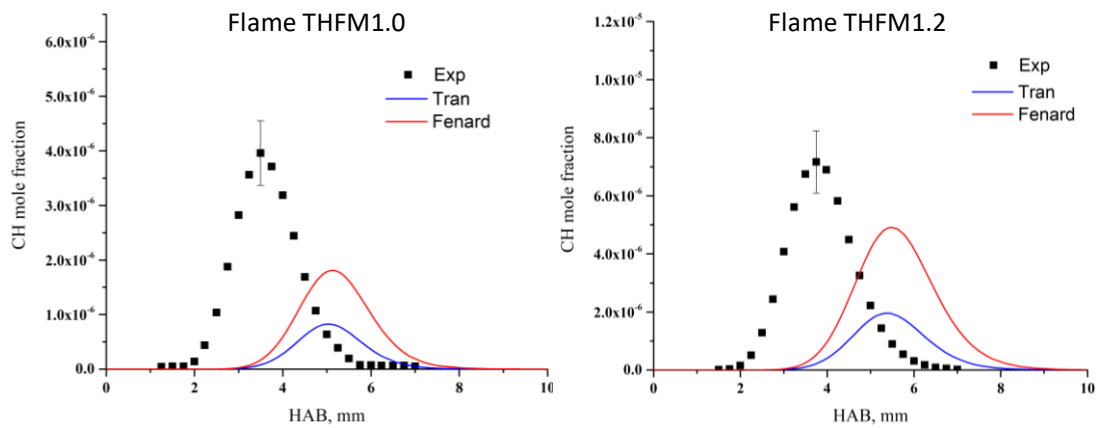


Fig.V.41: CH profiles measured by LIF in THFM1.0 and THFM1.2, THF doped flames.

Comparison with the simulated ones by using TRAN [6] and FENARD [7]

By observing the comparison between experimental and simulated CH profiles, it can be noticed that both models underestimate the CH peak mole fraction in the six flames. The phenomena is systematically more pronounced with the Tran mechanism [6].

Another point is that the position of the modelled CH peak mole fraction is invariably shifted towards burnt gases, with respect to the experimental results for both models.

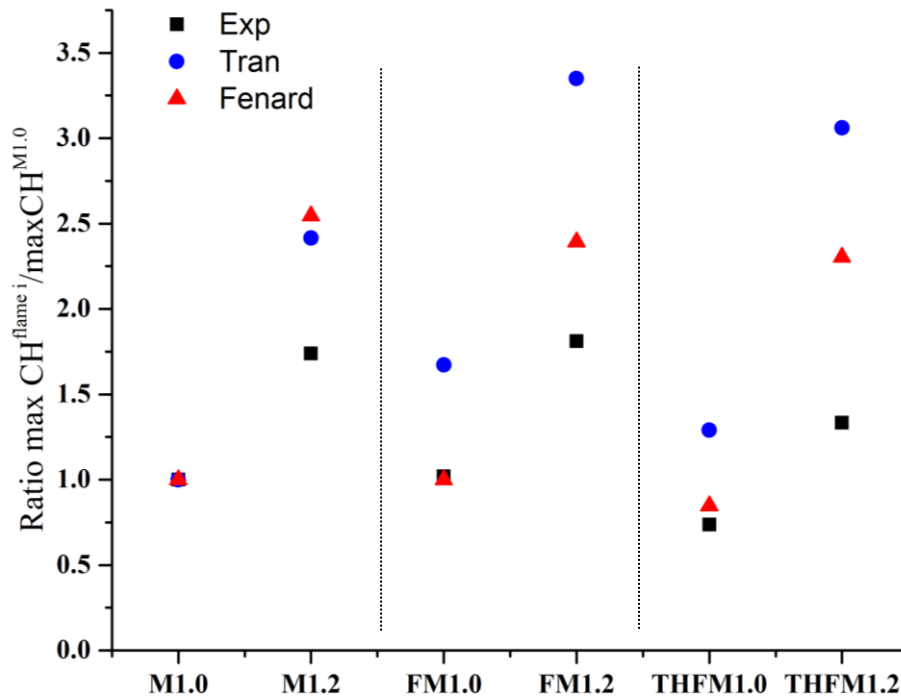


Fig.V.42: Ratio of CH peak mole fraction of each flames to the CH peak in flame M1.0 ($CH^{flame i}/CH^{M1.0}$) for experimental and simulated results.

In order to evaluate the ability of the two kinetic mechanisms to correctly predict CH radical evolution (and thus NO from prompt-NO) with the fuel mixture (methane, furan-methane, or THF-methane), we have also examined the prediction of the relative variation of the amount of CH for the six experimental conditions. For that we have calculated the ratio of the peak value of CH mole fraction of each flames with the peak value in stoichiometric methane flame M1.0 ($CH^{flame i}/CH^{M1.0}$) for experimental and simulated results. The results are presented in Fig.V.42.

The experimental ratio for stoichiometric flames for all fuel conditions is better predicted by the Fenard mechanism. The Tran mechanism overestimates this ratio by about 34% with respect to the experimental values.

For rich conditions, both mechanisms overestimate the ratio $CH^{flame i}/CH^{M1.0}$. For the methane/air flame, the two mechanisms overpredict the ratio value of about 25%. Instead, in furan doped flames the ratios are overestimated by about 42% for the Tran mechanism and by about 20% with Fenard mechanism. For the THF-methane flames, the overestimation reaches 55% with the Tran mechanism and near 40% with Fenard one.

This preliminary analysis shows that the two models, which are used for the first time for CH prediction, require some improvements before being coupled to the sub-mechanism for NO formation [8].

6. Conclusions

In this chapter, the determination of NO and CH concentrations by laser induced fluorescence in CH₄/Furan-THF/O₂/N₂ low-pressure flames has been presented. The experimental methodology we chose, and the results we obtained have been discussed with reference to the literature.

NO and CH were qualitatively detected by Laser-Induced Fluorescence (LIF). A tunable dye laser was used to excite NO on the Q₂(27) transition of the A-X (0,0) at 225.58 nm and CH on the P₂(8) transition of the C-X (0,0) at 317 nm.

Fluorescence signal was collected at 90° through a spectrometer with a spectral bandwidth adjusted to collect the entire vibrational band A-X (0-2) of NO, and the Q-branch C-X (0-0) of CH.

Absolute calibration was performed for NO by using NO doping method in a reference flame and for CH by comparison with results obtained by Cavity ring-down spectroscopy (CRDS) in a similar methane flame as ours.

The experimental results show that the different molecular structure of furan and THF also affects NO formation which depends on the CH_i radicals production during the fuel oxidation. In the same way, furan oxidation promotes (i) CH formation in both examined equivalence ratio conditions compared to THF seeded flames, and (ii) NO formation compared to methane flames. The unsaturated chemical structure of furan favors the formation of intermediate species, such as acetylene, which promotes the formation of radicals that could be involved in prompt-NO mechanism. More information will be obtained when the reaction pathway analysis will be performed.

By comparing CH experimental results with simulated profiles from the kinetic mechanisms proposed by Tran et al.[6] and Fenard et al. [7], the preliminary modelling approach indicates that the investigated mechanisms need first to be improved for CH formation before being coupled to a NO-sub mechanism for fulfilling the final aim of this thesis.

General conclusions and perspectives

The use of biofuels allows a reduction of the dependence to petroleum-based fuels and should limit the increase of total amount of greenhouse gases in the atmosphere. In this regard, unsaturated and saturated cyclic ethers produced from lignocellulosic biomass, are attractive oxygenated fuels, due to their combustion properties comparable to those of commercial gasolines. The use of these compounds may represent a very interesting alternative to fossil fuels, but their impact on the emissions of pollutants needs further experimental and theoretical evaluations, particularly for NO_x.

In this study, we decided to study furan (F) and tetrahydrofuran (THF) as model-biofuels because they are the core of the oxidation of the most complex furanic compounds. In particular, we were interested in understanding how the different degree of unsaturation of these oxygenated compounds can affect the prompt-NO formation.

In this context, the objectives of this thesis were (1) to study the chemical structure of flames of methane/furan and methane/tetrahydrofuran blends in stoichiometric and slightly rich conditions, and (2) to evaluate the impact of the combustion of these oxygenated compounds on the prompt-NO formation.

The first step in this work was therefore the chemical structure analysis of CH₄/F/THF/O₂/N₂ laminar flames. The laboratory reactor used is a flat flame burner positioned in a low pressure combustion chamber. Six premixed low-pressure laminar flames (5.3 kPa) were studied under stoichiometric and slightly rich conditions ($\phi = 1.2$). The considered fuel compositions are: (i) pure methane, which is used as a reference flame, (ii) a furan (50%)/methane (50%) mixture to study the effect of furan, and (iii) tetrahydrofuran (50%)/methane (50%) to evaluate the impact of THF. The structure of these flames was characterized by establishing the mole fraction profiles of stable intermediates and products using Gas Chromatography. Two GC devices are used: a first GC -Mass Spectrometer (MS) for the identification of species; a second GC coupled with Flame Ionisation Detector (FID) and Thermal Conductivity Detector (TCD) for the quantification of the detected compounds. Calibration of absolute

concentration profiles was performed using appropriate standard mixtures. In particular a new method to calibrate formaldehyde was presented.

Sixty-five chemical species were identified and quantified in the six examined flames. Despite the similar structure of these two biofuels, the various detected compounds indicate the different kinetic behaviors of F and THF, notably due to the different degree of unsaturation of the molecules. The formation of hydrocarbon species, in particular dienes and alkynes, is enhanced by F with respect to THF. Acetylene (C_2H_2) is the most abundant C_2 hydrocarbons in furan/methane flames, while in THF/methane flames ethylene (C_2H_4) is the most important one. Propene (C_3H_6) is enhanced in both fuel mixtures, supported also by the copious radical pool issued from methane oxidation. This could be an example of synergy between the methane and furanic compounds. Oxygenated species formation is enhanced in methane/THF flames with respect to F/methane flames. Acetaldehyde (CH_3CHO) is the most abundant oxygenated species issued by F flames, while in THF oxidation it is formaldehyde (CH_2O). Some typical low temperature combustion oxygenated species were also detected in our flames such as butanedial ($C_4H_6O_2$) and methyl-oxirane (C_3H_6O).

NO and CH were qualitatively detected by Laser-Induced Fluorescence (LIF). A tunable dye laser was used to excite NO on the $Q_2(27)$ transition of the A-X (0,0) at 225.58 nm and CH on the $P_2(8)$ transition of the C-X (0,0) at 317 nm. Absolute calibration was performed for NO by using NO doping method in a reference flame and for CH by comparison with previous results obtained by Cavity ring-down spectroscopy (CRDS).

The experimental results show that the different molecular structure of furan and THF also affects NO formation which depends on the CH_i radicals production during the fuel oxidation. In the same way, F oxidation promotes (i) CH formation in both examined equivalence ratio conditions compared to THF seeded flames, and (ii) NO formation compared to methane flames. The unsaturated chemical structure of furan favors the formation of intermediate species, such as acetylene, which promotes the formation of radicals that could be involved in prompt-NO mechanism. In THF flames we observed an important reduction of the formation of CH radicals with respect to other fuels mixture in both equivalent ratio conditions. Some hypotheses are proposed to explain the obtained results in F and THF flames; but more information will be obtained when the reaction pathway analysis will be performed.

In addition to this experimental work, two literature chemical mechanisms have then been evaluated in our flame conditions: the mechanism of Tran et al. [6] and the mechanism of Fenard et al. [7]. The comparison of the modelling results carried out by using the Cantera code usually leads to a satisfactory agreement with the experimental profiles, particularly by using Fenard mechanism. However, divergences remain for some hydrocarbons and oxygenated intermediates, which may impact the prediction of prompt-NO.

By comparing CH experimental results with simulated profiles from the kinetic mechanisms proposed by Tran et al.[6] and Fenard et al. [7], we observed that both models underestimate the formation of this key radical in all flames. Significant variations from one model to another are found.

The preliminary modelling of CH mole fractions indicates that the investigated mechanisms need first to be improved for CH formation before being coupled to a NO-sub-mechanism for fulfilling the final aim of this thesis. This improvement will be based (1) on the analysis of the two mechanisms in order to identify the predominant reactional pathways involved in CH formation during oxidation of these biofuels, and (ii) on the adjustment of some rate constants to improve the experiment-modelling agreement.

In the light of this experimental study, more attention should be given to the kinetic behavior of fuels from the point of view of their degree of unsaturation with respect to the formation of NO_x, particularly for aromatic fuels (such as benzene, toluene) and biofuels (such as tetrahydropyran, anisole, vanillin,..) which are increasingly used as additives in commercial gasolines and diesel to improve combustion in engine conditions.

References

- [1] IEA (International Energy Agency), “World energy balances 2018: Overview,” 2018.
- [2] “Directive 2003/30/EC of the European Parliament and of the Council of 8 May 2003 on the promotion of the use of biofuels or other renewable fuels for transport.” [Online]. Available: <https://eur-lex.europa.eu/legal-content/EN/ALL/?uri=celex%3A32003L0030>.
- [3] Ş. Altun, “Effect of the degree of unsaturation of biodiesel fuels on the exhaust emissions of a diesel power generator,” *Fuel*, vol. 117, pp. 450–457, 2014.
- [4] A. Balakrishnan, R. N. Parthasarathy, and S. R. Gollahalli, “Effects of degree of fuel unsaturation on NO_x emission from petroleum and biofuel flames,” *Fuel*, vol. 182, pp. 798–806, 2016.
- [5] M. Lapuerta, J. Rodríguez-Fernández, and E. F. de Mora, “Correlation for the estimation of the cetane number of biodiesel fuels and implications on the iodine number,” *Energy Policy*, vol. 37, no. 11, pp. 4337–4344, 2009.
- [6] L. S. Tran, Z. Wang, H. H. Carstensen, C. Hemken, F. Battin-Leclerc, and K. Kohse-Höinghaus, “Comparative experimental and modeling study of the low- to moderate-temperature oxidation chemistry of 2,5-dimethylfuran, 2-methylfuran, and furan,” *Combust. Flame*, vol. 181, pp. 251–269, 2017.
- [7] Y. Fenard, A. Gil, G. Vanhove, H. H. Carstensen, K. M. Van Geem, P. R. Westmoreland, O. Herbinet, and F. Battin-Leclerc, “A model of tetrahydrofuran low-temperature oxidation based on theoretically calculated rate constants,” *Combust. Flame*, vol. 191, pp. 252–269, 2018.
- [8] N. Lamoureux, H. El Merhubi, L. Pillier, S. de Persis, and P. Desgroux, “Modeling of NO formation in low pressure premixed flames,” *Combust. Flame*, vol. 163, pp. 557–575, 2016.
- [9] “NO_x - CITEPA.” [Online]. Available: <https://www.citepa.org/fr/air-et-climat/polluants/aep-item/oxydes-d-azote>.
- [10] “Standards - Air Quality - Environment - European Commission.” [Online]. Available: <http://ec.europa.eu/environment/air/quality/standards.htm>.
- [11] C. Russo, L. Giarracca, F. Stanzione, B. Apicella, A. Tregrossi, and A. Ciajolo, “Sooting structure of a premixed toluene-doped methane flame,” *Combust. Flame*, vol. 190, pp. 252–259, 2017.
- [12] “Global Greenhouse Gas Emissions Data | Greenhouse Gas (GHG) Emissions | US EPA.” [Online]. Available: <https://www.epa.gov/ghgemissions/global-greenhouse-gas-emissions-data>.
- [13] “EUR-Lex - 32003L0017 - EN - EUR-Lex.” [Online]. Available: <https://eur-lex.europa.eu/legal-content/EN/TXT/?qid=1435618704689&uri=CELEX:32003L0017>.
- [14] “EUR-Lex - 31993L0012 - EN,” *Official Journal L 074*, 1993. [Online]. Available: <https://eur-lex.europa.eu/legal-content/EN/TXT/HTML/?uri=CELEX:31993L0012&qid=1435619606375&from=EN>.

- [15] IEA, “Energy Technology RD&D budgets 2018 : overview,” 2018.
- [16] “Histoire de l’utilisation des biocarburants.” [Online]. Available: <https://www.connaissancedesenergies.org/le-biocarburant-est-une-innovation-du-xxie-siecle>.
- [17] D. Ballerini and N. Alazard-Toux, *Les biocarburants : état des lieux, perspectives et enjeux du développement*. Paris: Éditions Technip, 2006.
- [18] B. GAGNEPAIN, “Biocarburants,” *Tech. l’ingénieur Énergies renouvelables*, vol. base docum, no. ref. article : be8550, 2016.
- [19] “La 1re génération de biocarburants.” [Online]. Available: <http://www.ifpenergiesnouvelles.fr/Espace-Decouverte/Les-grands-debats/Quel-avenir-pour-les-biocarburants/La-fabrication-des-biocarburants-2-generations/La-1re-generation-de-biocarburants>.
- [20] “Industry Statistics – Renewable Fuels Association.” [Online]. Available: <https://ethanolrfa.org/resources/industry/statistics/>.
- [21] R. Sims, M. Taylor, J. Saddler, and W. Mabee, “From 1st to 2nd Generation Bio Fuel Technologies: An overview of current industry and RD&D activities,” 2008.
- [22] M. Combe, “Les biocarburants de première génération limités ? | Techniques de l’ingénieur,” *Techniques de l’ingénieur*, 2015.
- [23] D. Lorne, “Des biocarburants à partir de microalgues : comment ça marche ? | Techniques de l’ingénieur,” *Techniques de l’ingénieur*, 2011.
- [24] M. Kumar and M. P. Sharma, “Kinetics of Transesterification of Chlorella Protothecoides Microalgal Oil to Biodiesel,” *Waste and Biomass Valorization*, vol. 7, no. 5, pp. 1123–1130, 2016.
- [25] H. Xu, X. Miao, and Q. Wu, “High quality biodiesel production from a microalga Chlorella protothecoides by heterotrophic growth in fermenters,” *J. Biotechnol.*, vol. 126, no. 4, pp. 499–507, 2006.
- [26] U. Ihemere, D. Arias-Garzon, S. Lawrence, and R. Sayre, “Genetic modification of cassava for enhanced starch production,” *Plant Biotechnol. J.*, vol. 4, no. 4, pp. 453–465, Jul. 2006.
- [27] “Generations of Biofuels - Energy from waste and wood.” [Online]. Available: <http://energyfromwasteandwood.weebly.com/generations-of-biofuels.html>.
- [28] “The Secretary of Synthetic Biology - Resilience.” [Online]. Available: <https://www.resilience.org/stories/2009-03-27/secretary-synthetic-biology/>.
- [29] E.-M. Aro, “From first generation biofuels to advanced solar biofuels,” *Ambio*, vol. 45, no. S1, pp. 24–31, 2016.
- [30] C. Halfmann, L. Gu, W. Gibbons, and R. Zhou, “Genetically engineering cyanobacteria to convert CO₂, water, and light into the long-chain hydrocarbon farnesene,” *Appl. Microbiol. Biotechnol.*, vol. 98, no. 23, pp. 9869–9877, 2014.
- [31] F. Broust, P. Girard, L. Van, and D. E. Steene, “Biocarburants de seconde génération,” 2008.

- [32] F. H. Isikgor and C. Remzi Becer, "Lignocellulosic Biomass: A Sustainable Platform for Production of Bio-Based Chemicals and Polymers."
- [33] D. W. Wakerley, M. F. Kuehnel, K. L. Orchard, K. H. Ly, T. E. Rosser, and E. Reisner, "Solar-driven reforming of lignocellulose to H₂ with a CdS/CdOx photocatalyst," *Nat. Energy*, vol. 2, no. 4, p. 17021, 2017.
- [34] D. Kumari and R. Singh, "Pretreatment of lignocellulosic wastes for biofuel production: A critical review," *Renew. Sustain. Energy Rev.*, 2018.
- [35] Bio-based industries Consortium, "Mapping European Biorefineries | Bio-Based Industries Consortium." [Online]. Available: <https://biconsortium.eu/news/mapping-european-biorefineries>.
- [36] A. Bouter and D. Lorne, "IFPEN Tableau de bord biocarburants 2018," pp. 1–4, 2018.
- [37] R. Réocreux, C. Michel, C. Grison, and J. Barrault, "Rational design of heterogeneous catalysts for biomass conversion - Inputs from computational chemistry," *Curr. Opin. Green Sustain. Chem.*, vol. 10, pp. 51–59, 2018.
- [38] C. Cavallotti, A. Cuoci, T. Faravelli, A. Frassoldati, M. Pelucchi, and E. Ranzi, "Detailed Kinetics of Pyrolysis and Combustion of Catechol and Guaiacol, as Reference Components of Bio-Oil from Biomass," in *Chemical Engineering Transactions*, , vol. 65, 2018
- [39] E. Ranzi, M. Costa, M. Pelucchi, T. Faravelli, A. Frassoldati, G. Sribala, G. B. Marin, and K. M. Van Geem, "Experimental and Kinetic Modeling Study of Pyrolysis and Combustion of Anisole," in *Chemical Engineering Transactions*, vol. 65. 2018.
- [40] J. S. Luterbacher, D. Martin Alonso, and J. A. Dumesic, "Targeted chemical upgrading of lignocellulosic biomass to platform molecules," *Green Chem.*, vol. 16, no. 12, pp. 4816–4838, 2014.
- [41] F. M. Yedro, H. Grénman, J. V. Rissanen, T. Salmi, J. García-Serna, and M. J. Cocero, "Chemical composition and extraction kinetics of Holm oak (*Quercus ilex*) hemicelluloses using subcritical water," *J. Supercrit. Fluids*, vol. 129, pp. 56–62, 2017.
- [42] Y. Luo, Z. Li, X. Li, X. Liu, J. Fan, J. H. Clark, and C. Hu, "The production of furfural directly from hemicellulose in lignocellulosic biomass: A review," *Catal. Today*, pp. 1–0, 2018.
- [43] S. Thion, A. M. Zaras, M. Szóri, and P. Dagaut, "Theoretical kinetic study for methyl levulinate: oxidation by OH and CH₃ radicals and further unimolecular decomposition pathways," *Phys. Chem. Chem. Phys.*, vol. 17, no. 36, pp. 23384–23391, 2015.
- [44] L. S. Tran, B. Sirjean, R. Fournet, and F. Battin-Leclerc, "Progress in detailed kinetic modeling of the combustion of oxygenated components of biofuels," *Energy*, vol. 43, no. 1, pp. 4–18, 2012.
- [45] N. Xu, J. Gong, and Z. Huang, "Review on the production methods and fundamental combustion characteristics of furan derivatives," *Renew. Sustain. Energy Rev.*, vol. 54, pp. 1189–1211, 2016.
- [46] T. Kessler, E. R. Sacia, A. T. Bell, J. H. Mack, and J. H. Mack, "Artificial neural network based predictions of cetane number for furanic biofuel additives," *Fuel*, vol. 206, pp. 171–179, 2017.

- [47] A. Sudholt, L. Cai, J. Heyne, F. M. Haas, H. Pitsch, and F. L. Dryer, "Ignition characteristics of a bio-derived class of saturated and unsaturated furans for engine applications," *Proc. Combust. Inst.*, vol. 35, no. 3, pp. 2957–2965, 2015.
- [48] L. S. Tran, "Etude De La Formation De Polluants Lors De La Combustion De Carburants Oxygenes," 2013.
- [49] H. Zhao, J. E. Holladay, H. Brown, and Z. C. Zhang, "Metal Chlorides in Ionic Liquid Solvents Convert Sugars to 5-Hydroxymethylfurfural," *Science (80-.)*, vol. 316, no. 5831, pp. 1597–1600, 2007.
- [50] M. Mascal and E. B. Nikitin, "Direct, High-Yield Conversion of Cellulose into Biofuel," *Angew. Chemie Int. Ed.*, vol. 47, no. 41, pp. 7924–7926, 2008.
- [51] Y. Román-Leshkov, C. J. Barrett, Z. Y. Liu, and J. A. Dumesic, "Production of dimethylfuran for liquid fuels from biomass-derived carbohydrates," *Nature*, vol. 447, no. 7147, pp. 982–985, 2007.
- [52] S. Sitthisa, W. An, and D. E. Resasco, "Selective conversion of furfural to methylfuran over silica-supported NiFe bimetallic catalysts," *J. Catal.*, vol. 284, no. 1, pp. 90–101, 2011.
- [53] M. A. Grela, V. T. Amorebieta, and A. J. Colussi, "Very low pressure pyrolysis of furan, 2-methylfuran and 2,5-dimethylfuran. The stability of the furan ring," *J. Phys. Chem.*, vol. 89, no. 1, pp. 38–41, 1985.
- [54] M. M. Thornton, P. C. Malte, and A. L. Crittenden, "Oxidation of furan and furfural in a well-stirred reactor," *Twenty-first Symp. Combust. Combust. Inst.*, pp. 979–989, 1986.
- [55] A. Lifshitz, M. Bidani, and S. Bidani, "Thermal reactions of cyclic ethers at high temperatures. III. Pyrolysis of furan behind reflected shocks," *J. Phys. Chem.*, vol. 90, no. 21, pp. 5373–5377, 1986.
- [56] P. P. Organ and J. C. Mackie, "Kinetics Pyrolysis Furan," *J. Chem. Soc. Faraday Trans.*, vol. 87, no. 6, pp. 815–823, 1991.
- [57] D. Fulle, A. Dib, J. H. Kiefer, Q. Zhang, J. Yao, and R. D. Kern, "Pyrolysis of furan at low pressures: Vibrational relaxation, unimolecular dissociation, and incubation times," *J. Phys. Chem. A*, vol. 102, no. 38, pp. 7480–7486, 1998.
- [58] K. Sendt, G. B. Bacskay, and J. C. Mackie, "Pyrolysis of Furan : Ab Initio Quantum Chemical and Kinetic Modeling Studies," *J. Phys. Chem. A*, vol. 104, pp. 1861–1875, 2000.
- [59] A. G. Vasiliou, M. R. Nimlos, J. W. Daily, and G. B. Ellison, "Thermal decomposition of furan generates propargyl radicals," *J. Phys. Chem. A*, vol. 113, no. 30, pp. 8540–8547, 2009.
- [60] Z. Tian, T. Yuan, R. Fournet, P.-A. Glaude, B. Sirjean, F. Battin-Leclerc, K. Zhang, and F. Qi, "An experimental and kinetic investigation of premixed furan/oxygen/argon flames," *Combust. Flame*, vol. 158, no. 4, pp. 756–773, 2011.
- [61] L. Wei, C. Tang, X. Man, X. Jiang, and Z. Huang, "High-temperature ignition delay times and kinetic study of furan," *Energy and Fuels*, vol. 26, no. 4, pp. 2075–2081, 2012.
- [62] D. Liu, C. Togbé, L.-S. Tran, D. Felsmann, P. Oßwald, P. Nau, J. Koppmann, A.

- Lackner, P.-A. Glaude, B. Sirjean, R. Fournet, F. Battin-Leclerc, and K. Kohse-Höinghaus, "Combustion chemistry and flame structure of furan group biofuels using molecular-beam mass spectrometry and gas chromatography – Part I: Furan," *Combust. Flame*, vol. 161, no. 3, pp. 748–765, 2014.
- [63] Z. Cheng, Y. Tan, L. Wei, L. Xing, J. Yang, L. Zhang, Y. Guan, B. Yan, G. Chen, and D. Y. C. Leung, "Experimental and kinetic modeling studies of furan pyrolysis: Fuel decomposition and aromatic ring formation," *Fuel*, vol. 206, pp. 239–247, 2017.
- [64] A. Lifshitz, C. Tamburu, and R. Shashua, "Decomposition of 2-methylfuran. Experimental and modeling study," *J. Phys. Chem. A*, vol. 101, no. 6, pp. 1018–1029, 1997.
- [65] L. Wei, Z. Li, L. Tong, Z. Wang, H. Jin, M. Yao, Z. Zheng, C. Wang, and H. Xu, "Primary combustion intermediates in lean and rich low-pressure premixed laminar 2-methylfuran/oxygen/argon flames," *Energy and Fuels*, vol. 26, no. 11, pp. 6651–6660, 2012.
- [66] K. P. Somers, J. M. Simmie, F. Gillespie, U. Burke, J. Connolly, W. K. Metcalfe, F. Battin-Leclerc, P. Dirrenberger, O. Herbinet, P.-A. Glaude, and H. J. Curran, "A high temperature and atmospheric pressure experimental and detailed chemical kinetic modelling study of 2-methyl furan oxidation," *Proc. Combust. Inst.*, vol. 34, no. 1, pp. 225–232, 2013.
- [67] A. C. Davis and S. M. Sarathy, "Computational study of the combustion and atmospheric decomposition of 2-methylfuran," *J. Phys. Chem. A*, vol. 117, no. 33, pp. 7670–7685, 2013.
- [68] L. Wei, C. Tang, X. Man, and Z. Huang, "Shock-tube experiments and kinetic modeling of 2-methylfuran ignition at elevated pressure," *Energy and Fuels*, vol. 27, no. 12, pp. 7809–7816, 2013.
- [69] K. P. Somers, J. M. Simmie, W. K. Metcalfe, and H. J. Curran, "The pyrolysis of 2-methylfuran: A quantum chemical, statistical rate theory and kinetic modelling study," *Phys. Chem. Chem. Phys.*, vol. 16, no. 11, pp. 5349–5367, 2014.
- [70] L.-S. Tran, C. Togbé, D. Liu, D. Felsmann, P. Oßwald, P.-A. Glaude, R. Fournet, B. Sirjean, F. Battin-Leclerc, and K. Kohse-Höinghaus, "Combustion chemistry and flame structure of furan group biofuels using molecular-beam mass spectrometry and gas chromatography – Part II: 2-Methylfuran," *Combust. Flame*, vol. 161, no. 3, pp. 766–779, Mar. 2014.
- [71] Y. Uygun, S. Ishihara, and H. Olivier, "A high pressure ignition delay time study of 2-methylfuran and tetrahydrofuran in shock tubes," *Combust. Flame*, vol. 161, pp. 2519–2530, 2014.
- [72] A. Lifshitz, C. Tamburu, and R. Shashua, "Thermal Decomposition of 2,5-Dimethylfuran. Experimental Results and Computer Modeling," *J. Phys. Chem. A*, vol. 102, pp. 10655–10670, 1998.
- [73] J. M. Simmie and H. J. Curran, "Formation Enthalpies and Bond Dissociation Energies of Alkylfurans . The Strongest C - X Bonds Known ? Formation Enthalpies and Bond Dissociation Energies of Alkylfurans . The Strongest C s X Bonds Known ?," *J. Phys. Chem. A*, vol. 113, pp. 5128–5137, 2009.

- [74] X. Wu, Z. Huang, T. Yuan, K. Zhang, and L. Wei, "Identification of combustion intermediates in a low-pressure premixed laminar 2,5-dimethylfuran/oxygen/argon flame with tunable synchrotron photoionization," *Combust. Flame*, vol. 156, no. 7, pp. 1365–1376, 2009.
- [75] X. Wu, Z. Huang, C. Jin, X. Wang, B. Zheng, Y. Zhang, and L. Wei, "Measurements of laminar burning velocities and Markstein lengths of 2, 5dimethylfuran-air-diluent premixed flames," *Energy and Fuels*, vol. 23, no. 9, pp. 4355–4362, 2009.
- [76] X. Wu, Z. Huang, X. Wang, C. Jin, C. Tang, L. Wei, and C. K. Law, "Laminar burning velocities and flame instabilities of 2,5-dimethylfuran–air mixtures at elevated pressures," *Combust. Flame*, vol. 158, no. 3, pp. 539–546, 2011.
- [77] X. Wu, Z. Huang, C. Jin, X. Wang, and L. Wei, "Laminar Burning Velocities and Markstein Lengths of 2,5-Dimethylfuran–Air Premixed Flames at Elevated Temperatures," *Combust. Sci. Technol.*, vol. 183, no. 3, pp. 220–237, 2010.
- [78] M. Djokic, H.-H. Carstensen, K. M. Van Geem, and G. B. Marin, "The thermal decomposition of 2,5-dimethylfuran," *Proc. Combust. Inst.*, vol. 34, pp. 251–258, 2013.
- [79] B. Sirjean and R. Fournet, "Theoretical study of the reaction 2,5-dimethylfuran + H → products," *Proc. Combust. Inst.*, vol. 34, pp. 241–249, 2013.
- [80] B. Sirjean and R. Fournet, "Unimolecular decomposition of 2,5-dimethylfuran: a theoretical chemical kinetic study," *Phys. Chem. Chem. Phys.*, vol. 15, no. 2, pp. 596–611, 2013.
- [81] B. Sirjean, R. Fournet, P.-A. Glaude, F. Battin-Leclerc, W. Wang, and M. A. Oehlschlaeger, "A Shock Tube and Chemical Kinetic Modeling Study of the Oxidation of 2,5-Dimethylfuran," *J. Phys. Chem. A*, vol. 117, no. 7, pp. 1371–1392, 2013.
- [82] K. P. Somers, J. M. Simmie, F. Gillespie, C. Conroy, G. Black, W. K. Metcalfe, F. Battin-Leclerc, P. Dirrenberger, O. Herbinet, P.-A. Glaude, P. Dagaut, C. Togbé, K. Yasunaga, R. X. Fernandes, C. Lee, R. Tripathi, and H. J. Curran, "A comprehensive experimental and detailed chemical kinetic modelling study of 2,5-dimethylfuran pyrolysis and oxidation," *Combust. Flame*, vol. 160, no. 11, pp. 2291–2318, 2013.
- [83] C. Togbé, L.-S. Tran, D. Liu, D. Felsmann, P. Oßwald, P.-A. Glaude, B. Sirjean, R. Fournet, F. Battin-Leclerc, and K. Kohse-Höinghaus, "Combustion chemistry and flame structure of furan group biofuels using molecular-beam mass spectrometry and gas chromatography – Part III: 2,5-Dimethylfuran," *Combust. Flame*, vol. 161, no. 3, pp. 780–797, 2014.
- [84] Z. Cheng, L. Xing, M. Zeng, W. Dong, F. Zhang, F. Qi, and Y. Li, "Experimental and kinetic modeling study of 2,5-dimethylfuran pyrolysis at various pressures," *Combust. Flame*, vol. 161, no. 10, pp. 2496–2511, 2014.
- [85] S. M. Sarathy, S. Vranckx, K. Yasunaga, M. Mehl, P. Oßwald, W. K. Metcalfe, C. K. Westbrook, W. J. Pitz, K. Kohse-Höinghaus, R. X. Fernandes, and H. J. Curran, "A comprehensive chemical kinetic combustion model for the four butanol isomers," *Combust. Flame*, vol. 159, no. 6, pp. 2028–2055, 2012.
- [86] W. Yang and A. Sen, "One-Step Catalytic Transformation of Carbohydrates and Cellulosic Biomass to 2,5-Dimethyltetrahydrofuran for Liquid Fuels," *ChemSusChem*,

- vol. 3, no. 5, pp. 597–603, 2010.
- [87] G. W. Huber, S. Iborra, and A. Corma, “Synthesis of transportation fuels from biomass: Chemistry, catalysts, and engineering,” *Chem. Rev.*, vol. 106, no. 9, pp. 4044–4098, 2006.
- [88] J. P. Lange, E. Van Der Heide, J. Van Buijtenen, and R. Price, “Furfural-A promising platform for lignocellulosic biofuels,” *ChemSusChem*, vol. 5, no. 1, pp. 150–166, 2012.
- [89] S. F. Paul, “Alternative fuel. No patent 5697987 United States Patent and Trademark Office,” 1997.
- [90] W. R. Leppard, “The Autoignition Chemistry of n-Butane: An Experimental Study,” *SAE-The Eng. Soc. Adv. Mobil. L. Sea Air Sp.*, 1987.
- [91] W. R. Leppard, “A Comparison of Olefin and Paraffin Autoignition chemistries: A Motored-Engine Study,” *SAE-The Eng. Soc. Adv. Mobil. L. Sea Air Sp.*, 1989.
- [92] W. R. Leppard, “The Autoignition Chemistries of Octane-Enhancing Ethers and Cyclic Ethers: A Motored Engine Study,” *SAE Trans.*, vol. 100, pp. 589–604, 1991.
- [93] O. Herbinet, B. Husson, Z. Serinyel, M. Cord, V. Warth, R. Fournet, P.-A. Glaude, B. Sirjean, F. Battin-Leclerc, Z. Wang, M. Xie, Z. Cheng, and F. Qi, “Experimental and modeling investigation of the low-temperature oxidation of n-heptane,” *Combust. Flame*, vol. 159, pp. 3455–3471, 2012.
- [94] C. H. Klute and W. D. Walters, “The Thermal Decomposition of Tetrahydrofuran,” *J. Am. Chem. Soc.*, vol. 68, no. 3, pp. 506–511, 1946.
- [95] G. McDonald, N. M. Lodge, and W. D. Walters, “The Effect of Added Gases upon the Thermal Decomposition of Tetrahydrofuran,” *J. Am. Chem. Soc.*, vol. 550, no. 1946, pp. 15–18, 1951.
- [96] A. Lifshitz, M. Bidani, and S. Bidani, “Thermal reactions of cyclic ethers at high temperatures. Part 3. Pyrolysis of tetrahydrofuran behind reflected shocks,” *J. Phys. Chem.*, vol. 90, no. 15, pp. 3422–3429, 1986.
- [97] M. J. Molera, a. Couto, and J. a. Garcia-Dominguez, “Gas phase oxidation of tetrahydrofuran,” *Int. J. Chem. Kinet.*, vol. 20, no. 9, pp. 673–685, 1988.
- [98] P. Dagaut, M. McGuinness, J. M. Simmie, and M. Cathonnet, “The Ignition and Oxidation of Tetrahydrofuran: Experiments and Kinetic Modeling,” *Combust. Sci. Technol.*, vol. 135, no. 1–6, pp. 3–29, 1998.
- [99] T. Kasper, A. Lucassen, A. W. Jasper, W. Li, P. R. Westmoreland, K. Kohse-Höinghaus, B. Yang, J. Wang, T. A. Cool, and N. Hansen, “Identification of tetrahydrofuran reaction pathways in premixed flames,” *Zeitschrift für Phys. Chemie*, vol. 225, no. 11–12, pp. 1237–1270, 2011.
- [100] M. Verdicchio, B. Sirjean, L. S. Tran, P.-A. Glaude, and F. Battin-Leclerc, “Unimolecular decomposition of tetrahydrofuran: Carbene vs. diradical pathways,” *Proc. Combust. Inst.*, vol. 35, no. 1, pp. 533–541, 2015.
- [101] L.-S. Tran, M. Verdicchio, F. Monge, R. C. Martin, R. Bounaceur, B. Sirjean, P.-A. Glaude, M. U. Alzueta, and F. Battin-Leclerc, “An experimental and modeling study of the combustion of tetrahydrofuran,” *Combust. Flame*, vol. 162, no. 5, pp. 1899–1918, 2015.

- [102] G. Vanhove, Y. Yu, M. A. Boumehdi, O. Frottier, O. Herbinet, P. A. Glaude, and F. Battin-Leclerc, "Experimental Study of Tetrahydrofuran Oxidation and Ignition in Low-Temperature Conditions," *Energy and Fuels*, vol. 29, no. 9, pp. 6118–6125, 2015.
- [103] J.-C. Lizardo-Huerta, B. Sirjean, P.-A. Glaude, and R. Fournet, "Pericyclic reactions in ether biofuels," *Proc. Combust. Inst.*, vol. 36, pp. 569–576, 2016.
- [104] K. Moshhammer, S. Vranckx, H. K. Chakravarty, P. Parab, R. X. Fernandes, and K. Kohse-Höinghaus, "An experimental and kinetic modeling study of 2-methyltetrahydrofuran flames," *Combust. Flame*, vol. 160, no. 12, pp. 2729–2743, 2013.
- [105] R. Tripathi, C. Lee, R. X. Fernandes, H. Olivier, H. J. Curran, S. M. Sarathy, and H. Pitsch, "Ignition characteristics of 2-methyltetrahydrofuran: An experimental and kinetic study," *Proc. Combust. Inst.*, vol. 36, pp. 587–595, 2017.
- [106] Y. Fenard, M. A. Boumehdi, and G. Vanhove, "Experimental and kinetic modeling study of 2-methyltetrahydrofuran oxidation under engine-relevant conditions," *Combust. Flame*, vol. 178, pp. 168–181, 2017.
- [107] R. De Bruycker, L.-S. Tran, H.-H. Carstensen, P.-A. Glaude, F. Monge, M. U. Alzueta, F. Battin-Leclerc, and K. M. Van Geem, "Experimental and modeling study of the pyrolysis and combustion of 2-methyl-tetrahydrofuran," *Combust. Flame*, vol. 176, pp. 409–428, 2017.
- [108] "Fifth Assessment Report - Mitigation of Climate Change." [Online]. Available: <https://www.ipcc.ch/report/ar5/wg3/>.
- [109] CITEPA, "Centre Interprofessionnel Technique d'Etudes de la Pollution Atmosphérique," 2018. [Online]. Available: <https://www.citepa.org/fr/air-et-climat/polluants/aep-item/oxydes-d-azote>.
- [110] Y. Zeldovich, "The oxidation of nitrogen in combustion and explosions.," *Acta Physicochim USSR*, vol. 21, pp. 577–628, 1946.
- [111] P. Glarborg, J. A. Miller, B. Ruscic, and S. J. Klippenstein, "Modeling nitrogen chemistry in combustion," *Prog. Energy Combust. Sci.*, vol. 67, pp. 31–68, 2018.
- [112] C. P. Fenimore, "Formation of nitric oxide in premixed hydrocarbon flames," *Symp. Combust.*, vol. 13, no. 1, pp. 373–380, 1971.
- [113] L. V. Moskaleva and M. C. Lin, "The spin-conserved reaction $\text{CH} + \text{N}_2 \rightarrow \text{H} + \text{NCN}$: A major pathway to prompt NO studied by quantum/statistical theory calculations and kinetic modeling of rate constant," *Proc. Combust. Inst.*, vol. 28, no. 2, pp. 2393–2401, 2000.
- [114] A. Barnun And S. H. Bauer, "Mechanism Of Production Of Cn In Shock Heated Mixtures Of Nitrogen And Acetylene," In *Abstracts Of Papers Of The American Chemical Society*, , No. Mar-A, P. 120, 1971
- [115] G. G. De Soete, "Overall reaction rates of NO and N₂ formation from fuel nitrogen," *Symp. Combust.*, vol. 15, no. 1, pp. 1093–1102, 1975.
- [116] C. T. Bowman, "Control of combustion-generated nitrogen oxide emissions: Technology driven by regulation," *Symp. Combust.*, vol. 24, no. 1, pp. 859–878, 1992.
- [117] A. J. Dean, R. K. Hanson, and C. T. Bowman, "High temperature shock tube study of

- reactions of CH and C-atoms with N₂,” *Symp. Combust.*, vol. 23, no. 1, pp. 259–265, Jan. 1991.
- [118] D. Lindackers, M. Burmeister, and P. Roth, “Perturbation studies of high temperature C and CH reactions with N₂ and NO,” *Symp. Combust.*, vol. 23, no. 1, pp. 251–257, 1991.
- [119] J. A. Miller and S. P. Walch, “Prompt NO: Theoretical prediction of the high-temperature rate coefficient for CH + N₂ ? HCN + N,” *Int. J. Chem. Kinet.*, vol. 29, no. 4, pp. 253–259, 1997.
- [120] L. V. Moskaleva and M. C. Lin, *The spin-conserved reaction CH+N₂→H+NCN: A major pathway to prompt no studied by quantum/statistical theory calculations and kinetic modeling of rate constant*, vol. 28, no. 2. Elsevier, p. 2393–2401, 2000
- [121] G. P. Smith, “Evidence of NCN as a flame intermediate for prompt NO,” *Chem. Phys. Lett.*, vol. 367, no. 5–6, pp. 541–548, 2003.
- [122] A. El bakali, L. Pillier, P. Desgroux, B. Lefort, L. Gasnot, J. F. Pauwels, and I. da Costa, “NO prediction in natural gas flames using GDF-Kin@3.0 mechanism NCN and HCN contribution to prompt-NO formation,” *Fuel*, vol. 85, no. 7–8, pp. 896–909, 2006.
- [123] Venkatesh Vasudevan, Ronald K. Hanson, Craig T. Bowman, A. David M. Golden, and D. F. Davidson, “Shock Tube Study of the Reaction of CH with N₂: Overall Rate and Branching Ratio,” 2007.
- [124] L. B. Harding, S. J. Klippenstein, and J. A. Miller, “Kinetics of CH + N₂ revisited with multireference methods,” *J. Phys. Chem. A*, vol. 112, no. 3, pp. 522–532, 2008.
- [125] J. A. Sutton, B. A. Williams, and J. W. Fleming, “Laser-induced fluorescence measurements of NCN in low-pressure CH₄/O₂/N₂ flames and its role in prompt NO formation,” *Combust. Flame*, vol. 153, no. 3, pp. 465–478, 2008.
- [126] N. Lamoureux, X. Mercier, C. Western, J. F. Pauwels, and P. Desgroux, “NCN quantitative measurement in a laminar low pressure flame,” *Proc. Combust. Inst.*, vol. 32, no. 1, pp. 937–944, 2009.
- [127] N. Lamoureux, P. Desgroux, A. El Bakali, and J. F. Pauwels, “Experimental and numerical study of the role of NCN in prompt-NO formation in low-pressure CH₄-O₂-N₂ and C₂H₂-O₂-N₂ flames,” *Combust. Flame*, vol. 157, no. 10, pp. 1929–1941, 2010.
- [128] E. Goos, C. Sickfeld, F. Mauß, L. Seidel, B. Ruscic, A. Burcat, and T. Zeuch, “Prompt NO formation in flames: The influence of NCN thermochemistry,” *Proc. Combust. Inst.*, vol. 34, no. 1, pp. 657–666, 2013.
- [129] A. A. Konnov, “Implementation of the NCN pathway of prompt-NO formation in the detailed reaction mechanism,” *Combust. Flame*, vol. 156, no. 11, pp. 2093–2105, 2009.
- [130] R. T. Bise, H. Choi, and D. M. Neumark, “Photodissociation dynamics of the singlet and triplet states of the NCN radical,” *J. Chem. Phys.*, vol. 111, no. 11, p. 4923, 1999.
- [131] J. Dammeier and G. Friedrichs, “Thermal Decomposition of NCN₃ as a High-Temperature NCN Radical Source: Singlet–Triplet Relaxation and Absorption Cross Section of NCN(³Σ⁺),” *J. Phys. Chem. A*, vol. 114, no. 50, pp. 12963–12971, 2010.
- [132] N. Faßheber, J. Dammeier, and G. Friedrichs, “Direct measurements of the total rate

- constant of the reaction $\text{NCN} + \text{H}$ and implications for the product branching ratio and the enthalpy of formation of NCN ,” *Phys. Chem. Chem. Phys.*, vol. 16, no. 23, pp. 11647–11657, 2014.
- [133] J. A. Miller, M. C. Branch, W. J. McLean, D. W. Chandler, M. D. Smooke, and R. J. Kee, “The conversion of HCN to NO and N_2 in $\text{H}_2\text{--O}_2\text{--HCN--Ar}$ flames at low pressure,” *Symp. Combust.*, vol. 20, no. 1, pp. 673–684, 1985.
- [134] P. Dagaut, P. Glarborg, and M. U. Alzueta, “The oxidation of hydrogen cyanide and related chemistry,” *Prog. Energy Combust. Sci.*, vol. 34, no. 1, pp. 1–46, 2008.
- [135] P. Glarborg, P. G. Kristensen, S. H. Jensen, and K. Dam-Johansen, “A flow reactor study of HNCO oxidation chemistry,” *Combust. Flame*, vol. 98, no. 3, pp. 241–258, 1994.
- [136] P. Glarborg and P. Marshall, “Importance of the Hydrogen Isocyanide Isomer in Modeling Hydrogen Cyanide Oxidation in Combustion,” *Energy & Fuels*, vol. 31, no. 3, pp. 2156–2166, 2017.
- [137] C. P. Fenimore and G. W. Jones, “Oxidation of ammonia in flames,” *J. Phys. Chem.*, 1961.
- [138] P. C. Malte and D. T. Pratt, “The role of energy-releasing kinetics in noxformation: Fuel-Lean, Jet-Stirred CO-Air combustion,” *Combust. Sci. Technol.*, 1974.
- [139] A. N. Hayhurst and E. M. Hutchinson, “Evidence for a New Way of Producing NO via NNH in Fuel-Rich Flames at Atmospheric Pressure,” *Combust. Flame*, vol. 114, no. 1–2, pp. 274–279, 1998.
- [140] J. W. Bozzelli and A. M. Dean, “ $\text{O} + \text{NNH}$: A possible new route for NO_x formation in flames,” *Int. J. Chem. Kinet.*, vol. 27, no. 11, pp. 1097–1109, 1995.
- [141] A. A. Konnov, G. Colson, and J. De Ruyck, “The new route forming NO via NNH ,” *Combust. Flame*, vol. 121, no. 3, pp. 548–550, 2000.
- [142] M. M. K. Bhuiya, M. G. Rasul, M. M. K. Khan, N. Ashwath, A. K. Azad, and M. A. Hazrat, “Prospects of 2nd generation biodiesel as a sustainable fuel – Part 2: Properties, performance and emission characteristics,” *Renew. Sustain. Energy Rev.*, vol. 55, pp. 1129–1146, Mar. 2016.
- [143] L. Coniglio, H. Bennadji, P. A. Glaude, O. Herbinet, and F. Billaud, “Combustion chemical kinetics of biodiesel and related compounds (methyl and ethyl esters): Experiments and modeling – Advances and future refinements,” *Prog. Energy Combust. Sci.*, vol. 39, no. 4, pp. 340–382, 2013.
- [144] S. K. Hoekman and C. Robbins, “Review of the effects of biodiesel on NO_x emissions,” *Fuel Process. Technol.*, vol. 96, pp. 237–249, 2012.
- [145] M. Lapuerta, O. Armas, and J. Rodríguez-Fernández, “Effect of biodiesel fuels on diesel engine emissions,” *Prog. Energy Combust. Sci.*, vol. 34, no. 2, pp. 198–223, 2008.
- [146] C. H. Cheng, C. S. Cheung, T. L. Chan, S. C. Lee, C. D. Yao, and K. S. Tsang, “Comparison of emissions of a direct injection diesel engine operating on biodiesel with emulsified and fumigated methanol,” *Fuel*, vol. 87, no. 10–11, pp. 1870–1879, 2008.

- [147] F. Wu, J. Wang, W. Chen, and S. Shuai, "A study on emission performance of a diesel engine fueled with five typical methyl ester biodiesels," *Atmos. Environ.*, vol. 43, no. 7, pp. 1481–1485, 2009.
- [148] M. J. Ramos, C. M. Fernández, A. Casas, L. Rodríguez, and Á. Pérez, "Influence of fatty acid composition of raw materials on biodiesel properties," *Bioresour. Technol.*, vol. 100, no. 1, pp. 261–268, 2009.
- [149] N. D. Love, R. N. Parthasarathy, and S. R. Gollahalli, "Effect of iodine number on NO_x formation in laminar flames of oxygenated biofuels," *Int. J. Green Energy*, vol. 6, no. 4, pp. 323–332, 2009.
- [150] E. Cécile, C. Depcik, A. Duncan, J. Guo, M. Mangus, E. Peltier, S. Stagg-Williams, and Y. Zhong, "Investigation of the effects of biodiesel feedstock on the performance and emissions of a single-cylinder diesel engine," *Energy and Fuels*, vol. 26, no. 4, pp. 2331–2341, 2012.
- [151] M. D. Sylla, N. Lamoureux, and L. Gasnot, "Impact of methyl butanoate oxidation on NO formation in laminar low pressure flames," *Fuel*, vol. 207, pp. 801–813, 2017.
- [152] O. I. Awad, R. Mamat, O. M. Ali, N. A. C. Sidik, T. Yusaf, K. Kadirgama, and M. Kettner, "Alcohol and ether as alternative fuels in spark ignition engine: A review," *Renew. Sustain. Energy Rev.*, vol. 82, pp. 2586–2605, 2018.
- [153] I. M. Yusri, R. Mamat, G. Najafi, A. Razman, O. I. Awad, W. H. Azmi, W. F. W. Ishak, and A. I. M. Shaiful, "Alcohol based automotive fuels from first four alcohol family in compression and spark ignition engine: A review on engine performance and exhaust emissions," *Renew. Sustain. Energy Rev.*, vol. 77, pp. 169–181, 2017.
- [154] H. Suhaimi, A. Adam, A. G. Mrwan, Z. Abdullah, M. F. Othman, M. K. Kamaruzzaman, and F. Y. Hagos, "Analysis of combustion characteristics, engine performances and emissions of long-chain alcohol-diesel fuel blends," *Fuel*, vol. 220, pp. 682–691, 2018.
- [155] M. A. Ghadikolaei, C. S. Cheung, and K.-F. Yung, "Study of combustion, performance and emissions of diesel engine fueled with diesel/biodiesel/alcohol blends having the same oxygen concentration," *Energy*, vol. 157, pp. 258–269, 2018.
- [156] E. Koivisto, N. Ladommatos, and M. Gold, "Systematic study of the effect of the hydroxyl functional group in alcohol molecules on compression ignition and exhaust gas emissions," *Fuel*, vol. 153, pp. 650–663, 2015.
- [157] B. Rajesh Kumar and S. Saravanan, "Partially premixed low temperature combustion using dimethyl carbonate (DMC) in a DI diesel engine for favorable smoke/NO_x emissions," *Fuel*, vol. 180, pp. 396–406, 2016.
- [158] P. Rounce, A. Tsolakis, P. Leung, and A. P. E. York, "A Comparison of Diesel and Biodiesel Emissions Using Dimethyl Carbonate as an Oxygenated Additive," *Energy & Fuels*, vol. 24, no. 9, pp. 4812–4819, 2010.
- [159] B. Rajesh Kumar, S. Saravanan, B. Sethuramasamyraja, and D. Rana, "Screening oxygenates for favorable NO_x/smoke trade-off in a DI diesel engine using multi response optimization," *Fuel*, vol. 199, pp. 670–683, 2017.
- [160] N. Lamoureux, A. El-Bakali, L. Gasnot, J. F. Pauwels, and P. Desgroux, "Prompt-NO formation in methane/oxygen/nitrogen flames seeded with oxygenated volatile organic

- compounds: Methyl ethyl ketone or ethyl acetate,” *Combust. Flame*, vol. 153, no. 1–2, pp. 186–201, 2008.
- [161] R. Daniel, G. Tian, H. Xu, M. L. Wyszynski, X. Wu, and Z. Huang, “Effect of spark timing and load on a DISI engine fuelled with 2,5-dimethylfuran,” *Fuel*, vol. 90, pp. 449–458, 2011.
- [162] S. Zhong, R. Daniel, H. Xu, J. Zhang, D. Turner, M. L. Wyszynski, and P. Richards, “Combustion and Emissions of 2,5-Dimethylfuran in a Direct-Injection Spark-Ignition Engine,” *Energy & Fuels*, vol. 24, no. 5, pp. 2891–2899, 2010.
- [163] H. Liu, J. Xu, Z. Zheng, S. Li, and M. Yao, “Effects of fuel properties on combustion and emissions under both conventional and low temperature combustion mode fueling 2,5-dimethylfuran/diesel blends,” *Energy*, vol. 62, pp. 215–223, 2013.
- [164] Y. Qian, L. Zhu, Y. Wang, and X. Lu, “Recent progress in the development of biofuel 2,5-dimethylfuran,” *Renew. Sustain. Energy Rev.*, vol. 41, pp. 633–646, 2015.
- [165] C. Wang, H. Xu, R. Daniel, A. Ghafourian, J. M. Herreros, S. Shuai, and X. Ma, “Combustion characteristics and emissions of 2-methylfuran compared to 2,5-dimethylfuran, gasoline and ethanol in a DISI engine,” *Fuel*, vol. 103, pp. 200–211, 2013.
- [166] H. Wei, D. Feng, G. Shu, M. Pan, Y. Guo, D. Gao, and W. Li, “Experimental investigation on the combustion and emissions characteristics of 2-methylfuran gasoline blend fuel in spark-ignition engine,” *Appl. Energy*, vol. 132, pp. 317–324, 2014.
- [167] H. Xiao, P. Zeng, Z. Li, L. Zhao, and X. Fu, “Combustion performance and emissions of 2-methylfuran diesel blends in a diesel engine,” *Fuel*, vol. 175, pp. 157–163, 2016.
- [168] T. W. Rudolph and J. J. Thomas, “NO_x, NMHC and CO Emissions from Biomass Derived Gasoline Extenders,” 1988.
- [169] K. Alexandrino, Á. Millera, R. Bilbao, and M. U. Alzueta, “Interaction between 2,5-dimethylfuran and nitric oxide: Experimental and modeling study,” *Energy and Fuels*, vol. 28, no. 6, pp. 4193–4198, 2014.
- [170] R. M. Fristrom and A. . Westenberg, “Fundamental processes and laminar flame structure,” *APL Tech. Dig.*, 1962.
- [171] “Burners.” [Online]. Available: <http://www.flatflame.com/burner-description.html>.
- [172] S. de Ferrieres, “Combustion de melanges gaz naturel/hydrogene dans des flammes laminaires premelangees. Etude experimentale et modelisation,” Université des Sciences et Technologies de Lille, 2008.
- [173] J. C. BIORDI, C. LAZZARA, and J. F. PAPP, “Molecular Beam Mass Spectrometry Applied to Determining the Kinetics of Reactions in Flames. I. Empirical Characterization of Flame Perturbation by Molecular Beam Sampling Probes,” *Combust. FLAMES*, vol. 23, pp. 79–82, 1974.
- [174] A. El Bakali, J.-L. Delfau, and C. Vovelle, “Kinetic modeling of a rich, atmospheric pressure, premixed n-heptane/O₂/N₂ flame,” *Combust. Flame*, vol. 118, no. 3, pp. 381–398, 1999.
- [175] J.-L. Delfau, J. Biet, M. Idir, L. Pillier, and C. Vovelle, “Experimental and numerical

- study of premixed, lean ethylene flames,” *Proc. Combust. Inst.*, vol. 31, no. 1, pp. 357–365, 2007.
- [176] B. Lefort, “Cinétique de combustion de flammes prémélangées riches méthane/éthane/propane. Etude expérimentale et modélisation,” Université des Sciences et Technologies de Lille, 2006.
- [177] R. L. Grob, *Modern practice of gas chromatography 2end Edition*. 1985.
- [178] I.-Y. Kim, S.-H. Suh, I.-K. Lee, and R. R. Wolfe, *Applications of Stable, Nonradioactive Isotope Tracers in In vivo Human Metabolic Research*, vol. 48. 2016.
- [179] M. D. Smooke, “Solution of Burner-Stabilized Premixed Laminar Flames by Boundary Value Methods,” *J. Comput. Phys.*, vol. 48, pp. 72–105, 1982.
- [180] D. G. Goodwin, H. K. Moffat, and R. L. Speth, “Cantera: An Object-oriented Software Toolkit for Chemical Kinetics, Thermodynamics, and Transport Processes. Version 2.3.0,” 2017.
- [181] S. Gordon and B. J. McBride, “Computer Program for Calculation of Complex Chemical Equilibrium Compositions, Rocket Performance, Incident and Reflected Shocks, and Chapman-Jouguet Detonations. Interim Revision, March 1976,” 1976.
- [182] J. T. Scanlon and D. E. Willis, “Calculation of flame ionization detector relative response factors using the effective carbon number concept,” *J. Chromatogr. Sci.*, vol. 23, no. 8, pp. 333–340, 1985.
- [183] F. Battin-Leclerc, “Detailed chemical kinetic models for the low-temperature combustion of hydrocarbons with application to gasoline and diesel fuel surrogates,” *Prog. Energy Combust. Sci.*, vol. 34, no. 4, pp. 440–498, 2008.
- [184] J. M. Simmie, “Detailed chemical kinetic models for the combustion of hydrocarbon fuels,” *Prog. Energy Combust. Sci.*, vol. 29, no. 6, pp. 599–634, 2003.
- [185] B. Rajesh Kumar and S. Saravanan, “Use of higher alcohol biofuels in diesel engines: A review,” *Renew. Sustain. Energy Rev.*, vol. 60, pp. 84–115, 2016.
- [186] N. Lebrun, P. Dhamelinourt, C. Focsa, B. Chazallon, J. L. Destombes, and D. Prevost, “Raman analysis of formaldehyde aqueous solutions as a function of concentration,” *J. Raman Spectrosc.*, vol. 34, no. 6, pp. 459–464, 2003.
- [187] V. Brandani and G. Di Giacomo, “Effect of small amounts of methanol on the vapour-liquid equilibrium for the water-formaldehyde system,” *Fluid Phase Equilib.*, vol. 24, pp. 307–333, 1985.
- [188] A. Oancea, “Étude de la solubilité et de l’incorporation du formaldéhyde dans l’eau et la glace,” Université Lille 1, 2010.
- [189] P. Delcroix, “Theoretical and experimental studies of the interactions of formaldehyde with water,” Université de Lille 1, 2013.
- [190] J. F. Walker, *Formaldehyde*, (3rd ed. New York NY: Reinhold Publishing Company, 1964.
- [191] J. A. Riddick, W. B. Bunger, and T. K. Sakano, *Organic Solvents: Physical Properties and Methods of Purification.*, 4th Editio. New York., 1986.

- [192] L. S. Tran, B. Sirjean, P. A. Glaude, K. Kohse-Höinghaus, and F. Battin-Leclerc, "Influence of substituted furans on the formation of Polycyclic Aromatic Hydrocarbons in flames," *Proc. Combust. Inst.*, vol. 35, no. 2, pp. 1735–1743, 2015.
- [193] K. Alexandrino, Á. Millera, R. Bilbao, and M. U. Alzueta, "2-methylfuran Oxidation in the Absence and Presence of NO," *Flow, Turbul. Combust.*, vol. 96, no. 2, pp. 343–362, 2016.
- [194] N. Xu, Y. Wu, C. Tang, P. Zhang, X. He, Z. Wang, and Z. Huang, "Experimental study of 2,5-dimethylfuran and 2-methylfuran in a rapid compression machine: Comparison of the ignition delay times and reactivity at low to intermediate temperature," *Combust. Flame*, vol. 168, pp. 216–227, 2016.
- [195] N. Xu, C. Tang, X. Meng, X. Fan, Z. Tian, and Z. Huang, "Experimental and Kinetic Study on the Ignition Delay Times of 2,5-Dimethylfuran and the Comparison to 2-Methylfuran and Furan," *Energy & Fuels*, vol. 29, no. 8, pp. 5372–5381, 2015.
- [196] S. H. Mousavipour, S. Ramazani, and Z. Shahkolahi, "Multichannel RRKM-TST and direct-dynamics VTST study of the reaction of hydroxyl radical with furan," *J. Phys. Chem. A*, vol. 113, no. 12, pp. 2838–2846, 2009.
- [197] W. K. Metcalfe, S. M. Burke, S. S. Ahmed, and H. J. Curran, "A hierarchical and comparative kinetic modeling study of C1- C2hydrocarbon and oxygenated fuels," *Int. J. Chem. Kinet.*, vol. 45, no. 10, pp. 638–675, 2013.
- [198] A. C. Eckbreth, *Laser diagnostics for combustion temperature and species / Alan C. Eckbreth*. Tunbridge Wells, Kent ; Cambridge, Mass. : Abacus Press, 1988.
- [199] D. E. Heard, J. B. Jeffries, G. P. Smith, and D. R. Crosley, "LIF measurements in methane/air flames of radicals important in prompt-NO formation," *Combust. Flame*, vol. 88, no. 2, pp. 137–148, 1992.
- [200] L. Gasnot, P. Desgroux, J. . Pauwels, and L. . Sochet, "Detailed analysis of low-pressure premixed flames of CH₄ + O₂ + N₂: a study of prompt-NO," *Combust. Flame*, vol. 117, no. 1–2, pp. 291–306, 1999.
- [201] D. D. Thomsen, F. F. Kuligowski, and N. M. Laurendeau, "Background corrections for laser-induced-fluorescence measurements of nitric oxide in lean, high-pressure, premixed methane flames.," *Appl. Opt.*, vol. 36, no. 15, pp. 3244–3252, 1997.
- [202] P. Desgroux, P. Devynck, L. Gasnot, J.-F. Pauwels, and L.-R. Sochet, "Disturbance of laser-induced-fluorescence measurements of NO in methane–air flames containing chlorinated species by photochemical effects induced by 225-nm-laser excitation," *Appl. Opt.*, vol. 37, no. 21, p. 4951, 1998.
- [203] P. A. Berg, G. P. Smith, J. B. Jeffries, and D. R. Crosley, "Nitric oxide formation and reburn in low-pressure methane flames," *Symp. Combust.*, vol. 27, no. 1, pp. 1377–1384, 1998.
- [204] L. Pillier, A. El Bakali, X. Mercier, A. Rida, J.-F. Pauwels, and P. Desgroux, "Influence of C₂ and C₃ compounds of natural gas on NO formation: an experimental study based on LIF/CRDS coupling," *Proc. Combust. Inst.*, vol. 30, no. 1, pp. 1183–1191, 2005.
- [205] V. M. van Essen, A. V. Sepman, A. V. Mokhov, and H. B. Levinsky, "Pressure dependence of NO formation in laminar fuel-rich premixed CH₄/air flames," *Combust.*

- Flame*, vol. 153, no. 3, pp. 434–441, 2008.
- [206] O. A. Powell, P. Papas, and C. B. Dreyer, “Flame structure measurements of NO in premixed hydrogen-nitrous oxide flames,” *Proc. Combust. Inst.*, vol. 33, no. 1, pp. 1053–1062, 2011.
- [207] B. Li, Y. He, Z. Li, and A. A. Konnov, “Measurements of NO concentration in NH₃-doped CH₄+air flames using saturated laser-induced fluorescence and probe sampling,” *Combust. Flame*, vol. 160, no. 1, pp. 40–46, 2013.
- [208] A. V. Sepman, S. E. Abtahizadeh, A. V. Mokhov, J. A. van Oijen, H. B. Levinsky, and L. P. H. de Goey, “Numerical and experimental studies of the NO formation in laminar coflow diffusion flames on their transition to MILD combustion regime,” *Combust. Flame*, vol. 160, no. 8, pp. 1364–1372, 2013.
- [209] M. D. Sylla, N. Lamoureux, and L. Gasnot, “Impact of methyl butanoate oxidation on NO formation in laminar low pressure flames,” 2017.
- [210] W. P. Partridge Jr., M. S. Klassen, D. D. Thomsen, and N. M. Laurendeau, “Experimental assessment of O₂ interferences on laser-induced fluorescence measurements of NO in high-pressure, lean premixed flames by use of narrow-band and broadband detection,” *Appl. Opt.*, vol. 34, pp. 4890–4904, 1996.
- [211] J. R. Reisel, C. D. Carter, and N. M. Laurendeau, “Einstein coefficients for rotational lines of the (0, 0) band of the NO A $2\Sigma^+$ -X 2π system,” *J. Quant. Spectrosc. Radiat. Transf.*, vol. 47, no. 1, pp. 43–54, 1992.
- [212] R. H. GILLETTE and E. H. EYSTER, “The Fundamental Rotation-Vibration Band of Nitric Oxide,” *Phys. review*, vol. 56, pp. 1113–1119, 1939.
- [213] R. J. Cattolica, J. A. Cavolowsky, and T. G. Mataga, “Laser-fluorescence measurements of nitric oxide in low-pressure H₂/O₂/No flames,” *Symp. Combust.*, vol. 22, no. 1, pp. 1165–1173, 1989.
- [214] H. El Merhubi, “Application de diagnostics spectroscopiques pour la mesure d’espèces clés impliquées dans la formation du NO précoce dans des flammes de prémélange à basse pression,” University of Lille, 2013.
- [215] “Furan.” [Online]. Available: <https://webbook.nist.gov/cgi/cbook.cgi?ID=C110009&Mask=400#UV-Vis-Spec>.
- [216] L. Pillier, “Formation de monoxyde d’azote dans des flammes pré-mélangées CH₄/C₂H₆/C₃H₈/O₂/N₂: étude expérimentale par diagnostics laser et modélisation,” Université Lille1, 2003.
- [217] J. Brzozowski, P. Bunker, N. Blander, and P. Erman, “Predissociation Effects In The A, B, And C States Of CH And The Interstellar Formation Rate Of CH Via Inverse Predissociation,” *Astrophys. J.*, vol. 207, pp. 414–424, 1976.
- [218] G. Herzberg and J. W. C. Johns, “New Spectra Of The CH Molecule,” *Astrophys. J.*, vol. 158, 1969.
- [219] M. Ortiz and J. Campos, “Lifetimes of excited state of CH,” *Physica*, vol. 114C, pp. 135–139, 1982.
- [220] R. J. Cattolica, D. Stepowski, D. Puechberty, and M. Cottreau, “Laser-induced fluorescence of the CH molecule in a low-pressure flame,” *J. Quant. Spectrosc. Radiat.*

- Transf.*, vol. 32, no. 4, pp. 363–370, 1984.
- [221] K. T. Walsh, M. B. Long, M. a. Tanoff, and M. D. Smooke, “Experimental and computational study of CH, CH*, and OH* in an axisymmetric laminar diffusion flame,” *Symp. Combust.*, vol. 27, no. 1, pp. 615–623, 1998.
- [222] L. Gasnot, P. Desgroux, J. F. Pauwels, and L. R. Sochet, “Detailed Analysis of Low-pressure Premixed Flames of CH₄+O₂+N₂: A Study of Prompt-NO,” *Combust. Flame*, vol. 117, no. 98, pp. 291–306, 1999.
- [223] X. Mercier, P. Jamette, J. . Pauwels, and P. Desgroux, “Absolute CH concentration measurements by cavity ring-down spectroscopy in an atmospheric diffusion flame,” *Chem. Phys. Lett.*, vol. 305, no. 5–6, pp. 334–342, 1999.
- [224] J. Luque, R. J. H. Klein-Douwel, J. B. Jeffries, and D. R. Crosley, “Collisional processes near the CH B 2 $\Sigma - v = 0, 1$ predissociation limit in laser-induced fluorescence flame diagnostics,” *Appl. Phys. B*, vol. 71, pp. 85–94, 2000.
- [225] P. A. Berg, D. A. Hill, A. R. Noble, G. P. Smith, J. B. Jeffries, and D. R. Crosley, “Absolute CH concentration measurements in low-pressure methane flames: comparisons with model results,” *Combust. Flame*, vol. 121, no. 1–2, pp. 223–235, 2000.
- [226] C. Moreau, E. Therssen, P. Desgroux, J. F. Pauwels, A. Chapput, and M. Barj, “Quantitative measurements of the CH radical in sooting diffusion flames at atmospheric pressure,” *Appl. Phys. B*, vol. 76, no. 5, pp. 597–602, 2003.
- [227] S. V. Naik and N. M. Laurendeau, “LIF measurements and chemical kinetic analysis of methylidyne formation in high-pressure counter-flow partially premixed and non-premixed flames,” *Appl. Phys. B Lasers Opt.*, vol. 79, no. 7, pp. 891–905, 2004.
- [228] N. Lamoureux, P. Desgroux, A. El Bakali, and J.-F. Pauwels, “Corrigendum to ‘Experimental and numerical study of the role of NCN in the prompt-NO formation in low pressure CH₄/O₂/N₂ and C₂H₂/O₂/N₂ flames’ [Combust. Flame 157 (2010) 1929–1941],” *Combust. Flame*, vol. 160, no. 3, pp. 745–746, 2013.
- [229] A. Hirano, M. Ippommastu, and M. Tsujishita, “Two-dimensional digital imaging of the CH distribution in a natural gas/oxygen flame at atmospheric pressure and detection of A-state emission by means of C-state excitation,” *Opt. Lett.*, vol. 17, no. 4, p. 303, 1992.
- [230] M. Tsujishita, M. Ipponmatsu, and A. Hirano, “Visualization of the CH Molecule by Exciting C₂ Σ^+ ($v=1$) State in Turbulent Flames by Planar Laser-Induced Fluorescence,” *Jpn. J. Appl. Phys.*, vol. 32, pp. 5564–5569, 1993.
- [231] C. D. Carter, S. Hammack, and T. Lee, “High-speed flamefront imaging in premixed turbulent flames using planar laser-induced fluorescence of the CH C–X band,” *Combust. Flame*, vol. 168, pp. 66–74, 2016.
- [232] C. M. Mitsingas, S. D. Hammack, E. K. Mayhew, R. Rajasegar, B. Mcgann, A. W. Skiba, C. D. Carter, and T. Lee, “ARTICLE IN PRESS Simultaneous high speed PIV and CH PLIF using R-branch excitation in the C 2 +X 2 (0,0) band,” *Proc. Combust. Inst.*, vol. 000, pp. 1–9, 2018.
- [233] J. Luque and D. R. Crosley, “LIFbase: Database and spectral simulation Program.” 1999.

- [234] X. Mercier, “Mesure de concentrations absolues d’espèces réactives minoritaires dans les flammes par la technique d’absorption Cavity Ring Down Spectroscopy (CRDS),” University of Lille 1, 2000.
- [235] L. Pillier, M. Idir, J. Molet, A. Matynia, and S. De Persis, “Experimental study and modelling of NO_x formation in high pressure counter-flow premixed CH₄/air flames,” *Fuel*, vol. 150, pp. 394–407, 2015.
- [236] G. J. Gibbs and H. F. Calcote, “Effect of molecular structure on burning velocity.,” *J. Chem. Eng. ...*, vol. 4, no. 3, pp. 226–237, 1959.
- [237] O. Park, P. S. Veloo, and F. N. Egolfopoulos, “Flame studies of C₂hydrocarbons,” *Proc. Combust. Inst.*, vol. 34, no. 1, pp. 711–718, 2013.
- [238] S. J. Klippenstein, J. A. Miller, and L. B. Harding, “Resolving the mystery of prompt CO₂: the HCCO + O₂ reaction,” *Proc. Combust. Inst.*, vol. 29, pp. 1209–1217, 2002.
- [239] X. Shen, X. Yang, J. Santner, J. Sun, and Y. Ju, “Experimental and kinetic studies of acetylene flames at elevated pressures,” *Proc. Combust. Inst.*, vol. 35, pp. 721–728, 2015.
- [240] B. A. Williams and J. W. Fleming, “Experimental and modeling study of NO formation in 10 torr methane and propane flames: Evidence for additional prompt-NO precursors,” *Proc. Combust. Inst.*, vol. 31, no. 1, pp. 1109–1117, 2007.
- [241] A. A. Konnov, “On the role of C₂O radicals in prompt-NO mechanism,” *Combust. Explos. Shock Waves*, vol. 44, no. 5, pp. 497–501, 2008.
- [242] P. Dagaut, J. Luche, and M. Cathonnet, “The kinetics of C₁ to C₄ hydrocarbons/NO interactions in relation with reburning,” *Proc. Combust. Inst.*, vol. 28, pp. 2459–2465, 2000.
- [243] I. V. Tokmakov, L. V. Moskaleva, D. V. Paschenko, and M. C. Lin, “Computational study of the HCCO + NO reaction: Ab initio MO/vRRKM calculations of the total rate constant and product branching ratios,” *J. Phys. Chem. A*, vol. 107, no. 7, pp. 1066–1076, 2003.
- [244] M. U. Alzueta, V. Aranda, F. Monge, Á. Millera, and R. Bilbao, “Oxidation of methyl formate and its interaction with nitric oxide,” 2013.
- [245] A. El Bakali, D. Boufflers, C. Betrancourt, and P. Desgroux, “Experimental and numerical investigation of atmospheric laminar premixed n-butane flames in sooting conditions,” *Fuel*, vol. 211, pp. 548–565, 2018.
- [246] A. Denisov, G. Colmegna, and P. Jansohn, “Temperature measurements in sooting counterflow diffusion flames using laser-induced fluorescence of flame-produced nitric oxide,” *Appl. Phys. B Lasers Opt.*, vol. 116, no. 2, pp. 339–346, 2014.

Annex A

Mass flow controller calibration

The thermal mass flow meter/controller consists of a stainless steel capillary tube with resistance thermometer elements connected to a Wheatstone bridge. A part of the gas flows is forced through this bypass sensor, and it is warmed up by heating elements. The temperature profile in the capillary tube drifts apart for effect of the passage of a gas flow and this difference is directly proportional to mass flow through the sensor. A precise control valve and a microprocessor based PID controller swiftly adjust the desired flow rate to a set-point value.

The mass flow controllers are calibrated for reference gases and calibration curves are available from the manufacturer if gases with different heat capacities are used. Anyway, a calibration procedure is generally performed before starting a measuring campaign by using a DryCal control and calibration unit. The measuring principle of the DryCal is similar to the bubble flowmeter, indeed the time required for a frictionless piston to traverse a known volume is precisely measured with optical sensors and an internal computer calculates the volumetric flow.

Furan volumetric flow controller calibration

Balloons method

The calibration of the heated-MFC used to feed furan to the flame is performed by an in-house calibration system. It allows the determination of the pressure variation vs time - dP/dt - for fixed values of the MFC set point.

The volumetric flux Q_x can be obtained from the ideal gas law equation $PV=nRT$. Indeed, Q_x is the ratio of the gas volume for unit time at standard temperature and pressure T_n and P_n :

$$Q_x = n \frac{V_m}{t} \quad (\text{A.1})$$

Where n is the number of moles of the gas and V_m the molar volume. From the ideal gas law, V_m is given by:

$$V_m = R \frac{T_n}{P_n} \quad (\text{A.2})$$

Combining the two relations:

$$PV = Q_x P_n \frac{T}{T_n} t \quad (\text{A.3})$$

If a pressure variation dP occurs in a time interval dt :

$$VdP = Q_x P_n \frac{T}{T_n} dt \quad (\text{A.4})$$

by integrating:

$$\int_P^{P+\Delta P} VdP = \int_t^{t+\Delta t} Q_x P_n \frac{T}{T_n} dt \quad (\text{A.5})$$

and

$$Q_x = \frac{V}{\Delta t} \frac{\Delta P}{P_n} \frac{T_n}{T} \quad (\text{A.6})$$

The calibration apparatus is sketched in Fig.A.1. The system is composed of a glass vessel (balloon) connected to the furan heater. A MFC is between the furan vessel and the balloon and it is connected to the vessel with a valve. The total volume of the system, i.e. the balloon and the connection tubes, has a volume V_1 . A pressure gauge located at the top of the balloon measures the pressure variation in the system. The system is connected to a vacuum pump to create the desired vacuum pressure. Once fixed a set point on the MFC, the valve between the MFC and the vessel is opened and the furan vapor enters the volume V_1 . Pressure is detected each 10 s, as shown in Figure.1.7, and a curve ΔP vs Δt is obtained. The slope of the linear range of the ΔP vs Δt curve is used to calculate the volumetric flux Q_x of furan by equation (A.6).

The calibration is repeated for different values of the set-points so that a calibration curve is obtained.

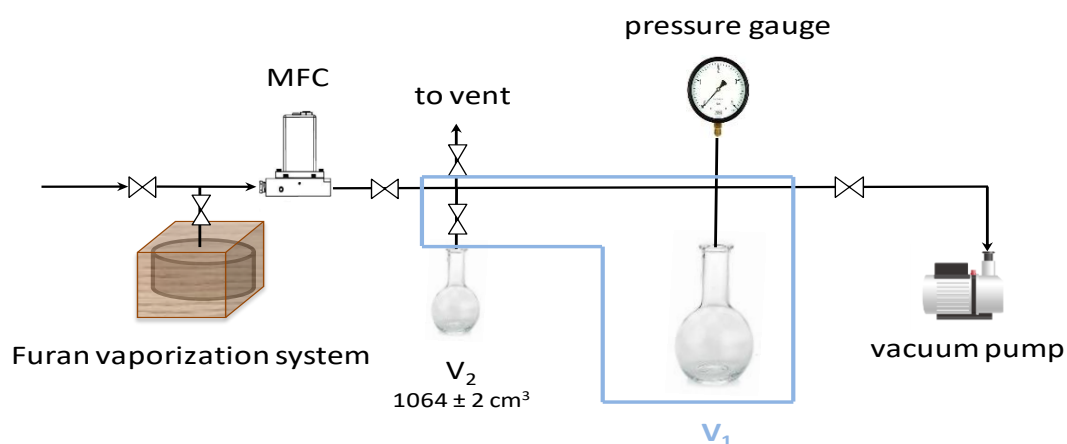


Fig.A.1: Schematic view of the calibration apparatus.

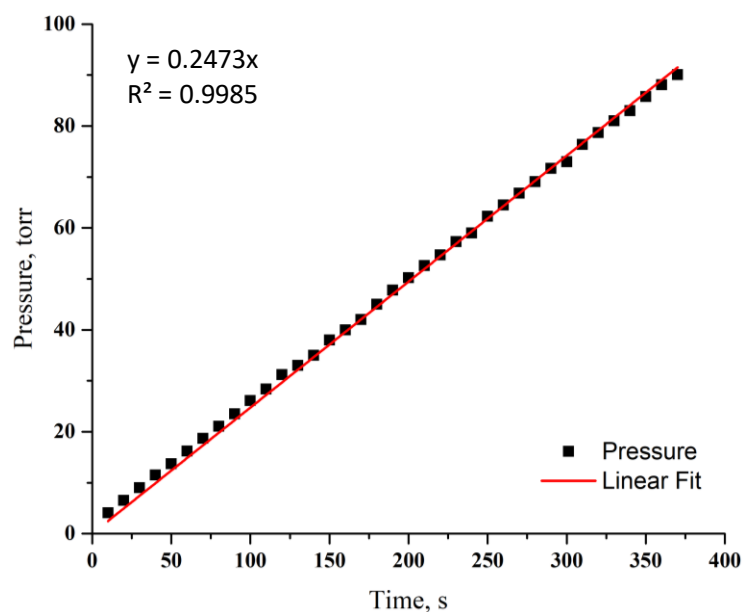


Figure 1.7: ΔP vs Δt at fixed set-point value

An important step in the calibration procedure is the determination of the volume V_1 of the calibration system. To do it, a second balloon is connected in parallel to the first one by a valve. It has a known volume V_2 (in our system $V_2 = 1064 \pm 2 \text{ cm}^3$). The valve connecting the second balloon to the calibration system is opened and the entire system, $V_1 + V_2$, is pumped with air at the atmospheric pressure (P_n). Thereafter, the valve connecting the volume V_2 is closed and the volume V_1 , connected to the vacuum pump, is maintained at a desired vacuum pressure (P_1). The valve connecting the vacuum pump is closed and that connecting the volume V_2 opened so that air from V_2

flows to the volume V_1 under vacuum reaching a final pressure P_f . At this point, the volume V_1 of the calibration system can be obtained by the Boyle law, $PV = \text{const.}$, knowing the pressures and the volume V_2 :

$$V_1 = \frac{P_n - P_f}{P_f - P_1} * V_2 \quad (\text{A.7})$$

Fig.A.2 reports the calibration curve obtained with the procedure above described.

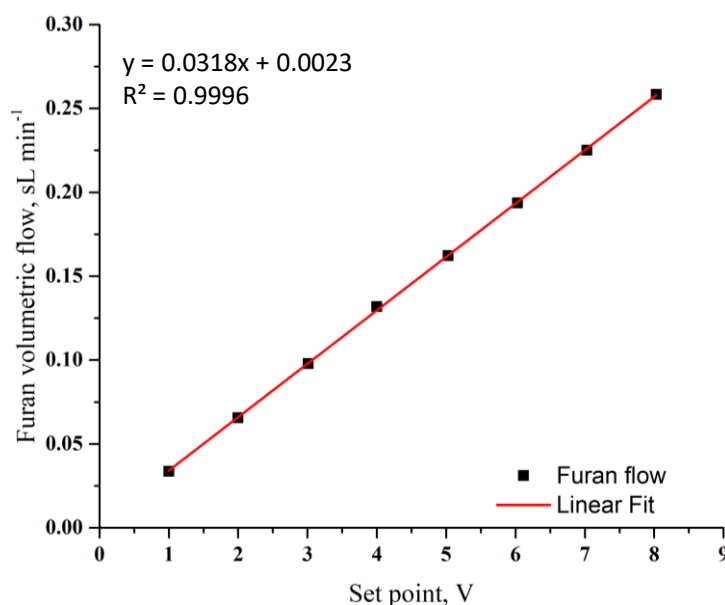


Fig.A.2: Calibration curve for Furan. Flow rates in STP ($P=1 \text{ atm}$ and $T=273 \text{ K}$).

Mass Consumption Calibration (CMC)

The “Balloons” method is reliable procedure to calibrate the heated MFC for fuel in liquid phase at ambient temperature. However, this method could present some problems as gaseous leaks. Because of the dangerous nature of the used compound, we decided in the second part of this thesis to develop a new method to calibrate the heated mass flow controller.

This new procedure is based on the evaluation of the consumption of the liquid compounds (F or THF) in function of the time.

Firstly, we measure the weight of the hermetic container (M_{tare}). We filled the vessel with a known volume of liquid and we weigh the vessel filled (M°) using a precision

scale.

We choose a set value on the heated MFC and ignite the flame for a certain known time. When the thermal equilibrium is re-established inside the vessel, we weight again the vessel after the experience (M).

Knowing the mass of fuel consumed (M° -M) and the time of the experience we can calculate the mol/min consumed:

$$n_x(\text{mol}/\text{min}) = \frac{(M^{\circ} - M)}{MW_x * t_{exp}} \quad (\text{A.8})$$

and then we can obtain the NL/min thanks to the gas law equation:

$$Q_F(\text{sL}/\text{min}) = \frac{n_x * R * T}{P} \quad (\text{A.9})$$

We repeat this procedure for different set point of the heated MFC and we obtain a calibration curve of the volumetric flow of the compound in function of the set values.

The verification of the coherence of this procedure with the “Baloons” methods is obtained by comparing the volumetric flow obtained for furan with “Baloons” and the CMC procedure at the same set point. We find a 0.66% of difference between the two methods.

Fig.A.3 shows the calibration curves of heated MFC obtained with the CMC procedures for THF.

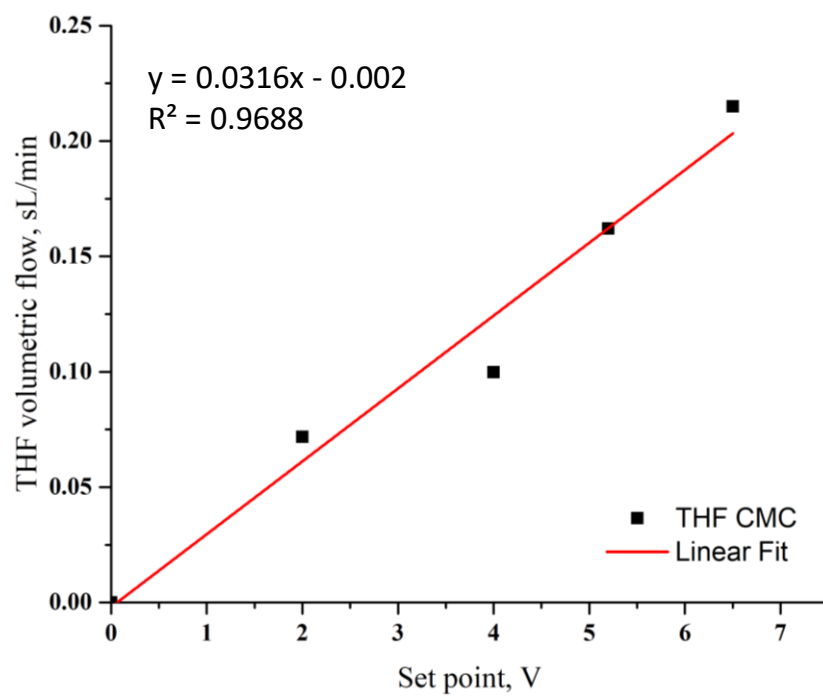


Fig.A.3: Calibration curve for THF with CMC method. Flow rates in STP ($P=1$ atm and $T=273$ K).

Annex B

Temperature measurements by multi-line NO-LIF thermometry

In this work, temperatures were determined using the multi-line NO-LIF thermometry method following a procedure described in [245]. Measurements have been performed by N. Lamoureux and P. Desgroux.

The laser system consists of a frequency-doubled Nd:YAG-seeded laser (SLM Q-smart 850) pumping a dye laser (Quantel TDL+). Wavelengths around 225 nm were obtained by mixing the residual infrared radiation of the YAG laser with the doubling of the fundamental dye radiation. The 6-ns duration pulse has a bandwidth at 225nm around 0.2 cm^{-1} . We have selected the spectral range from 225.30 to 225.35 nm proposed by Denisov et al. [246]. The laser energy fluctuations were monitored by a photodiode located after the burner. The laser beam was introduced unfocused parallel to the burner surface and shaped using a horizontal slit of 0.4 mm in front of the burner.

The LIF signal was collected with a two-lens system and focused on the entrance slit of a monochromator (Acton Spectrapro 2500i). The entrance slit, adjusted to width 300 μm and height 7.5 mm, was parallel to the laser axis, and the output slit was adjusted to provide a 7-nm band pass adapted to collect the A–X(0,2) fluorescence band under investigation. The fluorescence signals were collected with a Philips XP2020Q photomultiplier tube.

The fluorescence and laser intensity signals were stored by a digital scope (LECROY 9354, 8 bit, 500 MHz bandwidth, 2 GS/s sampling rate). 0.01% of NO was seeded into the flame to improve the signal to noise ratio without perturbing the flame temperature. The excitation LIF spectrum was recorded with a scan rate of the fundamental dye wavelength of 0.35 pm/s and by averaging the LIF signals over 7 laser pulses. The baseline was determined for each spectrum around 225.3 nm and subtracted all along the recorded spectrum.

A post-treatment consisting of a Savitzky–Golay smoothing filter with a moving window of 7 points was applied. Temperature was determined from the least mean square between the experimental and the simulated spectra library generated using

LIFBASE [233] and considering a Voigt lineshape.

Temperatures near the burner surface were measured using a K-thermocouple (500 μm).

The temperature profiles measured in the investigated flames are presented in Fig. B.1 and B.2. Temperature has been measured in flames M1.0, M1.2 THFM1.0 and THFM1.2 (see table III.1 Chapter III). Fig. B.2 shows a comparison of all the measured temperature profiles in the reaction zone.

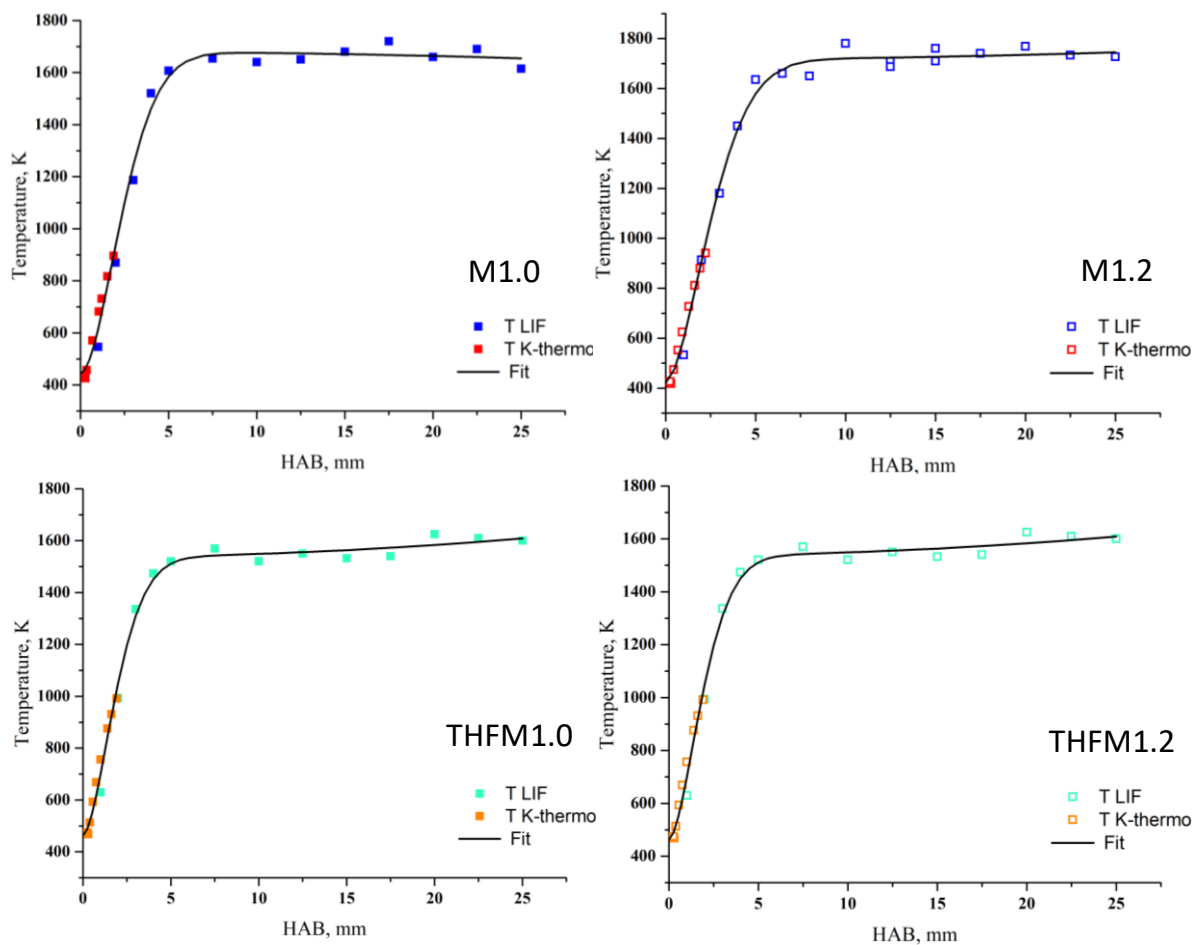


Fig. B.1: Experimental temperature profiles of the flames M1.0, M1.2, THFM1.0 and THFM1.2.

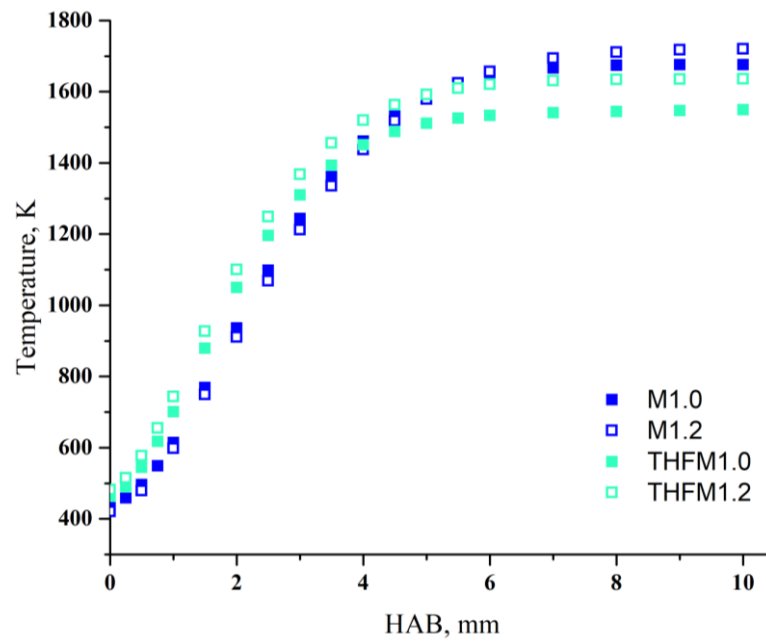


Fig. B.2: Zoom of the temperature profiles of the flames M1.0, M1.2, THFM1.0 and THFM1.2.

These data are preliminary. They need to be confirmed by supplementary measurements currently in progress. Note that temperature measurements have been performed without microprobe and that the computations have been performed without any spatial shift of the temperature profiles.

Annex C

Mole profiles of chemical species in each flame

Flame M1.0

Stable species

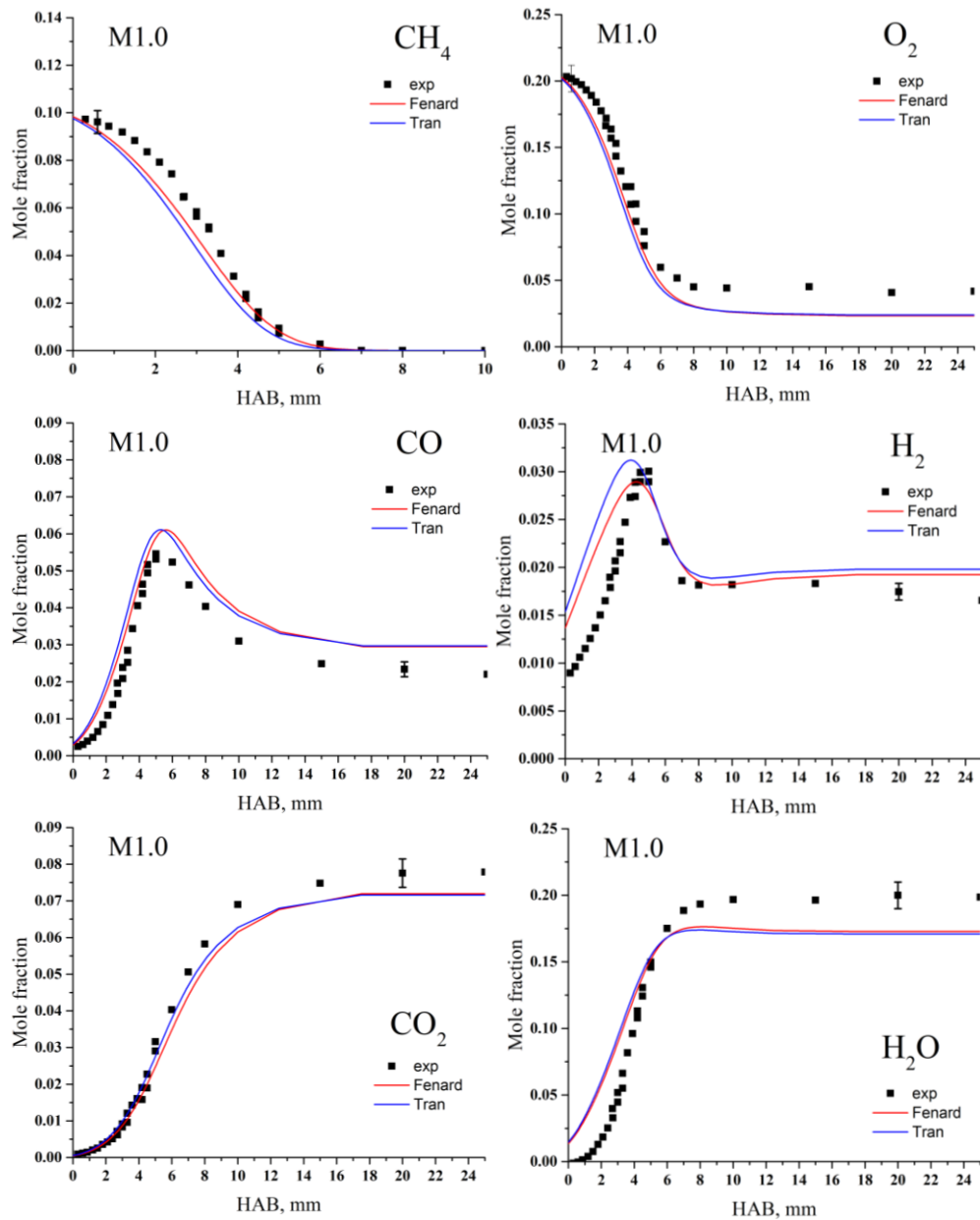


Fig. C.1: Comparison between experimental and modeled mole fraction profiles for major species in M1.0 flame.

Hydrocarbons

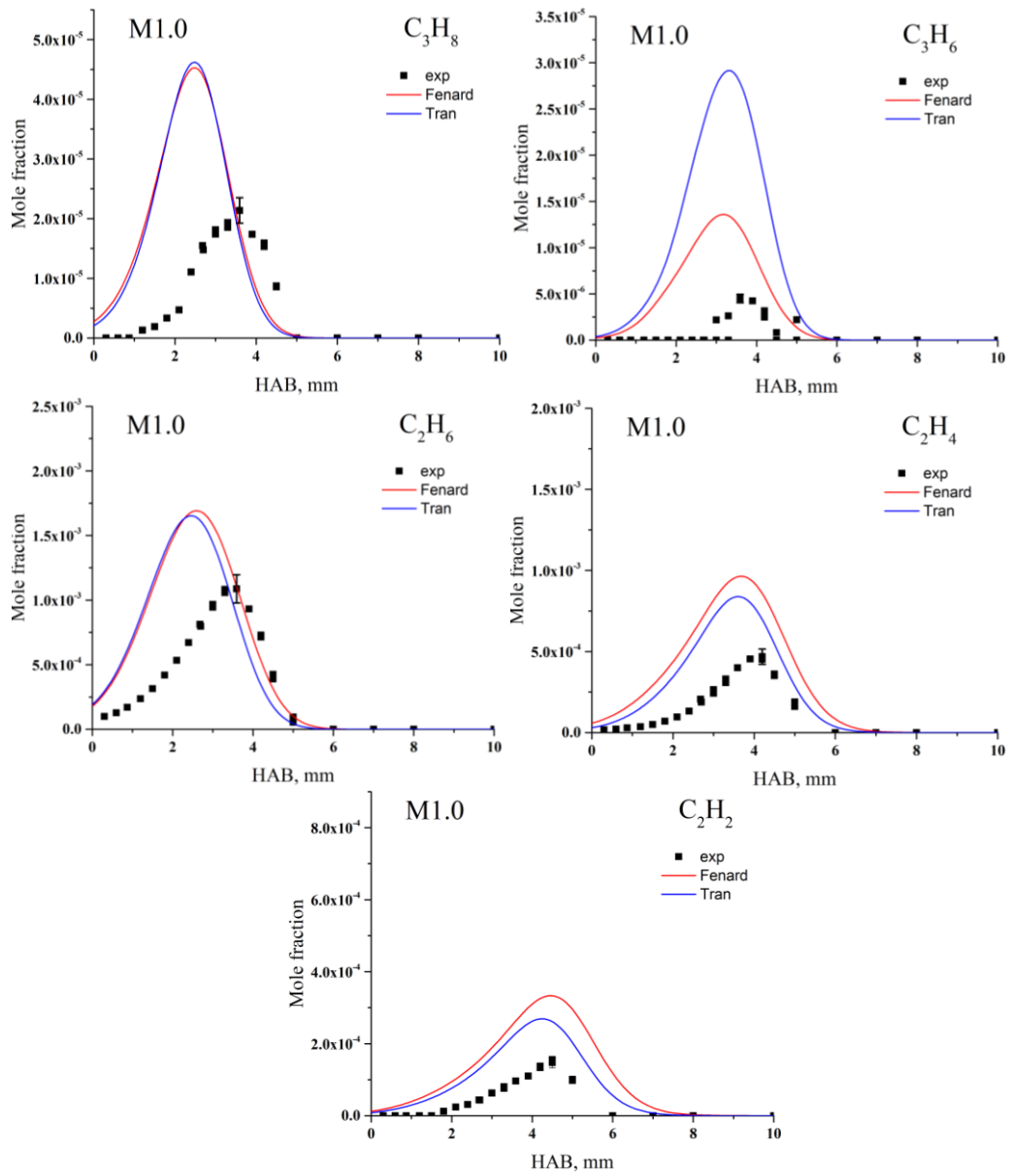


Fig.C.2: Comparison between experimental and modeled mole fraction profiles for hydrocarbon species in M1.0 flame.

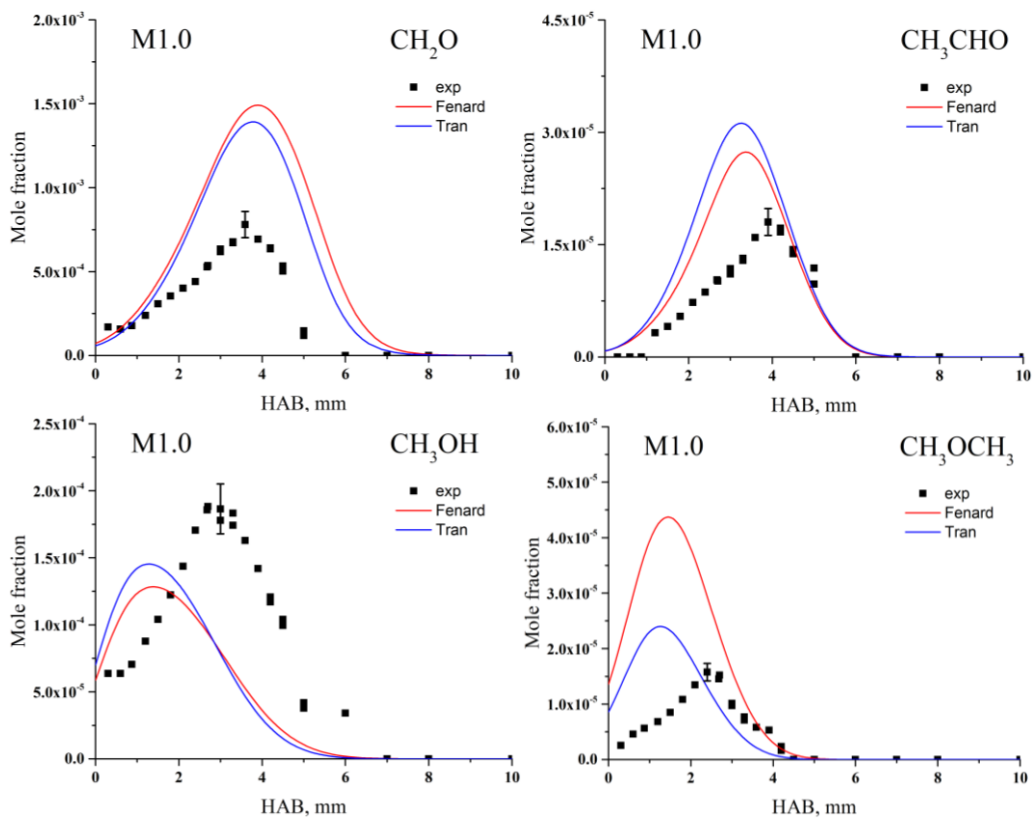
Oxygenated species

Fig. C.3: Comparison between experimental and modeled mole fraction profiles for oxygenated species in M1.0 flame

Flame M1.2

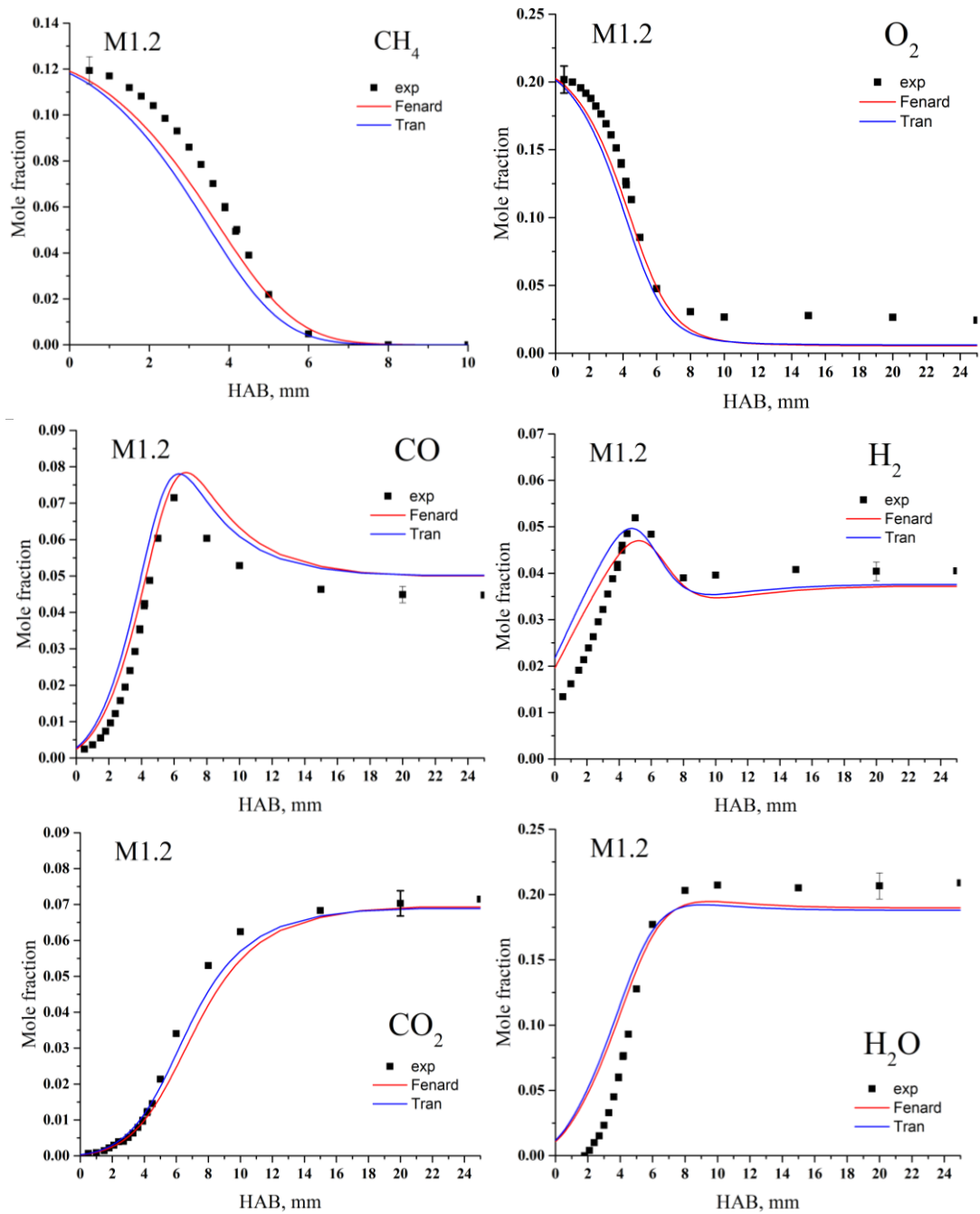
Stable species

Fig. C.4: Comparison between experimental and modeled mole fraction profiles for major species in M1.2 flame.

Hydrocarbons

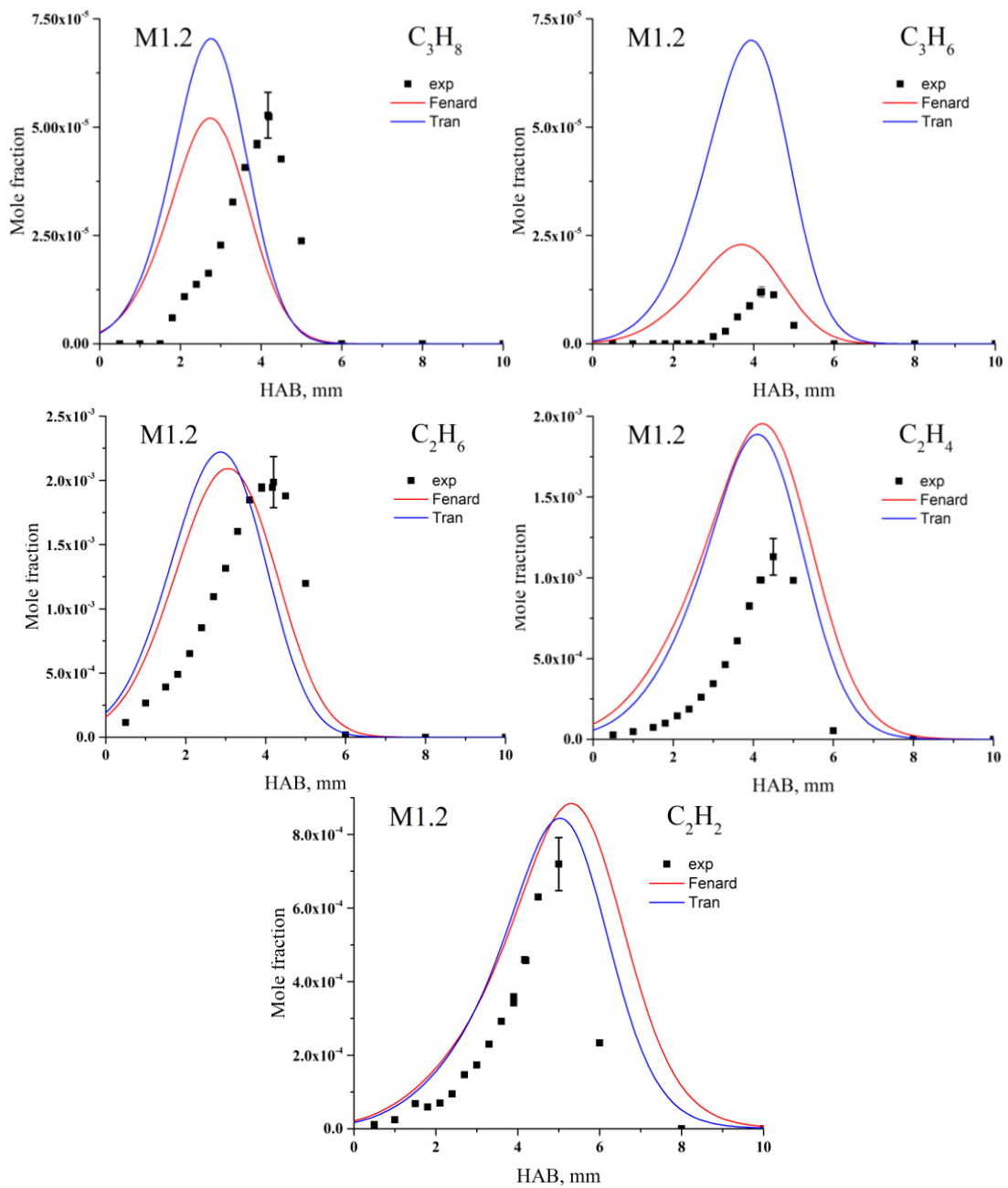


Fig.C.5: Comparison between experimental and modeled mole fraction profiles for hydrocarbon species in M1.2 flame.

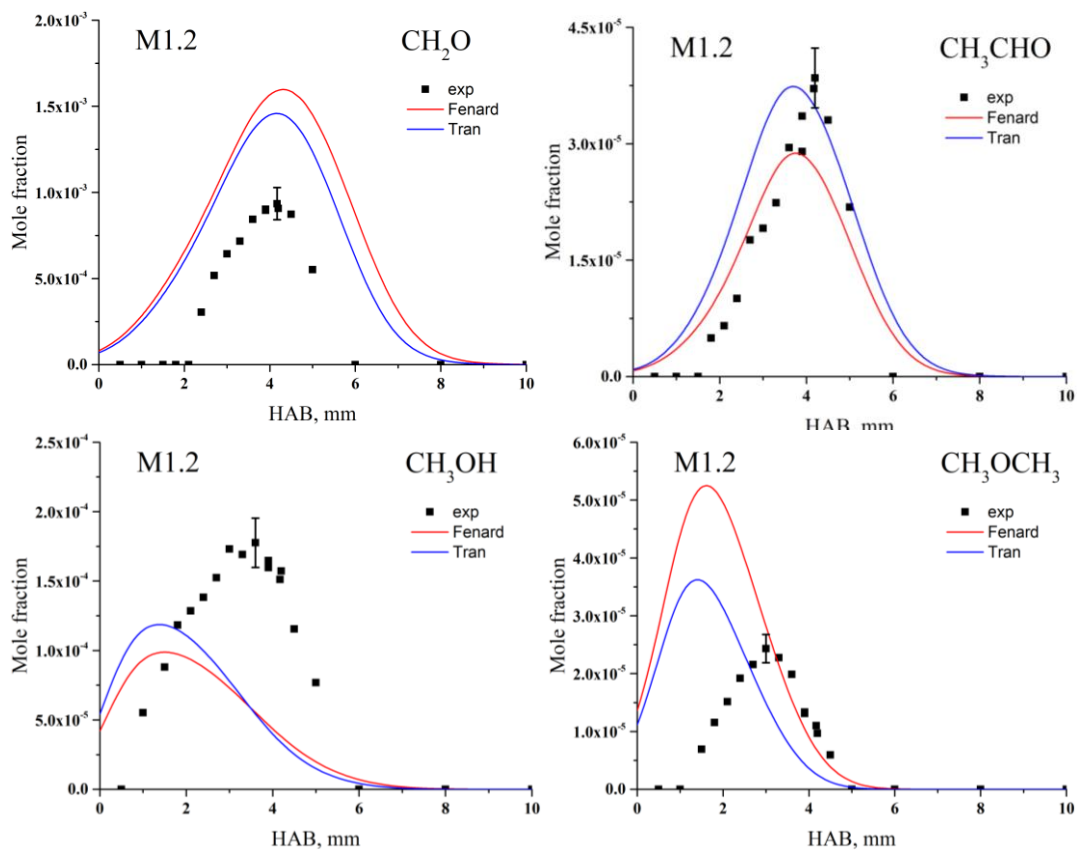
Oxygenated species

Fig. C.6: Comparison between experimental and modeled mole fraction profiles for oxygenated species in M1.2 flame

Flame FM1.0

Stable species

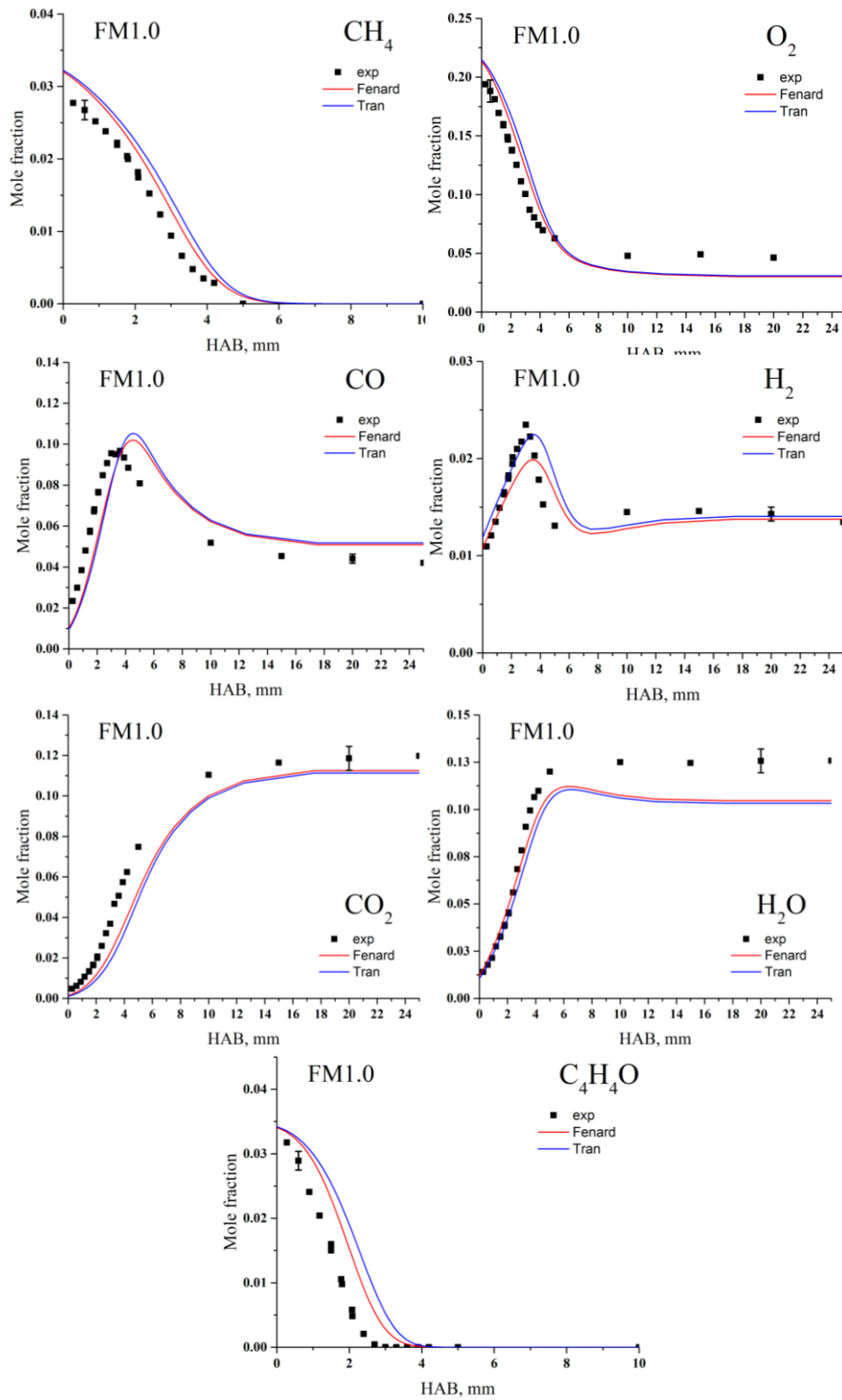


Fig. C.7: Comparison between experimental and modeled mole fraction profiles for major species in FM1.0 flame.

Hydrocarbons

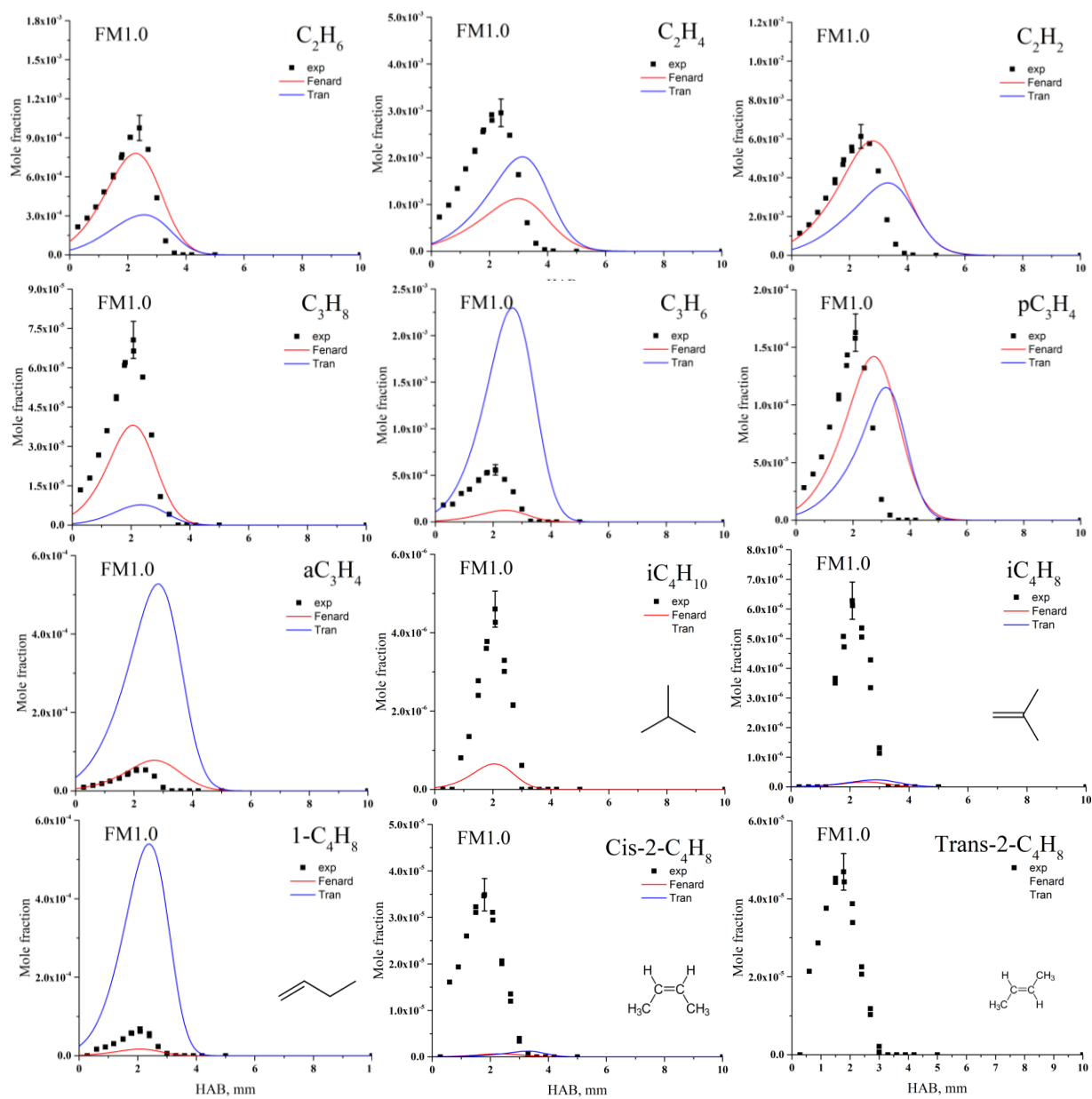


Fig.C.8: Comparison between experimental and modeled (if present) mole fraction profiles for hydrocarbon species in FM1.0 flame (in order: ethane, ethylene, acetylene, propane propene, propyne, allene, isobutane, isobutene, 1-butene, cis-2-butene, trans-2-butene)

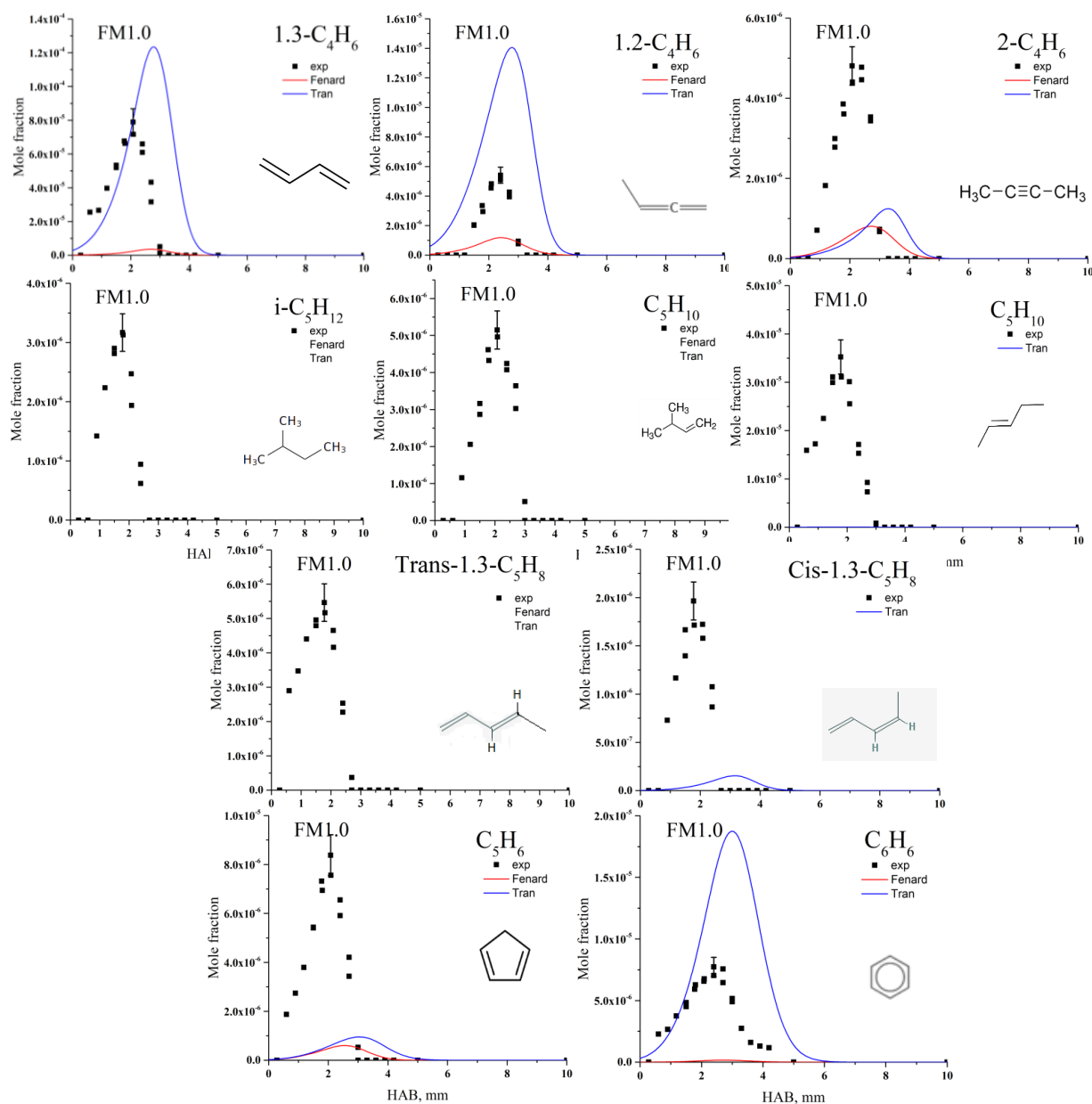


Fig.C.9: Comparison between experimental and modeled (if present) mole fraction profiles for hydrocarbon species in FM1.0 flame (in order: 1,3-butadiene, 1,2-butadiene, 2-butyne, isopentane, 3-methyl-1-butene, 2-pentene, trans-1,3-pentadiene, cis-1,3-pentadiene, cyclopentadiene, benzene).

Oxygenated species

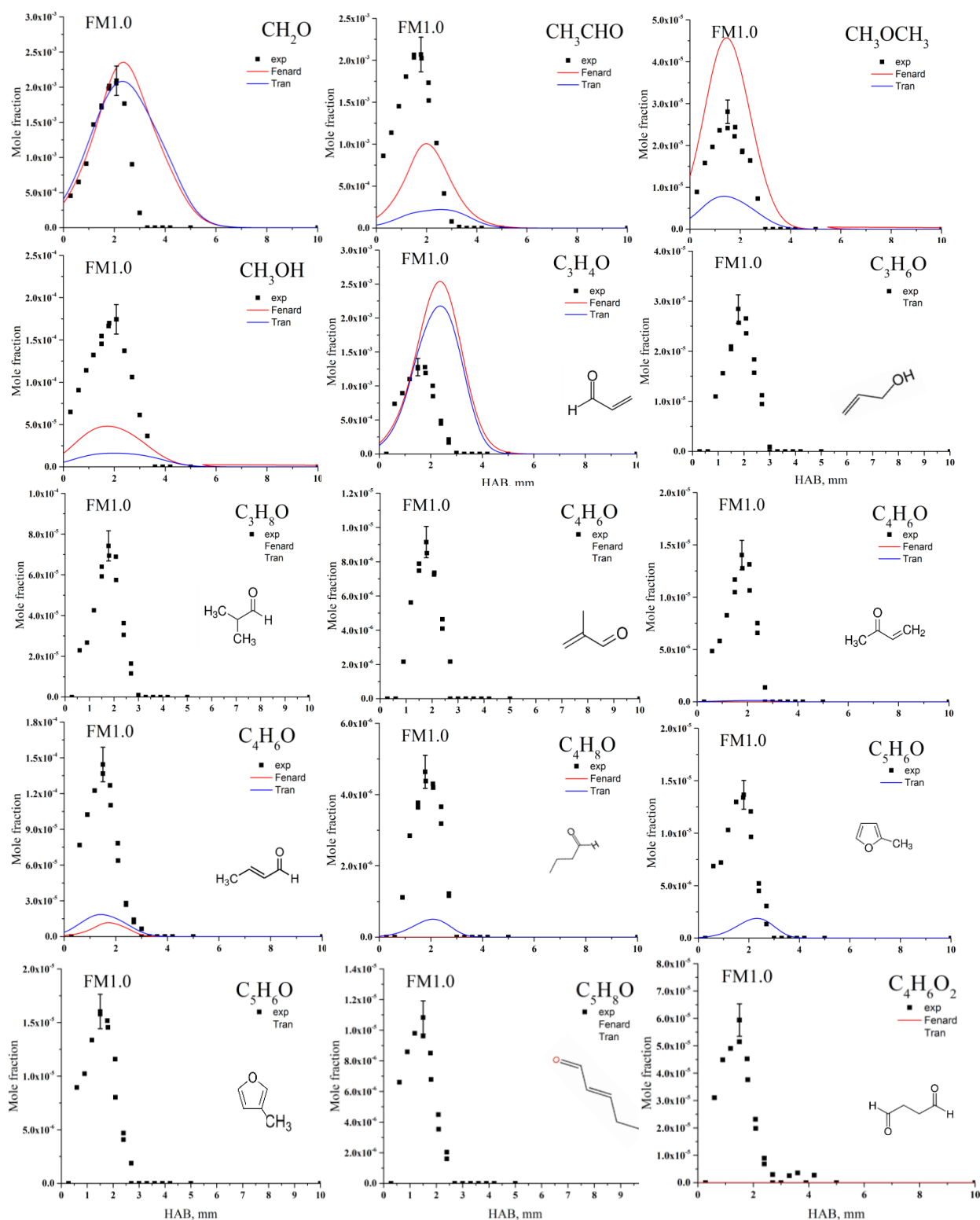


Fig.C.10: Comparison between experimental and modeled (if present) mole fraction profiles for oxygenated species in FM1.0 flame (in order: formaldehyde, acetaldehyde, dimethyl ether, methanol, acrolein, allylic alcohol, isobutanol, methacrolein, methyl vinyl ketone, 2-butenal, butanal, 2-methyl furan, 3-methyl furan, 2-pentalen, butanedial).

Flame FM1.2

Stable species

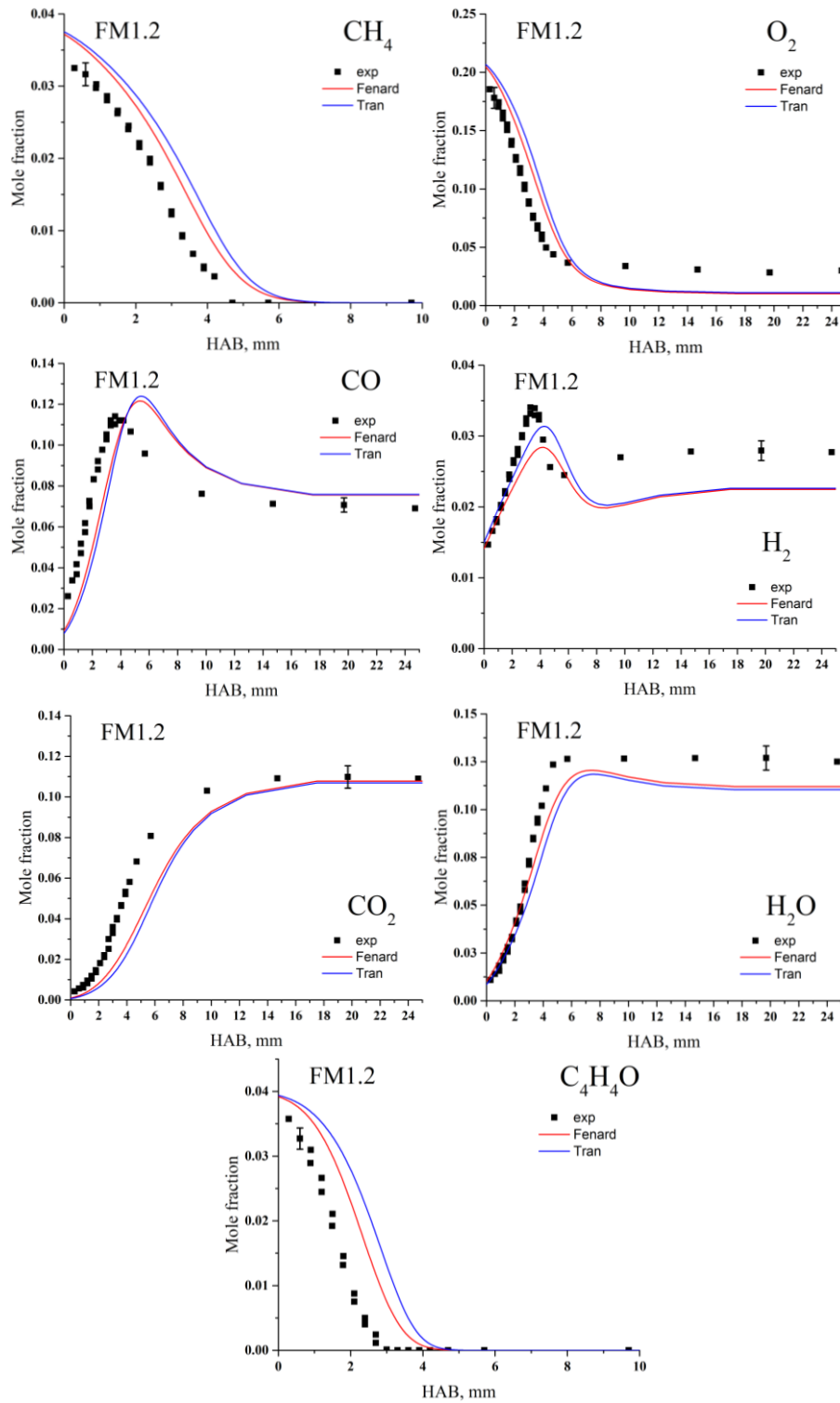


Fig. C.11: Comparison between experimental and modeled mole fraction profiles for major species in FM1.2 flame.

Hydrocarbons

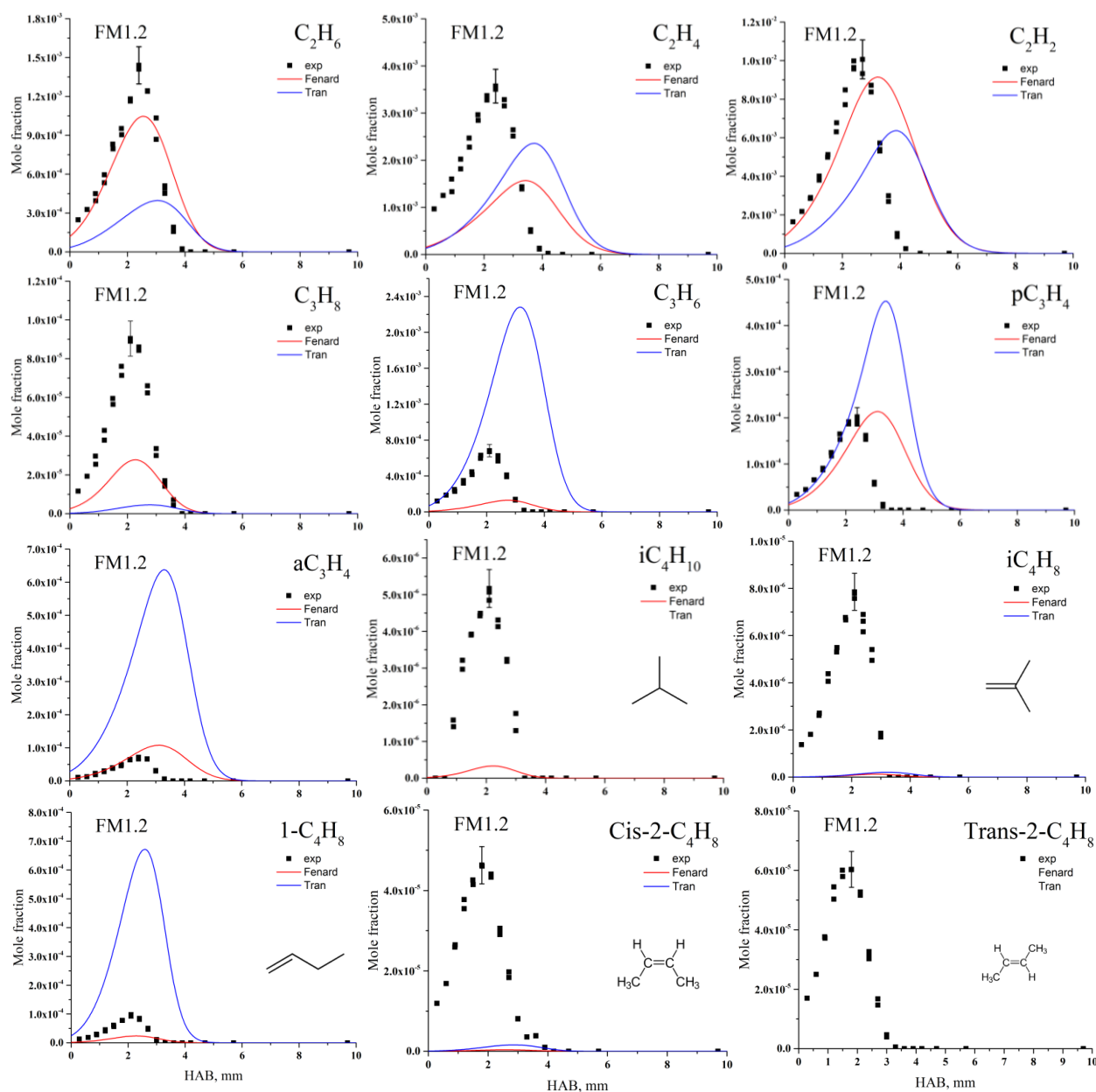


Fig.C.12: Comparison between experimental and modeled (if present) mole fraction profiles for hydrocarbon species in FM1.2 flame (in order: ethane, ethylene, acetylene, propane propene, propyne, allene, isobutane, isobutene, 1-butene, cis-2-butene, trans-2-butene)

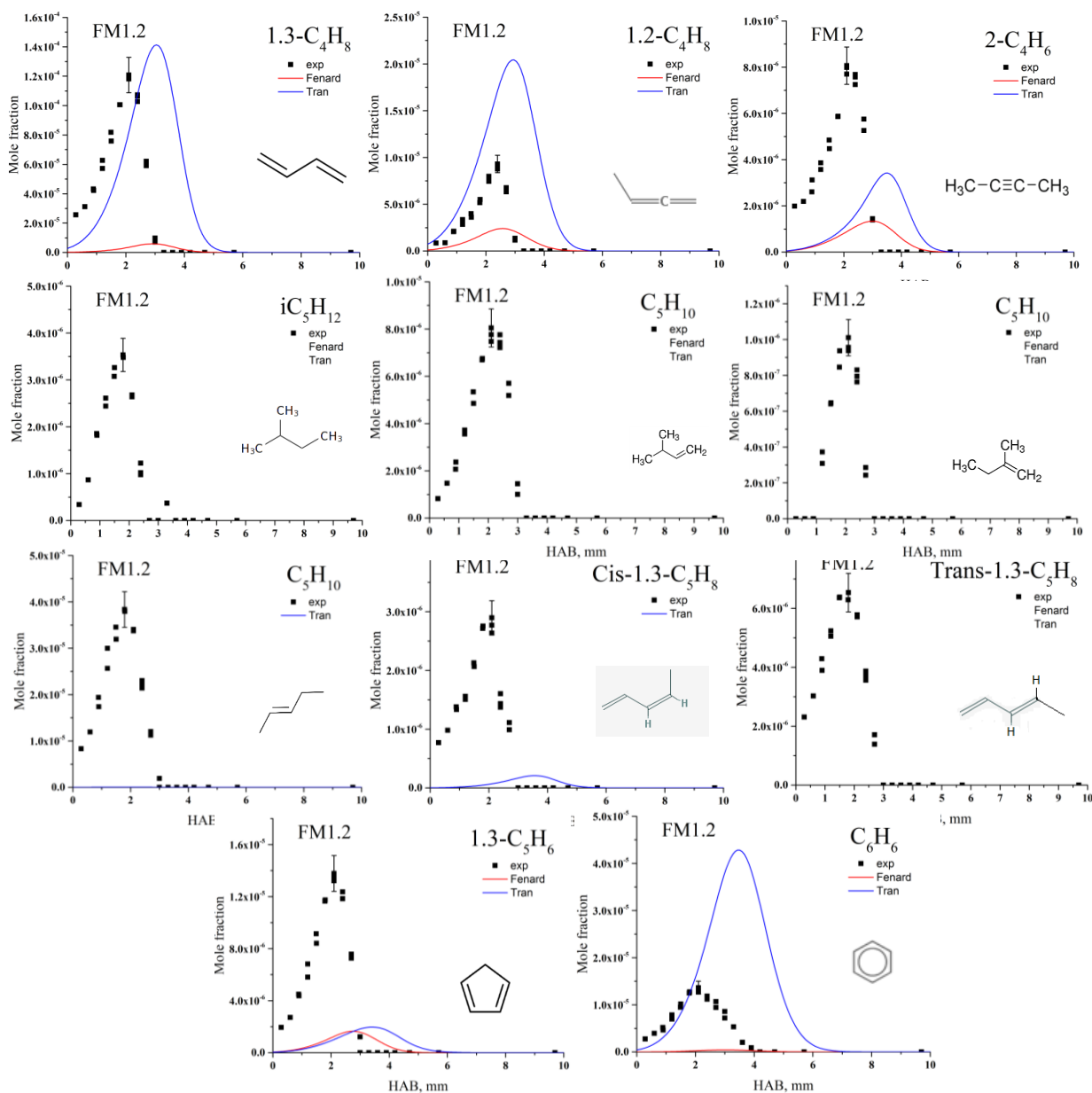


Fig.C.13: Comparison between experimental and modeled (if present) mole fraction profiles for hydrocarbon species in FM1.2 flame (in order: 1,3-butadiene, 1,2-butadiene, 2-butyne, isopentane, 3-methyl-1-butene, 2-methyl-1-butene, 2-pentene, trans-1,3-pentadiene, cis-1,3-pentadiene, cyclopentadiene, benzene).

Oxygenated species

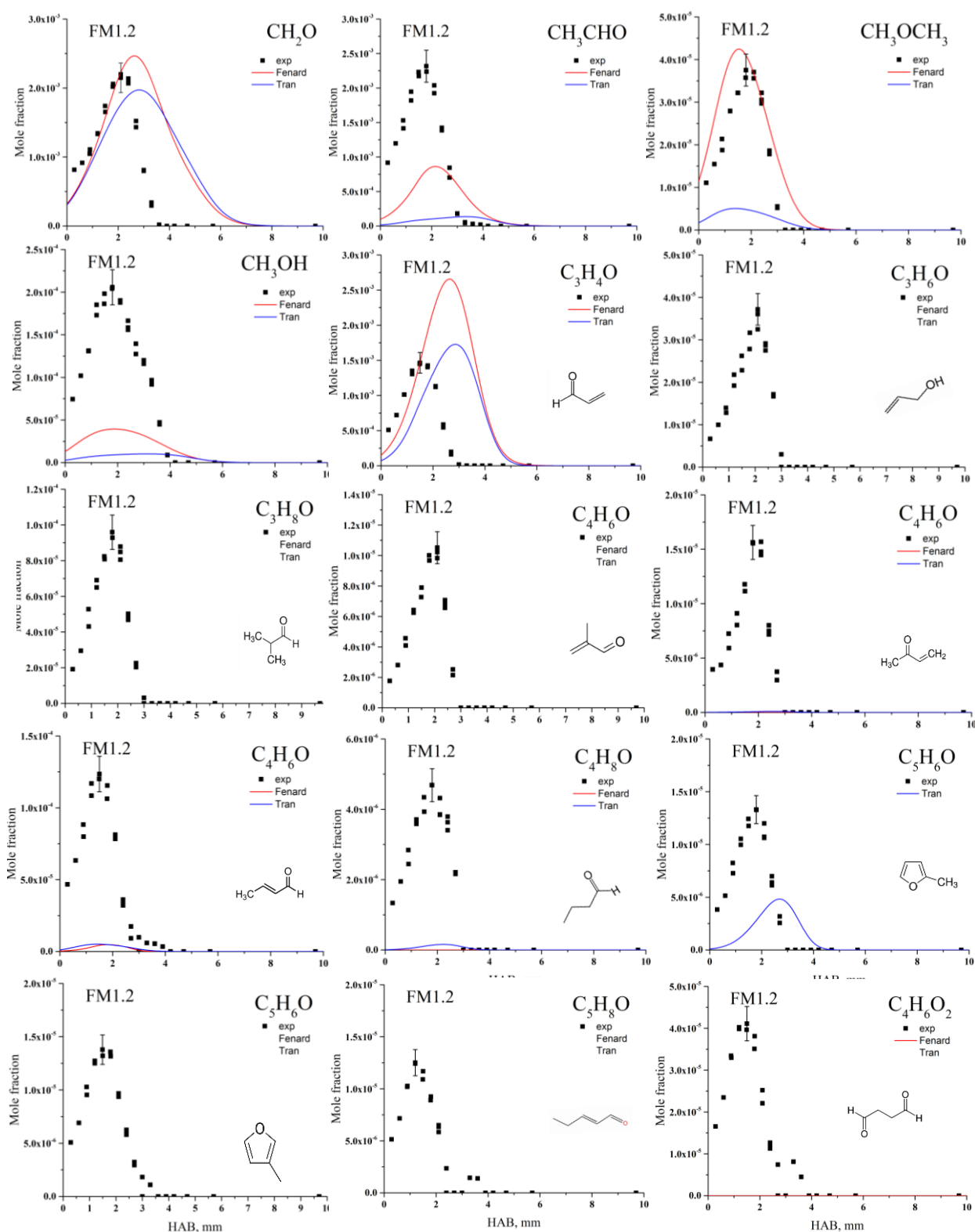


Fig.C.14: Comparison between experimental and modeled (if present) mole fraction profiles for oxygenated species in FM1.2 flame (in order: formaldehyde, acetaldehyde, dimethyl ether, methanol, acrolein, allylic alcohol, isobutanol, methacrolein, methyl vinyl ketone, 2-butenal, butanal, 2-methyl furan, 3-methyl furan, 2-pentalen, butanedial).

Flame THFM1.0

Stable species

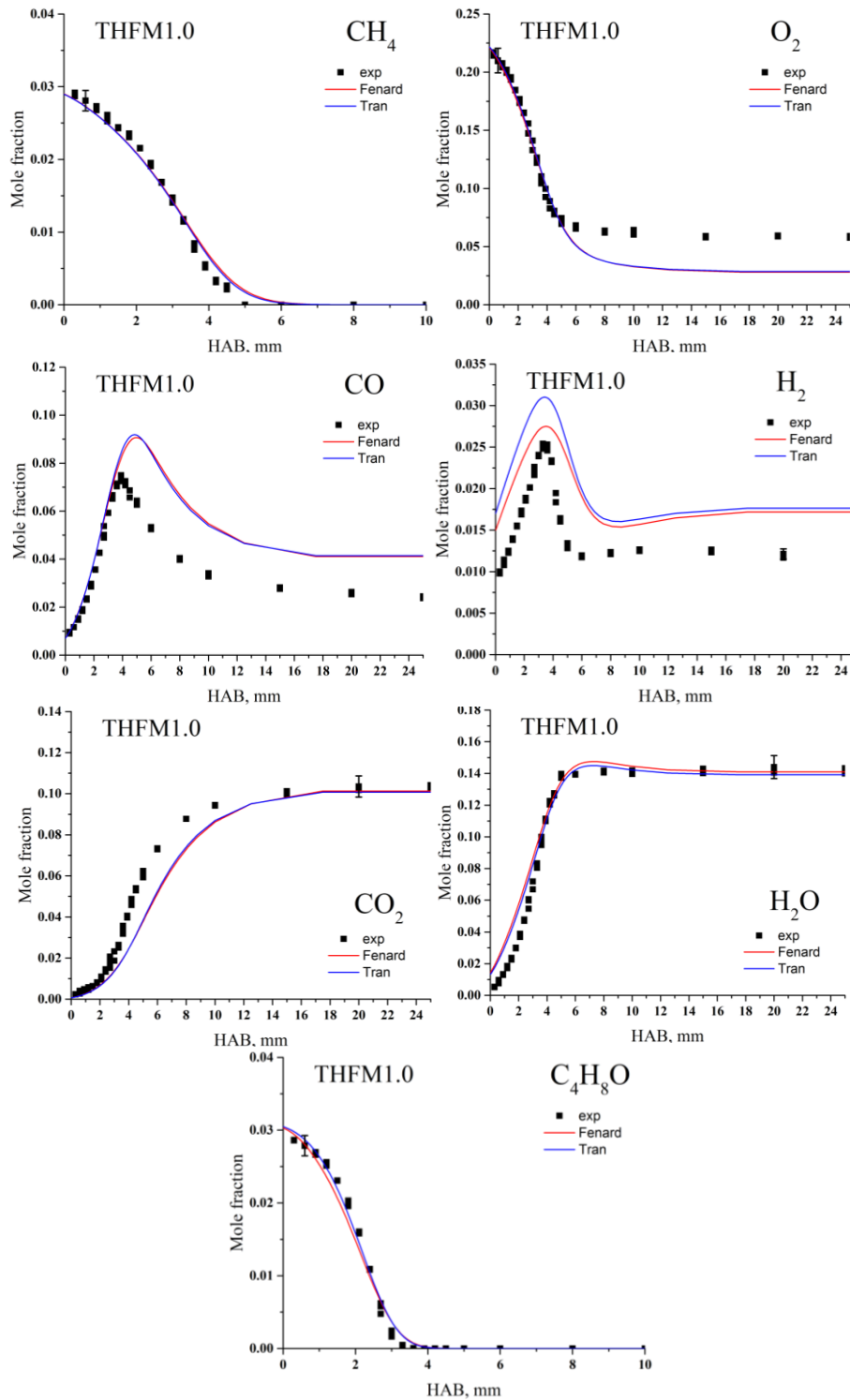


Fig. C.15: Comparison between experimental and modeled mole fraction profiles for major species in THFM1.0 flame.

Hydrocarbons

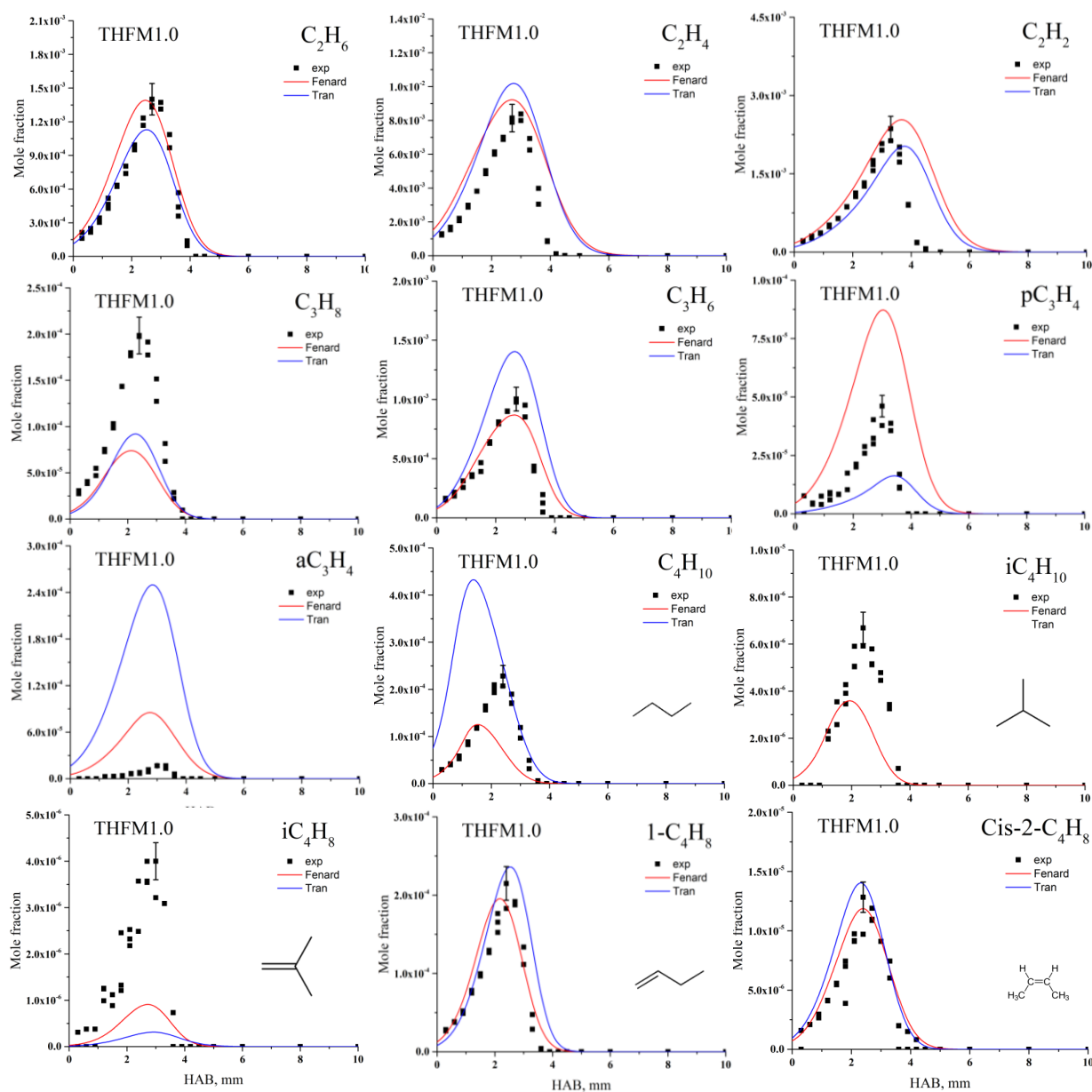


Fig.C.16: Comparison between experimental and modeled (if present) mole fraction profiles for hydrocarbon species in THFM1.0 flame (in order: ethane, ethylene, acetylene, propane propene, propyne, allene, butane, isobutane, isobutene, 1-butene, cis-2-butene)

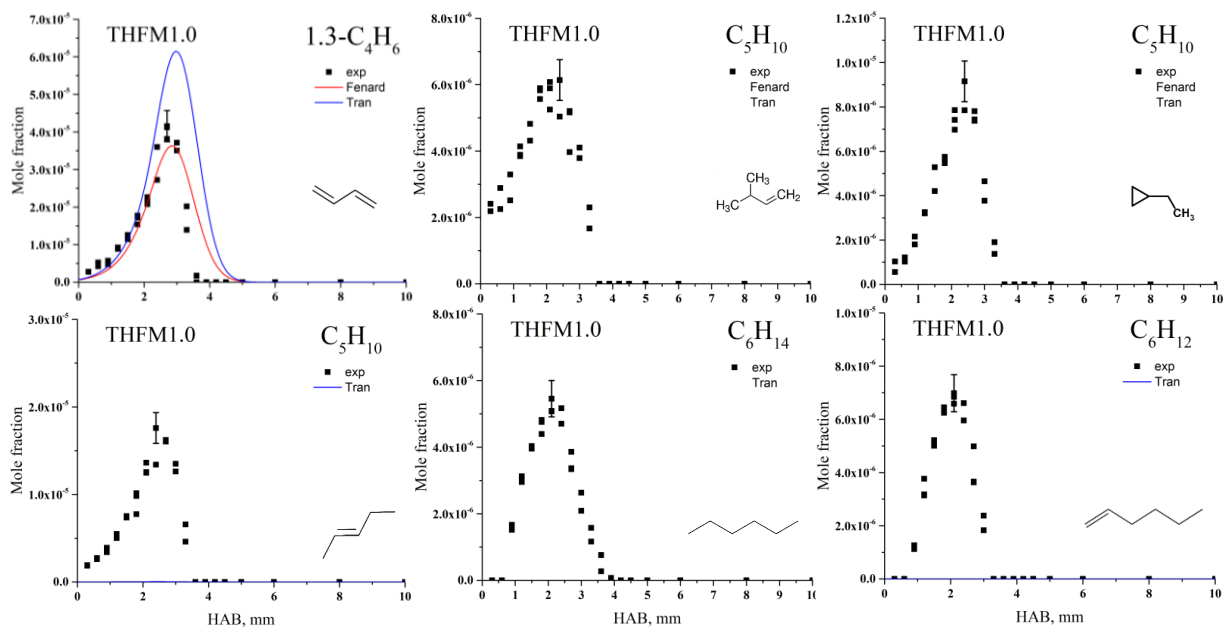


Fig.C.17: Comparison between experimental and modeled (if present) mole fraction profiles for hydrocarbon species in THFM1.0 flame (in order: 1,3-butadiene, 3-methyl-1-butene, ethylcyclopropane, 2-pentene, hexane, 1-hexene).

Oxygenated species

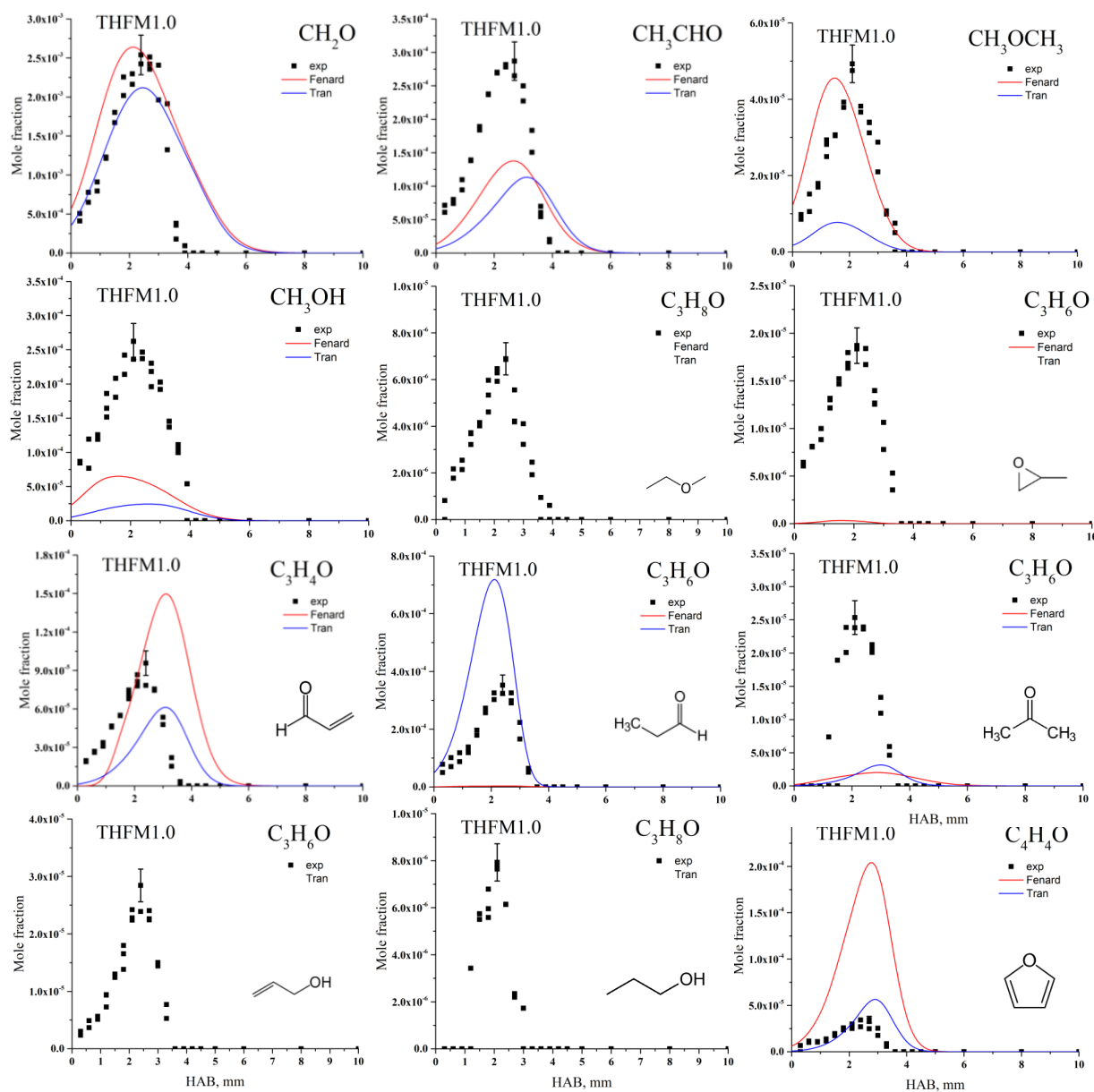


Fig.C.18: Comparison between experimental and modeled (if present) mole fraction profiles for oxygenated species in THFM1.0 flame (in order: formaldehyde, acetaldehyde, dimethyl ether, methanol, methoxyethane, propylene oxide, acrolein, propanal, acetone, allylic alcohol, propanol, furan,).

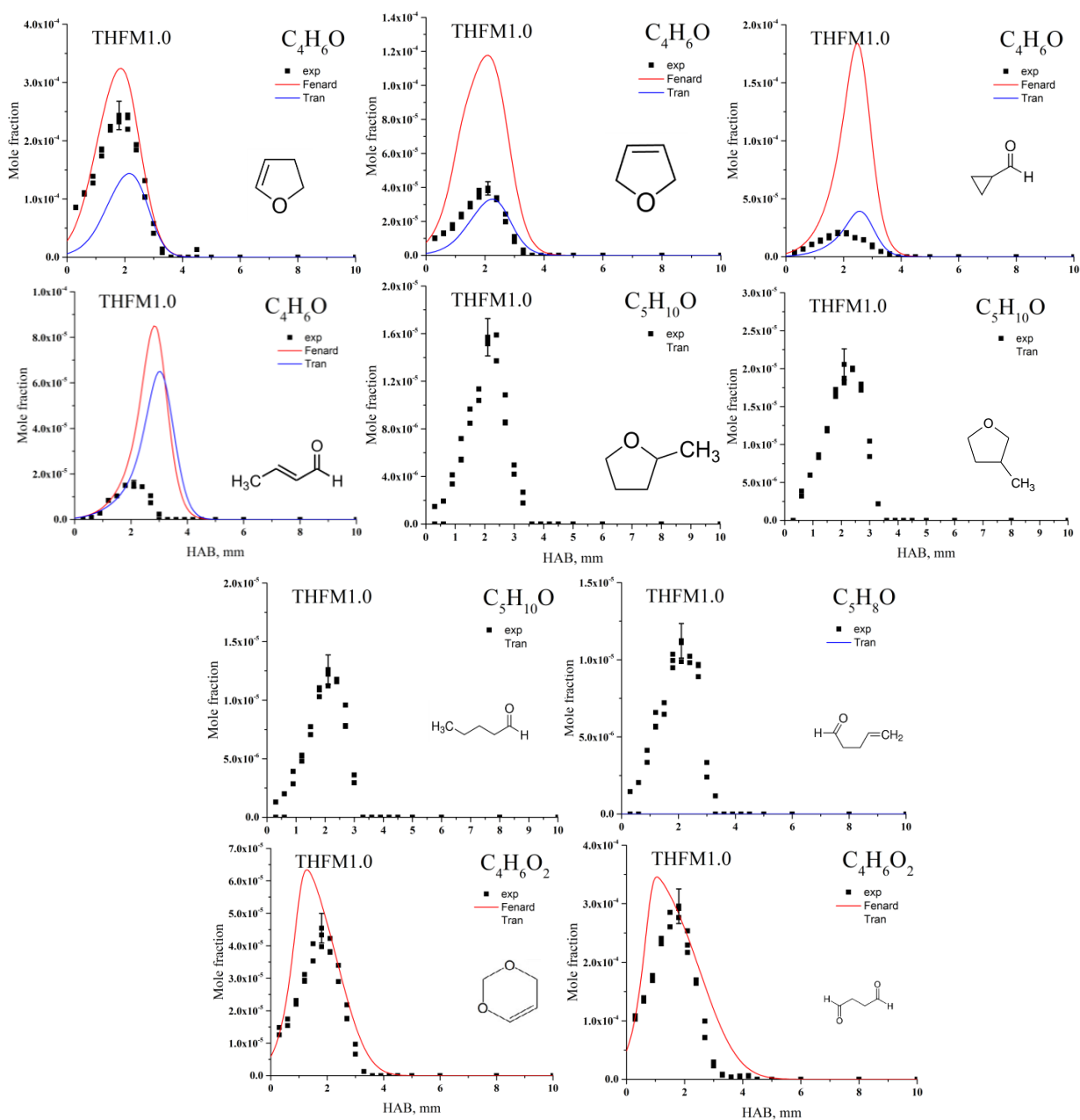


Fig.C.19: Comparison between experimental and modeled (if present) mole fraction profiles for oxygenated species in THFM1.0 flame (in order: 2,3-dihydrofuran, 2,5-dihydrofuran, cyclopropanecarboxaldehyde, 2-butenal, 2-methyl tetrahydrofuran, 2-methyl tetrahydrofuran, pentanal, 4-pentenal, 1,3 dioxene, butanedial).

Flame THFM1.2

Stable species

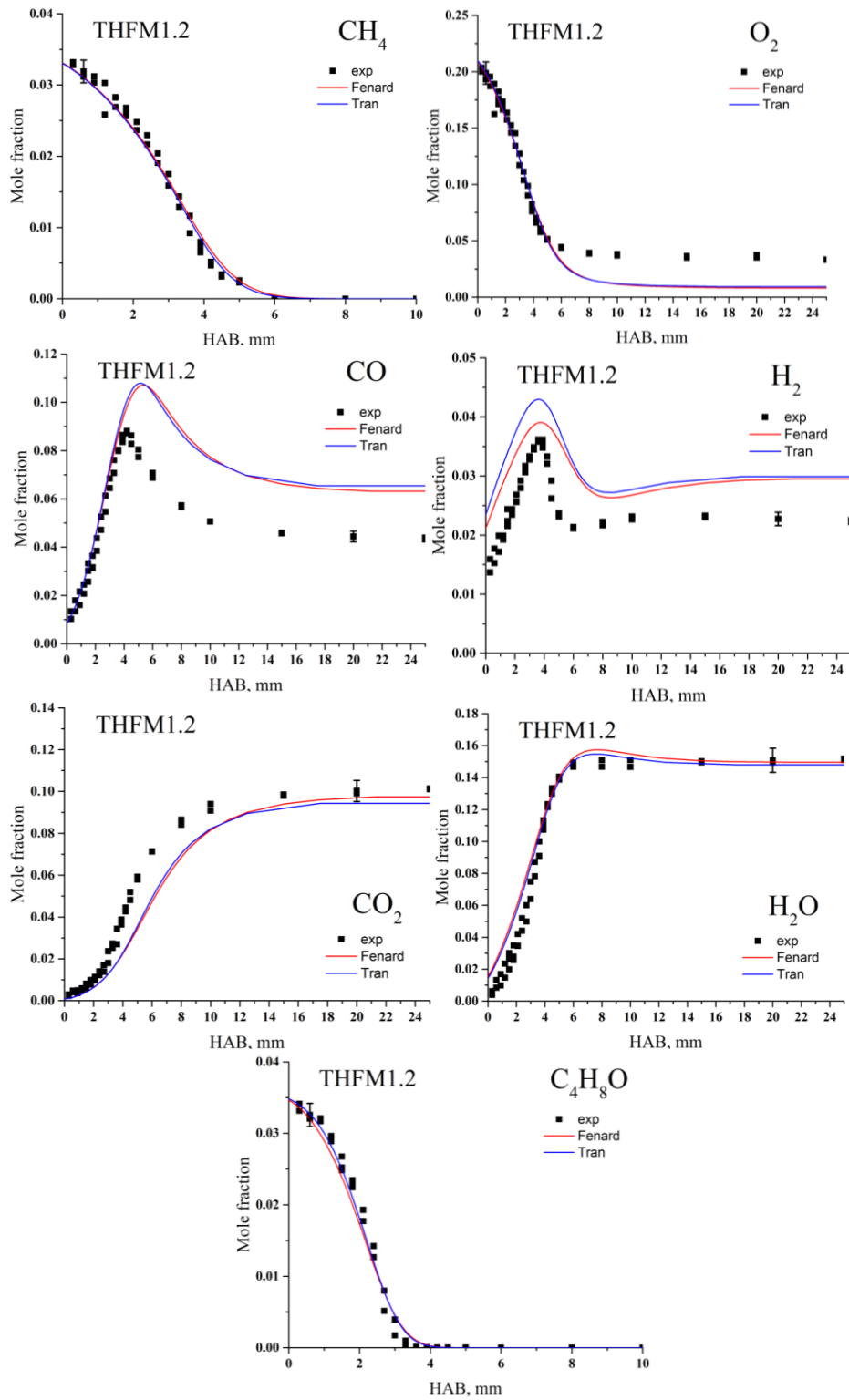


Fig. C.20: Comparison between experimental and modeled mole fraction profiles for major species in THFM1.2 flame.

Hydrocarbons

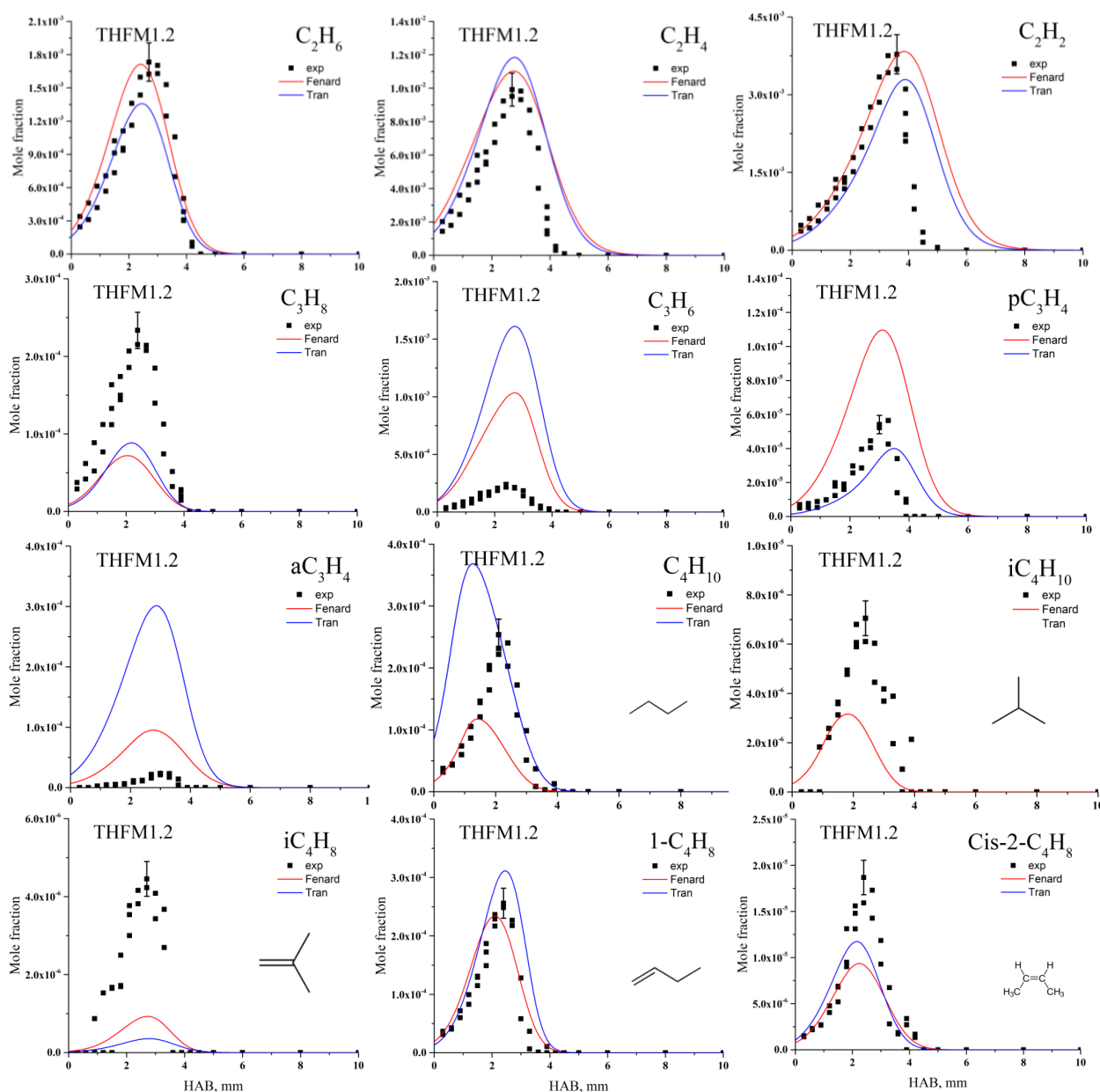


Fig.C.21: Comparison between experimental and modeled (if present) mole fraction profiles for hydrocarbon species in THFM1.2 flame (in order: ethane, ethylene, acetylene, propane propene, propyne, allene, butane, isobutane, isobutene, 1-butene, cis-2-butene)

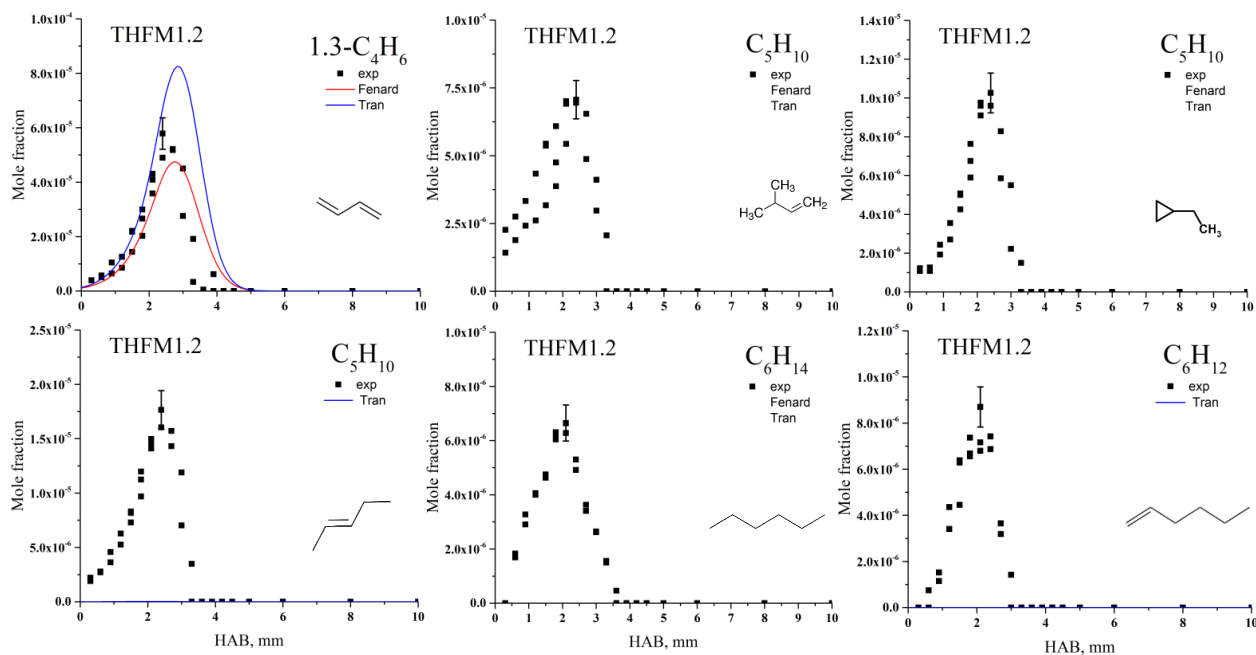


Fig.C.22: Comparison between experimental and modeled (if present) mole fraction profiles for hydrocarbon species in THFM1.2 flame (in order: 1,3-butadiene, 3-methyl-1-butene, ethyl-cyclopropane, 2-pentene, hexane, 1-hexene).

Oxygenated species

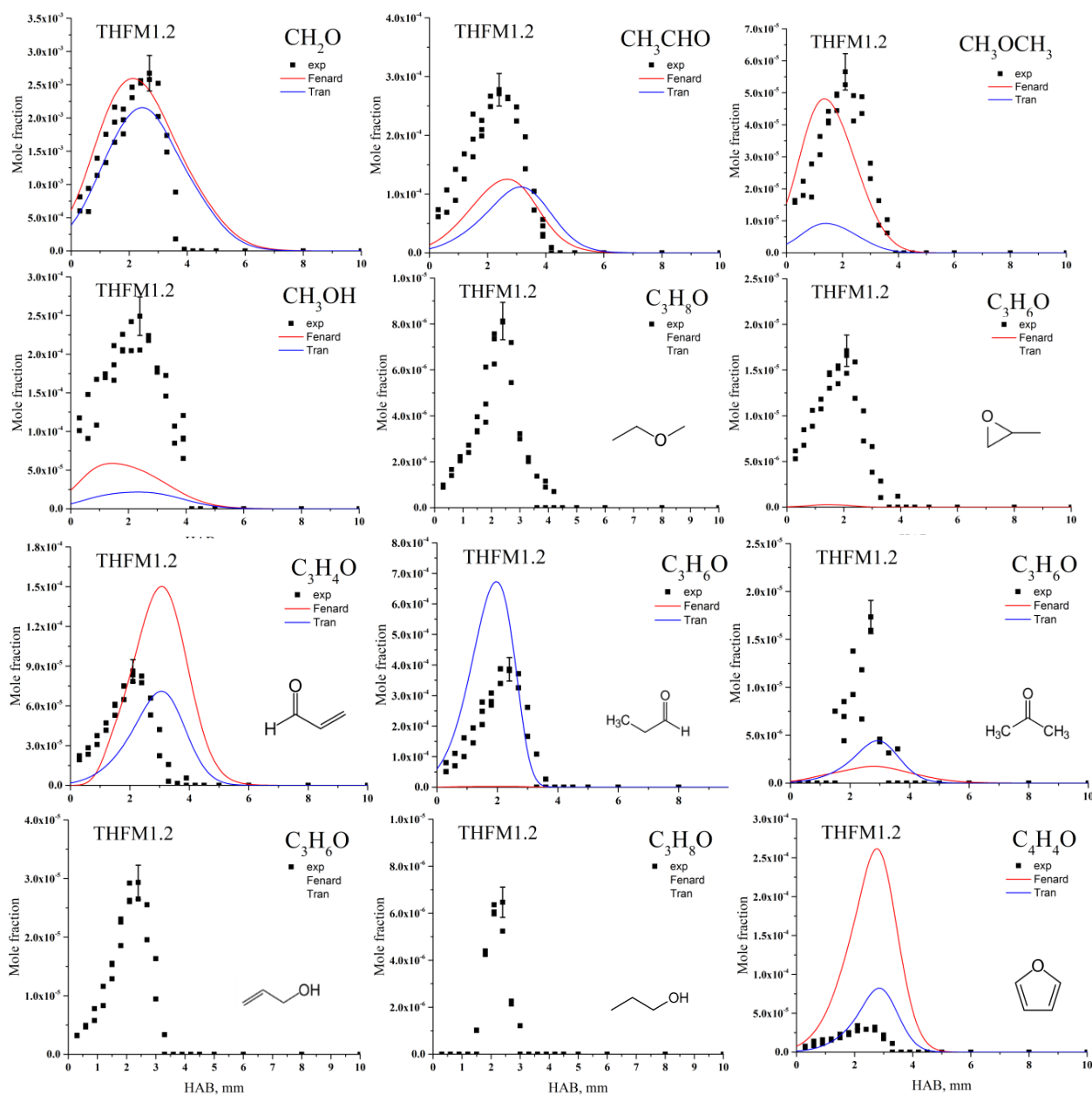


Fig.C.23: Comparison between experimental and modeled (if present) mole fraction profiles for oxygenated species in THFM1.2 flame (in order: formaldehyde, acetaldehyde, dimethyl ether, methanol, methoxyethane, propylene oxide, acrolein, propanal, acetone, allylic alcohol, propanol, furan,).

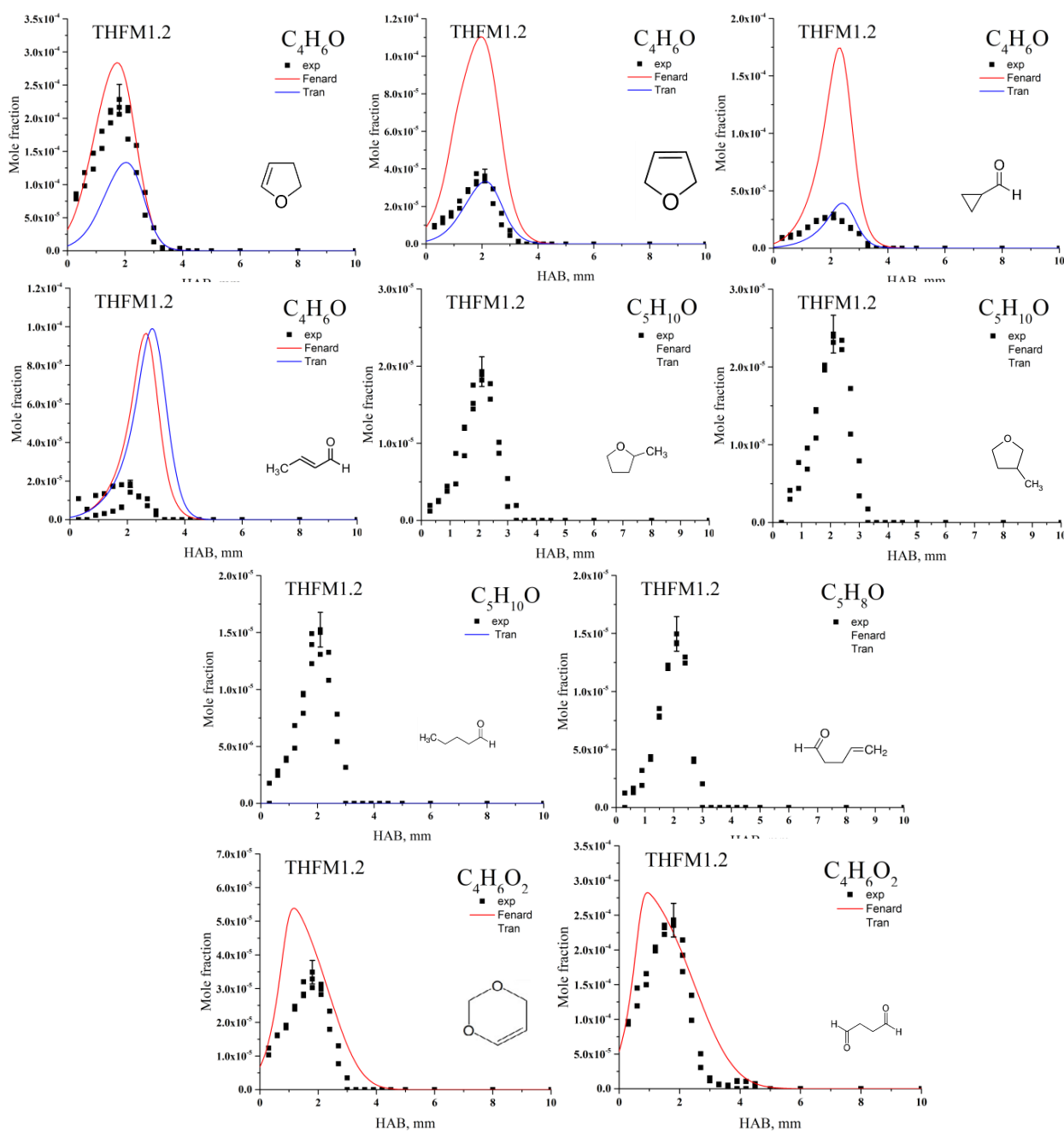


Fig.C.24: Comparison between experimental and modeled (if present) mole fraction profiles for oxygenated species in THFM1.2 flame (in order:2,3-dihydrofuran, 2,5-dihydrofuran, cyclopropanecarboxaldehyde, 2-butenal, 2-methyl tetrahydrofuran, 2-methyl tetrahydrofuran, pentanal, 4-pentenal, 1,3 dioxene, butanedial).

Experimental peak mole fractions in each flame

Name	M1.0	M1.2	FM1.0	FM1.2	THFM1.0	THFM1.2
Carbon Monoxide	$5.77 \cdot 10^{-2}$	$7.68 \cdot 10^{-2}$	$1.01 \cdot 10^{-1}$	$1.19 \cdot 10^{-1}$	$7.54 \cdot 10^{-2}$	$8.84 \cdot 10^{-2}$
Methane	$9.80 \cdot 10^{-2}$	$1.20 \cdot 10^{-1}$	$2.84 \cdot 10^{-2}$	$3.25 \cdot 10^{-2}$	$2.87 \cdot 10^{-2}$	$3.24 \cdot 10^{-2}$
Carbon Dioxide	$8.65 \cdot 10^{-2}$	$7.93 \cdot 10^{-2}$	$1.29 \cdot 10^{-1}$	$1.18 \cdot 10^{-1}$	$1.08 \cdot 10^{-1}$	$1.06 \cdot 10^{-1}$
Ethylene	$4.87 \cdot 10^{-4}$	$1.16 \cdot 10^{-3}$	$3.03 \cdot 10^{-3}$	$3.65 \cdot 10^{-3}$	$8.20 \cdot 10^{-3}$	$9.82 \cdot 10^{-3}$
Acetylene	$1.63 \cdot 10^{-4}$	$7.54 \cdot 10^{-4}$	$6.27 \cdot 10^{-3}$	$1.00 \cdot 10^{-2}$	$2.33 \cdot 10^{-3}$	$3.75 \cdot 10^{-3}$
Ethane	$1.11 \cdot 10^{-3}$	$2.03 \cdot 10^{-3}$	$9.99 \cdot 10^{-4}$	$1.46 \cdot 10^{-3}$	$1.38 \cdot 10^{-3}$	$1.72 \cdot 10^{-3}$
Formaldehyde	$7.95 \cdot 10^{-4}$	$9.55 \cdot 10^{-3}$	$2.15 \cdot 10^{-3}$	$2.22 \cdot 10^{-3}$	$2.49 \cdot 10^{-3}$	$2.64 \cdot 10^{-3}$
Propene	$4.59 \cdot 10^{-6}$	$1.23 \cdot 10^{-5}$	$5.71 \cdot 10^{-4}$	$6.77 \cdot 10^{-4}$	$9.91 \cdot 10^{-4}$	$1.10 \cdot 10^{-3}$
Propane	$2.18 \cdot 10^{-5}$	$5.39 \cdot 10^{-5}$	$7.21 \cdot 10^{-5}$	$9.12 \cdot 10^{-5}$	$1.95 \cdot 10^{-4}$	$2.30 \cdot 10^{-4}$
Allene			$5.56 \cdot 10^{-5}$	$7.04 \cdot 10^{-5}$	$1.66 \cdot 10^{-5}$	$2.34 \cdot 10^{-5}$
Propyne			$1.67 \cdot 10^{-4}$	$2.01 \cdot 10^{-4}$	$4.50 \cdot 10^{-5}$	$5.59 \cdot 10^{-5}$
Dimethyl Ether	$1.58 \cdot 10^{-5}$	$2.42 \cdot 10^{-5}$	$2.87 \cdot 10^{-5}$	$3.71 \cdot 10^{-5}$	$4.79 \cdot 10^{-5}$	$5.56 \cdot 10^{-5}$
Methyl alcohol	$1.89 \cdot 10^{-5}$	$1.79 \cdot 10^{-5}$	$1.79 \cdot 10^{-4}$	$2.05 \cdot 10^{-4}$	$2.55 \cdot 10^{-4}$	$2.42 \cdot 10^{-4}$
Acetaldehyde	$1.85 \cdot 10^{-5}$	$3.93 \cdot 10^{-5}$	$2.11 \cdot 10^{-3}$	$2.33 \cdot 10^{-3}$	$2.84 \cdot 10^{-4}$	$2.74 \cdot 10^{-4}$
Isobutane			$4.70 \cdot 10^{-6}$	$5.12 \cdot 10^{-6}$	$6.54 \cdot 10^{-6}$	$6.95 \cdot 10^{-6}$
Isobutene			$6.42 \cdot 10^{-6}$	$7.87 \cdot 10^{-6}$	$3.96 \cdot 10^{-6}$	$4.39 \cdot 10^{-6}$
1-butene			$6.84 \cdot 10^{-5}$	$9.46 \cdot 10^{-5}$	$2.10 \cdot 10^{-4}$	$2.52 \cdot 10^{-4}$
1.3-butadiene			$8.06 \cdot 10^{-5}$	$1.21 \cdot 10^{-4}$	$4.08 \cdot 10^{-5}$	$5.63 \cdot 10^{-5}$
1.2 butadiene			$5.54 \cdot 10^{-6}$	$9.24 \cdot 10^{-6}$		
Trans-2-butene			$4.78 \cdot 10^{-5}$	$6.06 \cdot 10^{-5}$		
Cis-2-butene			$3.54 \cdot 10^{-5}$	$4.66 \cdot 10^{-5}$	$1.31 \cdot 10^{-5}$	$1.84 \cdot 10^{-5}$
Butane					$2.23 \cdot 10^{-4}$	$2.48 \cdot 10^{-4}$
Methoxyethane					$6.78 \cdot 10^{-6}$	$8.02 \cdot 10^{-6}$
2-butyne			$4.91 \cdot 10^{-6}$	$8.06 \cdot 10^{-6}$		
Propylene Oxide					$1.83 \cdot 10^{-5}$	$1.67 \cdot 10^{-5}$
Acrolein			$1.31 \cdot 10^{-3}$	$1.46 \cdot 10^{-3}$	$9.36 \cdot 10^{-5}$	$8.41 \cdot 10^{-5}$
Furan			$3.25 \cdot 10^{-2}$	$3.58 \cdot 10^{-2}$	$3.41 \cdot 10^{-5}$	$3.27 \cdot 10^{-5}$
Propanal					$3.45 \cdot 10^{-4}$	$3.81 \cdot 10^{-4}$
Acetone					$2.47 \cdot 10^{-5}$	$1.72 \cdot 10^{-5}$
Iso-pentane			$3.23 \cdot 10^{-6}$	$3.55 \cdot 10^{-6}$		
1-butene-3-methyl			$5.26 \cdot 10^{-6}$	$7.97 \cdot 10^{-6}$	$6.01 \cdot 10^{-6}$	$6.89 \cdot 10^{-6}$
1-butene-2-methyl			$6.07 \cdot 10^{-7}$	$1.00 \cdot 10^{-6}$		
Ethyl-Cyclopropane					$8.95 \cdot 10^{-6}$	$1.01 \cdot 10^{-5}$
1.3-cyclopentadiene			$8.56 \cdot 10^{-6}$	$1.37 \cdot 10^{-5}$		
2-pentene			$3.59 \cdot 10^{-5}$	$3.86 \cdot 10^{-5}$	$1.72 \cdot 10^{-5}$	$1.72 \cdot 10^{-5}$
Allylic alcohol			$2.90 \cdot 10^{-5}$	$3.68 \cdot 10^{-5}$	$2.78 \cdot 10^{-5}$	$2.89 \cdot 10^{-5}$
2,3-dihydrofuran					$2.38 \cdot 10^{-4}$	$2.28 \cdot 10^{-4}$
Trans-1.3-pentadiene			$5.57 \cdot 10^{-6}$	$6.46 \cdot 10^{-6}$		
Cis-1.3-pentadiene			$2.00 \cdot 10^{-6}$	$2.87 \cdot 10^{-6}$		
Isobutenal			$9.33 \cdot 10^{-6}$	$1.04 \cdot 10^{-6}$		
1-propanol					$7.70 \cdot 10^{-6}$	$6.38 \cdot 10^{-6}$
Isobutanal			$7.57 \cdot 10^{-5}$	$9.65 \cdot 10^{-5}$	$8.33 \cdot 10^{-6}$	$7.98 \cdot 10^{-6}$
2.5-dihydrofuran					$3.84 \cdot 10^{-5}$	$3.74 \cdot 10^{-5}$

Methyl vinyl ketone			$1.43 \cdot 10^{-5}$	$1.57 \cdot 10^{-5}$		
Tetrahydrofuran					$2.82 \cdot 10^{-2}$	$3.32 \cdot 10^{-2}$
Furan 2 methyl			$1.38 \cdot 10^{-5}$	$1.34 \cdot 10^{-5}$		
Butanal			$4.73 \cdot 10^{-6}$	$4.72 \cdot 10^{-6}$		
Furan-3-methyl			$1.64 \cdot 10^{-5}$	$1.38 \cdot 10^{-5}$		
Cyclopropanacarboxaldehyde					$2.03 \cdot 10^{-5}$	$2.80 \cdot 10^{-5}$
2-butenal			$1.48 \cdot 10^{-4}$	$1.23 \cdot 10^{-4}$	$1.52 \cdot 10^{-5}$	$1.83 \cdot 10^{-5}$
1-hexene					$6.78 \cdot 10^{-6}$	$8.49 \cdot 10^{-6}$
Hexane					$5.30 \cdot 10^{-6}$	$6.49 \cdot 10^{-6}$
Benzene			$7.92 \cdot 10^{-6}$	$1.35 \cdot 10^{-5}$		
2-methyl tetrahydrofuran					$1.56 \cdot 10^{-5}$	$1.88 \cdot 10^{-5}$
3-methyl tetrahydrofuran					$2.01 \cdot 10^{-5}$	$2.36 \cdot 10^{-5}$
4-pentenal					$1.10 \cdot 10^{-5}$	$1.46 \cdot 10^{-5}$
Pentanal					$1.23 \cdot 10^{-5}$	$1.49 \cdot 10^{-5}$
1,3-dioxene					$4.45 \cdot 10^{-5}$	$3.43 \cdot 10^{-5}$
2-pentenale			$1.11 \cdot 10^{-5}$	$1.24 \cdot 10^{-5}$		
Butanedial			$6.08 \cdot 10^{-5}$	$4.09 \cdot 10^{-5}$	$2.89 \cdot 10^{-5}$	$2.42 \cdot 10^{-4}$
Hydrogen	$3.21 \cdot 10^{-2}$	$5.44 \cdot 10^{-2}$	$2.42 \cdot 10^{-2}$	$3.54 \cdot 10^{-2}$	$2.52 \cdot 10^{-2}$	$3.64 \cdot 10^{-2}$
Oxygen	$2.05 \cdot 10^{-1}$	$2.03 \cdot 10^{-1}$	$1.99 \cdot 10^{-1}$	$1.86 \cdot 10^{-1}$	$2.13 \cdot 10^{-1}$	$1.98 \cdot 10^{-1}$
Nitrogen	$7.14 \cdot 10^{-1}$	$6.81 \cdot 10^{-1}$	$7.04 \cdot 10^{-1}$	$6.86 \cdot 10^{-1}$	$6.86 \cdot 10^{-1}$	$6.91 \cdot 10^{-1}$

Table.C.1: Experimental maximum value of each species detected in each flame.

Résumé

Impact de l'oxydation des biocarburants lignocellulosiques sur la formation des oxydes d'azote dans les flammes laminaires prémélangées.

La lutte contre le réchauffement climatique et la raréfaction des ressources pétrolières conduisent à un intérêt croissant pour les énergies renouvelables. Les composés furaniques, qui peuvent être produits à partir de biomasse lignocellulosique, présentent des propriétés de combustion comparables à celles des carburants commerciaux. L'utilisation de ces composés peut représenter une alternative aux combustibles fossiles. Il est cependant nécessaire d'évaluer leur effet sur la formation d'émissions polluantes. Très peu d'études ont considéré leur impact sur la formation des oxydes d'azote (NO_x), qui constituent une grande famille de polluants dans les procédés de combustion et jouent un rôle crucial dans la chimie de l'atmosphère. Ce travail de thèse porte sur le rôle de l'oxydation des biocarburants lignocellulosiques dans la cinétique de formation des oxydes d'azote. Les objectifs de ce travail de thèse sont (i) étudier la cinétique d'oxydation des éthers insaturés et saturés, furane et tétrahydrofurane (THF) afin de disposer d'une base de données expérimentales en condition de flamme laminaire de pré-mélange, (ii) tester des mécanismes cinétiques détaillés de l'oxydation de ces biocarburants disponibles dans la littérature sur la formation du NO précoce. Six flammes laminaires prémélangées à basse pression (5.3 kPa) ont été étudiées en conditions stœchiométriques et légèrement riches ($\varphi = 1.2$). Les compositions de combustible considérées sont : (i) le méthane pur, qui est utilisé comme flammes de référence, (ii) un mélange furane (50%) / méthane (50%) pour étudier l'effet du furane, et (iii) un mélange tétrahydrofurane (50%) / méthane (50%) pour évaluer l'impact du THF. La structure de ces flammes a été caractérisée en établissant les profils de fraction molaire des produits et espèces intermédiaires stables en fonction de la distance au brûleur, à l'aide de la chromatographie en phase gazeuse couplée à des détecteurs FID/TCD/MS. Les profils de fraction molaire du NO et du radical CH ont été détectés quantitativement par Fluorescence Induite par Laser (LIF). Les résultats expérimentaux montrent que la structure moléculaire différente de ces éthers cycliques produit des différences significatives dans la formation d'espèces intermédiaires et de polluants. L'oxydation du furane favorise la formation de CH et la formation de NO dans les conditions de richesse examinées par rapport aux flammes de méthane. En revanche, l'oxydation du tétrahydrofurane réduit la formation de CH et la formation de NO dans les

mêmes conditions. Les profils expérimentaux ont été comparés aux profils simulés issus de deux modèles cinétiques détaillés, indiquant des variations notables d'un modèle à l'autre. L'approche préliminaire de modélisation indique que les mécanismes étudiés doivent d'abord être améliorés pour la formation de CH, pour être ensuite couplés avec le sous-mécanisme de formation du NO validé au laboratoire PC2A pour atteindre les objectifs de cette thèse.

Abstract

Impact of lignocellulosic biofuels on NO_x formation in premixed laminar flames

The use of biofuels enables a reduction of the dependence to petroleum-based fuels and should limit the increase of total amount of greenhouse gases emitted in the atmosphere. Unsaturated and saturated cyclic ethers produced from lignocellulosic biomass, such as furan derivatives, or tetrahydrofuran (THF) derivatives, are attractive oxygenated fuels, due to their combustion properties comparable to those of commercial gasolines. The use of these compounds may represent a very interesting alternative to fossil fuels, though their impact on the emissions of pollutants needs further experimental and theoretical evaluations. Few studies have considered their effect on the formation of nitrogen oxides (NO_x), which is an important family of pollutants in combustion processes and play a crucial role in atmospheric chemistry. This work investigates the role of oxidation of lignocellulosic biofuels in the formation of nitrogen oxides (NO_x) in flames. The objectives of this thesis are (i) to study the oxidation of unsaturated and saturated ethers, furan and tetrahydrofuran (THF) in order to have an experimental database under premixed laminar flame conditions, (ii) to test detailed kinetic mechanisms available in literature of oxidation of these biofuels on the prompt-NO mechanism. Six premixed low-pressure laminar flames (5.3 kPa) were studied under stoichiometric and slightly rich conditions ($\phi = 1.2$). The considered fuel compositions are: (i) pure methane, which is used as a reference flame, (ii) a furan (50%) / methane (50%) mixture to study the effect of furan, and (iii) tetrahydrofuran (50%) / methane (50%) to evaluate the impact of THF. The structure of these flames was characterized by establishing the mole fraction profiles of stable intermediates and products as a function of the height above the burner (HAB), using gas chromatography coupled with FID / TCD/ MS detectors. The mole fraction profiles of NO and CH radical were quantitatively detected by Laser Induced Fluorescence (LIF). The experimental results show that the different molecular structure of these cyclic ethers leads to significant differences in the formation of intermediate species and pollutants. For CH and NO, results show that oxidation of furan promotes CH and NO formation with respect to methane flames, whereas oxidation of tetrahydrofuran reduces the formation of CH and NO in the same conditions. The experimental profiles were compared with the simulated profiles using two detailed kinetic models. Significant variations from one

model to another are found. The preliminary modeling study indicates that the studied mechanisms require some improvements on the prediction of CH formation, before being coupled with the sub-mechanism of NO formation validated in the PC2A laboratory for fulfilling the aims of this thesis.

